Synthesis and Polymerization of Monomer Building Blocks from Sustainable Raw Materials

Dissertation

Submitted to the

University of Hamburg

Department of Chemistry

With the Aim of Achieving the Doctoral Degree

at the Faculty of Mathematics, Informatics and Natural Sciences

Sarah-Elisabeth Gertrud Dechent

Hamburg 2023

The following evaluators recommend the admission of the dissertation:

1. Evaluator: Prof. Dr. G. A. Luinstra
2. Evaluator: Priv. Doz. Dr. C. Wutz

Oral Defense Committee:

Prof. Dr. G. A. Luinstra

Prof. Dr. P. Burger

Dr. W. Pauer

Date of Oral Defense: 9th June 2023

Date of Approval to publish: 19th December 2023

The experimental work described in this thesis was carried out at the Institute for Technical and Macromolecular Chemistry of the University of Hamburg in the group of Professor Dr. Gerrit A. Luinstra from July 2016 to end of 2020.

List of Publications

1. **Fully bio-derived CO$_2$ polymers for non-isocyanate based polyurethane synthesis**
   Sarah-Elisabeth Dechent, Arjan W. Kleij, Gerrit A. Luinstra
   Green Chem., 2020, **22**, 969, DOI: 10.1039/c9gc03488a

2. Antonella Pizzolante, Sarah-Elisabeth Dechent, Arjan W. Kleij, Christopher M. Kozak (2019). 16. Sustainable feedstock for conversion of CO$_2$ to cyclic and polycarbonates. In Michael North, Peter Styring (Eds.), *Transformations* (pp. 303–328). Berlin, Boston: De Gruyter. https://doi.org/10.1515/9783110665147-016

Table of Content

List of Abbreviations

APC	Aliphatic Polycarbonate
CA	Complexing Agent
co-CA	Co-complexing Agent
cPC	Cyclic Propylene Carbonate
CTA	Chain Transfer Agent
Đ	Dispersity
DCM	Dichloromethane
DMC	Double Metal Cyanide
DSC	Differential Scanning Calorimetry
e.g.	For Example *or* Exempli Gratia (lat.)
EA	Elemental Analysis
EDX	Energy Dispersive X-ray Spectroscopy
EP	Epoxide-value
eq.	Equation
FTIR	Fourier-transform Infrared
g	Gram
GHS	Globally Harmonized System of Classification, Labelling and Packaging of Chemicals
Glu	Glutaric Acid
GPC	Gel Permeation Chromatography
h	Hour
HDA	Hexadecylamine
hh	Head-to-head
ht	Head-to-tail
i.e.	That Is *or* Id Est (lat.)
L	Liter
M	Molar
MALDI	Matrix-assisted Laser Desorption/Ionisation
MEK	Methyl Ethyl Ketone
mL	Milliliter
M_n	Number Average Molar Mass
MS	Mass Spectrometry
M_w	Mass Average Molar Mass
NH_3-TPD	Temperature-programmed Ammonia-desorption
NIPU	Non-isocyanate Polyurethane
NMR	Nuclear Magnetic Resonance

ODA	1,8-Octanediamine; Octadecylamine
PBD	Polybutadiene
PC-PBD	Partly Carbonated Polybutadiene
PDA	1,5-Pentanediamine; Cadaverine
PDI	Polydispersity Index
PE-PBD	Partly Epoxidized Polybutadiene
PO	Propylene Oxide
PPC	Poly(propylene Carbonate)
ppm	Parts Per Million
PPN-Br	Bis(triphenylphosphine)iminium Bromide
PPN-Cl	Bis(triphenylphosphine)iminium Chloride
PPN-I	Bis(triphenylphosphine)iminium Iodide
PU	Polyurethane
RDS	Rate Determining Step
RT	Room Temperature
SEC	Size-exclusion Chromatography
SEM	Scanning Electron Microscopy
TBA	*tert*-Butyl Alcohol
TBAB	Tetra-*n*-butylammonium Bromide
TBAC	Tetra-*n*-butylammonium Chloride
TBAI	Tetra-*n*-butylammonium Iodide
T_d	Decomposition Temperature
T_g	Glass-transition Temperature
TGA	Thermogravimetric Analysis
THF	Tetrahydrofuran
T_m	Melting Temperature
TOF	Time of Flight
tt	Tail-to-tail
vs.	Versus
wt%	Weight Percent
X	Conversion
x	Molar Fraction (in Solution)
XRD	X-Ray Diffraction
Δ	Delta; Mathematical Difference
Θ	Molar Fraction on the Surface

Zusammenfassung

Die Erderwärmung und die Erschöpfung globaler Ressourcen erfordern die Entwicklung wissenschaftlicher Lösungen, die die sozialen, ökologischen und wirtschaftlichen Errungenschaften des 20. Jahrhunderts auf eine neue Grundlage stellen. Lösungsansätze umfassen die Speicherung und die chemische Reduktion von Kohlenstoffdioxid (CO_2), die Entwicklung umweltschonender Prozesse und Materialien. In dieser Arbeit wird diskutiert, wie CO_2 als Monomerbaustein für die Synthese von biologisch abbaubaren Polypropylencarbonaten (PPC) und als Synthon für die Synthese von nicht-isocyanat basierten Polyurethanen (NIPU) verwendet werden kann.

PPC lässt sich leicht aus Propylenoxid (PO) und CO_2 unter Verwendung heterogener Katalysatoren wie Doppelmetallcyanide (DMC) und Zinkglutarat darstellen. Es ist bekannt, dass große Anteile an Carbonateinheiten und eventuell stereoreguläre Strukturen notwendig sind, um dem Polymer wirtschaftlich relevante Materialeigenschaften zu verleihen, wie u. a. einem angemessenen T_g (Glasübergangstemperatur). Die Mikrostruktur des Polymerprodukts hängt entscheidend vom ausgewählten Katalysator und den gewählten Reaktionsbedingungen (Druck und Temperatur) ab. Um die synthetischen Bemühungen in der Katalysatorsynthese entsprechend zu lenken, bleibt es weiterhin entscheidend den Einfluss der Katalysatorstrukturen und -zusammensetzungen auf die Bildung des Polymerprodukts zu kennen. In einem ersten Projekt wurde der Einfluss der Lewis-Säure mehrerer heterogener Katalysatoren auf die Polymerzusammensetzung und die Mikrostruktur analysiert. Sechs Doppelmetallcyanidkatalysatoren und Zinkglutarat wurden detailliert charakterisiert und als Katalysator für die PPC-Bildung verwendet. Die Lewis-Saurestärke aktiver Zentren wurde mittels NH_3-temperaturprogrammierter Desorption (NH_3-TPD) bestimmt und so vergleichbar gemacht. Der Grad der Azidität korreliert mit den Bindungsenergien der Elektronen in der K 2p Ebene der Metallkerne der DMC-Katalysatoren. Ein Zusammenhang zwischen der Lewis-Säurestärken des Katalysators und dem CO_2-Gehalten und der Regioregularitäten im Polymerprodukt wurde ebenso festgestellt. Beide Polymermerkmale nehmen mit der Lewis-Säurestärke der aktiven Zentren zu. Die Kinetik dieser Reaktion wurde mathematisch, ausgehend von den etablierten Modellen von Langmuir-Hinshelwood und Eley-Rideal analysiert und mit den experimentellen Ergebnissen verglichen. Es zeigte sich, dass ein mikrokinetischer Mechanismus, der einen Protonentransfer von einem Alkohol auf die Katalysatoroberfläche erlaubt und damit die CO_2-Insertion ermöglicht, die Unterschiede in der Wirkung der DMC-Katalysatoren besser beschreibt. Es wird angenommen, dass starke Lewis-Säuren diesen Transfer verstärken und damit zu einer Zunahme an regioregulären Carbonateinheiten beitragen.

In einem zweiten Projekt wurden nicht-isocyanat basierte Polyurethan-Netzwerke aus teil-carboxylierten Polybutadienen und (biologisch abgeleiteten) Diaminen synthetisiert. NIPUs sind umweltfreundliche Alternativen zu herkömmlichen PU-Materialien, da sie die Anwendung

gefährlicher Cyanide und Phosgen umgehen. Die Synthese cyclischer Carbonatkomponenten basiert vermehrt auf der Reaktion von CO_2- und Epoxideinheiten, leidet jedoch an harten Reaktionsbedingungen und langen Reaktionszeiten, da eine effiziente Katalyse nach wie vor fehlt. Vier verschiedene Polybutadiene von niedrigen bis hohen Molekulargewichten und unterschiedlichen Mikrostrukturen wurden teil-epoxidiert. Der Carboxylierungsprozess wurde optimiert und skaliert. Eine detaillierte Strukturanalyse jedes polymeren Intermediates und der Produkte wird bereitgestellt. Metallfreie Bis(triphenylphosphin)iminiumhalogenid (PPN-X)-Salze als Organokatalysatoren zeigten eine nahezu quantitative CO_2-Cycloaddition, die den Zugang zu neuen Arten nachhaltiger Duroplaste ermöglicht.

Abstract

Global warming and the depletion of global resources urge for the development of scientific solutions that can help to preserve social, ecological and economic achievements of the 20th century. Diverse attempts of combating global warming include the capture and chemical reduction of carbon dioxide (CO_2), and the development of biological benign processes. In this work, it will be shown how CO_2 can be used as a monomer building block for the synthesis of bio-degradable poly(propylene carbonate) (PPC) and as a synthon for the synthesis of non-isocyanate polyurethanes (NIPU).

   PPC is easily prepared from propylene oxide (PO) and CO_2 through the mediation of heterogeneous double metal cyanide (DMC) and zinc glutarate (ZnGlu) catalysts. High amounts of carbonate units and stereoregular structures are known to be necessary to provide the polymer with satisfactory material properties, e.g., an adequate T_g (glass transition temperature). The content of carbonate entities in the polymer backbone is crucially dependent on the selected catalyst in relation to the reaction conditions (pressure and temperature). It is useful to gain knowledge on the action of catalysts in regard to their structures and in respect to the composition of the polymer product. The first project of this thesis pertains to mapping the influence of the Lewis acidic nature of several heterogeneous catalysts on polymer composition and microstructure. Six double metal cyanide catalysts next to zinc glutarate were applied and analyzed in detail. Lewis acidities of the catalysts were determined by temperature-programmed ammonia-desorption (NH_3-TPD) measurements. The Lewis acidity is correlated to the K 2p core-level binding energies of the internal metal in the DMC catalysts. A trend was found linking the Lewis acidic strength of the catalyst to the CO_2 contents and regioregularities in the polymer product. Both structural polymer features appear to increase with the Lewis acidic property of the active sites. A mathematical approach to analyzing the kinetics of this reaction, founded on the well-established models of Langmuir-Hinshelwood and Eley-Rideal was elaborated. The experimental findings were discussed within the model prediction. It was found that a proposed microkinetic protonation driven mechanism that depicts a proton transfer from an alcohol to the catalyst surface which consecutively allows for a CO_2 insertion step would describe the differences in the action of the DMC catalysts more accurately. Higher Lewis acidities are regarded to enhance this transfer leading to increased amounts of regioregular carbonate units.

   Non-isocyanate polyurethane (NIPU) networks were synthesized from partly carboxylated polybutadienes and (bio-derived) diamines in a second project. NIPUs are environmentally benign alternatives to conventional PU materials as they exclude the application of hazardous isocyanates or phosgene. The cyclic carbonate component is known to be easily introduced from the combination of CO_2 and epoxide moieties, but the route lacks an efficient catalysis, leaving it with harsh reaction conditions and long reaction times. Metal-free bis(triphenylphosphine)iminium halide (PPN-X) salts as organocatalysts showed virtually quantitative CO_2 cycloaddition providing

access to new types of sustainable thermosets. Thus, four different polybutadienes with low to high molecular weights and various microstructures were partly epoxidized and the carboxylation process was optimized and scaled up. A detailed structural analysis of each polymer precursor and product is provided.

1 Introduction and Theory

Polymeric materials are an important part of our modern society. Their great versatility offers unique material properties which find application in, e.g., electrical and electronic devices, in the modern automobile sector, in construction and/or packaging tasks. As functional additives, they appear mostly unnoticed in daily products such as detergents, cosmetics and pharmaceutical commodities.[1] However, global warming and the depletion of fossil fuels demands the development of also polymeric materials under more sustainable and environmentally friendly reaction conditions.[2] In this regard, carbon dioxide (CO_2) represents a (so-called) renewable non-toxic natural C1 building block of low cost and high abundance. Its versatility has been proven in chemical synthesis.[3–5] Broadly, the use of comparably low toxic materials like CO_2 which is readily available, cheap and non-toxic can be advantageous over current industrial routes which utilize hazardous substances such as dichloromethane and phosgene.[6,7]

Catalysis remains key in polymerization processes forming polyolefins and likewise in producing copolymers from epoxides and carbon dioxide.[1,8] The use of catalysis in post-polymerization modifications (PPMs) further makes it a remarkable tool in the production of tailor-made materials.[1,9] The next Section 1.1. will focus on catalytic methods to afford CO_2-based poly(propylene carbonate) (PPC) using heterogeneous catalysis.

1.1 Catalytic Synthesis of Poly(propylene Carbonate)

Poly(propylene carbonate) (PPC) in a larger context is an aliphatic polycarbonate (APC). It was first reported on by Inoue et al. in 1969.[10] A simple catalyst based on diethyl zinc and water was described to generate copolymers from oxiranes and CO_2. Unlike aromatic bisphenol-A based polycarbonates, which gained much attention since the 1950s, APCs remained commercially quite unexplored until the 1990s. This may be related to their unfavourable physical and mechanical properties for standard applications.[6,11] Much effort has been made since the first report towards the development of new, more efficient catalysts that are also applicable to a wider range of (bio-based) epoxide substrates.[12] Progress in polymerization techniques, functional monomer synthesis and the exploration of many new applications further increased the number of reports on PPC.[7,11,12] Today, PPC is applied in films, foams and fibers.[13] The biocompatibility and (bio)degradability of APCs make them promising candidates for biomedical applications like tissue engineering and drug delivery.[7,14] PPC was further integrated as solid and gel polymeric electrolytes in battery applications. The large fraction of carbonyl groups facilitates salt dissociation and the low glass transition temperature (T_g) favours ion transport. PPC also burns cleanly and completely, and thus can be applied as sacrificial binder in ceramics and electronics fabrication.[7] Low molecular weight polyols with a low percentage of carbonate linkages serve as

feedstock for polyurethane (PU) manufacturing. The latter finds application in the fabrication of foams, adhesives, sealants, coatings and elastomers.[7,13]

1.1.1 Mechanism and Microstructure

The reaction of PO with CO_2 may lead to a plethora of products. Two products of importance for this report are PPC and cyclic propylene carbonate (cPC) (Figure 1a).[12] cPC is formed in the polymerization process after backbiting of an alkoxide or a carbonate chain end, which may be bound to the catalyst surface (pink dotted line, Figure 1b) or in form of an alcohol or carbonic acid after protonation. The copolymerization is initiated by the coordination of the epoxide and the consecutive ring-opening is performed by the attack of a potential nucleophile (green boxes, Figure 1b). The metal alkoxide species may undergo a consecutive CO_2 insertion and a metal-carbonate intermediate is formed. Catalytic repetition of this cycle (another coordinated PO is ring-opened and then CO_2 is inserted) yields perfectly alternating copolymers. However,
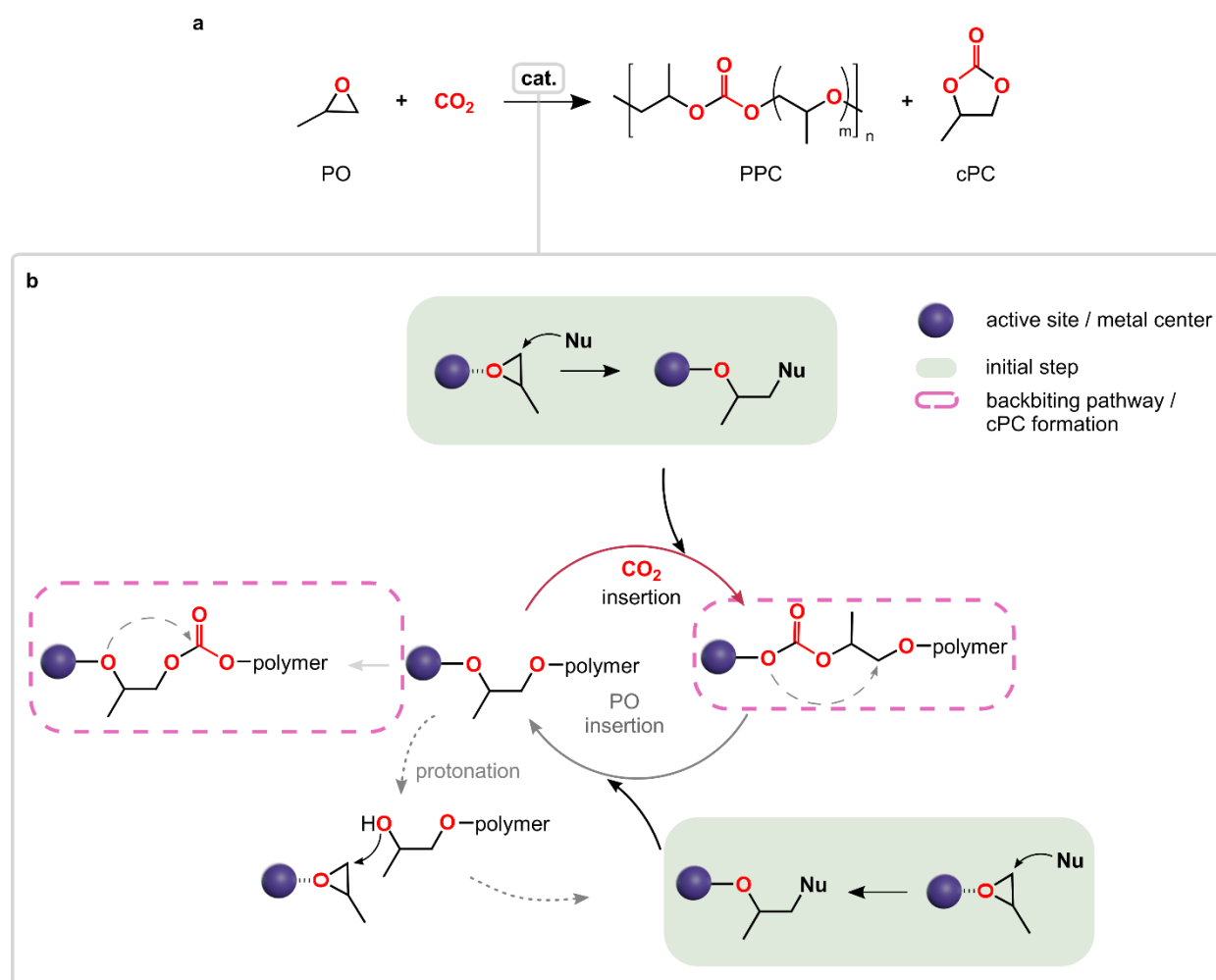

Figure 1. (a) The catalyzed reaction of PO and CO_2 yielding the desired copolymer PPC and the side-product cPC. (b) The catalytic cycle to produce alternating PPC and ether defects (dotted grey arrow) and the backbiting pathway leading to cPC.
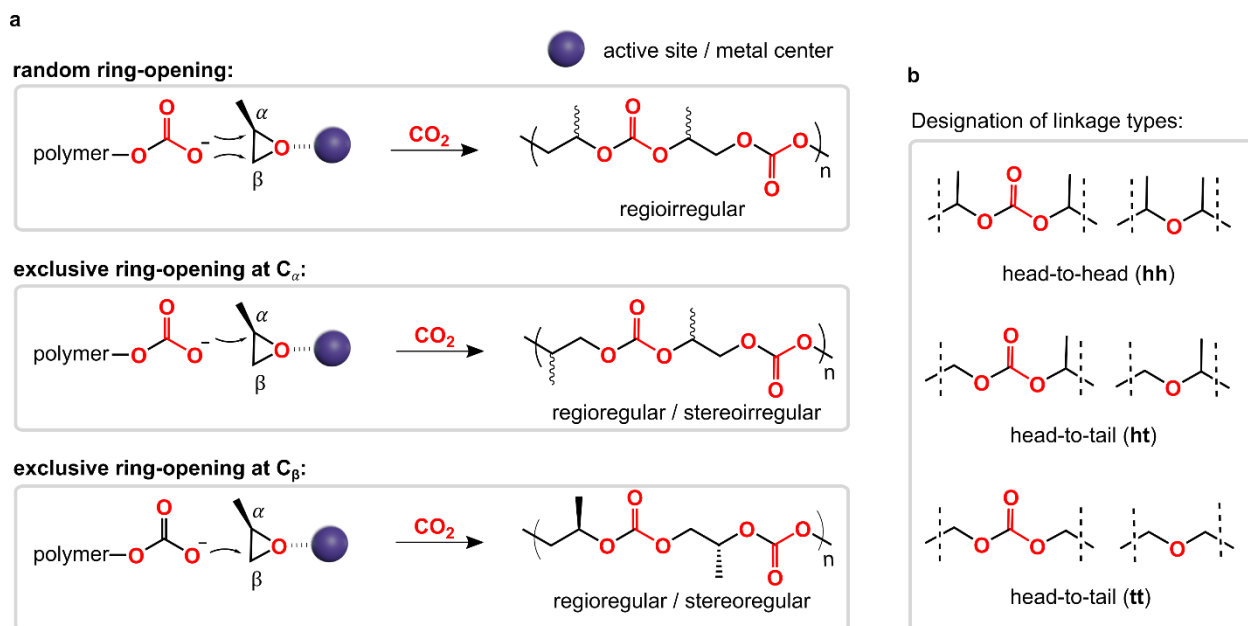
Figure 2. (a) Stereochemistry involved in the copolymerization of (enantiopure) PO and CO_2, and (b) denotation of methyl group orientation in carbonate and ether linkages.

especially on heterogeneous catalysts, longer ether segments form the polymer backbone as successive PO ring-opening is competitive to the CO_2 insertion reaction (grey dotted arrow, Figure 1b).[7] Those ether blocks impact the physical properties as they gradually lower the T_g. Further influence on the material properties is given by the various microstructures of the corresponding PPC products. The PO ring-opening can be performed regioselectively either at the methine C_α-O or the methylene C_β-O position. In either fashion, mainly head-to-tail (ht) linkages are obtained and regioregular chains are formed (Figure 2). In the case of random ring-opening, regioirregular products are obtained and thus substantial concentrations of head-to-head (hh) and tail-to-tail (tt) linkages are expected. Higher concentrations of ht-linkages, are advantageous for a higher T_g.[7,15] Highly regioregular isotactic polymers require regioselective ring-opening at the methylene C_β position of one PO isomer. A T_g of 47°C was reported for isotactic PPC which was found 10 - 12°C higher than that of its atactic analogue.[7]

1.1.2 Catalysts

PPC is readily synthesized by the action of homogeneous and heterogeneous catalysts. Typical homogeneous catalysts comprise, e. g., metalloporphyrins, zinc phenolates, zinc phenoxides, β-diiminate zinc alkoxides and amides, metal-salen or -salan complexes next to bimetallic macrocyclic derivatives.[7,13] The active centers of homogeneous complexes can be designed by steric and electronic properties of the ligands. Those engineered catalysts may be highly active, possess high stereo- and enantioselectivities in the PO ring opening and provide narrow molecular weight distributions.[7,16] However, from a technical point of view, these homogeneous catalysts hold enough of drawbacks to challenge their usefulness in industrial processes.[17] The

reagents for their synthesis are usually expensive, the synthetical procedures are complex and careful handling of the air/moisture sensitive components is needed. Additionally, the separation of the catalysts from the bulk appears mostly way too expensive for positive economics of production. Mainly heterogeneous catalysis is thus applied in industrial production of commodities or commodity-like products. Most commonly used heterogeneous catalysts for the manufacture of PPC are zinc glutarate (and other zinc carboxylates) and double metal cyanides, next to undefined mixtures of rare-earth metal coordination compounds from the combination of zinc alkyls and protic reagents (all with elaborate work-ups).[7,13]

Zinc glutarate. Many improvements on zinc-based catalysts were attained since the pioneering work of Inoue. The discovery of the catalytic action of zinc glutarate (ZnGlu)[18] in 1981 from the reaction of zinc hydroxide and glutaric acid in acetone appeared to be one breakthrough in heterogeneous catalysis. This catalyst showed to be highly active and economically viable. Today, a couple of industrial processes rely on ZnGlu (readily synthesized from zinc oxide and glutaric acid) and other polycarboxylate zinc complexes owing to their inexpensive, benign components and robust nature. Much work was invested in recent years to further enhance the activity and selectivity of ZnGlu. Various synthetic routes, alternative zinc and glutarate sources, additives and stirring methods were screened for improvements. Studies implied that high crystallinity and large surface areas are crucial for catalytic acivities.[6,13,16] The structure of ZnGlu was determined by single-crystal X-ray diffraction measurements.[19] ZnGlu has a layered organization of alternating zinc and glutarate ions in which each zinc is tetrahedrally coordinated by four oxygen atoms provided by four different glutarate moieties. The interactions of PO and CO_2 with the ZnGlu surface were investigated by near edge X-ray absorption spectroscopy (NEXAFS) which revealed that both, CO_2 and PO bind reversibly to the surface. A PO-Zn bond was formed prior to the CO_2 insertion into the Zn-O bond.[20] These observations suggest a PO initiated ZnGlu-catalyzed copolymerization. The interpretation is in good agreement with studies on well-defined organometallic derivatives.[21]

Double metal cyanides. Double metal cyanides (DMCs) show excellent activities in polyether polyol production proving them highly suitable for PO activation.[16] Kruper and Swart[22] from Dow Chemical Company pioneered the CO_2/PO copolymerization reaction by applying a Zn-Fe^{III}-DMC catalyst in 1985. Various DMC catalysts were developed for CO_2-based copolymer applications since then.[6,13,14,16] DMCs are Prussian blue analogues. They exhibit a coordinated polymeric inorganic structure with the general formula $M^1_m[M^2(CN)_6]_n \cdot xH_2O$. The corresponding three-dimensional framework is formed via several cyano-bridges between the M^1 and M^2 metal centers (blue sphere (M_1) and green sphere (M_2), Figure 3a). $[M^2(CN)_6]_n$ vacancies may occur.[14,16] These inorganic polymers are easily varied in composition, stoichiometry and electronic properties. The number of vacancies, for instance, is influenced by the stoichiometry and thus the oxidation state of the metal atoms. Divalent metal ions such as Zn^{2+}, Fe^{2+}, Co^{2+}, Ni^{2+} are

commonly chosen for the M^1 position. The M^2 role is usually taken by the transition metal ions: Fe^{2+}, Fe^{3+}, Co^{2+}, Co^{3+}, Ni^{2+} and so on.[16] The M^1 metal is broadly considered to be the active site on the catalyst surface as its coordination is unsatured.[14] Today, several crystalline structures are known in DMC catalysts. They comprise cubic, monoclinic, hexagonal, and rhombohedral formations.[16] DMCs are readily prepared by precipitation reactions. Typically, an aqueous solution of a metal halide is reacted with an aqueous solution of a hexacyano metallate or vice versa.[6,16] The addition of complexing agents (CAs, coordinating organic molecules) enhances the catalytic activity. CAs can be employed during the crystallization step or the subsequent washing procedure. Surfactants (denoted as co-complexing agents or co-CAs) are further used to induce mesoporosity. They act as capping agents and prevent crystal growth. A catalyst with a favourable, large surface area is obtained. Depending on the synthetic procedure, CAs and co-CAs are incorporated into the catalyst and might coordinate directly to the M^1 metal center.
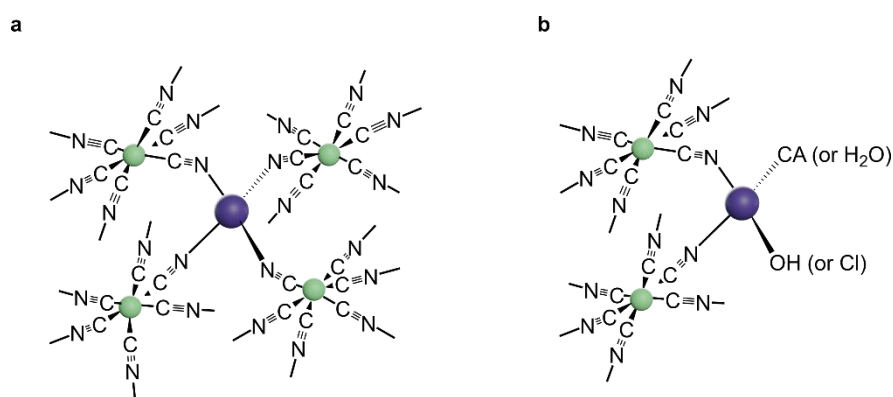

Figure 3. (a) Bulk structure of a type of DMC catalysts and (b) the proposed coordination of H_2O, CAs, halides, and/or OH^- and so on to the active metal center. The blue and green spheres correspond to M_1 and M_2 in the general formula $M^1_m[M^2(CN)_6]_n$.

Similar applies for other potential ligands such as halides or water (blue sphere, Figure 3b).[16] The ligands affect the electron densities at the M^1 metal centers, alter their Lewis acidity and may have an effect on the activity and selectivity of the catalyst. Additional aspects may further have an influence on the catalyst performance: the combination of cyanometallate/metal halide (or other anions like acetates, sulfates and nitrates) precursors, type of applied CAs and co-CAs, alkali impurities, temperature of synthesis, mode and order of reagent addition, aging time, the resulting degree of crystallinity and type of crystalline phase (usually amorphous materials are preferred), particle size, and so on.[13,14,16] DMCs usually exhibit multiple active sites that cause polymer products with a broad molecular weight distribution (if no chain transfer agent is used), irregular polymer compositions and low molecular weights. Anyway, DMCs still appear valuable for industrial processes due to their low costs, low toxicity, easy preparation, and handling.[13,14]

1.1.3 Initiation Mechanisms

The CO_2/PO copolymerization reaction has been described as promoted by typical initiators such as alcohols or polyols, or by other components in the catalyst mixture (Figure 4). Although no direct evidence is available, it is proposed that an initiator coordinates to the active center and thereafter ring-opens a coordinated PO (Figure 4a). This step is followed by the multiple alternating insertion of CO_2 and subsequent ring-opening of coordinated PO. The polymerization sequence is eventually interrupted by a chain transfer initiated by a (so-called) chain transfer agent (CTA). A rapid and reversible chain transfer leads to a narrow PDI. In the absence of an initiator, the polymerization starts with the coordination of a CO_2 or PO molecule to the active center (Figure 4b). Coordinated CAs such as *tert*-butanol (*t*BuOH, later denoted as TBA), but also

a

Copolymerization in the presence of initiators:

b

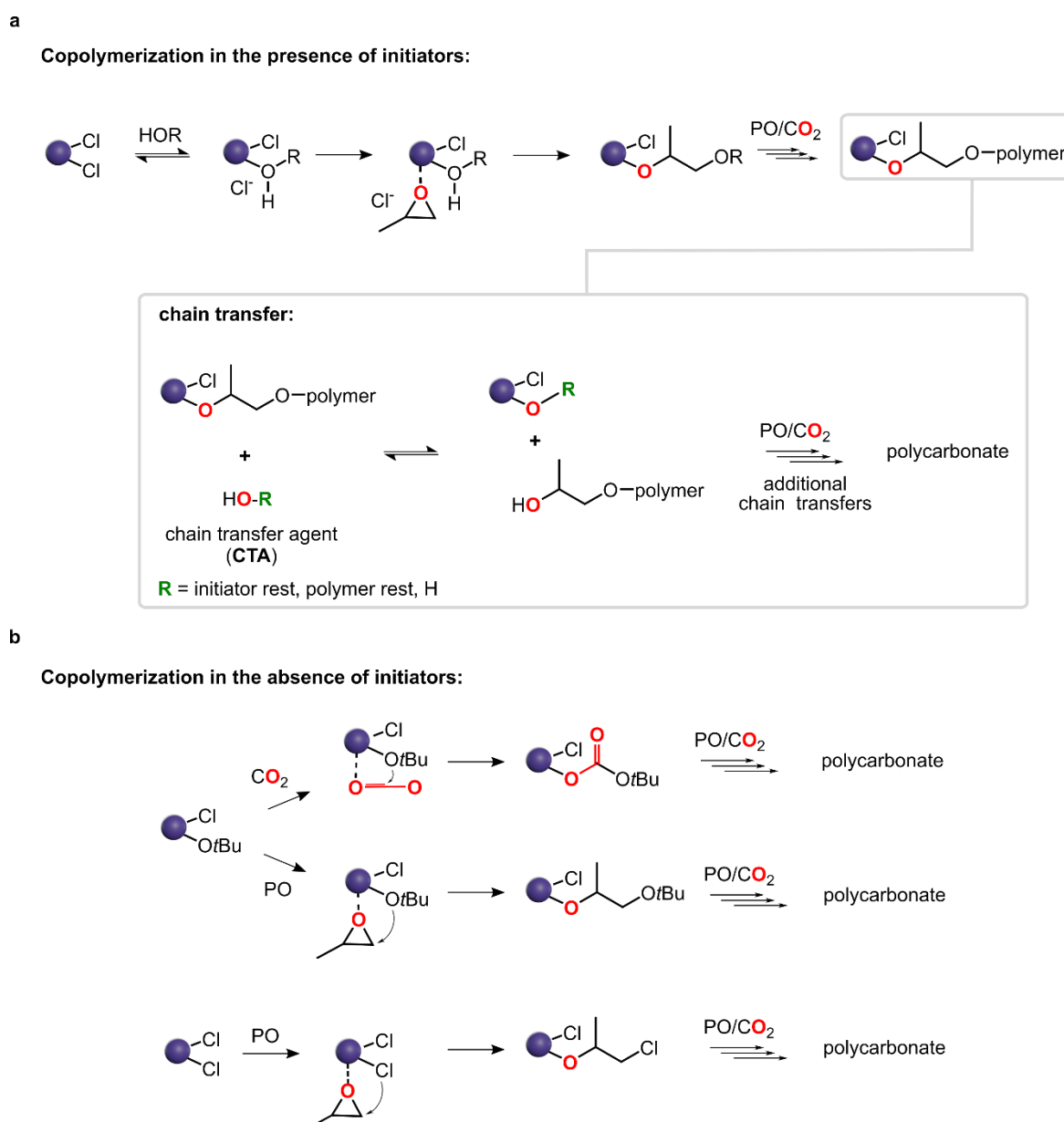Copolymerization in the absence of initiators:

Figure 4. Proposed mechanisms for the activation and propagation of CO_2/PO copolymerization in (a) the presence and (b) the absence of an initiator.

coordinated halides or OH⁻ residues on the metal center may then react with CO_2 and/or PO to initiate the copolymerization. All groups are incorporated into the polymer chains as end groups.[16,23]

1.2 Polybutadienes for Catalytic Sequential Post-modifications

Polybutadienes (PBDs), educts in the second project, were first commercialized in 1920s and represent a global scale commodity. Their high content of easily accessible double bonds enables (industrial) post-polymerization modification (PPM) reactions to form diversified, functionalized structural analogues (Figure 5).[24,25]
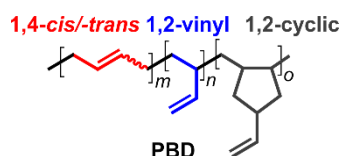

Figure 5. Typical microstructural features of commercial PBDs.

PPM, which is also known as polymer analogues modification, is a powerful tool to produce tailor-made polymers. A library of functionalized analogues can be established providing descendants with the same tacticity, molecular weight of the main chain and similar molecular weight distribution. PPM can provide a selective and quantitative conversion at relative mild conditions and enables a deeper understanding of structure-property relationships. Established modifications comprise addition, substitution, elimination, and isomerization reactions.[26]

PBDs can be readily prepared by anionic and/or radical polymerization techniques and depending on the reaction conditions (temperature, solvent, initiator, catalyst and so on), a variety of different microstructures are obtainable with optional hydroxyl or carboxyl end groups. The physical properties are directly connected to the associated microstructure and molecular weight of each type of PBD. Despite the relatively high reactivities of the double bonds toward additions, differences were noted between the 1,4-*cis*, 1,4-*trans*, 1,2-vinyl and 1,2-cyclic moieties. Further impact has the relative position of each entity on the polymer backbone and the applied type of modification. For instance, neighbouring groups in hydrogenation reactions may affect the result.[25]

PBDs are frequently used in tire manufacturing and in (styrene-based) plastics as impact modifiers. However, their strong hydrophobicity limits their scope of applications as they show not to be compatible with inorganic substrates or common reagents such as water. (Sequential) PPM represents an interesting method to tune properties and structures and thus allows for the production of tailor-made PBD based materials.[25]

1.2.1 Epoxidation as an Attractive Intermediate Step

Common options for PPM using PBDs as platform polymers comprise hydrogenation, isomerization, π-bond metathetical reactions, oxidation reactions to form oxo derivatives, and epoxidation. Epoxidation reactions give reactive intermediates for further sequential PPM modifications. Epoxidizing agents are typically *meta*-chloro peroxy benzoic acid (*m*-CPBA), dimethyl dioxirane (DMD) (freshly distilled or prepared in-situ by reacting of acetone with the potassium monopersulfate compound Oxone®), peroxides or DMD in combination with transition metal catalysts, or in situ prepared percarboxylic acids. The latter may be accessed from the corresponding carboxylic acid and hydrogen peroxide. This reaction is favoured in large scale and industrial applications, also on account of costs. The save application of percarboxylic acids is in a biphasic system of water and hydrocarbons or chlorinated solvents that dissolve the PBDs (Figure 6). In general, peracids show higher solubilities in the organic phase where it oxidizes the PBD double bonds. The resulting carboxylic acid subsequently transfers to the aqueous phase and undergoes a "recharge" by the hydrogen peroxide through a transesterification reaction. Catalytic amounts of the carboxylic acids are sufficient to convert up to 70 % of the double bonds without major side-reactions or gelling of the polymer. Higher amounts of the acid catalysts are unfavorable as the selectivity of the epoxidation suffers. The ability of formic acid to autocatalyze its peracid formation makes it the most attractive choice for such epoxidizing systems.[25] However, the application of acetic or propionic acid has also been described.[27] On a laboratory scale, the solvents dichloromethane or chloroform are preferred as higher polarities generally improve the reaction rates. Toluene is favoured at larger scales even though its π-donor aromaticity competes with the olefin for the coordination to the positively charged acidic carbonyl carbon. Surfactants or phase transfer agents can lead to an enhancement of reaction rates.[25]

Different reaction rates for undergoing epoxidation for the various types of double bonds in the PBDs can be expected. The electrophilic oxygen atom will react significantly faster with the
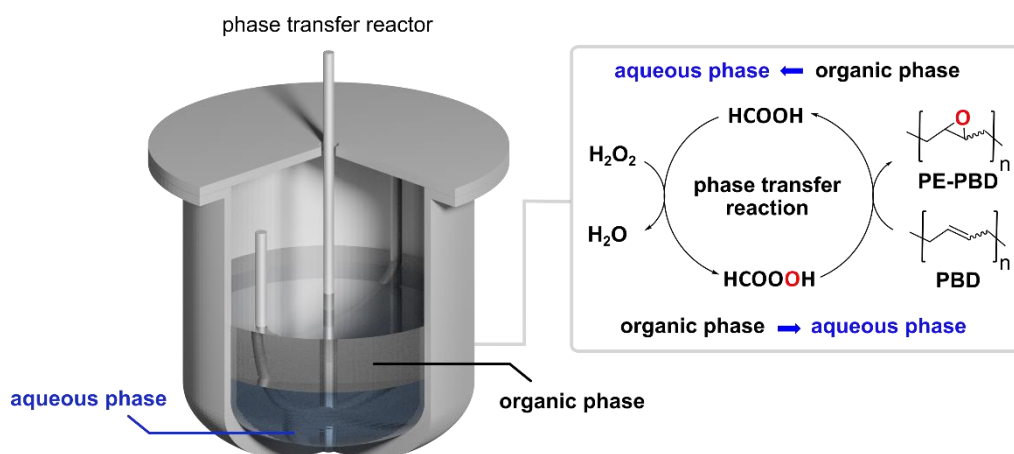

Figure 6. Reactor set-up and mechanism of the phase transfer reaction for the epoxidation of PBD using hydrogen peroxide and formic acid.
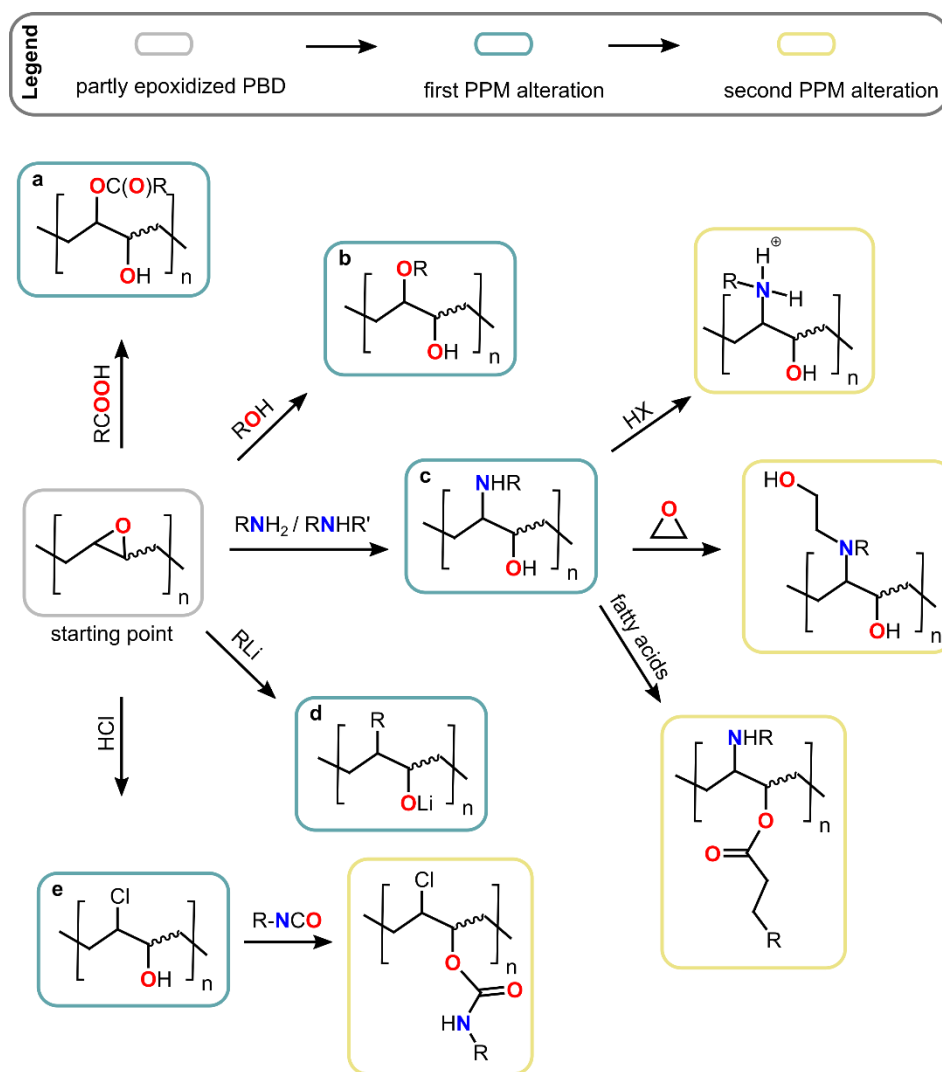
Figure 7. Stepwise functionalization of (partly) epoxidized PBDs to yield (a) hydroxy esters, (b) poly-α-hydroxyl ethers, (c) hydroxy amines, (d) lithium alkoxides, and (e) chlorinated *sec.* alcohols. Second PPM reactions (yellow) aim, for instance, to yield quaternary amines or isocyanates.

electron-rich disubstituted 1,4-*cis* and -*trans* double bonds. For instance, performic and peracetic acids are not capable of converting 1,2-vinylic moieties in anionically synthesized PBDs. The difference in reactivity between the two types of 1,4-substituted units is much smaller and may vary with the PBD used.[25]

Several steps in sequential PPM are feasible for partly epoxidized PBDs (PE-PBDs, Figure 7). PE-PBDs are predominantly used for epoxy resins in which curing is performed by the (nucleophilic) addition of amines, carboxylic acids, anhydrides, or Lewis acids. Non-cross-linking reactions further include the addition of alcohols, organo-lithium groups, carboxylic acids, and so on. Radical cross-linking is typically prevented. The amine modification allows for water compatibility and is used in industry to produce PBD based aqueous coating dispersions, additives for shampoos and hair cosmetic products, flocculation agents (PBD based quaternary amine derivatives produced from *tert.* amines) for water treatment applications, and polycations.

PE-PBDs can react with hydrogen chloride yielding polyols, which are subsequently used for PU formation.[25]

Catalysis is mostly the key for the addition of carboxylic acids (to form hydroxy esters) and alcohols (to form poly-α-hydroxyl ethers) or at least remains advantageous for many applications. Hydroxy esters and poly-α-hydroxyl ethers are used as additives in lubricants and in mineral oils to, for example, prevent corrosion, enhance the viscosity, or act as detergents.[25]

1.3   Principles in Homogeneous and Heterogeneous Catalysis

Roughly 75 % of industrial chemical transformations are catalyzed reactions and nearly 90 % of newly developed processes contain catalytic steps.[28] Catalysis enables the diversion of reaction paths and to reach equilibrium. It enhances the reaction kinetics, but leaves the thermodynamics untouched.[29,30] Catalysis can be performed under various conditions (in liquids or gases) and it is common to distinguish between three types of catalysis: homogeneous, heterogeneous and biocatalysis.[29,30] The former two will be applied in this work.

1.3.1   Homogeneous Catalysis

Homogeneous catalysis refers to a reaction in which both, the catalyst and the reactants are in the same phase. Reactions in liquid media are most common.[28–30] The catalysts are mostly well-defined, i.e., in terms of chemical composition and structure. Techniques such as NMR spectroscopy or in situ IR techniques allow to study reaction kinetics and/or reaction pathways by the identification of intermediates under operating conditions. Homogeneous catalysts can be tuned to show high activities and selectivities. Reaction steps are, in contrast to heterogeneous counterparts, mostly not impeded by mass-transfer limitations. Organometallic complexes are a common type of homogeneous catalysts in industry for the production of fine or bulk chemicals.[28,29] However, the number of commercialized homogeneous catalysts remains rather small as complicated recovery and recycle processes are mostly involved. Such catalysts are usually too costly to remain in the product or would cause problems in applications.[29]

Organocatalysis. Homogeneous organocatalysts are soluble organic compounds which usually contain C, H, O, N, S, and/or P atoms. This type of homogeneous catalysis belongs to the group of classic acid/base catalysis as its catalytic molecules generally show typical Brönstedt and Lewis acid and/or base characteristics. These catalysts are of low-cost, readily available, less toxic, and mostly air- and water-stable. The lack of a metal atoms avoids metal separation and recovery. The main interest in homogeneous catalysis is still concentrated on organometallic compounds. However, more attention is given to organocatalysis.[29,31,32] Representative examples

10

are the Knoevenagel condensation[29], the Suzuki[33] and Sonogashira[34] cross-coupling reactions, and various applications for asymmetric molecule synthesis[29,31,35].

1.3.2 Heterogeneous Catalysis

Heterogeneous catalysis is essential to roughly 90 % of all chemical processes in the chemical, food, pharmaceutical, automobile and petrochemical industry.[29,36] Processes based on heterogeneous catalysts are in general superior to their homogeneous counterparts in industrial application. They are more robust and allow for easy catalyst separation from the gaseous/liquid reactants or products. This allows for continuous flow operations, also under more harsh reaction conditions. Consequently, large-scale industrial processes were established once heterogeneous catalysis was discovered in the early years of the 19th century.[36,37] New applications emerged in the fields of fuel cells, green chemistry, nanotechnology, biorefining, and biotechnology.[36]

Heterogeneous catalysis is complex and interdisciplinary in nature. The development and characterization of (new) catalysts and processes requires the cooperation of chemists, physicists, material scientists, reaction engineers and theorists.[29,36] The state-of-the-art in these interdisciplinary methods is only recently becoming mature enough to fundamentally understand the complex catalytic process happening at the solid/liquid interface. Computational and spectroscopic methods provide important tools to link the catalyst activity and selectivity to chemical structures and compositions. The future goal is the feasibility of predicting the right catalytic material for a desired product/process. But despite of all (computer assisted) achievements in this field, experimental conditions and processes remain far too complex to be properly reflected by the given analytical techniques. However, the experimental data itself, which could be collected by the great number of experiments in the last years, is still highly valuable to identify trends and fits for catalytic materials and processes.[37,38]

Heterogeneous catalytic reactions are typically performed on high temperatures and (if needed) high pressures. An ideal catalyst provides high surface areas for the highest numbers of active sites. The accessibility of the surface is directly connected to the particle size. Small particles are generally preferred due to superior surface to volume ratios but might reveal drawbacks as the surface can be poisoned diminishing the catalyst performance. Additionally, the placement of too small particles in a reactor at high temperatures may result into agglomeration and very high back pressures. Such packing problems are typically addressed by using (porous) supports providing high surface areas (catalyst pellet, Figure 8). These supports are often made up of solids like silica, alumina, or carbon and catalytic active components are finely dispersed onto their surfaces. Mass and heat transfer processes in a bed of catalyst particles are also important. The heat of reaction, for instance, must be dissipated equally throughout the particles and the reactor wall to evade hotspots with the complication of sintering and runaway reactions.
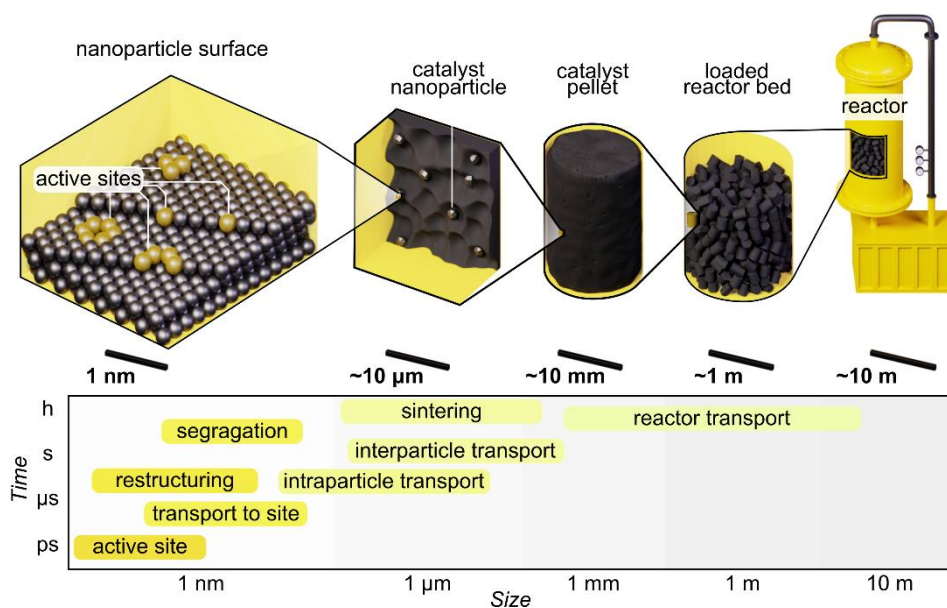
Figure 8. Schematic set-up of a continuous flow reactor and the placement of the heterogeneous catalyst inside. Processes are addressed according to time and size dimension.

Reactants must diffuse through the particles into the catalysts´ pores to adsorb on the surface, to travel to an active site, react which includes formation or conversion of various adsorbed intermediates, likely involving surface diffusing steps, and desorb. Variations in any of these dimensions may alter the outcome of a reaction and explains the increased complexity of heterogeneous catalysis.[29,36,38]

The active sites provide the basis for all heterogeneous catalysis, but it is seldomly the case that all active sites are identical. In addition, industrial heterogeneous catalysts are often amorphous, multiphase solids and/or multicomponent compounds adding to the variety of sites. Those components can show different arrangements in bulk and on the surface. Especially particles on a nanometric scale expose a variation of sites which are associated with terraces, edges, kinks, and vacancies. Operating conditions further change the surroundings of the active sites as surface composition and structure are altered by the process conditions.[29,36]

Mechanisms and theories. In heterogeneous catalysis, it is necessary that at least one reactant is adsorbed to the surface. Langmuir was first to investigate those reactions and formulated in the early years of the 20th century the following equation

$$\theta_A = \frac{K_A p_A}{1+K_A p_A}. \tag{1}$$

It contains the surface coverage θ_A of the species A as a function of its (partial) pressure p_A in the gas phase and an adsorption-desorption equilibrium constant K_A. He assumed all adsorption sites to be equal and that adsorbed molecules do not interact. The adsorption is reversible, and the adsorbate behaves like an ideal gas. An extended case pertains to the competitive adsorption of two molecules A and B:

$$A + * \underset{k_{-1}}{\overset{k_1}{\rightleftharpoons}} A^* \tag{2}$$

and

$$B + * \underset{k_{-2}}{\overset{k_2}{\rightleftharpoons}} B^*. \tag{3}$$

The equilibrium equations consequently are

$$\theta_A = K_A p_A \theta^*, \tag{4}$$

$$\theta_B = K_B p_B \theta^*, \tag{5}$$

and the conservation of sites requires

$$1 = \theta_A + \theta_B + \theta^*. \tag{6}$$

Inserting eq. (4) and (5) into eq. (6) and adding the corresponding transformations, the respective coverages become

$$\theta_A = \frac{K_A p_A}{1 + K_A p_A + K_B p_B}, \tag{7}$$

$$\theta_B = \frac{K_B p_B}{1 + K_A p_A + K_B p_B}, \tag{8}$$

and

$$\theta^* = \frac{1}{1 + K_A p_A + K_B p_B}. \tag{9}$$

Langmuir postulated three reaction mechanisms which today are assigned as follows:

1. **Langmuir-Hinshelwood mechanism**: a reaction takes place between two adsorbed molecules if they find themselves in adjacent active sites (Figure 9a).
2. **Mars-van Krevelen mechanism**: molecules in an adsorbed film react with entities of the underlying solid. The latter is regenerated in a subsequent step.
3. **Eley-Rideal mechanism**: a molecule from the gas phase collides with an adsorbed species on the surface. Adsorbed and non-adsorbed species react and form the product (Figure 9b).

Hinshelwood used the Langmuir isotherm in eq. (1) to explain the reaction kinetics of two molecules adsorbed to a surface. In case the surface reaction is rate determining, the reaction rate of a molecule A and B forming the product AB is given by

$$r = k\theta_A \theta_B \tag{10}$$

with the surface coverage θ_A and θ_B, and the reaction constant k. The number of sites on the catalyst surface is considered to be constant and coverage values add up to unity:

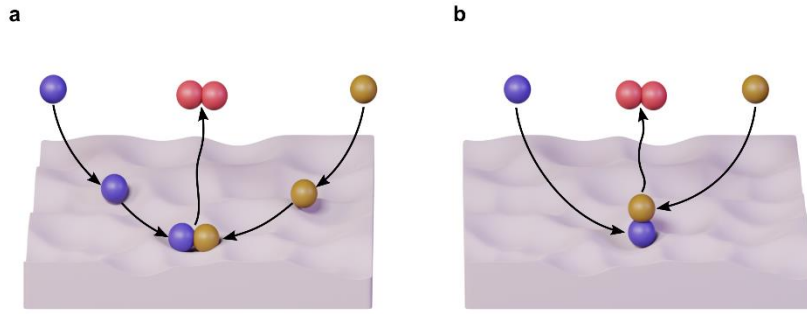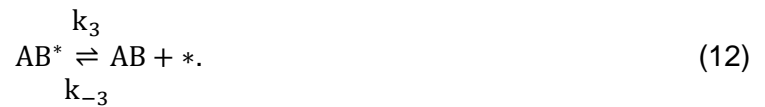$$1 = \theta_A + \theta_B + \theta_{AB} + \theta^*. \tag{11}$$

13

Figure 9. Illustration of a binary reaction according to (a) the Langmuir-Hinshelwood mechanism and (b) the Eley-Rideal mechanism**.**

It should be noted that the product AB is part of the ad- and desorption equilibrium:

$$AB^* \underset{k_{-3}}{\overset{k_3}{\rightleftharpoons}} AB + *. \tag{12}$$

The catalytic action for such systems can either be described numerically or by an approximation leading to a function:

- The **steady-state approximation**, for instance, assumes that the concentration of one reactant remains unchanged (e.g., $\frac{d\theta_A}{dt} = 0$) throughout a reaction.

- The **quasi-equilibrium approximation** supposes that one elementary step determines the overall rate (rate determining step (RDS)). The remaining steps are sufficiently fast and are assumed to be in an equilibrium state. The assumption of several slow steps can be appropriate in other cases as well. The derivation of a function then is more elaborated but may be simpler than a full numerical description.

- The **irreversible step approximation** is used in case that one molecule shows low concentrations e.g., on the surface of the catalyst or in the gaseous phase. The equation can then be simplified by taking out the corresponding reaction step (e.g., readsorption step of the product AB after desorption from the surface).

- The presence of the **MARI** (Most Abundant Reaction Intermediate) might dominate the surface as it binds much stronger than all other reactants. The surface coverage can thus be simplified to

$$\theta_{MARI} = \frac{K_{MARI}p_{MARI}}{1+K_{MARI}p_{MARI}}, \theta_B \cong 0, \theta_{AB} \cong 0, \theta^* \cong 1 - \theta_A. \tag{13}$$

- For the approximation of a **nearly empty surface**, one may correspondingly use

$$\theta^* \cong 1. \tag{14}$$

The proposal of the mechanisms of binary reactions (e.g., Langmuir-Hinshelwood or Eley-Rideal, Figure 9) follows their kinetic description. In fact, Rideal proposed that the reaction can happen between a chemisorbed molecule and molecule from the gas phase or a van-der-Waals layer

above the chemisorbed reactants.[29,30,39] Additionally, those models were used to describe reactions in the liquid phase. However, the kinetic results were often too ambiguous for pinpointing the mechanism.[39] For a perfect solution/solid interface, an analogy to the Langmuir adsorption isotherm describing a binary system was given by Everett:

$$x_B^S = \frac{K_E f}{1 + K_E f}, K_E = \frac{K_B}{K_A}, f = \frac{x_B}{x_A}. \tag{15}$$

It contains the concentrations x_A and x_B of the molecules A and B in the solution, and the corresponding binding constants K_A and K_B.[40]

2 Motivation

2.1 Selectivity and Regioregularity in CO_2/PO Copolymerization Mediated by Heterogeneous Catalysts

Factors of interest for development of a synthetic procedure for CO_2-based polymers are those that influence the catalyst´s activity, selectivity in terms of PO/CO_2 ratio and isotacticity in the PPC product, and induction times.[6,13,14,16,41] As of now, full fundamental understanding of intrinsic properties directing desirable catalytic behaviour of DMC catalysis for CO_2 fixation is missing. The Lewis acidity of DMC catalysts was addressed many times in recent literature for various reaction types such as β-amino alcohols synthesis[42], nitrile synthesis[43], ring-rearrangements[44], ring-opening polymerization reactions of epoxides[45,46], and (trans)esterification reactions[47,48–50] including biodiesel production[51]. Its influence on epoxide/CO_2 copolymers has only been investigated in more detail in a few cases.[52,53] Thus, the accomplishment of a deeper understanding of the structure-activity relationships of DMC catalysts would be of great advantage to access a more rational design to future approaches. Therefore, DMC catalysts with either a zinc or a cobalt as active center should be prepared and systematically mapped in terms of their Lewis acidity derived from physical methods. Trends should be correlated to their catalytic action.

2.2 Preparation of Tunable Non-isocyanate Polyurethanes (NIPU) based on Post-modified Polybutadienes

In the development of synthetic pathways for the valorization of CO_2, it is key to overcome the need for harsh reaction conditions, temperatures, and CO_2 pressures. Therefore, investigations on the influence of various catalytic systems and solvents are of fundamental interest. Epoxide moieties, for instance, are readily reacted with CO_2 to form cyclic carbonates.[3,54,55] In addition to that, to overcome toxic pathways, cyclic carbonates can be made further relevant for the isocyanate and phosgene-free preparation of polyurethane (PU) materials.[54,56–58] So far, only a few studies have been undertaken using partly epoxidized polybutadienes (PBDs) as precursor for the formation of partially carbonated polybutadienes and virtually none were conducted with (bio-derivable) diamines to form NIPUs.[59–61] Partly epoxidized PBDs are already readily used in industry in epoxy resins and are converted into polyols applicable for PU production.[25] Therefore, partly epoxidized PBDs should be regarded as a viable starting point to further investigate various catalytic systems for the efficient CO_2 valorization and consecutive NIPU formation.

3 Results and Discussions

3.1 Selectivity and Regioregularity in CO_2/PO Copolymerization Mediated by Heterogeneous Catalysts

Six different double metal cyanide (**DMC**) catalysts and one zinc glutarate (**ZnGlu**) catalyst were analyzed in detail. Their activity for inducing the CO_2/PO copolymerization yielding copolymers with varying CO_2 contents and microstructures was mapped. The relative Lewis acidities of the catalysts were determined. An analysis of the nature and number of active sites and trends between relative Lewis acidic strengths and CO_2 contents/ht-linkages in the copolymers are presented. Different kinetic models for the CO_2/PO incorporation were mathematically analyzed according to the well-established Langmuir-Hinshelwood and Eley-Rideal mechanisms and compared to the experimental results. An Eley-Rideal mechanism modified with an Everett model approach is discussed in more detail and the model analysis was further extended by the proposal of a microkinetic protonation driven mechanism.

3.1.1 Catalyst Synthesis and Characterization

The **DMC** catalysts were prepared by applying several synthetic routes including the variation of complexing agents (CAs), solvents and metal sources (Figure 10). **Zn-Fe^{II}-** and **Zn-Fe^{III}-DMC** were synthesized in and taken from a previous project[62]. Same applies to **ZnGlu**[62]. **Zn-Ni-** and **Co-Ni-DMC** catalysts were prepared as published.[63,64] The synthetical routes towards **Co-Co-** and **Co-Fe-DMC** are analogously.
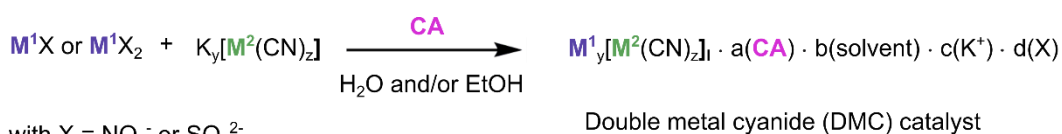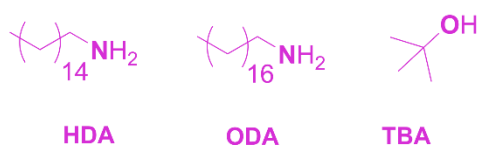

Figure 10. Schematic illustration of the procedures and complexing agents used for the synthesis of **ZnGlu** and the DMC catalysts **Zn-Fe^{II}-**, **Zn-Fe^{III}-**, **Zn-N**i-, **Co-Ni-**, **Co-Co-**, and **Co-Fe-DMC**.

Table 1. Elemental analysis and estimated precatalyst compositions determined by ICP/elemental analysis techniques.[a]

cat.	ICP-Mass [wt%]			elemental analysis [wt%]					estimated catalyst formulation
	M^1	M^2	K	C	H	N	O	S	
ZnGlu	30.7 ± 0.1	-	-	36.7 ± 0.1	4.61 ± 0.01	0.86 ± 0.0	28.4 ± 0.2	-	$Zn_{1.24}$Glu·0.18HDA·dH$_2$O·eNO$_3^-$ [c]
Zn-Fe^{II}	13.5 ± 0.1	5.33 ± 0.01	0.18 ± 0.00	58.1 ± 0.1	9.15 ± 0.01	11.7 ± 0.03	1.87 ± 0.14	-	$Zn_{2.16}$[Fe(CN)$_6$]·2.52ODA·1.36H$_2$O·0.05K$^+$·0.31NO$_3$ [c]
Zn-Fe^{III}	12.0 ± 0.2	5.94 ± 0.11	0.35 ± 0.08	59.6 ± 0.1	9.24 ± 0.00	11.4 ± 0.02	1.56 ± 0.22	-	$Zn_{3.48}$[Fe(CN)$_6$]$_2$·2.26ODA·xH$_2$O·0.17K$^+$·yNO$_3^-$ [c]
Zn-Ni	27.7 ± 0.2	22.7 ± 0.5	0.05 ± 0.01	19.7 ± 0.1	0.48 ± 0.07	22.8 ± 0.1	4.45 ± 0.04	-	$Zn_{1.10}$[Ni(CN)$_4$]·0.06TBA·0.62H$_2$O·0.21NO$_3^-$
Co-Ni	25.7 ± 0.1	25.4 ± 0.1	0.07 ± 0.04	21.3 ± 0.1	0.28 ± 0.04	24.8 ± 0.2	0.94 ± 0.09	0.24	$Co_{1.01}$[Ni(CN)$_4$]·0.32H$_2$O·0.02SO$_4^{2-}$
Co-Co	31.7 ± 0.3		0.78 ± 0.01	17.2 ± 0.02 (24.2 ± 0.1)[b]	3.84 ± 0.03 (1.23 ± 0.06)[b]	19.1 ± 0.1 (25.3 ± 0.1)[b]	22.4 ± 0.4 (6.10 ± 0.21)[b]	-	$Co_{2.95}$[Co(CN)$_6$]$_2$·0.51TBA·1.75H$_2$O· 0.07K$^+$·0.64NO$_3^-$
Co-Fe	23.6 ± 0.2	15.7 ± 0.2	0.98 ± 0.01	26.4 ± 0.3	1.87 ± 0.03	23.3 ± 0.1	6.98 ± 0.06	-	$Co_{2.85}$[Fe(CN)$_6$]$_2$·0.92TBA·2.08H$_2$O·0.18K$^+$·0.14NO$_3^-$

[a]Determined on two samples each. [b]Measured under Schlenk conditions. [c]Determined under the assumption EtOH was removed during catalyst activation.

The precatalysts´ compositions were determined by elemental analysis revealing CA, solvent and potassium residues (Table 1). Depending on the catalyst route of synthesis, either NO$_3^-$ or SO$_4^{2-}$ ions were detected.

The surface analysis by energy-dispersive X-ray (EDX) spectroscopy indicated comparably lower fractions of metal ions and higher fractions of organic components (Table 2).

Table 2. Elemental analysis determined by EDX measurements on the precatalysts´ surfaces.[a]

cat.	M^1 [wt%]	M^2 [wt%]	K [wt%]	C [wt%]	N [wt%]	O [wt%]	Cl [wt%]
ZnGlu	21.1 ± 2.6	-	-	30.9 ± 11.2	-	20.3 ± 7.9	-
Zn-Fe^{II}	6.48 ± 1.38	2.67 ± 0.32	-	107.8 ± 7.7	33.1 ± 5.5	7.78 ± 1.22	-
Zn-Fe^{III}	6.42 ± 0.56	3.17 ± 0.22	0.35 ± 0.60	43.4 ± 14.4	8.11 ± 3.47	5.12 ± 2.98	-
Zn-Ni	16.9 ± 0.8	13.8 ± 0.28	-	11.7 ± 1.9	14.0 ± 3.4	1.97 ± 0.77	-
Co-Ni	16.9 ± 1.8	13.8 ± 1.8	-	11.2 ± 1.6	12.2 ± 2.5	0.95 ± 0.36	-
Co-Co	29.7 ± 8.2		0.83 ± 0.19	24.8 ± 11.6	31.0 ± 14.7	-	0.44 ± 0.09
Co-Fe	15.6 ± 0.5	10.5 ± 0.7	0.82 ± 0.06	16.1 ± 4.1	15.4 ± 6.5	1.79 ± 0.83	-

[a]Determined at three different spots on each precatalyst surface.
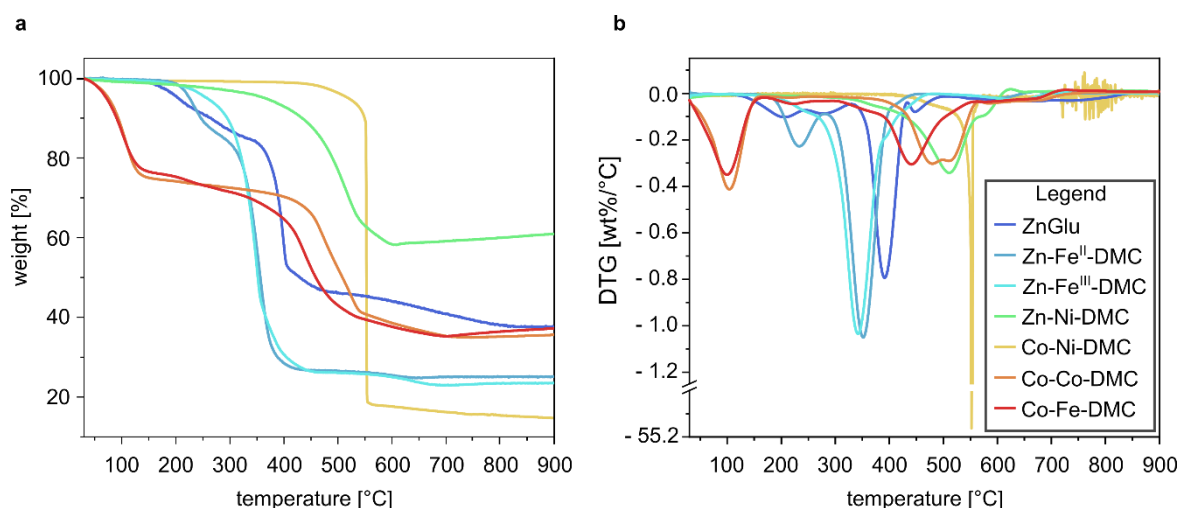
Figure 11. (a) TGA and (b) DTG curves of **ZnGlu** and **DMC** precatalysts measured under nitrogen atmosphere**.**

The existance of potassium residues were confirmed for **Zn-Fe^{II}-**, **Co-Co-** and **Co-Fe-DMC** precatalysts**.** Surprisingly, for the latter, traces of chlorine were detected.

The first weight losses in the precatalyst complexes **ZnGlu**, **Zn-Fe^{II}-**, **Zn-Fe^{III}-**, **Co-Co-** and **Co-Fe-DMC** on heating in thermogravimetric analysis (TGA) were assigned to water and/or TBA removal processes (stage I, respectively, Figure 11, Table 3). **Co-Co-** and **Co-Fe-DMC** precatalysts seem to contain water and TBA that are mostly losely bound, desorbing at their boiling points. Coordinatively bound water is assumed for **ZnGlu**, **Zn-Fe^{II}-** and **Zn-Fe^{III}-DMC** with desorption temperatures above 160°C. The additional weight loss between 240 and 330°C in the **ZnGlu** catalyst indicates the evaporation of HDA (stage II, Figure 11, Table 3), which was added

Table 3. Thermal decomposition steps assigned with temperature range and corresponding group release/degradational process.

| cat.	stage [wt%]			
	I	II	III	IV/V
ZnGlu	9.21 (100 - 244°C, H$_2$O)	6.34 (244 - 331°C, H$_2$O/HDA)	31.9 (331 - 433°C, Glu-decomp.)	6.52/ 8.22
Zn-Fe^{II}	12.7 (160 - 281°C, H$_2$O)	60.7 (281 - 459°C, CN-decomp.)	1.64	-
Zn-Fe^{III}	4.60 (160 - 264°C, H$_2$O)	69.7 (264 - 470°C, CN-decomp.)	2.80	-
Zn-Ni	35.5 (295 - 567°C, CN-decomp.)	6.14	-	-
Co-Ni	82.2 (429 - 571°C, CN-decomp.)	-	-	-
Co-Co	25.1 (30 - 161°C, H$_2$O/TBA)	1.86 (173 - 246°C, H$_2$O/TBA)	32.1 (314 - 568°C, CN-decomp.)	6.07
Co-Fe	24.0 (30 - 161°C, H$_2$O/TBA)	3.68 (173 - 258°C, H$_2$O/TBA)	32.6 (288 - 651°C, CN-decomp.)	4.18
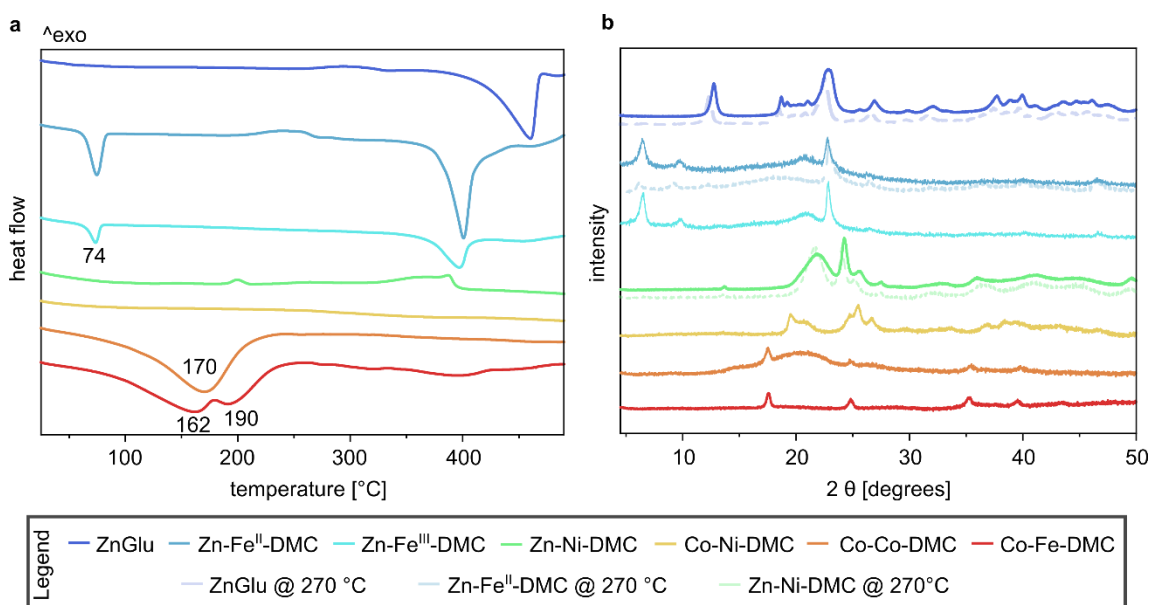
Figure 12. (a) DSC and (b) XRD measurements of **ZnGlu** and **DMC** precatalysts. XRD analysis was performed at RT and 270°C according to the maximum pre-treatment temperature applied in NH$_3$-TPD procedure.

during preparation. The onset temperatures of the cyanide related decompositions in **DMCs** vary between 280 and 430°C. The **Zn-Fe^{II}-** and **Zn-Fe^{III}-DMC** catalysts have the lowest thermal stability (stage II, each, Figure 11, Table 3) and **Co-Ni-DMC** the highest. Weight losses above the cyanide decomposition temperatures are to be related to further structural degradation of the catalysts´ residues.[65]

Differential scanning calorimetry (DSC) measurements on the complexes gave small exothermal signals for **Zn-Ni-DMC** at roughly 200°C, for **Zn-Fe^{II}-DMC** at 240°C and for **ZnGlu** at 290°C, respectively. Processes underlying these are of minor relevance to the structure. XRD measurements performed at 270°C gave no evidence for a structural reorganisation (dotted lines, Figure 12). Endothermal signals observed for **Zn-Fe^{II}-DMC**, **Zn-Fe^{III}-DMC** at 74°C represent the melting of ODA residues. Water and TBA surface desorption processes in **Co-Co-** and **Co-Fe-DMC** catalysts were detected around 170°C.

Preparation method, choice of reagents and mode of addition are known to influence the crystallinity and phase purity of **ZnGlu** and **DMC** catalysts (X-ray diffraction (XRD) patterns, Figure 12).[13,14,16] A cubic structure with the space group Fm3m is typical for Prussian blue analogues and such a structure was found for **Co-Co-** and **Co-Fe-DMC**: typical reflections at 2θ of 17.5° (200), 24.8° (220), 35.3° (400) and 39.5°(420) were found, respectively. An additional signal at 2θ of 43.5° (422) was found in **Co-Fe-DMC**.[66] Microcrystalline or amorphous phases were also observed for the precatalysts (except of **Co-Fe-DMC**), indicated by the broad reflection at 2θ around 20°. The reflection patterns of the **Zn-Fe^{II}-DMC**, **Zn-Fe^{III}-DMC** and **Zn-Ni-DMC** catalysts could not conclusively be interpreted. However, for the **Co-Ni-DMC** catalyst the reflection at 2θ of 19.5° and 24.7° match previous reports[67,68] and indicate a orthorhombic
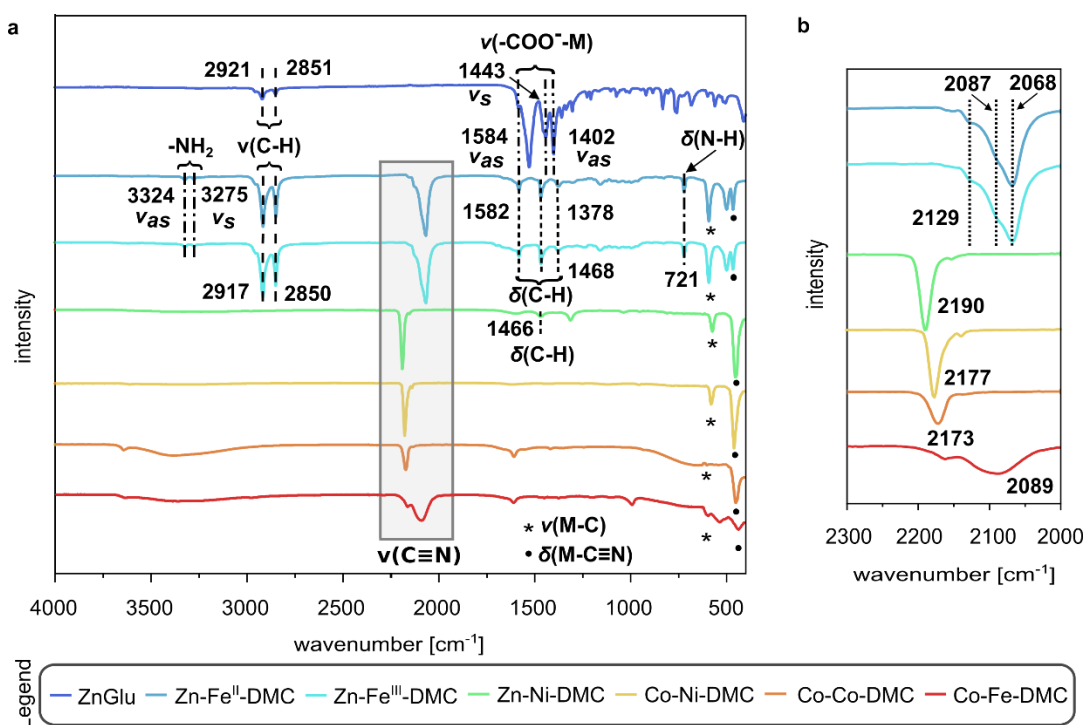
Figure 13. (a) ATR-IR spectra of **ZnGlu** and the **DMC** precatalysts, and (b) close-up look at the C≡N vibrations.

phase[69]. The reflections of the **ZnGlu** complex correspond to the patterns described previously[41,70,71] and show the catalytically favorable high crystallinity.

Infrared (IR) analysis allows for the characterization of the precatalysts' compositions and coordinational structures (Figure 13). The IR spectra of **ZnGlu**, **Zn-Fe^{II}-** and **Zn-Fe^{III}-DMC** reveal residues of remaining HDA and ODA molecules by showing corresponding C-H stretching vibrations at around 2920 and 2850 cm^{-1}. Complementary C-H stretching vibrations were detected at 1582, 1468 and 1378 cm^{-1}. Further proof for the existence of ODA residues is given by symmetrical and asymmetrical N-H stretching vibrations at 3324 and 3275 cm^{-1}. For the **Zn-Ni-DMC**, TBA residues were identified as the spectra shows corresponding bending δ(C-H) vibrations at 1466 cm^{-1}. These findings correspond well to the results found by elemental analysis, TGA and DSC measurements (Table 1, Figure 11 and 12a). Typical signals for cyanide groups in **DMC** precatalysts were identified by v(C≡N) bands at around 2100 cm^{-1} (Figure 13b).[72] **Zn-Fe^{II}-** and **Zn-Fe^{III}-DMC** showed three distinct signals in this area which are possibly caused by a structural symmetry in the catalysts, but also might indicate the existance of several active sites. The latter would be supported by the findings in the temperature-programmed ammonia-desorption (NH$_3$-TPD) measurements shown in Figure 14. The catalyst **ZnGlu** showed typical asymmetrical v_{as}(-COO$^-$-M) vibration bands at 1584 and 1402 cm^{-1}, respectively, and symmetrical v_s(-COO$^-$-M) bands at 1443 cm^{-1}, which have been described in previous literature.[41,71,73]
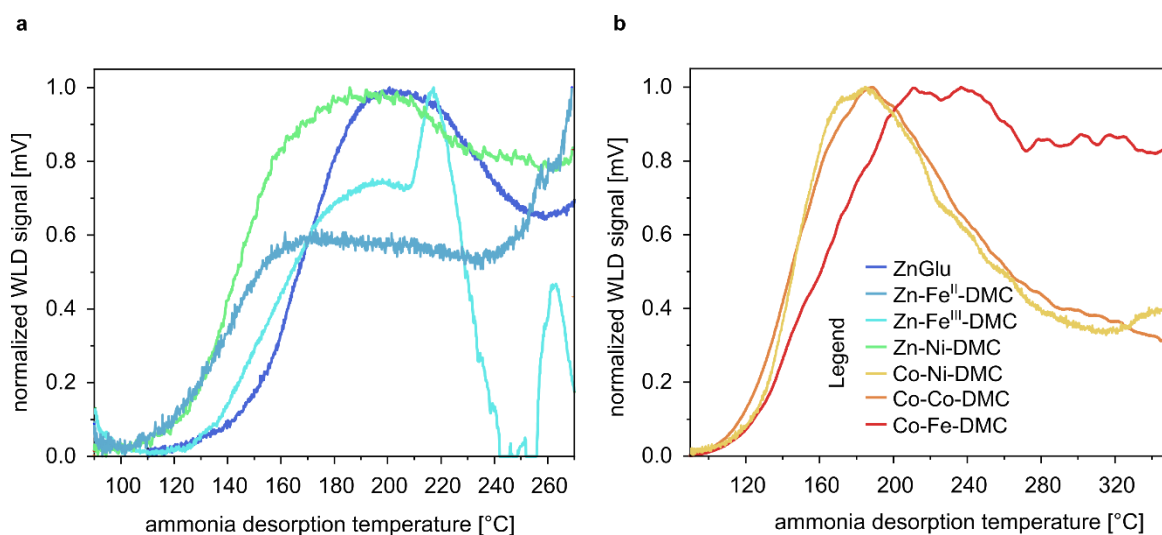
Figure 14. NH$_3$-TPD curves of (a) **ZnGlu**, **Zn-Fe^{II}-DMC**, **Zn-Fe^{III}-DMC,** and **Zn-Ni-DMC,** and (b) **Co-Ni-DMC, Co-Co-** and **Co-Fe-DMC**.

Temperature-programmed ammonia-desorption (NH$_3$-TPD) measurements were used to order the precatalysts for the Lewis acidity: the zinc-based precatalysts have the order of **Zn-Ni-DMC** < **Zn-Fe^{III}-DMC** (first peak) < **ZnGlu** (Figure 14a), the cobalt ones follow the order of **Co-Ni-DMC** < **Co-Co-DMC** < **Co-Fe-DMC** (Figure 14b). The order was taken from the temperature of maximum rate of ammonia desorption. The coordination of ammonia can be considered as a surrogate for PO, and the coordination strength of NH$_3$ hence as a measure for the PO repolarisation. A quantification of active sites could not be conducted since ammonia desorption signals are not consequently separated from desorption of the decomposition products. Brönstedt acid sites are not considered here as a source for the liberation of ammonia in DMCs. Brönstedt sites are in principle also capable of binding and releasing ammonia during measurements. However, their existence in DMCs is unlikely[42,46,48–52] and the structure of DMCs would be much more compatible with Lewis acidic sites.[74] Furthermore, the desorption temperature from **ZnGlu** was also considered as too high to originate from Brönstedt acidity. The CO$_2$/PO copolymerization is usually only mediated by the complexes of this study after an activation procedure. It can be assumed that coordinating nucleophiles (basic entities) such as water, TBA, ethanol are removed before PO can compete for coordination and hence activation. Such nucleophiles can also start chain growth as they are typically incorporated as starting groups in the polymer backbone.[75] These findings were evaluated by MALDI-TOF/TOF experiments which revealed complex spectra (Figure 15). The plethora of signal groups indicates that substantial fragmentation of the polymer takes place. This is not unusual for polyether carbonates. It is nevertheless anticipated that some of the signals would encompass a chain end. Indeed, masses were found that are compatible with a chain start by any of the several nucleophiles in the reactor in form of amines, nitrates and TBA or ethanol. It is however also clear, that a much deeper analysis of the spectra is necessary for a more convincing interpretation. Such an analysis should comprise the fragmentation pathways. It presumably also would need more data, e.g.,

Figure 15. MALDI-TOF/TOF spectra and peak assignments applying (a) **Zn-Fe^{III}-DMC**, (b) **Zn-Ni-DMC**, (c) **Co-Ni-DMC**, (d) **Co-Co-DMC**, (e) **Co-Fe-DMC**, and 5 bar CO$_2$ pressure for PPC formation.

23

from carboxy-propoxylations with the DMCs using a starter: The fragmentation pattern could not be elucidated with a high enough confidence and non-assignable signals remain for the products from using **Co-Ni-DMC** as a catalyst/starter combination.[76] The process of activation in the PO catalysis was mimicked in the NH_3-TPD by a process of heating under vacuum. Samples were heated up to 250°C (with a technical related short overheat up to 270°C) within 23.5 min and the temperature was held for additional 36.5 min prior to any ammonia adsorption to provide a close analogue to the intrinsic active site structures. Those liberated sites are presumably the active centers at which copolymerization processes are encountered, corresponding to the active metal centers $M^1 Zn^{2+}$ or Co^{2+}. The catalysts´ structures are unaltered during conditioning and NH_3-TPD measurements as demonstrated in TGA, DSC and XRD analysis (Figure 11 and 12, Table 3). Additionally, parts of ODA possibly evaporate in the conditioning (/activation) step (Figure 11). Two distinct desorption processes are observed for the **Zn-Fe^{III}-DMC** precatalyst. This observation hints to the presence of at least two different coordination sites. The desorption process in **Co-Fe-DMC** merges with the formation of decomposition products at 300°C (Figure 11).

The morphology of the **DMCs** was analyzed by scanning electron microscopy (SEM) imaging. The images indicate a microcrystalline habitat which is shown in **Zn-Fe^{II}**, **Zn-Fe^{III}-** and
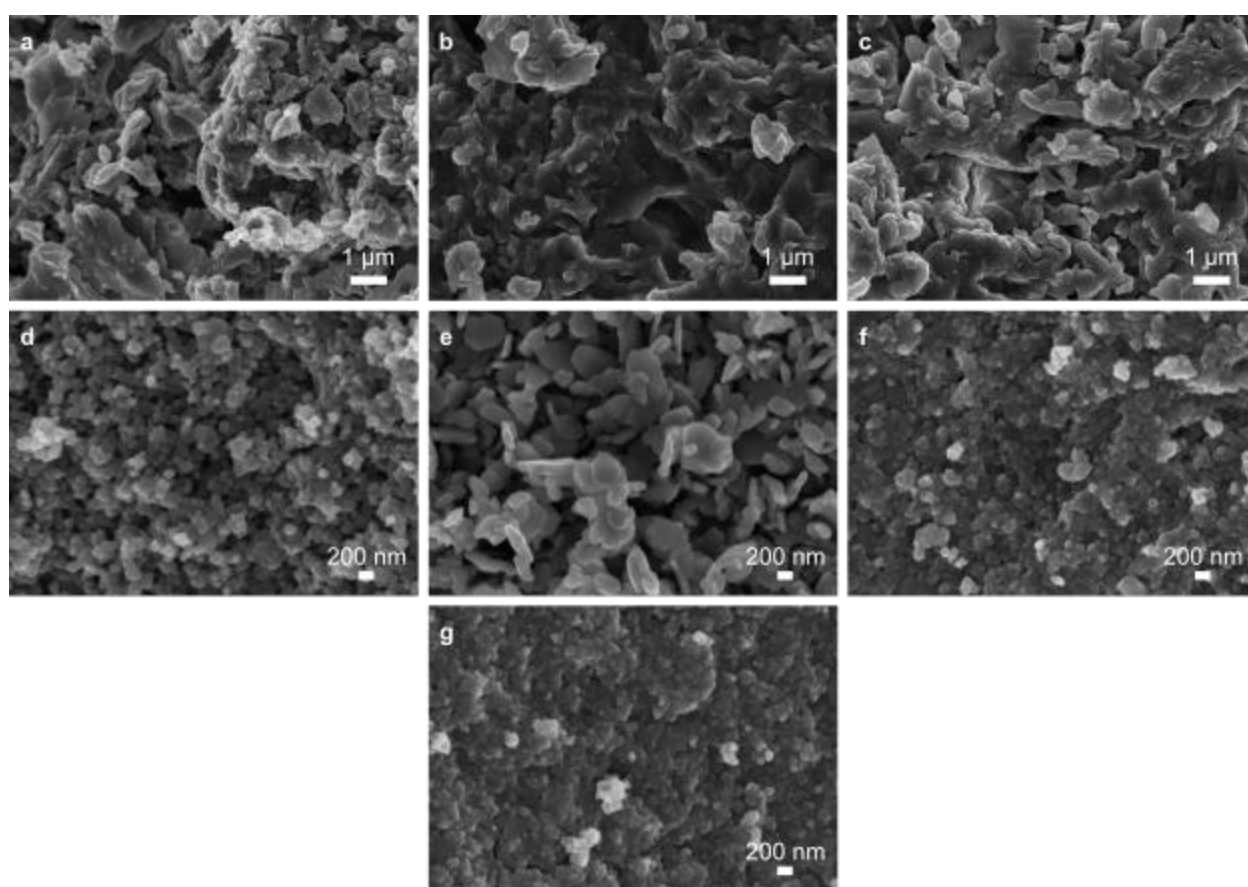

Figure 16. SEM images of (a) **ZnGlu**, (b) **Zn-Fe^{II}-DMC**, (c) **Zn-Fe^{III}-DMC**, (d) **Zn-Ni-DMC**, (e) **Co-Ni-DMC**, (f) **Co-Co-DMC**, and (g) **Co-Fe-DMC**.

Co-Ni-DMC by plate-like structures (Figure 16b, c and e) and in **Zn-Ni-**, **Co-Co-** and **Co-Fe-DMC** by granular agglomerates (Figure 16d, f and g), The particle dimensions ranged between ~ 80 and ~ 1200 nm for **Co-Ni-DMC** and between ~ 50 and ~ 250 nm for **Zn-Ni-DMC**, **Co-Co-DMC** and **Co-Fe-DMC**.

3.1.2 Correlation between the Intrinsic Catalyst Structures and the Lewis Acidity

The concept of Lewis acidity is framed by the interaction between an electron pair donor and receptor. Catalytic centers of the catalysts characterized in the previous section are metal atoms that can interact with ligands and substrates by coordinative and ionic bonds. The affinity of the catalytic centers towards basic substrates may be related to the "performance" of the catalysts as long as pre-equilibria and mass transfer limitations do not need consideration. The primitive building motive of all **DMC** catalysts is the M^1-N≡C-M^2 linkage, where M^1 has the role of the active site and M^2 serves to support the structure in the crystal. These metals are bridged by CN groups, and therefore they are orbitally coupled. The charge density distribution in the M^1-N≡C-M^2 linkage is connected to the π-back bonding in the M^2-C-linkages and the σ-bond in the M^1-N-connection. Both have a measurable impact on the CN (M^1-N and C-M^2) vibrations (Figure 13b).[77] Just recently, x-ray photoelectron spectroscopy (XPS) studies on DMCs revealed a direct connection between the K 2p core-level electron binding energy of the M^2-metal and the CN-vibrational shift in IR spectroscopy.[78–80] This means that the electronic structure of M^2 impacts the charge density at M^1. The XPS measurements reflect the changes in the core substrate affinity and are in tune with its structural counterpart M^2, that "pulls" or "pushes" electrons from the M^1 metal core.
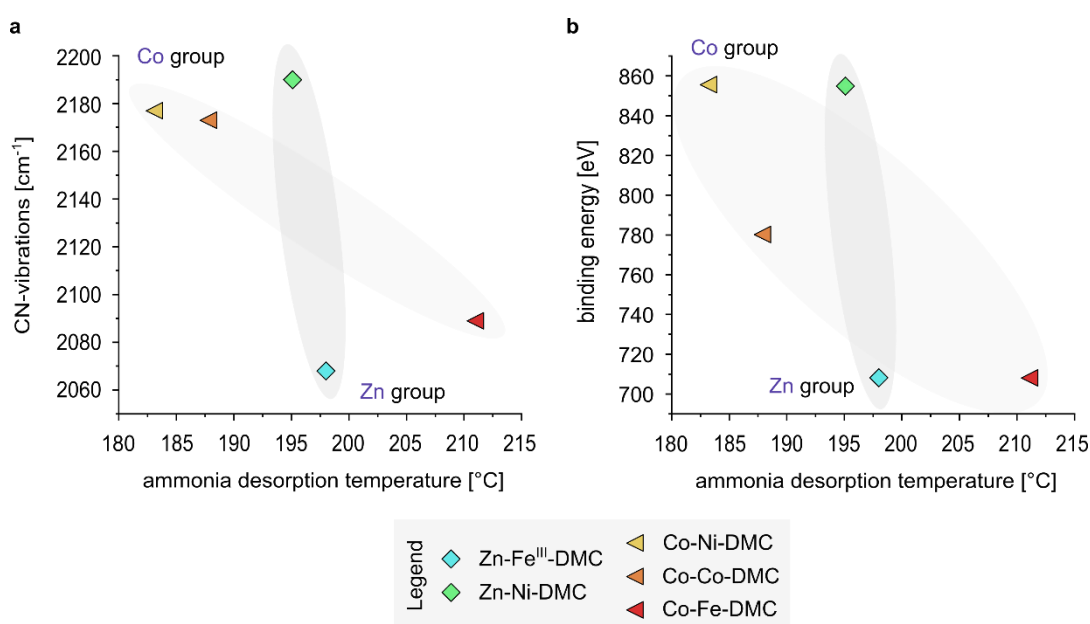

Figure 17. Maximum in NH$_3$-TPD and (a) the CN-vibration wavenumbers and (b) the 2p$_{3/2}$ core-level electron binding energy.
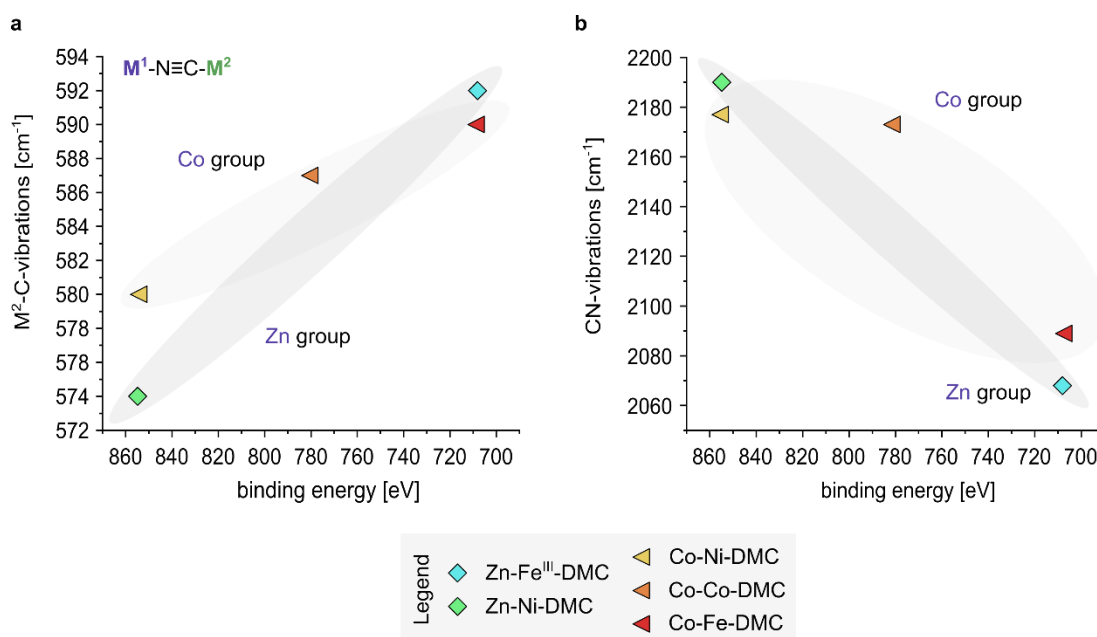
Figure 18. $2p_{3/2}$ core-level electron binding energy and (a) the M^2-C-vibrations wavenumbers and (b) CN-vibration wavenumbers.

Similar correlations between the K 2p core-level electron and IR vibrations exist for the Co-based and Zn-based catalyst groups in this work (Figure 17). The binding energies for these precatalysts are reported[67,78–80] and the IR spectra were recorded (Figure 13). This relation indeed corresponds well to the rough picture from simple orbital theory. Less oxidized metal centers form stronger M^2-C bonds, which is reflected in higher wavenumbers of their M-C vibrations. Consequently, the opposite trend is found for the $\nu(C\equiv N)$ vibrations as the electronic levels of C and N have better match (Figure 17b).

A similar correlation is indicated between the choice of M^2- and the M^1-group and the specific temperature of maximum ammonia loss from the corresponding (pseudo-activated) catalyst surface (Figure 18). A plot of the $\nu(C\equiv N)$ vibrations (or the K 2p core-levels in the M^2 metal) against the NH_3-TPD results mirrors the trends (Figure 18a resp. 18b). Although only a small number of complexes are part of this analysis, the readily accessible IR vibrations of the crystal core may be a measure for the Lewis acidity of the activated catalyst in a series of M^1. This finding will need substantiation, but for starters it seems of practical use for choosing of DMC catalysts for a transformation with a specific result.

3.1.3 PO/CO₂ Copolymerization Reactions

The precatalysts were subjected to favorable conditions for inducing the copolymerization of CO_2 and PO. These were therefore suspended in bulk propylene oxide (PO), applying CO_2 pressures between 5 and 40 bar. The CO_2 pressures were kept constant throughout the polymerization process by a mass flow controller and reactants/catalyst mixtures were typically held at 60°C. A
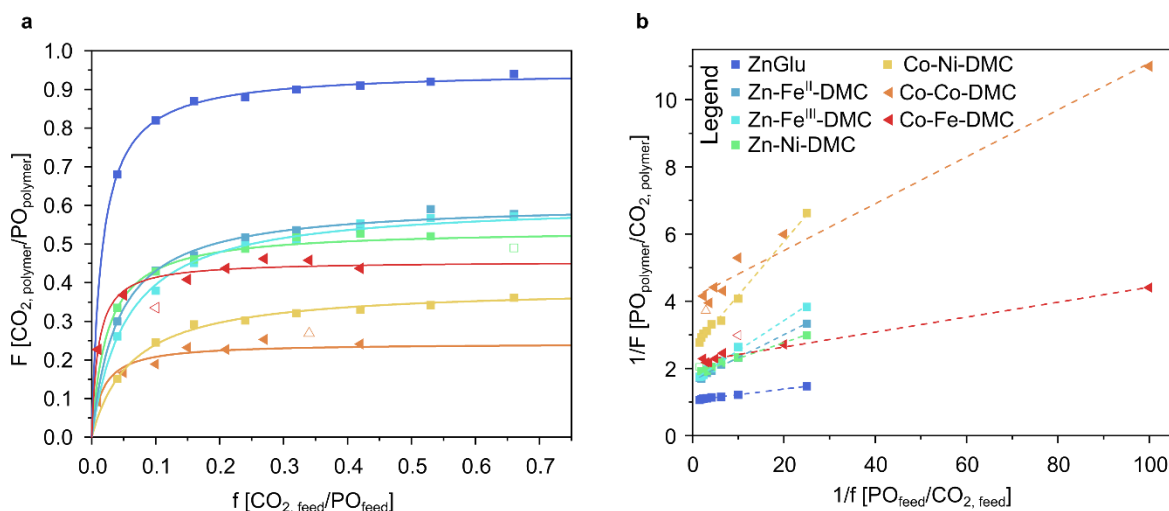
Figure 19. (a) CO_2/PO ratios F in the copolymer vs. in the feed f and (b) linearization using **ZnGlu**, **Zn-Fe^{II}-DMC**, **Zn-Fe^{III}-DMC**, **Zn-Ni-DMC**, and **Co-Ni-DMC** at 60°C, and **Co-Co-DMC** and **Co-Fe-DMC** at 80°C. The feed composition was determined by Henry's law (see Experimental Section 4.2.2).

higher reaction temperature of 80°C was used in cases of **Co-Co-DMC** and **Co-Fe-DMC** precatalysts for obtaining observable reaction rates. The CO_2/PO molar ratios F in the copolymer backbone were taken from integrals in ^{1}H NMR spectra. The molar ratio f of the concentration of CO_2 over the PO concentration in the reaction medium in dependence of the pressure have been published and validated.[81] These were used for calculating the f values. Copolymerization results for **ZnGlu** were taken from a previous study.[62]

ZnGlu is the zinc based catalyst that is most effective for CO_2 incorporation into the polymer, producing nearly alternating copolymers (F values near 1) followed by **Zn-Fe^{II}-**, **Zn-Fe^{III}**, **Zn-Ni-** and **Co-Ni-DMC** at high CO_2 pressures; the order changes to **ZnGlu** > **Zn-Ni-DMC** > **Zn-Fe^{II}-DMC** > **Zn-Fe^{III}-DMC** > **Co-Ni-DMC** at a lower pressure of 5 bar. The **Zn-Ni-DMC** thus shows a higher take up at low pressures, which is also found for the Co-based catalysts. The catalytic action of the **Co-Fe-DMC** complex gives more carbonate linkages in the polymer

Table 4. Data on the CO_2/PO copolymerization.

catalyst	slope, *a*	*y*-intercept [PO/CO$_2$]	ht'/ht-linkages at 40 bar [mol%]	coefficient of determination, R^2
ZnGlu	0.016	1.05	66*a*	0.993
Zn-Fe^{II}	0.068	1.64	23/42	0.994
Zn-Fe^{III}	0.089	1.64	26/40	0.994
Zn-Ni	0.047	1.83	27/36	0.991
Co-Ni	0.151	2.61	22/15	0.997
Co-Co	0.071	4.01	20/43	0.974
Co-Fe	0.022	2.20	19/48	0.990

*a*Addition of carbonate and ether carbonate linkages.

backbone than **Co-Co-DMC**.

The F values generally increase with the concentration of carbon dioxide in the feed to a certain level below 1 (Figure 19). A higher number for F than 1 is not to be expected, as a consecutive insertion of carbon dioxide is thermodynamically unfavorable. It is however unclear, why the upper limit of 1 is not approached at an ever increasing CO_2 concentration in the feed. Obviously, the levelling off of F with increasing f is specific for a type of catalyst: the maximum has a variety of values between 0.2 und 0.9 (Figure 19, Table 4). This indicates that chemical rather than physical (diffusion limitations) origines underlie these observations. An argumentation on the basis of physical phenomena is given in the next section to show that there is no such a reasonable cause for the differences in the action of the catalysts.

The approximate hyperbolic dependence (two asymptotes) of F on f allows to linearize the data through a double inversion according to equation $F = \frac{f}{a+yf}$, resp $\frac{1}{F} = \frac{a}{f} + y$ with slope *a* and the intercept *y*. Latter equation gives a linear dependence of the experimental data between 1/F and 1/f with high coefficients of determination R^2 (Figure 19b, Table 4). The dependency of F on f are thus reasonably described by the simple equation. The limiting value of F at high CO_2 pressures can then be taken from the *y*-intercept to have the order of catalysts of, starting with the highest F value: **ZnGlu** > **Zn-Fe^{II}-DMC** ≥ **Zn-Fe^{III}-DMC** > **Zn-Ni-DMC** > **Co-Ni-DMC** (Figure 19b, Table 4). The slope *a* can be interpreted as the capability of a catalyst to induce the incorporation of CO_2 at a given relative increase of CO_2 pressure. A small slope reflects an incorporation of CO_2 on much higher rates than the ratio in the feed would allow. **ZnGlu**, for instance, has a small slope, leading to a fast increase in carbonate content with pressure. The following order in slope values was found: **ZnGlu** < **Zn-Ni-DMC** < **Zn-Fe^{II}-DMC** < **Zn-Fe^{III}-DMC** < **Co-Ni-DMC**. **Co-Co-DMC** showed a larger slope than **Co-Fe-DMC**. Further analysis of the polymers is given in Appendix, Section A1.

3.1.4   Structure-performance Analysis of DMC and ZnGlu Catalysts

The relation between the Lewis acidity in terms of the NH_3-TPD measurements and the CO_2 content in the overall backbones in the PPC polymers could be evaluated along the parameter of *y*-intercept (application at 5 and 40 bar CO_2 pressure, Figure 20a and b, left). The relative amounts of head-to-tail linkages in the polymer microstructure were also linked to the results from the NH_3-TPD analysis (Figure 20a and b, right). Both polymer properties - CO_2 content and ht-linkages - increase with the Lewis acidity of the metal centers.

A maximum in head-to-tail linkages seems to exist at about 66 mol% for the **ZnGlu** catalyst. This result includes carbonate (ht) and ether carbonate (ht') linkages (compare Appendix 4.4.1). The increase in a head-to-tail selectivity (ht and ht' concentrations) is resulting from a more
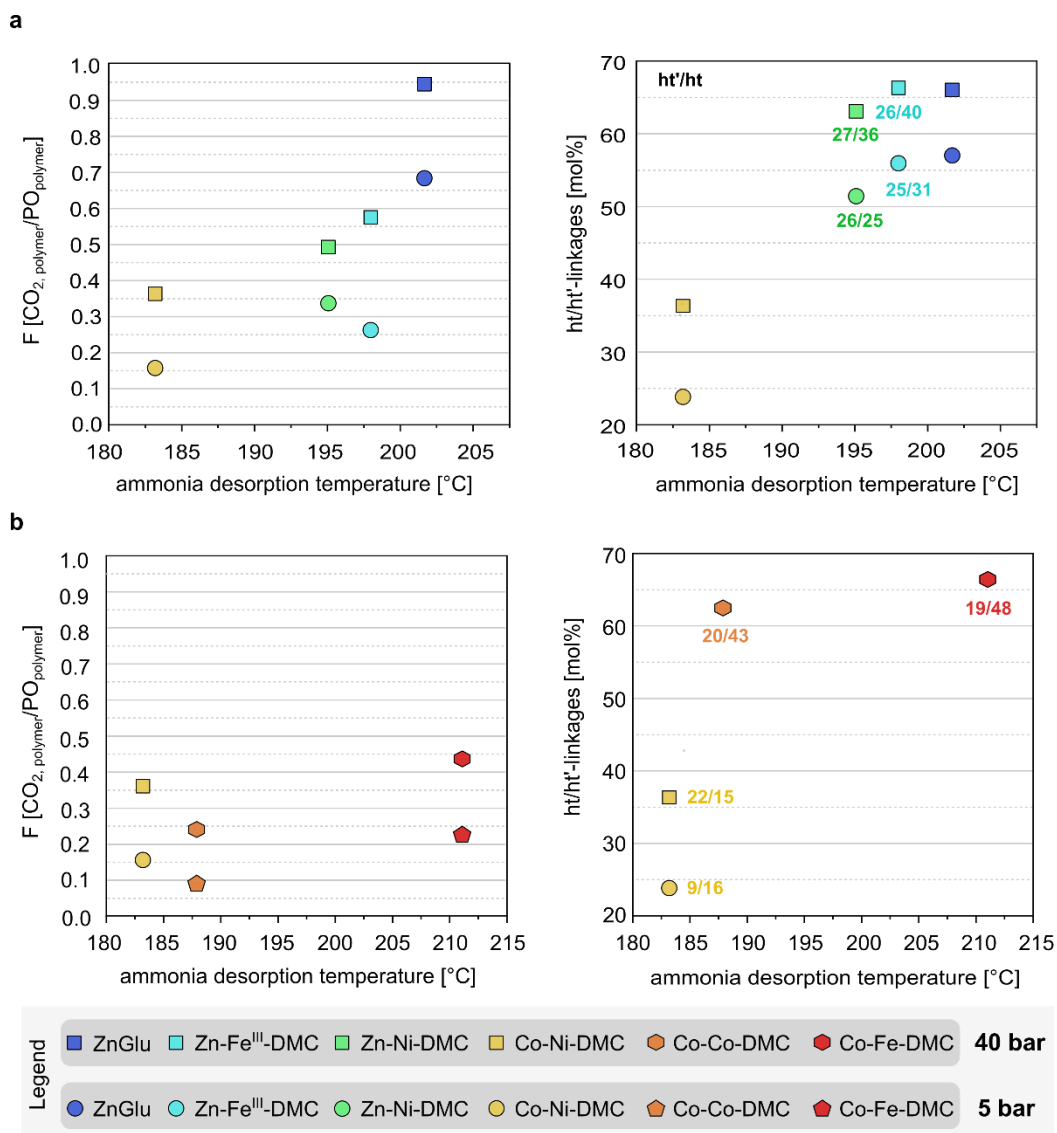
Figure 20. (a) Dependencies of F (left) and the amount of ht/ht'-linkages (right) on the ammonia desorption temperatures using **ZnGlu**, **Zn-Fe^{III}-DMC**, **Zn-Ni-DMC,** and **Co-Ni-DMC** at 5 and 40 bar CO_2 pressure. Polymerizations were conducted at 60°C. (b) Dependencies of F (left) and the amount of ht/ ht'-linkages (right) on the ammonia desorption temperatures using **Co-Ni-DMC**, **Co-Co-DMC,** and **Co-Fe-DMC** at 5 and 40 bars CO_2 pressure. Polymerizations were conducted at 80°C (except **Co-Ni-DMC** which was applied at 60°C). Ammonia desorption temperatures are taken from the maximum peaks in the NH_3-TPD curves, respectively.

selective ring-opening, either in the methylene (alpha position, more open site for a kinetic determined ring-opening) or the methine (beta position, electronically favored in particular in case of a late transition state). A stronger activation of PO by a stronger Lewis acid would lead to an earlier transition state, which would enhance the ring-opening in the alpha position to a larger extent. The concomitant formation of a metal *sec*-alkoxide renders a sterically more congested, but also more electron rich alkoxide. The reactivity of the *sec*-alkoxide may thus be different from a primary alkoxide. Increasing the CO_2 pressure for all catalysts generally leads to a higher selectivity for ring opening in the alpha position. It can be assumed that an electron rich secondary
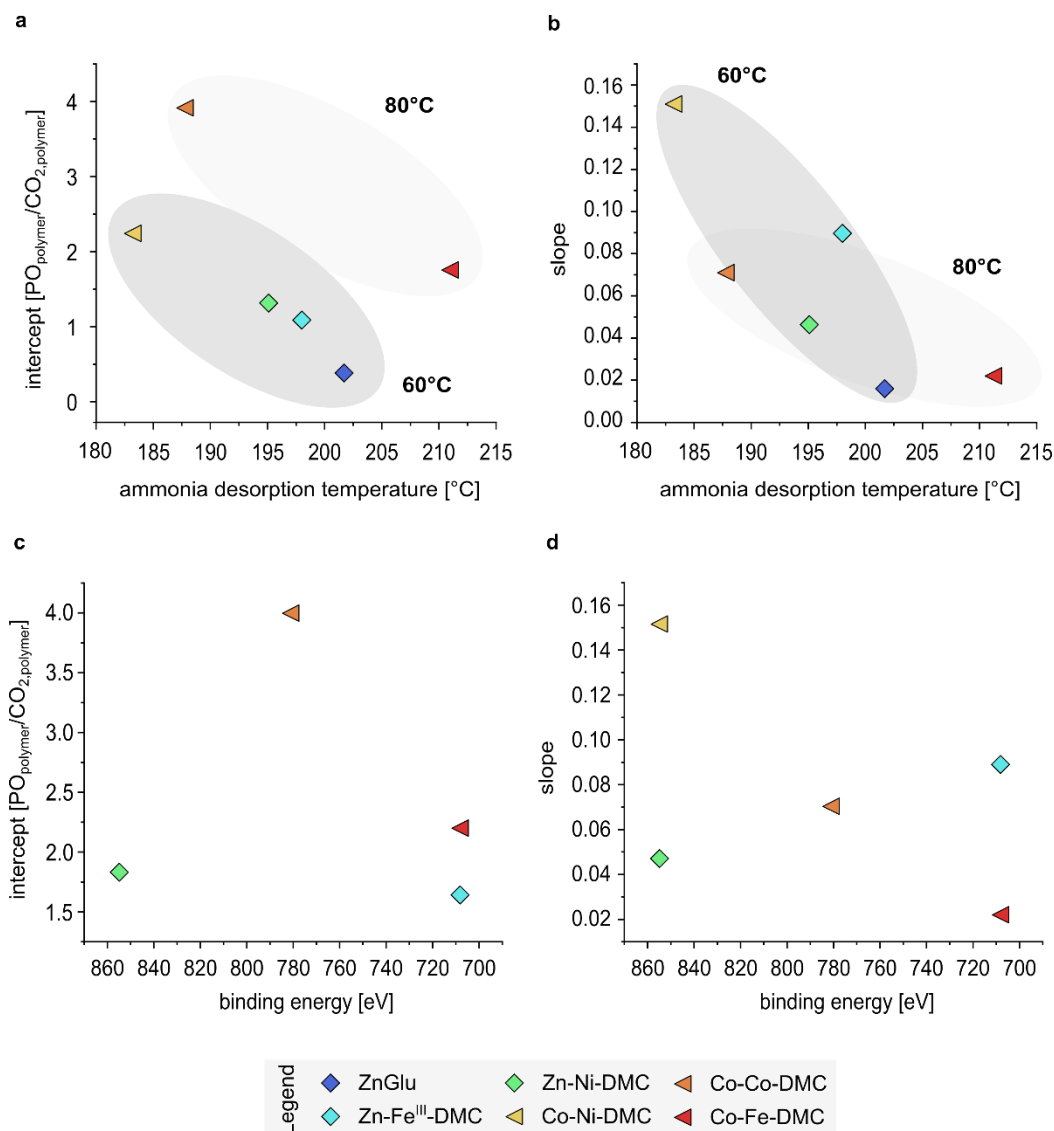
Figure 21. Dependencies of (a) the intercepts and (b) the slopes derived earlier representing the CO_2 uptake sensitivity towards the feed composition vs. the max. ammonia desorption temperature. Approaching 0 is stated the most independent case. Intercepts and slopes are shown for **ZnGlu**, **Zn-Fe^{III}-DMC**, **Zn-Ni-DMC,** and **Co-Ni-DMC** applied to polymerizations at 60°C and **Co-Co-DMC** and **Co-Fe-DMC** applied to polymerizations at 80°C**.** Dependencies of (c) the intercepts and (d) the slopes in relation to the $2p_{3/2}$ core-level electron binding energy.

alkoxide (formed by an attack at the alpha position) rather undergoes a protonation reaction as described in the mechanistic consideration in Scheme 1 in Section 3.1.5. A secondary alkoxide would be more nucleophilic than a metal-bound primary alkoxide and would react faster with a surface-bound CO_2 to form a carbonate moiety. This surface-bound carbonate would then react with another surface-bound PO. The stronger the Lewis acidity the more likely this attack will occur on the alpha position forming another secondary alkoxide. This eventually leads to another head-to-tail linkage and an increased regioregularity. This assumption goes along with the findings in Figure 20. The stronger the Lewis acidity the more enhanced the presence of head-to-tail linkages. This effect seems to be generally applicable as the mechanism would be

further enhanced by increased CO_2 pressures as partially more (adjacent) CO_2 is available on the surface. Except for **Co-Ni-DMC**, an expectable increase of especially carbonate ht-linkages can be observed. A similar effect was observed for **ZnGlu** previously.[62]

The *y*-intercepts related to the Lewis acidity reveals a trend of higher CO_2 contents with higher Lewis acidities. The effect is more pronounced at lower temperature with more CO_2 incorporation into the polymer backbone (Figure 21a), showing that the ether linkage formation has a higher activation energy. The Lewis acidities as taken from the ammonia desorption temperature also correlate positively to the inverse of the slope *a* (Figure 21b). The analysis of the $2p_{3/2}$ core-level electron binding energies of the internal metals M^2 in terms of the intercept and slope (Figure 21c and d) refers to the findings in Section 3.1.2. Lower binding energies will correspond to higher Lewis acidities and thus a higher rate of CO_2 insertion (vice versa). Catalysis by the zinc group **Zn-Fe^{III}-DMC** and **Zn-Ni-DMC** with lower and more similar values for the slope *a* show an opposite trend. These results indicate that the electronic data have to be interpreted with some care, i.e., Lewis acidity might not be the only factor influencing the capability of the incorporation of CO_2, also structure may be of importance (dual site catalysis, vide infra).

3.1.5 Mechanistic Considerations

DMCs and also **ZnGlu** are heterogeneous catalysts, and their action needs consideration in terms of all steps of such a catalysis. These are to be divided in macro (mass transport) and microkinetic (chemical) aspects. The analysis of the catalysts and the characteristics of their action in the PO/CO_2 copolymerization show some coarse correlations, which can be interpreted in terms of microkinetic (chemical) aspects. The fact that the limit of CO_2 insertions finds different limits for different catalysts also indicates that chemical and not physical phenomena underlie the observations, like was argued above. Macrokinetics (diffusion physical aspects) may play a role too in the catalysis, however, do not seem to give a conclusive model for an interpretation of the differences of the catalysts here. Different mechanistic models for the CO_2/PO copolymerization were mathematically analyzed according to well-established Langmuir-Hinshelwood and the Eley-Rideal mechanisms and compared to the experimental results. Initially, Langmuir-Hinshelwood and Eley-Rideal mechanisms are kinetically derived for reactions in the gas phase, but were also adopted to reactions in the liquid phase.[39] The saturation of the carbonate content of the copolymers below the maximum possible value of F of 1 is satisfactory described by $\frac{1}{F} = \frac{a}{f} + y$ with *y* smaller or equal to 1 (Table 4, Figure 19b) as described above. Starting with the case of a Langmuir mechanism and proceeding with the Eley-Rideal mechanism (variations and results are shown in Appendix, Section A2), an approach with a physisorbed CO_2 layer was used to match the experimental findings to a macrokinetic regime. The models were adjusted in the means of an additionally denoted as "physisorbed" layer (Figure 22). The reactants
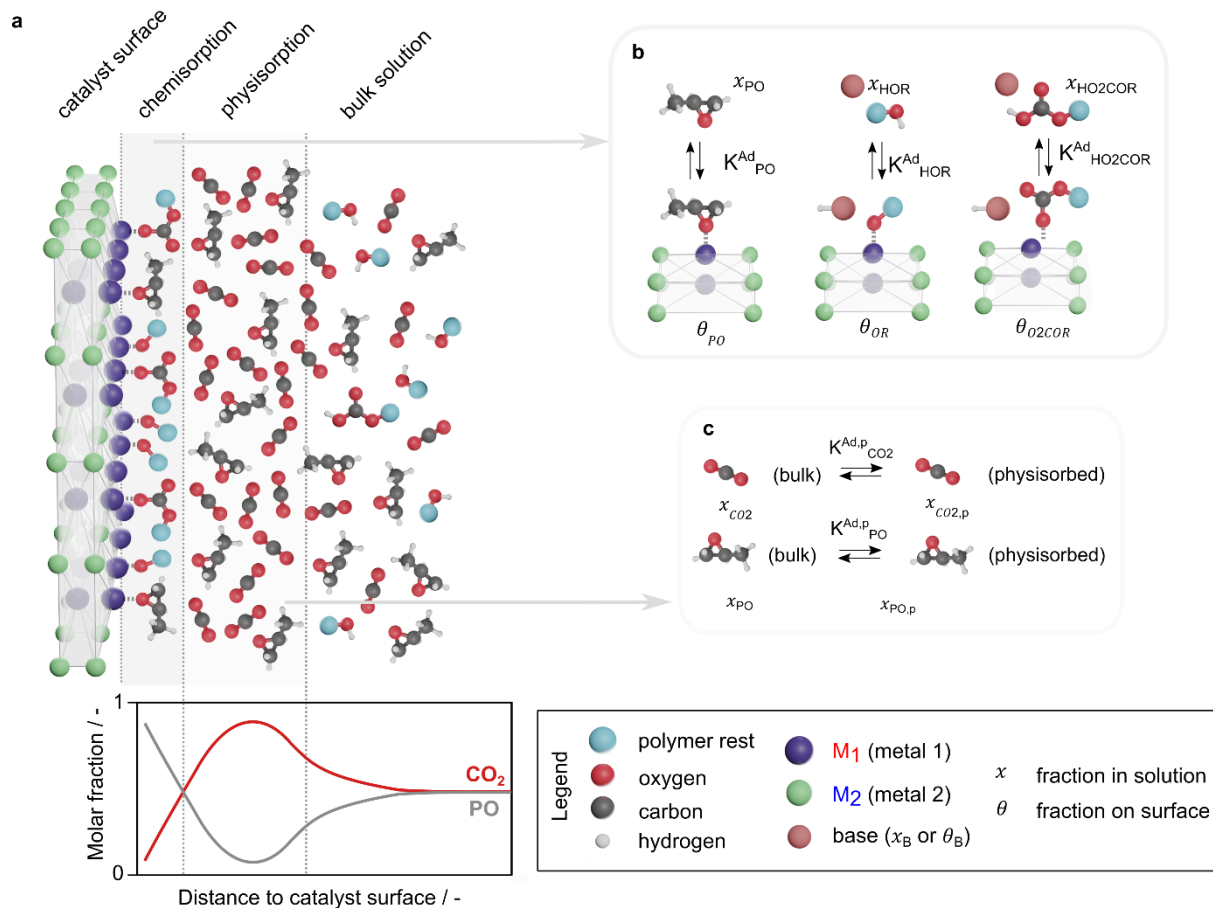
Figure 22. (a) Schematic model of the catalyst surface, the chemisorbed layer, the introduced physisorbed layer, and the bulk composition. The molar fraction distribution of PO and CO_2 in the individual sections is presented in the graph below. (b) Ad- and deadsorption pre-equilibria of reagents on the catalyst surface with corresponding equilibrium constants, and (c) equivalent equilibrium in the physisorbed layer for PO and CO_2 with corresponding equilibrium constants.

find themselves in an adsorption/desorption equilibrium with the surface (Figure 22b) or the introduced physisorbed layer (Figure 22c). The layer was assumed to mainly consist out of the most abundant species PO and CO_2 for simplification and practical reasons. The CO_2 molecule is assumed to be mainly in the physisorbed layer on the surface which lies within or above the chemisorbed layer interacting in some manner with the surface. This interaction, however, can be assumed to be weaker than that of other reagents. Such assumptions are not new, in contrary, they were already described by Eley. He regarded the reagent from the gas phase in some sort of pre-interaction with the surface before reacting with the adsorbed species.[39] An Everett-isotherm was chosen to describe such a binary layer. The corresponding isotherm equation describes the adsorption from a binary liquid system. The CO_2 layer was thus defined in competition with the most abundant species PO and the Everett isotherm was formulated as $x^p_{CO2} = \frac{K_E f}{1 + K_E f}$ with f corresponding to molar ratio of CO_2 and PO in the (liquid) feed, and K_E as the ratio of the binding constants of CO_2 ($K^{Ad,p}_{CO2}$) and PO ($K^{Ad,p}_{PO}$) combined into $K_E = \frac{K^{Ad,p}_{CO2}}{K^{Ad,p}_{PO}}$. The
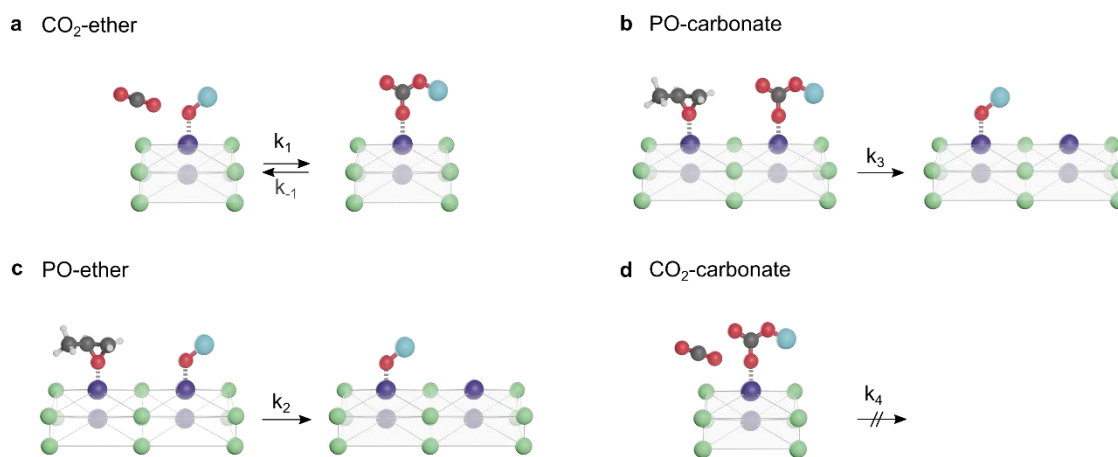
Figure 23 Considerable reaction steps and reaction constants in the adjusted Eley-Rideal model including (a) (reversible) physisorbed CO_2-ether insertion, (b) PO-carbonate ring-opening reaction, (c) PO-ether ring-opening reaction, and (d) CO_2-carbonate insertion.

mechanistic steps can be assumed as described (Figure 23). Basically, four different reaction steps are conceivable: CO_2-ether insertion (Figure 23a), PO-carbonate reaction (Figure 23b), PO-ether reaction (Figure 23c) and the thermodynamically excludable CO_2-carbonate insertion (Figure 23d). Taking these steps and the according reaction constants into account, the formulation of F can be accordingly described as $F = \frac{k_1 x_{CO2}^p \theta_{OR} - k_{-1}\theta_{O2COR} + k_3\theta_{O2COR}\theta_{PO}}{k_2\theta_{OR}\theta_{PO} + k_3\theta_{O2COR}\theta_{PO}}$. The reversibility of the CO_2 insertion can be formulated as $K_{car} = \frac{k_1}{k_{-1}} = \frac{\theta_{O2COR}}{\theta_{OR}x_{CO2}^p}$. Inserting gives the equation for experimentally fitting for $F = \frac{k_3 K_{car} x_{CO2}^p}{k_2 + k_3 K_{car} x_{CO2}^p}$, and thus $\frac{1}{F} = \frac{k_2}{k_3 K_{car} K_E}\frac{1}{f} + 1 + \frac{k_2}{k_3 K_{car}}$ can be formulated. According to the results, the intercept $\frac{k_2}{k_3 K_{car}}$ would be in relation to Lewis acidity and thus the $2p_{3/2}$ core-level electron binding energies of the internal metals M^2. With the introduction of the ratio of the binding constants K_E into the slope $\frac{k_2}{k_3 K_{car} K_E}$ another influential factor for the CO_2 insertion is introduced. The more than proportional CO_2 uptake from the feed thus not only is dependent on the Lewis acidity but also on the availability of CO_2 in close proximity which wouldn't be given by a physisorbed layer. This leads to the conclusion that microkinetic factors are of more importance for describing (the differences in) the action of the **DMC** catalysts.

The levelling-off of the CO_2 content at higher CO_2 pressures in the **DMC** based catalysts is consistent with a saturation of relevant surface entities with CO_2. CO_2 may coordinate to metals as a Lewis base, giving rise to also unusual geometries wherein the carbon atom becomes a stronger electrophile.[82] CO_2 in contrast may also react with basic entities to form a carbonato entity.[83] Latter seems of little importance to the catalysis, as such a constellation is obviously not on the pathway of forming a carboxylato entity from an alkoxide by CO_2 insertion. It seems thus of more relevance to the catalysis that CO_2 is coordinating as a base to the metal centers of the **DMC** surface, i.e., in competition to PO. This view is substantiated by the observation that the

presence of CO_2 decreases the general rate of PO conversion, i.e., the activity of the catalyst is lower and less ether linkages are formed per unit of time. The coverage of the surface with carbon dioxide is thus close to or in equilibrium with the concentration in solution and hence the partial pressure. The rate of CO_2 insertion will then become proportional to the coverage. The fractional coverage may be described by an adjusted Everett isotherm $\theta_{CO_2} = \frac{K \cdot p_{CO_2}}{1 + K \cdot p_{CO_2}}$, and the rate of carbonate linkage formation will be proportional to θ_{CO_2}. This presumption allows explaining the observation of a limit of carbonate linkage formation below the maximum of an alternating polymer with **DMC** catalysts.

A mechanistic proposal must comprise the adsorption of CO_2 and PO to the Lewis acidic centers of the **DMCs**, and a nucleophilic attack on both. The reactions leading to the polyether
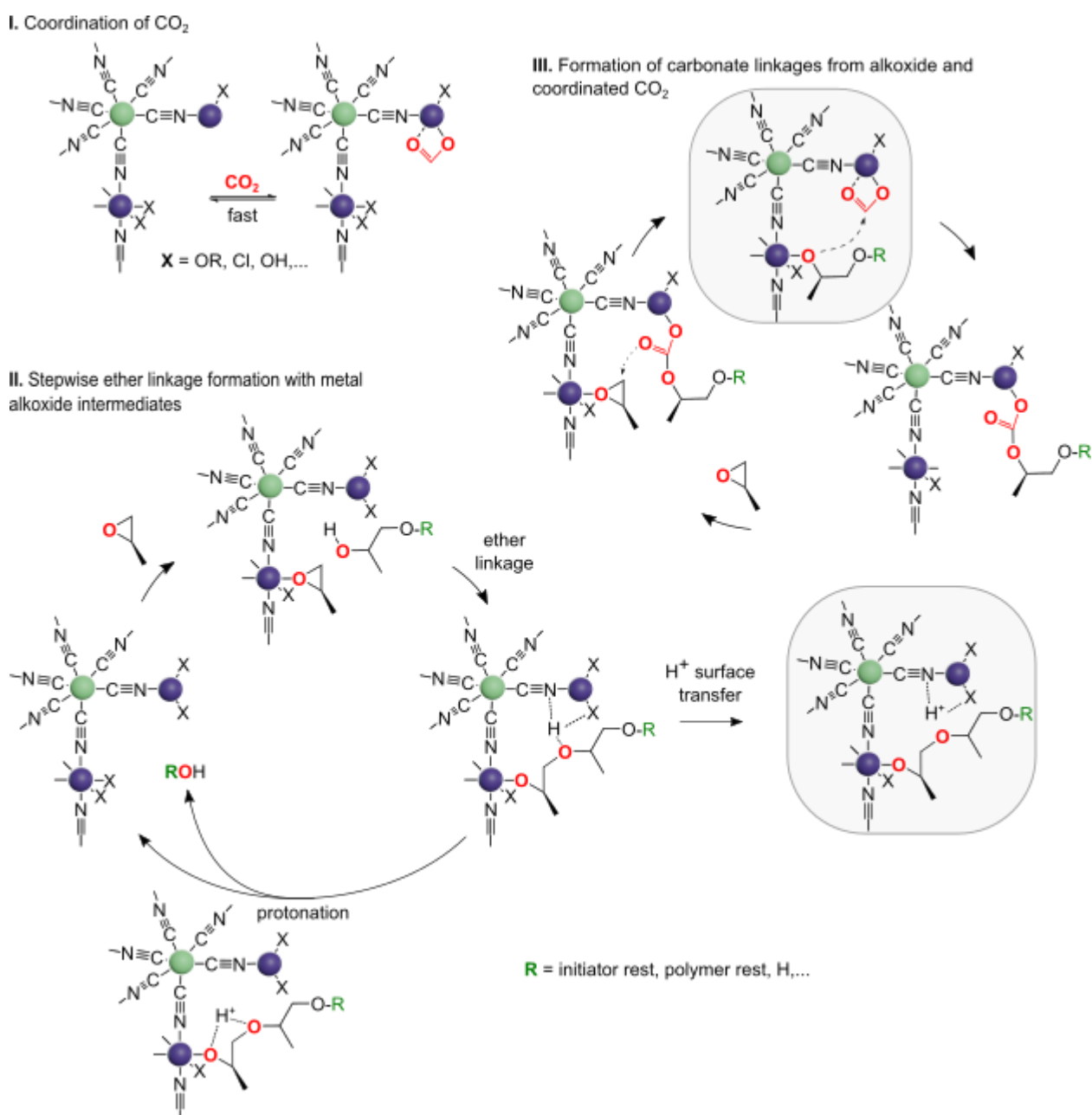
Scheme 1. Reaction pathways for the formation of PPC on a DMC surface.

carbonates are thus i) pre-equilibrium coordination of CO_2 and PO (in competition) to active sites on the **DMC** surface, ii) start of the propoxylation by nucleophilic attack of ROH on a coordinated PO to give a proton and a metal alkoxide, productively succeeded by either iiia) reaction with activated CO_2 to give a carboxylate entity, followed by coordination of PO and nucleophilic attack of the carboxylate to give the next metal alkoxide, or iiib) protonation to liberate a longer ROH (compare Scheme 1). The "insertion" of CO_2 and the base assisted ring-opening of PO by an external ROH molecule would profit from the close vicinity of two metal centers at the surface of the **DMC** (as has been put forward in the past; Scheme 1). The formation of carbonate and ether linkages have different pathways, although common intermediates in form of coordinated PO and metal alkoxides exist.[84] The main point of difference is the reaction of the alkoxide intermediate: protonation will lead to an alcohol and consecutively after reaction with PO to an ether linkage, whereas insertion of CO_2 will yield a carboxylato intermediate that directly can react with coordinated PO. In this view, the competition for ether or carbonate linkage formation is between the rate of protonation and CO_2 insertion or corresponding equilibria. This is supported by a previous study[85] in which it has been indicated that the ether linkage formation by ring opening of PO mediated by a DMC catalyst proceeds in a stepwise manner. In general, the reaction path of the proton has seldomly been given the attention it deserves in catalysis. The protonation may occur in a more or less concerted process accompanying the PO ring opening by the external ROH (either directly or of a nearby bound alkoxide) leading to propoxylated ROH. The proton on the other hand may be delocalized on the DMC surface and react at a different spot with an alkoxide. In either case, the protonation of the metal-bound alkoxide is in competition of latter reaction with activated CO_2.

The number of active sites will be set in the activation phase, wherein surface-bound neutral protonic nucleophiles (water, *t*BuOH, amine) will react with PO and generate alcohols and a proton, and some anionic nucleophiles (NO_3^-) to generate metal alkoxides. Latter reaction would generate basic sites on the surface that would react with the proton liberated from ROH in its reaction with coordinated PO (Figure 15). This would favor the formation of carbonate linkages, like was reported before.[84]

The action of the various **DMC** can be most easily ranked along the reactions in Scheme 1 at the high CO_2 concentration limit. The ratio of carbonate to ether linkages is given by the rate of protonation $k_{H^+}[H^+{}_{surf/local}][MOR]$ and carboxylation $k_{CO_2}\theta_{CO_2}[MOR]$. The $[H^+{}_{surf/local}]$ will be dependent on the number of active sites and the concentration of ROH. It may be expected that the stronger the Lewis acidity of the center is, the faster an alkoxide is formed, and the higher the H^+ concentration on the surface will be. At the same time, the surface concentration of PO will be lower as CO_2 is more readily adsorbed. Thus, the effect of a higher Lewis acidity on the H^+ concentration may go either way. Globally, it is found that the more Lewis acidic the **DMC** surface appears, the lower the pressure dependence on coordination of CO_2 (smaller slope *a*) is. This goes along with a higher incorporation with CO_2, i.e., the coordinated CO_2 is more susceptible to

nucleophilic attack. The protonation reaction apparently is less promoted by a stronger Lewis acidic metal center, indicating that CO_2 insertion is the process with the higher activation energy.

3.1.6 Conclusion

In this section, seven heterogeneous catalysts, including six different double metal cyanides (**DMCs**) and a zinc glutarate (**ZnGlu**) catalyst, were analyzed in detail and subjected to CO_2/PO copolymerization reactions. A clear trend was found between the Lewis acidic strengths of the catalyst centers and the electronic structure of the internal metal M^2. The Lewis acidity influences the composition and microstructure in poly(propylene carbonate) (PPC) polymers. Preferred high CO_2 ratios in the polymer backbones were found for strong Lewis acidic active sites, and vice versa the CO_2 ratios gradually decrease with less Lewis acidity. Similar results were obtained for the regioregularity. A strong Lewis acidity supports the formation of regioregular structures, and thus high ratios of carbonate and ether carbonate head-to-tail linkages. Further, it was found that the higher the Lewis acidity the more efficient the CO_2 uptake from comparably small concentrations in the feed.

Mechanistic considerations are presented including a discussion of a Eley-Rideal model (CO_2 is considered to be in a physisorbed state) and a microkinetic protonation dependent mechanism. The latter describes a proton transfer from an alcohol to the catalyst surface which consecutively allows for a CO_2 insertion step. More polar catalysts with a higher Lewis acidities are regarded to enhance this transfer, also leading to increased amounts of regioregular carbonate units. The evaluation led to the conclusion that microkinetic factors are of more importance for describing the differences in the action of the **DMC** catalysts. It is further considered that these structural performance insights should be valid for other substrates and future transformations and might improve future catalyst designs.

3.2 Preparation of Tunable Non-isocyanate Polyurethanes (NIPU) Based on Post-modified Polybutadienes

The results in this section were published in Green Chem., 2020, **22**, 969, DOI: 10.1039/c9gc03488a. Accordingly, graphical similarities and content related resemblances might occur. Introductory parts are taken from there:

"*The depletion of fossil fuels and the effects of global warming has inspired the development of novel polymeric materials under sustainable, mild and friendly reaction conditions, with a smaller environmental impact. Compliant polymer synthesis approaches should preclude the use of hazardous intermediates and toxic chemicals during production.[2] In this regard, carbon dioxide (CO_2) is a renewable non-toxic natural C1 feedstock of low cost and high abundance, and represents a versatile carbon building block in chemical synthesis.[3–5] The use of CO_2 can be made further relevant in the preparation of polyurethanes (PUs), materials that have gained importance on a global scale.[56,57,86] PUs are typically readily varied in their structure making them suitable for a range of diverse applications such as foams, coatings, sealants, elastomers, thermoplastics and components in adhesives and biomedical devices.*

Traditionally, polyurethanes (PUs) are primarily obtained by the polyaddition of diols (or polyols) to diisocyanates. Both isocyanates and their required precursors (i.e. phosgene) are highly toxic, environmentally hazardous compounds. As a consequence, over the last decade the interest in non-isocyanate based polyurethanes (NIPUs) has grown as a more sustainable alternative to conventional PUs. NIPUs are generally prepared from cyclic carbonate and amine compounds in an atom-efficient manner without the intermediacy of isocyanate or phosgene reagents.[54,56–58]

In recent years, several groups have examined NIPU formations using bio-based molecules such as vegetable oils[87], fatty acids[88] and terpenes[89]. Mühlhaupt et al.[90], for instance, achieved full bio-derivability through the reaction of multifunctional ß-amino alcohols (AAs) with polyfunctional cyclic carbonates which were both derived from the same bio-based polyglycidylethers. Directing towards polymer-based NIPUs, Chisholm et al.[91] developed soybean oil-derived polymers possesing 1, 4-cis cyclic carbonates on fatty acid ester side chains which were further cured with three bio-derived diamines. Interrestingly in the sense of polymeric materials and environtmentally friendly reaction conditions, Detrembleur et al.[92] exemplified recently the one-pot NIPU reaction of poly(ethylene glycol) dicyclic carbonate (PEG-di5CC) (derivable from comercially available polyethylene glycol diglycidyl ether) with polyamine polyethyleneimine (PEI). The reaction was conducted in water at room temperature.

NIPUs may show excellent behaviour in terms of chemical resistance, water absorption, thermal stability and reduced permeability.[58,93] In combination with their smaller sensitivity towards moisture, their potential in applications ranges from chemical resistant coatings to sealants and
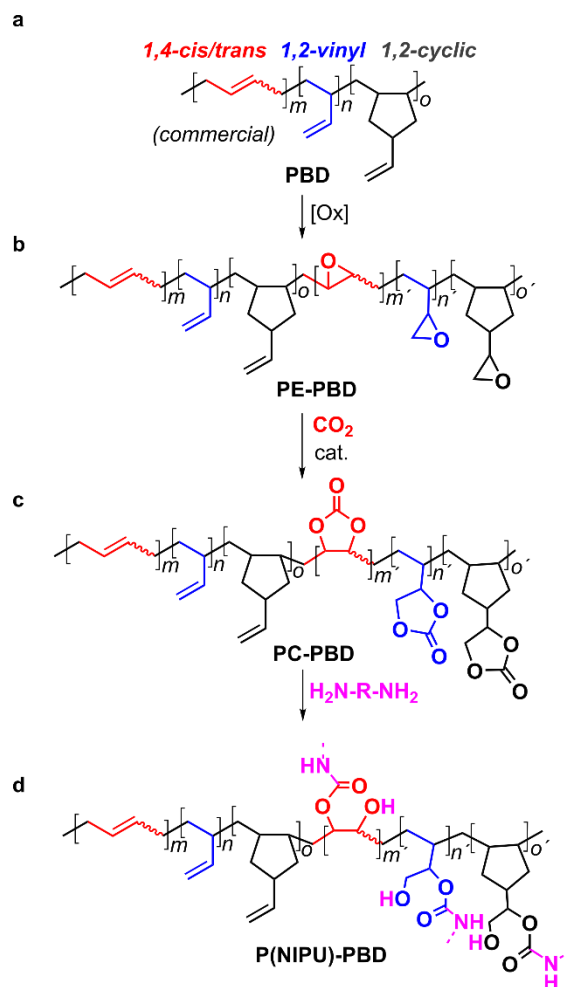
Scheme 1. *Sequential approach towards the preparation of NIPU based thermosets: (a) polybutadienes (**PBDs**) are (b) partially epoxidized to **PE-PBDs**. Thereafter, (c) the epoxy groups are converted into cyclic carbonates using CO_2 through catalysis leading to **PC-PBD**, which are (d) then finally treated with diamines to afford cross-linked **P(NIPU)-PBD** polymers.*

foams.[54,56,94] Furthermore, the hydroxyl groups emerging at the ß-carbon atom of the urethane unit after aminolysis of the cyclic carbonate offers opportunities for chemical and/or biological post-functionalizations.[56]

While cyclic carbonates can be prepared using several synthetic methods, the [3+2] cycloaddition of CO_2 to epoxides remains the most practical one. This results from the availability of its precursors and simple product purification.[56] Nonetheless, using cyclic carbonate precursors in NIPU synthesis has some challenges as long reaction times and rather harsh reaction conditions are typically required.[3,54,55] Current research interests are mainly focusing on developing (catalytic) protocols that enable NIPU production under mild reaction conditions, while controlling the overall selectivity and cost. Hybrid materials derived from epoxy resins that are partly modified with cyclic carbonates have shown an even greater promise. In these hybrids, the cyclic carbonate groups undergo ring-opening reactions in the presence of diamines to form urethane-based cross-linked structures within a simultaneously or subsequently curable epoxy resin. Depending on the epoxy/carbonate/urethane bond ratio and the type of diamine cross-linker

*applied, such networks may exhibit extended mechanical and chemical performance over those observed for typical NIPUs, classic PUs and epoxy resins alone. They have potential for application in coatings and adhesives; a family of hybrid NIPU based products has already been marketed and promoted as the next generation of PUs in Europe and the USA.[54,57,95] […] To date, the availability of 1,3-butadiene (1,3-BD) still heavily depends on crude oil (with fluctuating prices), which is expected to become a larger issue because of a more restricted future abundance on the market. It thus seems attractive to progress the development of bio-based, industrially competitive routes for **PBDs** in the next few years.[96–98] Production routes based on bioethanol as a feedstock represent already (re)consolidated alternatives[96,99] while further attempts have been made with biomass-derived butane diol[100,101], butanol[98,100], sugars[99], erythritol[102] and its derivatives[103].*

*Only a few studies seem to have been undertaken in the context of CO_2 based reactions for the modification of **PBD** epoxy resins and virtually none on **P(NIPU)-PBD** obtained from (bio-renewable) diamines and partially carbonated polybutadienes **PC-PBDs** (Scheme 1c-d). BASF, for instance, reported on epoxidised **PBDs** suitable for the formation of **PC-PBDs** by cycloaddition of CO_2 applying quaternary ammonium, tin or phosphorous based catalysts. The **PC-PBDs** could then be transformed into NIPU type networks in the presence of polyalkylene polyamides in order to produce coatings.[59] Apart from this example, moderate to low conversions were reported for CO_2 cycloaddition reactions reactions using epoxidised poly(acrylonitrile-co-butadiene) block copolymers, and catalysts such as LiBr, NaI and tetra-n-butylammonium bromide (TBAB) salts, however under rather drastic reactions conditions.[60] A further extension of the range of these type of metal catalysts has also been reported.[61]*

*Bio-based (industrial) production of 1, 3-BD combined with the development of green chemistry approaches towards the preparation of PBD-based NIPU thermosets has potential to lead to future sustainable, industrial relevant NIPU thermosets. Furthermore, the development of **P(NIPU)-PBD** would contribute to the variety of polymer-based NIPU materials."* […]

3.2.1 Introduction to Starting Polybutadienes (PBDs)

The starting polymers **PDB1 - PBD4** were analyzed prior to any modification. NMR analysis performed as described in previous reports[104,105] verified the existence of 1,4-*cis/-trans* butadiene inserted units and 1,2-cyclic/-vinyl double bonds in all four polymers (Figure 24, and for a more detailed analysis Table 5).
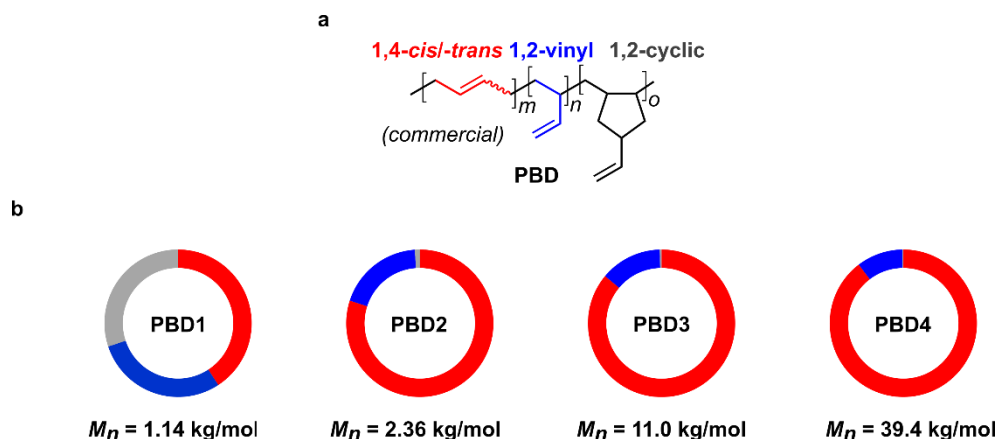
Figure 24. (a) Typical microstructural elements in PBD. (b) Microstructural composition determined by ¹H NMR analysis and number average molar masses (M_n) of **PDB1 - PBD4** determined by SEC.

Molecular weights (M_n) ranged between 1 and 40 kg/mol and showed dispersities (Đ) between 1.12 and 2.33 (Figure 24b, Table 5). The glass transition temperatures (T_g) were found to be between - 56 and - 99°C and the decomposition temperatures (T_d) were ranging between 249 and 365°C (Table 5). The amounts of double bonds were indirectly determined by epoxide titration (Experimental Part, Section 4.4.6) of partly epoxidized **PDB1 - PBD4** species (prepared by varying the preparation description in the Experimental Part, Section 4.4.6). The titrated

Table 5. Detailed properties of **PBD1 - PBD4**.

PBD	M_n [kg/mol]^a	Đ^a	double bond units [%]^b				double bond units [%]^c		double bonds [mmol/g]^d	T_g [°C]^e	T_d [°C]^f
			1,4-		1,2-		1,4-	1,2-			
			cis	*trans*	cyclic	vinyl	*cis/-trans*	cyclic/-vinyl			
1	1.14	2.33	40.8		30.1	29.1	40.7	59.3	11.7	- 56	249
2	2.63	2.58	44.4	36.6	1.1	18.9	81.4	18.6	16.0	- 94	347
3	11.0	1.12	42.1	44.0	0.4	13.5	88.1	11.9	16.7	- 94	351
4	39.4	1.12	45.8	43.9	0.2	10.2	91.6	8.40	14.2	- 99	365

^{a}Measured by GPC (THF, RT) using polystyrene standards. ^{b}Determined by ¹H NMR analysis. ^{c}Determined by ¹³C igated NMR analysis. ^{d}Measured by epoxide titration (see Experimental Part, Section 4.4.6). ^{e}Determined by DSC; data is taken from the second heating. ^{f}Decomposition temperature (T_d) determined by TGA at 1 % weight loss.
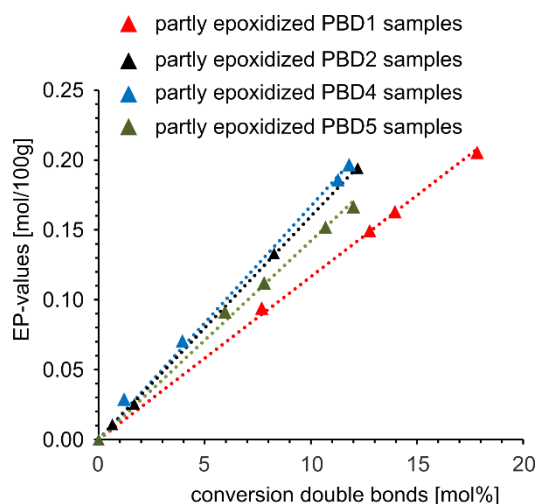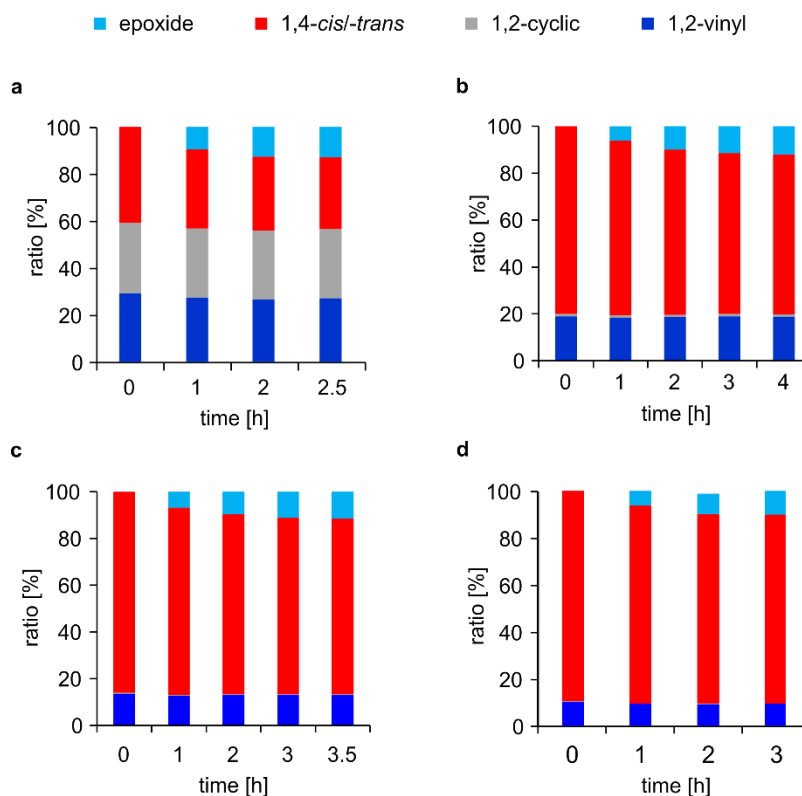
Figure 25. Applied linear fit to the relation between EP-numbers of partly epoxidized **PDB1 - PBD4** (determined by titration) and relative conversions of double bonds into epoxides determined by ^{1}H NMR analysis.

EP-numbers (amount of epoxide in 1 g of polymer) were applied to the amount of relative converted double bonds (determined by ^{1}H NMR analysis) in the corresponding **PBDs** and the resulting plots were linearly fitted and extrapolated (Figure 25, Table 6). The assumption of fully converted double bonds leads to their original amount in the **PBDs** which varied between 11.7 and 16.7 mmol/g. The theoretical value of 18.5 mmol/g is typically not reached as side reaction in the synthesis transfer double bonds into saturated components in the polymer chain.[105,106]

Table 6. Data derived by linear fit and extrapolation determined by the relation between EP-numbers and relative conversion of double bonds.

PBD	slope, a $[\frac{[mol/100g]}{mol\%}]$	coefficient of determination, R^2	EP-number at 100 % epoxide conversion [mol/100g]
1	0.0117	0.9990	1.17
2	0.0160	0.9998	1.60
3	0.0167	0.9967	1.67
4	0.0142	0.9962	1.42

3.2.2 Partial Epoxidation of PBD1 - PBD4

Partly epoxidized **PE-PBDs** were prepared in a water/toluene biphasic system using hydrogen peroxide as oxidizing agent and formic acid as phase transfer catalyst as it was described previously (Figure 26).[25,107]
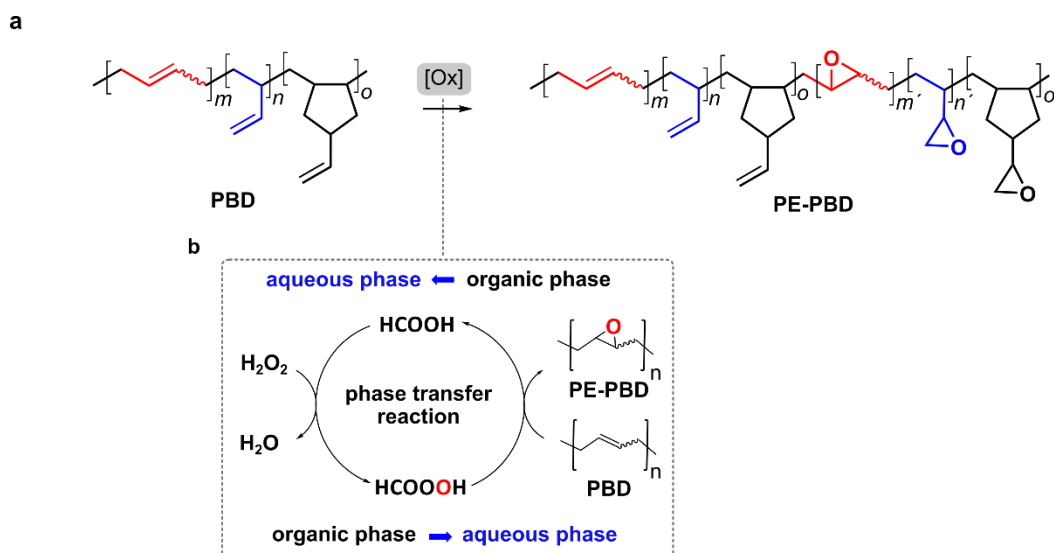
Figure 26. (a) Schematic representation and (b) mechanisms in the phase transfer reaction converting **PDB1 - PBD4** into **PE-PBD1 - PE-PBD4** using hydrogen peroxide as oxidizing agent and formic acid as phase transfer catalyst.

In accordance to previous reports,[108] 1,4-*cis* and -*trans* double bonds were mainly converted to epoxides while 1,2-vinyl and -cyclic moieties remained mostly unreacted (Figure 27, Table 7). The EP-number (amount of epoxide in 1 g of polymer) of each **PE-PBD** was determined

Table 7. Detailed properties of **PE-PBD1 - PE-PBD4**.

PE-PBD	M_n [kg/mol][a]	$Đ$[a]	epoxide units [%]				EP-number[d] [mmol/g]	T_g [°C][e]	ΔT_g [°C/mol%][b,c]	T_d [°C][f]
			total	1,4-[b] trans	cis	1,2-[b] cyclic/-vinyl				
1	1.10	2.43	13.9[b] 10.9[c]	6.50	5.95	1.47	1.62	- 45	0.79	259
2	2.64	2.56	8.26[b] 7.20[c]	3.85	4.02	0.39	1.33	- 87	0.85	322
3	11.5	1.16	11.8[b] 11.2[c]	5.74	5.95	0.07	1.96	- 83	0.93	362
4	39.7	1.13	10.7[b] 9.70[c]	5.13	5.32	0.20	1.51	- 88	1.03	375

[a]Measured by GPC (THF, RT) using polystyrene standards. [b]Determined by ^{1}H NMR analysis. [c]Determined by ^{13}C igated NMR analysis. [d]Measured by epoxide titration (see Experimental Part, Section 4.4.6). [e]Determined by DSC; data is taken from the second heating. [f]Decomposition temperature (T_d) determined by TGA at 1 % weight loss.

Figure 27. Microstructural compositions of (a) **PE-PBD1**, (b) **PE-PBD2**, (c) **PE-PBD3** and (d) **PE-PBD4** during the epoxidation process demonstrating the predominantly selective conversion of 1,4-*cis/-trans* double bonds into epoxides.

by titration and epoxide contents between 1.33 and 1.96 mmol/g were found (Table 7). The relative conversions of the double bonds, which were determined by ^{1}H NMR analysis, ranged between 8.26 for **PE-PBD2** and 13.9 % for **PE-PBD1** (between 7.20 and 10.9 % according to ^{13}C inverse gated NMR for same **PE-PBDs**). The glass transition temperatures (T_g) were found to be between - 45 and - 88°C. Depending on the microstructure, an increase between 0.8 and 1.0°C/mol% was detected, responding closely to values reported previously.[109] No cross-linking reactions had occurred during the synthesis of **PE-PBD1**, **PE-PBD2** and **PE-PBD4** as it was confirmed by GPC measurements. Some (11.9 mol%, 5.4 mol% in **PBD-3**) of a species with a double molecular weight was found in the GPC trace of **PE-PBD3** (compare Section 3.2.3, Figure 31). Any significant ether bond formation or ring-opening reactions were excluded by NMR and IR analysis (Appendix, Section A3) for all samples. The decomposition temperatures (T_d) showed an increase for all **PE-PBDs** and varied between 259 and 375°C (Table 5 and Table 7).

3.2.3 Cycloaddition of Carbon Dioxide to PE-PBD1 - PE-PBD4

The partly carbonated **PC-PBDs** were prepared by reacting **PE-PBD1 - PE-PBD4** (prepared in Section 3.2.2) with CO_2 in the presence of bis(triphenylphosphine)iminium (PPN) and tetra-*n*-butylammonium (TBA) salts with chloride, bromide and iodide as counterions (Figure 28).
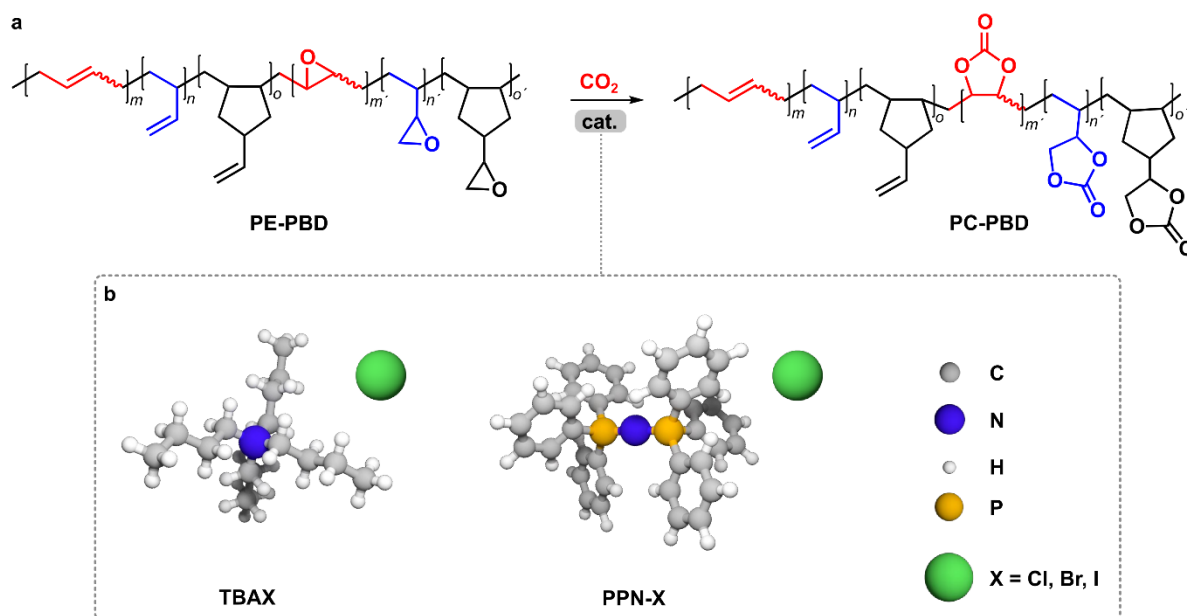
Figure 28. (a) Schematic representation of the cyclic carbonate formation using PPN-X and TBAX (X = Cl, Br, I). (b) Structural presentation of the PPN-X and TBAX (X = Cl, Br, I) salts.

The cyclic carbonate formation from an epoxide and CO_2 is promoted by an initial attack of a (suitable) halide nucleophile onto the epoxide ring yielding an alkoxide species, which is subsequently able to react with CO_2. The formed carbonate hemi-ester undergoes a consecutive ring-closing step resulting in a five-membered cyclic carbonate. Screening and scale-up experiments were performed to investigate the efficiencies of the catalysts presented above and to optimize the reaction conditions for all **PE-PBDs**.

Screening experiments. Starting with bis(triphenylphosphine)iminium (PPN)-Cl, -Br and -I, the catalytic activities were tested at different temperatures, CO_2 pressures, solvents and reaction times (Figure 29). The catalyst concentration was kept constant at 10 mol% with respect to the epoxy content determined for each **PE-PBD** in Section 3.2.2. First, tests were performed determining suitable reaction temperatures applicable for all **PE-PBDs**. Reactions conducted at 20 bar (CO_2), 70 - 110°C in methyl ethyl ketone (MEK) as solvent, revealed initial conversions at 90°C after 24 h. The increase in temperature up to 110°C resulted into satisfactory conversions for all **PE-PBDs** (Figure 29, blue circle/square/hexagon, respectively). Under the same conditions (20 bars, 110°C, 24 h reaction time, 10 mol% of catalyst), the substitution of MEK for toluene caused a significant performance drop (Figure 29, green circle/square/hexagon), by up to 60 %
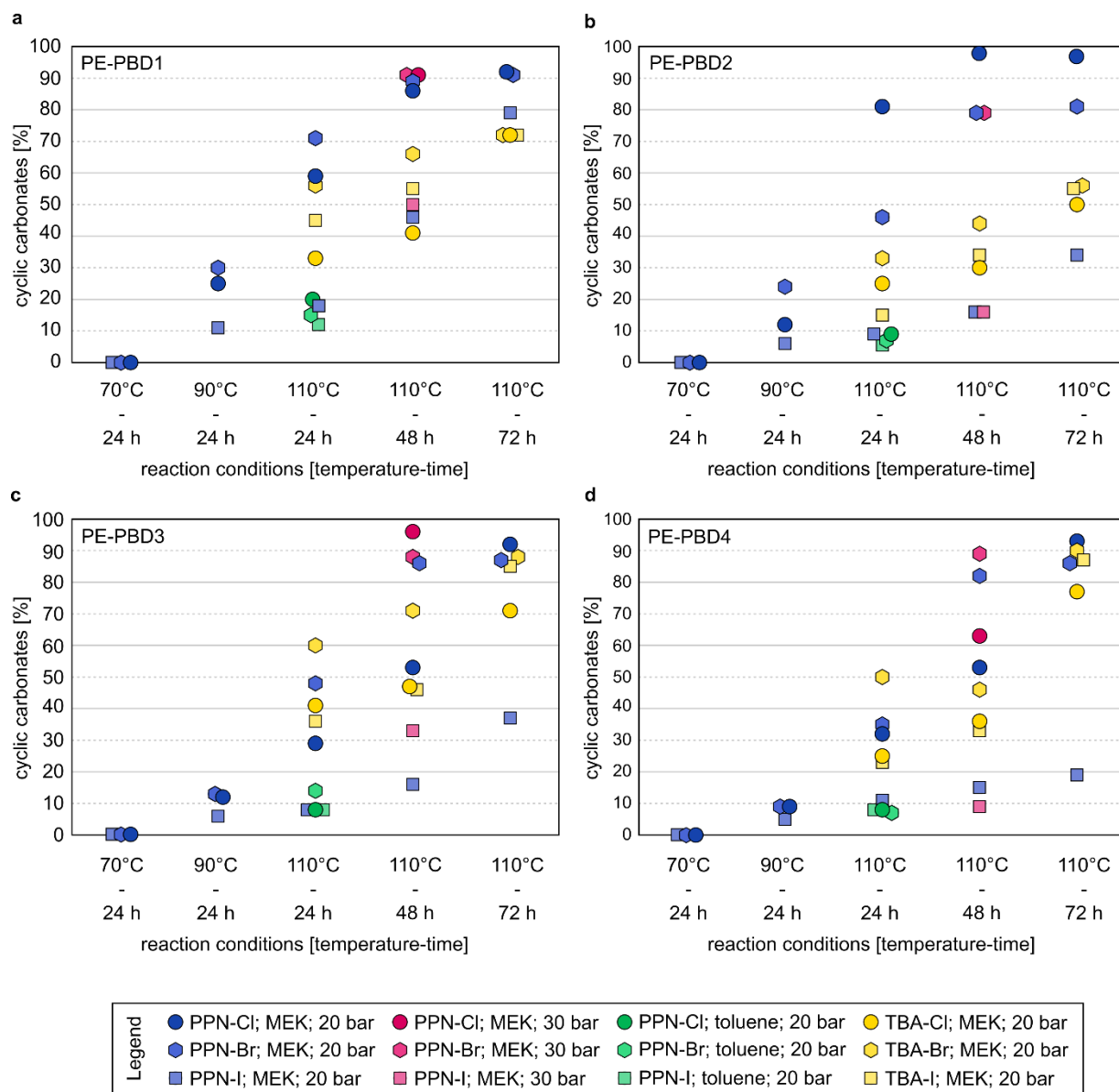
Figure 29. Optimization procedure towards the epoxide conversions into cyclic carbonates performed using 10 mol% of catalyst and various reaction conditions for (a) **PE-PBD1**, (b) **PE-PBD2**, (c) **PE-PBD3,** and (d) **PE-PBD4**, as determined by ^{1}H NMR.

for **PE-PBD2** using PPN-Br. Applying MEK from there on, the reaction time was increased to maintain comparably mild reaction conditions. For all **PE-PBDs,** excellent yields were detected after 48 - 72 h at 110°C and 20 bar CO_2 pressure. The increase of CO_2 pressures to 30 bar resulted into negligible performance improvements after 48 h (Figure 29, pink circle/square/hexagon). It showed that the molecular weight of the **PE-PBDs** negatively impacts the reactivity of the PPN catalysts which is exemplified by faster CO_2 cycloaddition reactions for the lower molecular weight **PE-PBD** precursors. With the increase in reaction time, PPN-Cl revealed overall the best catalytic performance using 110°C, 20 bar CO_2 pressure and MEK, confirming that smaller nucleophiles best convert sterically hindered epoxides present in the **PE-PBDs**. This was demonstrated in previous reports on the conversion of bulky 1,2-disubstituted oxiranes[110] and polycarbonates[111]. The examination of the cyclic carbonate content after 24 h in
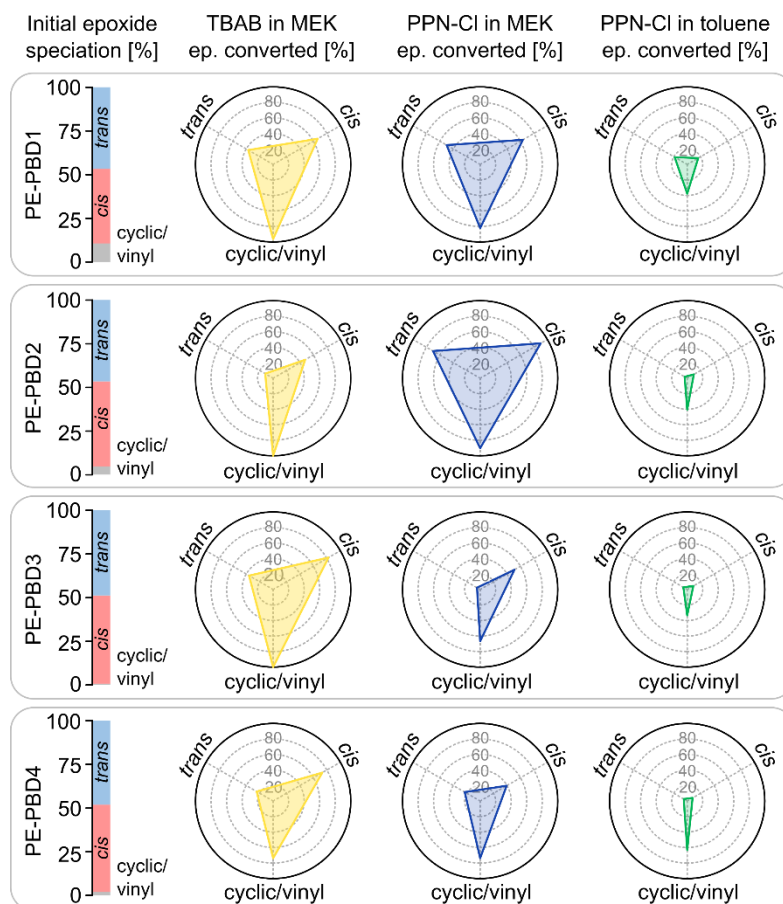
Figure 30. Selectivities towards the conversion of 1,2-cyclic/-vinyl, 1,4-*cis* and 1,4-*trans* epoxides after 24 h using different catalysts (10 mol% each) and solvents, for (a) **PE-PBD1**, (b) **PE-PBD2**, (c) **PE-PBD3,** and (d) **PE-PBD4** at 110°C and $p(CO_2)° = 20$ bar determined by ^{1}H NMR. Additional results for all screening/optimization conditions are given in the Appendix, Section A4.

MEK revealed a higher conversion applying PPN-Br as catalyst, which showed to be independent of the reaction temperature (90 and 110°C, Figure 29, blue circle/square/hexagon). Thus, a halide reactivity order of Br > Cl > I was found at the early stages of these reaction conditions. The reactivity order in toluene was determined to be Cl > Br > I for **PE-PBD1** and **PE-PBD2**. For **PE-PBD3** the reactivity order Br > Cl ≈ I was found after 24 h, respectively (Figure 29, green circle/square/hexagon). No clear trends could be observed for **PE-PBD4**. Subsequently, these findings were contrasted to the more established tetra-*n*-butylammonium bromide (TBAB) catalyst and the structurally related TBAC and TBAI (Figure 29, yellow circle/square/hexagon). In general, TBAB is exhibiting the highest levels of conversion under similar reaction conditions (*i.e.*, 110°C and 20 bar in MEK) independently of the reaction time (24 - 72 h) used. However, in comparison to PPN-Cl, overall lower conversions were determined for TBA salts. In early stages (24 h) and similar to the observations for PPN-Cl, the TBA catalysts showed reactivity orders of Br > Cl > I for **PE-PBD2 - 4**. For **PE-PBD1** a somewhat different order was determined: Br > I > Cl. For all **PE-PBDs** at later stages (72 h), I demonstrated better or equal catalytic performances in comparison to Cl. Analyzing the microstructural change in the **PE-PBD** precursors showed,
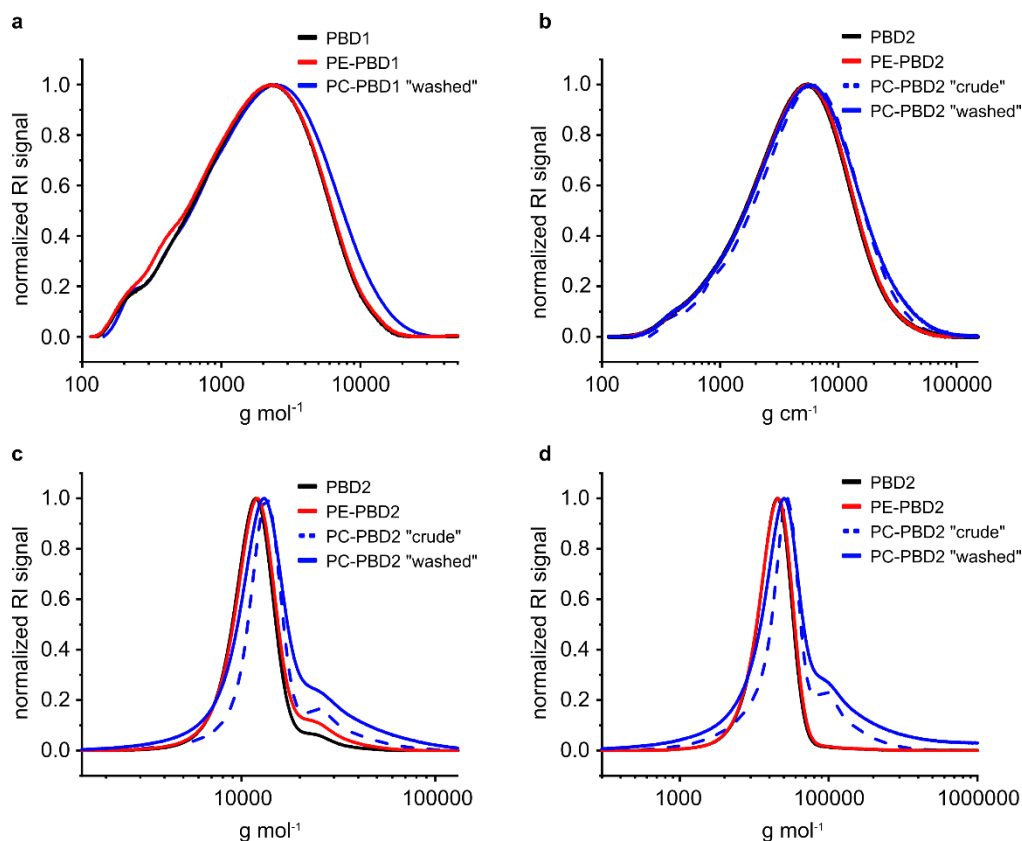
Figure 31. SEC results of and comparisons between parent and PPM altered (a) **PBD1**, (b) **PBD2**, (c) **PBD3,** and (d) **PBD4**.

independent of conditions, solvents and catalysts applied, 1,2-cyclic/-vinyl epoxides to be the most reactive moieties in the case of **PE-PBD1** followed by the 1,4-*cis* and 1,4-*trans* derived

Table 8. Scale-up experiments and data for the cycloaddition of CO_2 to **PE-PBDs** to form **PC-PBDs** utilising PPN-Cl.[a]

PE-PBD	M_n [kg/mol][b]	$Đ$[b]	conv.[c] [%]	conv.[d] [%]	select.[d, e] [%]	*cis:trans* [%][d]	T_g [°C][f]	ΔT_g [°C/mol%][g]	T_d [°C][h]
1	1.25	2.58	93	> 99	> 99	-	- 20	2.59	223
2	3.00	2.92 (2.57)[i]	91	> 99	> 99	24:76	- 74	2.42	237
3	13.2	1.48 (1.24)[i]	93	> 99	> 99	27:73	- 66	2.37	195
4	45.8	4.40 (2.48)[i]	93	> 99	> 99	22:78	- 72	2.52	273

[a]General procedure: 1.5 g of **PE-PBD**, 10.0 mol% PPN-Cl, $p(CO_2)°$ = 20 bar, 110°C (inside temperature), MEK (7.5 mL). [b]Measured by GPC (THF, RT) using polystyrene standards. [c]Conversion of epoxy groups determined by ^{1}H NMR. [d]Conversion of epoxy groups determined by ^{13}C igated NMR. [e]Regarding Meinwald rearrangement. [f]Determined by DSC; data is taken from the second heating. [g]With respect to the T_g of **PBD1 - 4** (Table 5). [h]Decomposition temperature (T_d) determined by TGA at 1 % weight loss. [i]Prior to catalyst removal.

epoxides. Similar trends were found for the formation of **PE-PBD2 - 4**, however, signals in the NMR are too small for a reliable quantification. As noted for **PE-PBD1**, the 1,4-*cis* epoxides were determined to be more reactive than the 1,4-*trans* ones. Figure 30 comprises selected results for the most efficient catalysts PPN-Cl and TBAB using MEK and toluene, 110°C, 20 bar CO_2 pressure and 24 h reaction time. More detailed information on the microstructures of the **PC-PBDs** prepared using the different conditions/catalysts presented in Figure 30 is given in the Appendix, Section A4.

Scale-up. The optimized reaction conditions (PPN-Cl, 110°C, 20 bar CO_2 pressure, 48 - 72 h, MEK) derived in the screening phase were consecutively applied in a larger scale preparation of the **PC-PBDs** to produce enough material and to gain a more detailed insight into the reaction progress (Table 8). With respect to the screening phase, comparable conversions were achieved for all **PE-PBDs**. An increase in the dispersity (*Đ*) caused by the appearance of a shoulder at double molecular weight in the GPC was observed for the higher molecular weight **PC-PBD3** and **PC-PBD4** (Table 8, Figure 31). It is likely that these shoulders are originating from cross-linking during the reaction and during the work-up, i.e., while removing the catalyst (Figure 29b - d). Meinwald rearrangements providing ketone moieties with signals typically detectable at 1720 cm^{-1} in the IR spectra and around 212, 26.6 and 26.5 ppm in the ^{13}C NMR[112] could not be observed for all **PE-PBDs** (Appendix, Section A3). In comparison to the initial amounts in the **PE-PBDs** precursors, analysis of the 1,4-*cis* and -*trans* carbonates by ^{13}C NMR techniques revealed a change in stereochemistry exhibiting higher amounts of *trans* units (Table 8). This isomerization is possibly caused by a (reversible) S_N1 type cyclization into a linear carbonate which was formed after the nucleophilic ring-opening of the epoxide

Table 9. Optimization of the scale-up conditions for the cycloaddition of CO_2 to **PE-PBDs** to form **PC-PBDs** utilising 24 h reaction time and PPN-Cl.[a]

PE-PBD	temperature, T [°C]	conversion [b] [%]	conversion [c] [%]	*cis*:*trans* [%]	selectivity[c, d] [%]
1	90	57	51	-	> 99
	110	90	>99	-	> 99
2	90	48	48	55:45	> 99
	110	>99	>99	37:63	> 99
3	90	59	51	59:41	> 99
	110	99	>99	34:66	> 99
4	90	43	49	53:47	> 99
	110	87	87	28:72	> 99

[a]General procedure: 0.5 g of **PE-PBD**, 10.0 mol% catalyst, $p(CO_2)° $ = 20 bar, 110°C (inside temperature), MEK (2.5 mL). [b]Conversion of epoxy groups determined by ^1H NMR. [c]Conversion of epoxy groups determined by ^{13}C inverse-gated NMR. [d]Regarding Meinwald rearrangements.
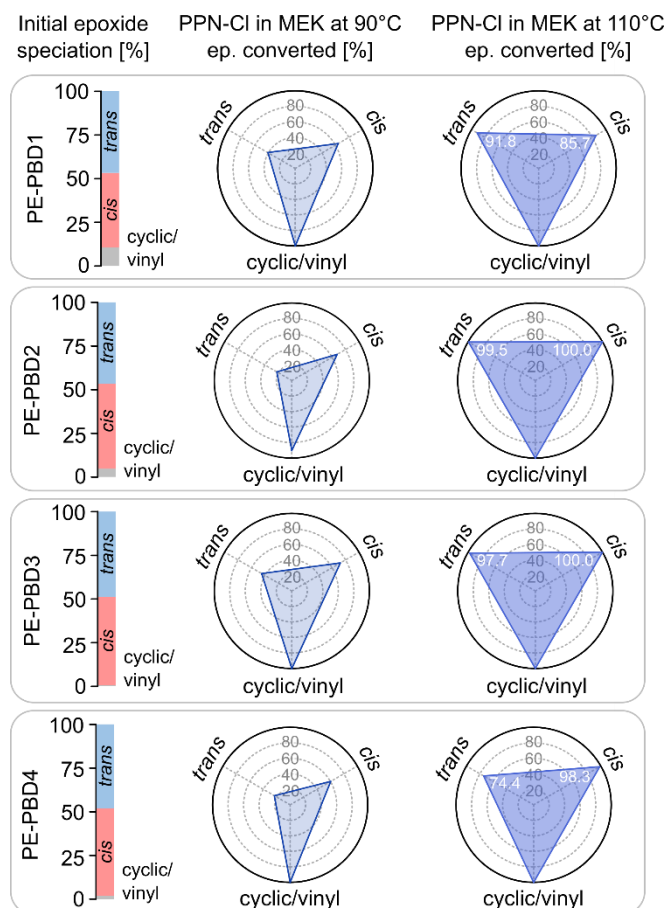
Figure 32. Selectivities in the scale-up optimization process towards the conversion of 1,2-cyclic/-vinyl, 1,4-*cis* and 1,4-*trans* epoxides after 24 h using PPN-Cl (10 mol%) in MEK, for (a) **PE-PBD1**, (b) **PE-PBD2**, (c) **PE-PBD3**, and (d) **PE-PBD4** at 110°C and $p(CO_2)° = 20$ bar determined by ^{1}H NMR.

and the reaction with CO_2.[113] The introduction of the cyclic carbonate moieties onto the polymer backbone of the **PE-PBDs** leads to a higher impact on the T_g of the polymers than the introduction of epoxide groups into **PBDs** as was revealed earlier (Table 7 and 8). Relative to the T_g of untreated **PBD1 - 4** and in dependence of the microstructure and the degree of the functionalization, the glass transition temperatures changed between 2.6 and 2.4ºC per mol% of introduced cyclic carbonate moieties. Comparing the T_d of untreated **PBD1 - 4** with those of **PC-PBD1 - 4** reveals a drop in thermal stability down to 195°C (1 % weight loss) for **PC-PBD3** caused by the introduction of the thermally less stable cyclic carbonate moieties. The reaction conditions were further optimized by conducting additional studies at larger scale (40 mL reactor). A reduction in reaction time down to 24 h for all **PE-PBDs** could be achieved possibly due to different mass/heat transfer conditions (Table 9). Meinwald rearrangements could not be detected for both reaction temperatures (90 and 110°C) giving very high selectivities (> 99 %). Applying 110°C, additional analysis of the 1,4-*cis* and -*trans* carbonates using ^{13}C NMR techniques showed a change in stereochemistry revealing an excess of *trans* units in comparison to initial amounts determined in **PE-PBDs** (Table 7). This finding corresponds to the ratios presented in Table 8 (110°C, 48 - 72 h).

In contrast, opposite results were found at 90°C showing higher amounts of *cis* units. Additional tests to reduce the catalyst concentration were not performed as smaller concentrations typically lead to harsher reaction conditions and/or longer reaction times. The analysis of the microstructure and in accordance with the screening phase, 1,2-cyclic/-vinyl moieties revealed to be most reactive in **PC-PBD1** followed by *cis* and *trans* units (Figure 32). For **PC-PBD2 - 4,** 1,2-cyclic/-vinyl amounts were again considered as too small to be accurately detected by NMR techniques, however, the reactivity trend *cis > trans* which was found in the screening phase could be confirmed.

3.2.4 Preparation of P(NIPU)-PBDs

The NIPU formation reactions were performed after the removal of the catalyst PPN-Cl using **PC-PBD1** and **PC-PBD2** as cyclic carbonate precursors. Both cross-linking agents 1,4-pentane diamine (**PDA**) and 1,8-octane diamine (**ODA**) (Figure 33), with **PDA** being bio-derivable from lysine by simple decarboxylation,[114] were reacted with the **PC-PBDs** leading to urethane linkages.
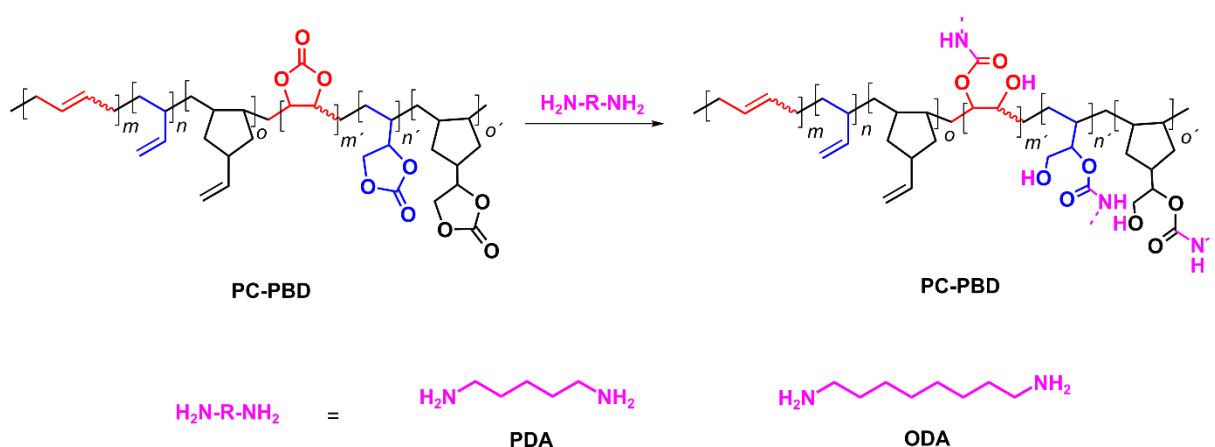
Figure 33. Urethane formation using *cis*/*trans* and pendant carbonate groups in the **PC-PBD** carbonate precursors and the diamines 1,4-pentane diamine (**PDA**) and 1,8-octane diamine (**ODA**).

The opening of the carbonate groups derived from the pendant 1,2-epoxides may lead to either primary or secondary hydroxy groups after nucleophilic attack (Figure 34).

The reaction mixtures were cured at 70°C for 16 h in a nitrogen atmosphere applying the molar ratios of carbonate to diamine of 1:1 and 1:2, respectively. The examination of the resultant products by IR analysis showed (besides the signals for the carbonate groups at 1801 cm^{-1}) bands at 1701 cm^{-1} being typical for hydrogen bonded carbamate fragments (Figure 35). The existence of free urethane –C=O functionalities is further indicated by a shoulder at 1715 cm^{-1}. The application of higher temperatures did not increase the conversion, neither in case of **PDA** nor of **ODA** (Figure 36). Experiments performed with (epoxy-based) **PE-PBD1** and **ODA** did not show
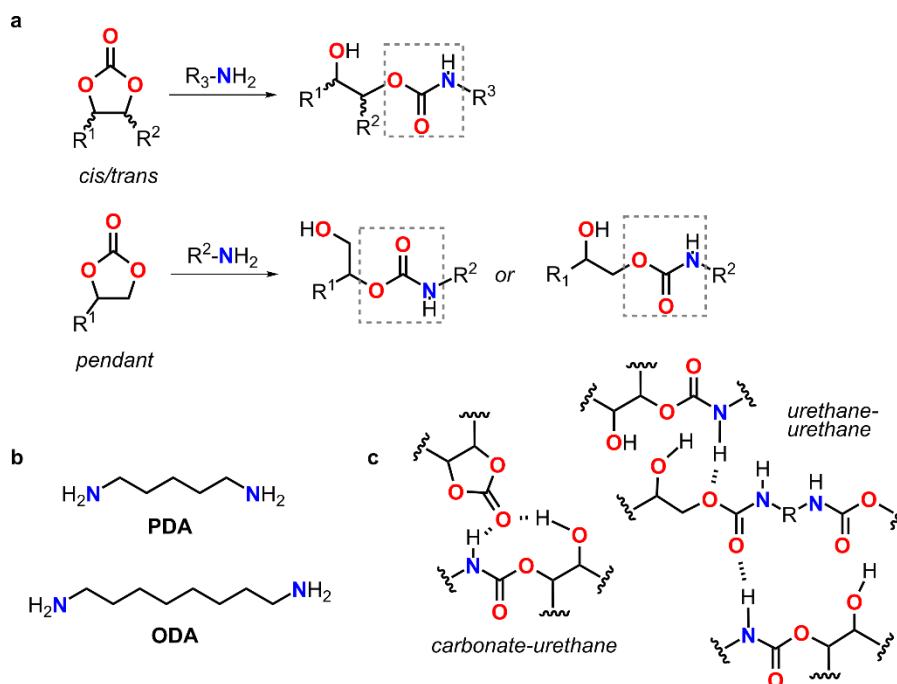
Figure 34. (a) Urethane formation using *cis/trans* pendant carbonate groups. (b) Diamines 1,4-pentane diamine (**PDA**) and 1,8-octane diamine (**ODA**) used for the NIPU cross-linking reactions with **PC-PBD1** and **PC-PBD2** forming (c) hydrogen bond interactions between cyclic carbonates and carbamate moieties and between carbamate-carbamate linkages.
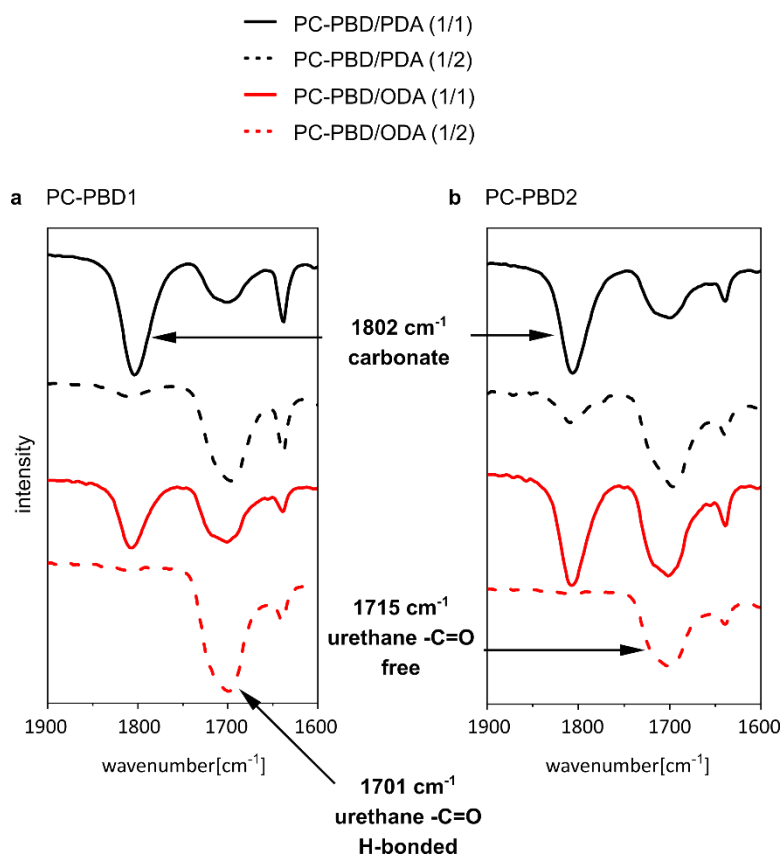
Figure 35. IR spectra of (a) **PC-PBD1** and (b) **PC-PBD2** cured with **PDA** and **ODA** at different molar ratios at 70°C for 16 h.
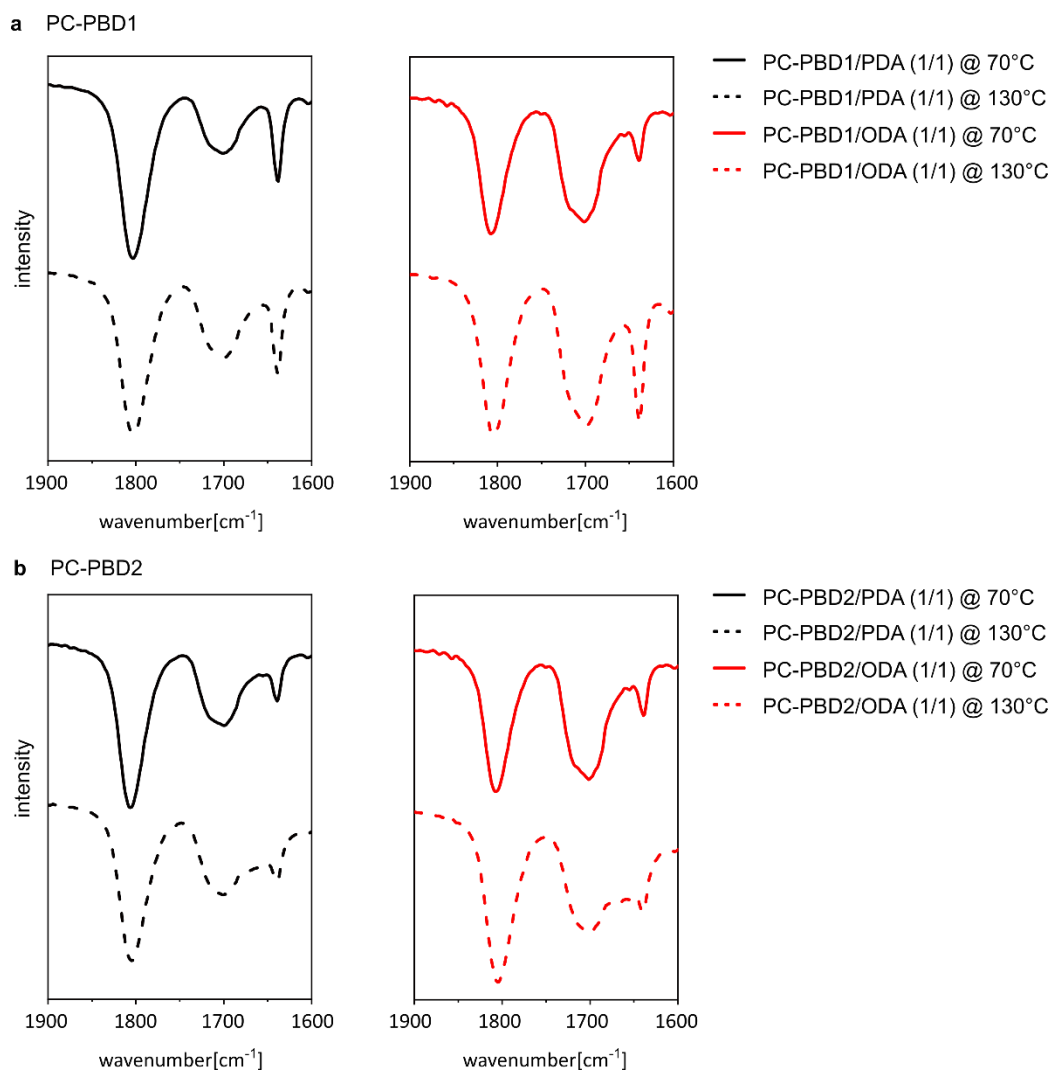
Figure 36. IR spectra of (a) **PC-PBD1** and (b) **PC-PBD2** cured with **PDA** and **ODA** at the molar ratio 1:1 using at 70°C and 130°C for 16 h.

observable cross-linking at comparable reaction conditions, proving a higher reactivity of the cyclic carbonate moieties in comparison to their epoxy precursors. Comparing the signals of the carbonate moieties with the carbamate ones revealed that the longer diamine **ODA** typically exhibited higher conversions at both molar ratios applied for both **PC-PBDs** than its shorter analogue **PDA** (Figure 35). With a larger excess of diamine (**PC-PBD**:**ODA** = 1:2), a virtual full conversion of carbonate groups was achieved for both **PC-PBDs**.

The thermal degradation behaviour of the prepared **P(NIPU)-PBDs** was investigated by thermogravimetric analysis (TGA). Onset temperatures (T_d's) of around 200°C were noted for the thermal degradation of the **P(NIPU)-PBDs**. Full degradation was detected at 500°C (Figure 37a and b). It showed that the product from **PC-PBD1** with **ODA** at a 1/1 ratio exhibits a slower decomposition, independent of the higher amount of possible urethane linkages that was formed in the same volume of **PC-PBD1/PDA** (1/1) (Figure 37a). This finding is may due to residual carbonate units in the **PC-PBD1**/**ODA** product (1/1 molar ratio) (Figure 34c) that might interact
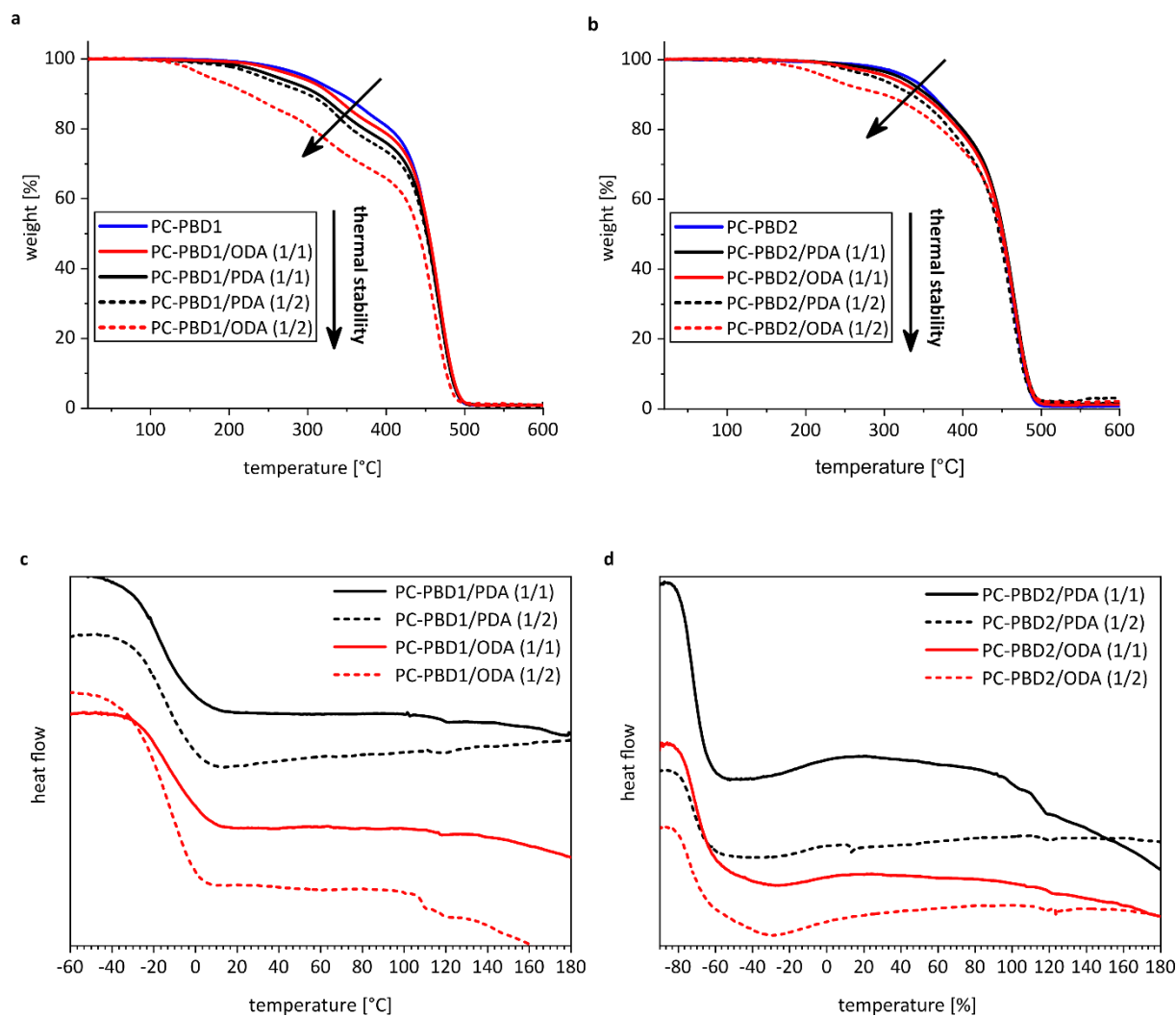
Figure 37. TGA measurements of (a) **PC-PBD1** and (b) **PC-PBD2** cured with **PDA** and **ODA** at different molar ratios at 70°C for 16 h. DSC measurements of (c) **PC-PBD1** and (d) **PC-PBD2** cured with **PDA** and **ODA** at different molar ratios at 70°C for 16 h. The heating rate was 10°C/min, in each case the trace of the second cycle is shown.

through hydrogen bond interactions with the urethane fragments, appearing next to urethane hydrogen-bond interactions, possibly leading to an enhanced network stability. The comparably high amount of 1,2-pendant carbonate units in **PBD1** in combination with a relatively low molecular weight of the carbonated **PBDs** would promote such stabilizing effects. The lower amount of cyclic carbonate functionalities in **PC-PBD2** (mostly derived from 1,4-epoxide moieties) resulting from the initial lower total amount of epoxides introduced to its backbone (Table 7) apparently leads, however, to thermally more stable **P(NIPU)-PBDs**.

Differential scanning calorimetry (DSC) measurements were performed and indicated an additional thermal feature at about 100 - 120°C in all **P(NIPU)-PBDs** (Figure 37c and d). This was associated with the melting point of the hard phases in the networks which were introduced by the presence of urethane moieties (Table 10, Figure 34c). The T_g's were ascribed to the soft

Table 10. DSC analysis of the products arising from the conversion of **PC-PBD1** and **PC-PBD2** in the presence of **PDA** and **ODA** at different ratios performed at 70ºC for 16 h. Data is taken from the second heating trace.

PC-PBD	diamine	ratio PC-PBD/diamine	T_g [ºC]	T_m [ºC]
	PDA	1/1	-16	121
1	PDA	1/2	-12	118
	ODA	1/1	-16	119
	ODA	1/2	-16	119
	PDA	1/1	-73	118
2	PDA	1/2	-72	121
	ODA	1/1	-70	122
	ODA	1/2	-73	118

PC-PBD segments, correspondingly (Table 10). Relative to the parent **PC-PBD1** and **PC-PBD2**, only small changes in the T_g´s were detected (Table 8 and 10).

3.2.5 Conclusion

The results in this section were published in Green Chem., 2020, **22**, 969, DOI: 10.1039/c9gc03488a leading to similar conclusions:

"In this work, we demonstrate that efficient cycloaddition of CO_2 to partially epoxidized polybutadienes (PE-PBDs) is feasible using the (organo)catalyst PPN-Cl. Nearly quantitative conversions were achieved for all samples after 24 h at 110°C and 20 bar CO_2 pressure independent of the molecular weight and PE-PBD microstructure. For PE-PBD1, the 1,2-cyclic/vinyl epoxides showed to be most reactive followed by the 1,4-cis and -trans moieties. For PE-PBD2–4, the 1,4-cis were more reactive than the corresponding -trans epoxides. No cross-linking reactions were observed or remained sufficient small for all reaction steps leading to the PC-PBDs. The formation of P(NIPU)-PBDs were successful, revealing a tunable rigid system, in which the carbonate conversion is adjusted by the chain length of the diamine linker. The epoxide groups did not show any reaction with the diamines at 70°C supporting the assumption that cyclic carbonates are significantly more reactive towards aminolysis and being convertible under much milder conditions without the requirement of a catalyst.41 Remaining carbonate units in incomplete cured networks show stabilizing effects putatively through hydrogen-bond interactions between urethane and carbonate moieties. Hard and soft phases were observed and assigned

to cross-linked and non-reacted sections of the parent PC-PBDs. Thus, a useful starting point is provided for the development of (crosslinked) PBDs based on NIPU technology."

4 Experimental Part

4.1 Materials

Zinc nitrate hexahydrate ($Zn(NO_3)_2 \cdot 6 H_2O$), cobalt sulfate heptahydrate ($CoSO_4 \cdot 7 H_2O$), potassium tetracyanonickelate(II) ($K_2[Ni(CN)_4]$), potassium hexacyanoferrate(III) ($K_3[Fe(CN)_6]$), and potassium hexacyanocobaltate(III) (($K_3[Co(CN)_6]$)) were obtained from Sigma Aldrich. Cobalt nitrate hexahydrate ($Co(NO_3)_2 \cdot 6 H_2O$) was acquired from Merck. *tert*-butyl alcohol (TBA) was purchased from Grüssing GmbH, propylene oxide (PO) from Gerling, Holz and & Co. Handels GmbH (GHC), and carbon dioxide (CO_2) from Linde AG. Acetone was acquired from BCD Chemie and ethanol from VWR Chemicals. Perlite (Dicalite 478) was provided by Dicalite Europe nv. **ZnGlu**, **Zn-Fe^{II}-**, and **Zn-Fe^{III}-DMCs** were used as they were prepared in previous studies.[62] Argon 4.6 and ammonia N38 (5 % mixture in helium N50 for NH_3-TPD measurements and pure for NH_3-TPD instrumental calibration) were provided by Air Liquide.

The polybutadienes (**PBDs**) Lithene ultra® AL (typical M_n = 750 g/mol), Lithene ultra® PM4 (typical M_n = 1500 g/mol), and Lithene ultra® N4-5000 (typical M_n = 5000 g/mol) were from Synthomer, and LBR-300 (typical M_n = 45000 g/mol) was provided by Kuraray. All polymers were used as received and denoted as **PBD1 - PBD4**, respectively. Toluene was purchased from BCD Chemie, hydrogen peroxide (30 % aqueous solution) from VWR Chemicals, sodium sulfate from Grüssing GmbH, and sodium chloride from JT Baker. Formic acid was acquired from VWR Chemicals. Methyl ethyl ketone (MEK), tetra-*n*-butylammonium chloride (TBAC) and iodide (TBAI), 1,5-pentanediamine and bis(triphenylphosphine)iminium chloride (PPN-Cl) were obtained from Sigma Aldrich. PPN-I and PPN-Br were prepared as described previously.[115] Tetra-*n*-butylammonium bromide (TBAB) was acquired from Acros Organics and 1,8-octanediamine was purchased from Fluka. Diethylether and dichloromethane (DCM) were obtained from TCI. Carbon dioxide (CO_2) was acquired from PRAXAIR. Deutered chloroform was purchased from Deutero GmbH.

4.2 Synthetical Procedures: Part I

4.2.1 Preparation of Double Metal Cyanide (DMC) Catalysts

Zn-Ni-DMC. $Zn[Ni(CN)_4]$ was prepared by using a modified procedure of Chen[63], substituting $ZnCl_2$ by $Zn(NO_3)_2 \cdot 6 H_2O$. Under vigorous stirring, 70 mL of a 0.2 M aqueous $K_2[Ni(CN)_4]$ solution was added dropwise into a solution consisting of 122.3 g $Zn(NO_3)_2 \cdot 6 H_2O$ (412 mmol), 280 mL of water, and 70 mL of the complexing agent TBA at 35°C. The yielding white suspension was centrifuged (5 min, 4000 rpm, 10°C) to isolate the precipitate and resuspended in a solution consisting of the complexing agent and water

(1:1 v/v) by vigorous stirring. Then, the suspension was centrifuged again. It was washed three times with gradually increasing portions of complexing agent against water to exclude potassium ions, which were detrimental to the catalyst activity. Finally the complex was suspended in pure TBA, centrifuged and dried *in vacuo* at 40°C for 3 d to yield the white solid $Zn[Ni(CN)_4]$ (2.85 g, 89 %).

Co-Ni-DMC. $Co(H_2O)_2[Ni(CN)_4] \cdot 4\ H_2O$ was prepared by using a modified procedure of Jacobsen[69] which was published by Coates[64]. Under vigorous stirring, 160 mL of a 0.23 M aqueous $K_2[Ni(CN)_4]$ solution was added to 160 mL of a 0.23 M aqueous $CoSO_4$ solution. A pink precipitate instantly formed and additional 40 mL of distilled water was added to reduce the viscosity of the suspension. The mixture was stirred for 1 h and then centrifuged (30 min, 4000 rpm, 10°C) to yield a pink microcrystalline material. The solid was washed three times with distilled water and the complex was dried *in vacuo* at 40°C for 5 d yielding the deep purple solid $Co[Ni(CN)_4]$ (6.69 g, 82 %).

Co-Co-DMC. Under vigorous stirring, 80 mL of a 0.25 M aqueous $K_3[Co(CN)_6]$ solution was added dropwise into a solution consisting of 10.48 g $Co(NO_3)_2 \cdot 6\ H_2O$ (36 mmol), 200 mL of water and 100 mL of the complexing agent TBA at 50°C. The yielding pink suspension was centrifuged (10 min, 4000 rpm, 10°C) to isolate the precipitate and resuspended in a solution consisting of the complexing agent and water (2:1 v/v) by vigorous stirring. Then, the suspension was centrifuged again. It was washed three times with TBA/water (2:1 v/v) solution, centrifuged, and finally dried *in vacuo* at 40°C for 3 d to yield the purple solid $Co_3[Co(CN)_6]_2$ (5.86 g, 97 %).

Co-Fe-DMC. Under vigorous stirring, 80 mL of a 0.25 M aqueous $K_3[Fe(CN)_6]$ solution was added dropwise into a solution consisting of 10.48 g $Co(NO_3)_2 \cdot 6\ H_2O$ (36 mmol), 200 mL of water and 100 mL of the complexing agent TBA at 50°C. The yielding red suspension was centrifuged (10 min, 4000 rpm, 10°C) to isolate the precipitate and resuspended in a solution consisting of the complexing agent and water (2:1 v/v) by vigorous stirring. Then, the suspension was centrifuged again. It was washed three times with TBA/water (2:1 v/v) solution, centrifuged, and finally dried *in vacuo* at 40°C for 3 d to yield the black solid $Co_3[Fe(CN)_6]_2$ (6.66 g, 56 %).

4.2.2 Determination of Feed Composition

The CO_2/PO feed ratios were calculated from previous data[81] covering the temperature range between 30 and 80°C. The provided data was consistent with an earlier report presenting comparably rough determinations.[116] By fitting the data linearly (Figure 38), the mole fraction of CO_2 in the feed (x_{CO2}) can be determined by the applied pressure according to

$$p_{CO2} = a \cdot x_{CO2} + p_0 \tag{16}$$

with a = 12.04 MPa and p_0 = 0.54 MPa at 80°C; a = 9.74 MPa and p_0 = 0.230 MPa at 60°C; a = 8.38 MPa and p_0 = 0.194 MPa at 50°C.
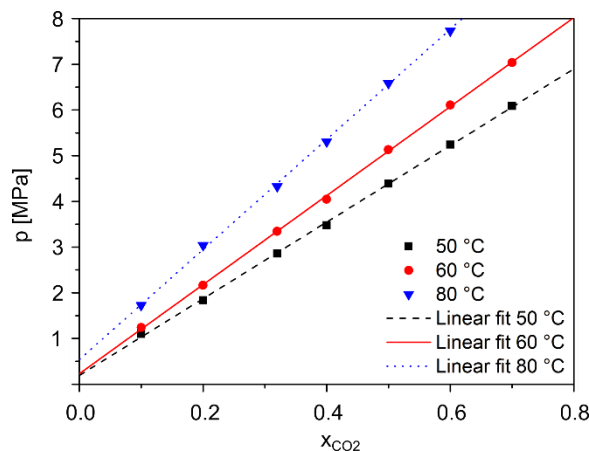
Figure 38. Liquid phase composition in the PO/CO_2 binary system.

The mole fraction of PO (x_{PO}) is calculated as followed:

$$x_{PO} = 1 - x_{CO2}. \tag{17}$$

4.2.3 Copolymerization of CO_2 and PO

Zn-Fe^{II}-/Zn-Fe^{III}-/Zn-Ni-/Co-Co-/Co-Fe-DMC. Experiments were performed in 300 mL stainless steel autoclaves (Parr Instrument Company, Series 4560 Mini Reactors) equipped with a propeller stirrer. The reactors were typically loaded with 100 mg of catalyst, sealed, evacuated to remove all volatiles and pressurized with 1 MPa of CO_2. PO (50 mL; 0.71 mol) was subsequently added with a HPLC pump (Bischoff Chromatography, HPD Multitherm 200) and the reactor was heated up to 60°C (80°C for **Co-Co-DMC** and **Co-Fe-DMC)**. The pressure was adjusted to the desired target pressure (0.6 - 4.1 MPa) and kept constant by a mass flow controller for 4 h of reaction time. Copolymerizations were quenched by cooling the reactors to RT. Then, the CO_2 pressure was released, and vacuum was applied to remove unreacted PO. The resulting product was dissolved in acetone. The viscous solution was cast onto an evaporating dish and dried at 40°C under a dynamic vacuum to a constant weight.

Co-Ni-DMC. Prior to the polymerization procedure described above (100 mg catalyst, 60°C reaction temperature), the catalyst needed to be activated for 20 min at 130°C under vacuum conditions.

4.2.4 Double Metal Cyanide (DMC) Catalyst Removal

Removal Co-Ni-DMC. The resulting polymers (0.6 g) were dissolved in 50 mL toluene, 3.5 g of the filter aid perlite was added, and the suspension was stirred for 10 min. Then, the suspension was filtered and the solvent was removed by rotary evaporation. The polymer was dried *in vacuo* at 40°C to a constant weight.

Removal Co-Co-DMC. The resulting polymers (0.6 g) were dissolved in 50 mL toluene, 3.5 g of the filter aid celite was added and the suspension was stirred for 10 min. Then, the suspension was filtered and the solvent was removed by rotary evaporation. The polymer was dried *in vacuo* at 40°C to a constant weight.

Removal Co-Fe-DMC. The resulting polymers (0.6 g) were dissolved in 30 mL ethyl acetate, 20 mL H_2O_2 (30 %) was added, and the mixture was stirred at 40°C. As soon as the oxidation of the catalyst has been completed and the resulting oxidized species were transferred to the aqueous phase, the solution was cooled to room temperature and the aqueous phase was removed. The filter aid perlite (1 g) was added, and the suspension was stirred for 10 min. Then, the suspension was filtered and the solvent was removed by rotary evaporation. The polymer was dried *in vacuo* at 40°C to a constant weight.

4.2.5 Cyclic Propylene Carbonate (cPC) Removal

The PPC samples were dissolved in small amounts of acetone and the resulting viscous solutions were precipitated in ethanol. The samples were centrifuged at 7000 rpm and the solvents were removed via decantation. The procedure was repeated at least twice and subsequently, polymer residues were subjected to *in vacuo* drying at 40°C to a constant weight.

4.3 Synthetical Procedures: Part II

4.3.1 Epoxidation of PBDs

In a typical procedure, a solution of the respective **PBD** (10 wt%) and toluene was placed in a 1 L round-bottom flask and heated up to 60°C. Under vigorous stirring, 0.64 wt% (for LBR-300: 0.62 wt%) of formic acid was added, followed by the addition of 2.9 wt% hydrogen peroxide. Stirring was continued up to 3.5 h and then the dispersion was slowly cooled down to RT. The organic phase was washed twice with a saturated aqueous $NaHCO_3$ solution, once with brine and was consecutively dried over Na_2SO_4. The solvent was removed by rotary evaporation and the remaining polymer was further dried in vacuum at 40°C until constant weight. By variation of the reaction conditions, a range of polymer samples with different oxirane oxygen contents were prepared and the total

number of unsaturated double bonds were derived by the titration method and ^{1}H-NMR spectroscopy described in Section 4.4.

4.3.2 Cycloaddition Reactions of PE-PBDs to afford PC-PBDs

Screening reactor. In a typical procedure, 100 mg of epoxidized **PBD**, catalyst (10 mol% with respect to the epoxide content), and MEK (0.5 mL) were mixed in a glass tube equipped with a magnetic stirring bar, placed in a stainless steel reactor, purged three times with 5 bar of CO_2, and pressurized with 20 bar of CO_2 at RT. The mixture was heated up to 110°C (external temperature) and stirred for 24 - 72 h. After cooling down in an ice/water bath, the reactor was slowly depressurized. The liquid phase was transferred into a vial and the glass tube was thoroughly rinsed with dichloromethane (DCM). All volatiles were removed at 40°C under vacuum.

Scale-up experiments. In a typical procedure, 1.5 g of epoxidized **PBD**, PPN-Cl (10 mol% with respect to the epoxide content) and MEK (7.5 mL) were mixed in a Teflon vessel equipped with a magnetic stirring bar, placed in a stainless steel reactor, purged three times with 5 bar of CO_2, and pressurized with 20 bar of CO_2 at RT. The mixture was heated to 110°C, measured inside the reactor, and stirred for 24 - 72 h. After cooling down in an ice/water bath, the reactor was slowly depressurized. The liquid phase was transferred into a flask and the Teflon insert S17 thoroughly rinsed with DCM. Removal of all volatiles in vacuum was followed by dissolving the residue in diethyl ether. The organic phase was washed three times with water and once with brine. In some cases, it was necessary to repeat this treatment to remove remaining PPN-Cl from the polymer product. After drying at 40°C under vacuum, up to 91 % isolated yield of the polymer could be obtained, and the product was then used for further analysis.

4.3.3 Preparation of Non-isocyanate Based PUs from PC-PBDs

Polybutadiene based NIPUs [**P(NIPU)-PBDs**] were synthesized by the reaction of the **PC-PBD** samples with 1,5-pentanediamine or 1,8-octanediamine. For the NIPU formation, the carbonated polybutadiene was mixed with the diamine (in a molar ratio of 1:1 or 1:2 with respect to the epoxide content) and was then cured through heating in a nitrogen atmosphere for 16 h.

4.4 Instrumentation and Measurements

4.4.1 Nuclear Magnetic Resonance (NMR) Spectroscopy

^{1}H NMR and ^{13}C NMR spectra were recorded at ambient conditions on Bruker AV-400 (400 MHz) or AV-500 (500 MHz) spectrometers in CDCl$_3$ and referenced to the respective residual deuterated solvent signal. All reported NMR values are given in parts per million (ppm).

^{1}H and ^{13}C NMR spectra evaluation of PBD1 - PBD4. Mole fractions (x_i) of 1,2-cyclic/-vinyl and 1,4-*cis*/-*trans* double bonds were determined from corresponding signals in ^{1}H NMR and ^{13}C NMR spectra. The assignment for the ^{1}H analysis is given in Figure 39. According to the signal assignment, fractions were calculated from ^{1}H NMR spectra according to

$$x_{\text{double bond type}} \, [\%] = \frac{I_{\text{double bond type}}}{I_{\text{double bonds,total}}} \cdot 100. \tag{18}$$

applying normalized integrals (I). The assignment for the ^{13}C NMR analysis is given in Figure 40. For ^{13}C NMR spectra, fractions were calculated from

$$x_{1,4-cis/-trans} \, [\%] = \frac{I_{1,4-cis/-trans} - I_{\text{styrene}}}{I_{\text{double bonds,total}} - I_{\text{styrene}}} \cdot 100 \tag{19}$$

and

$$x_{1,2-\text{cylic}/-\text{vinyl}} \, [\%] = \frac{I_{\text{terminal 1,2-cyclic}/-\text{vinyl}}}{I_{\text{total}} - I_{\text{styrene}}} \cdot 100, \tag{20}$$

using normalized integrals (I), respectively.
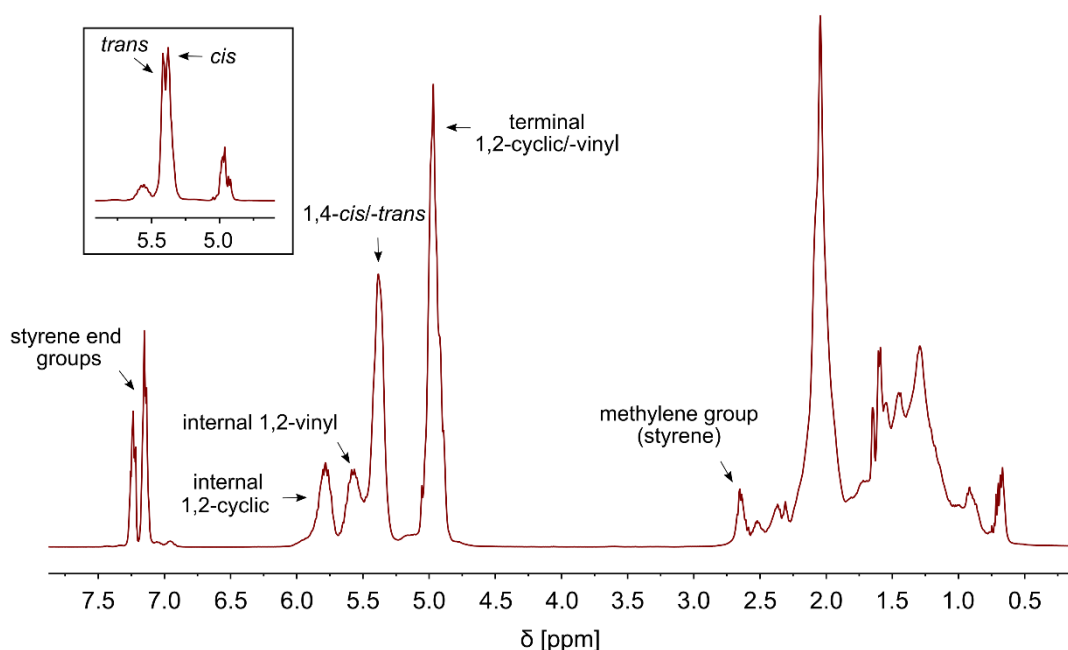
Figure 39. ^{1}H NMR spectrum of **PBD1** exemplifying the signal assignment applicable for all **PBDs**. With larger proportions, 1,4-*cis* and -*trans* double bond signals become distinguishable (frame on the up left, observable at **PBD2 - PBD4**).
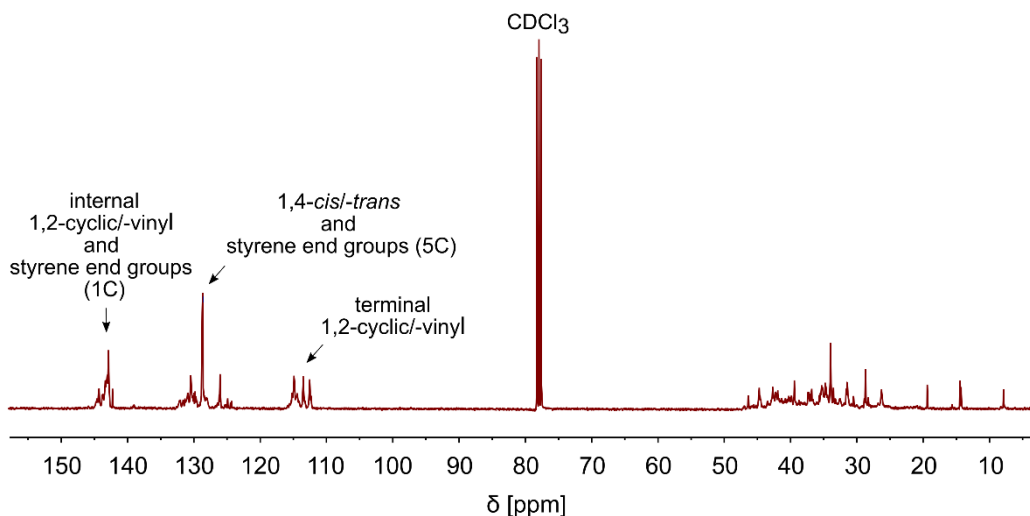
Figure 40. ^{13}C NMR spectrum of **PBD1** exemplifying the signal assignment applicable for all **PBDs**.

^{1}H and ^{13}C NMR spectra evaluation of PE-PBD1 - PE-PBD4. Mole fractions (x_i) of double bonds and epoxides (1,2-cyclic/-vinyl and 1,4-*cis*/-*trans*, respectively) were determined from corresponding signals in ^{1}H and ^{13}C NMR spectra. The assignment for the ^{1}H NMR analysis is given in Figure 41.

According to the signal assignment in the ^{1}H spectra, fractions were calculated according to
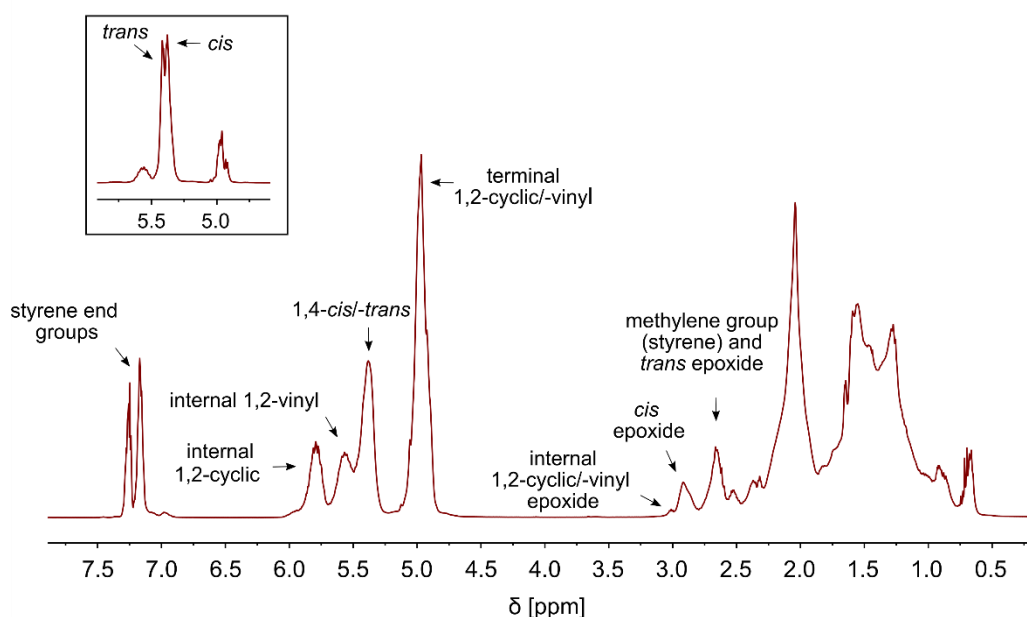
Figure 41. ^{1}H NMR spectrum of **PE-PBD1** exemplifying the signal assignment applicable for all **PBDs.** With larger proportions, 1,4-*cis* and -*trans* double bond signals become distinguishable (frame up left, observable at **PE-PBD2 - PE-PBD4**).
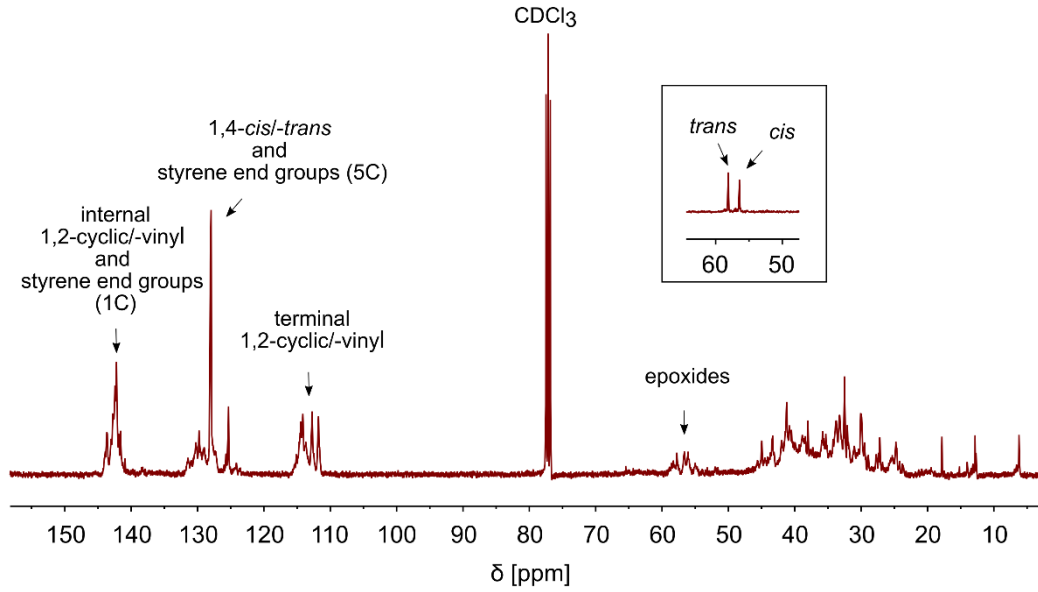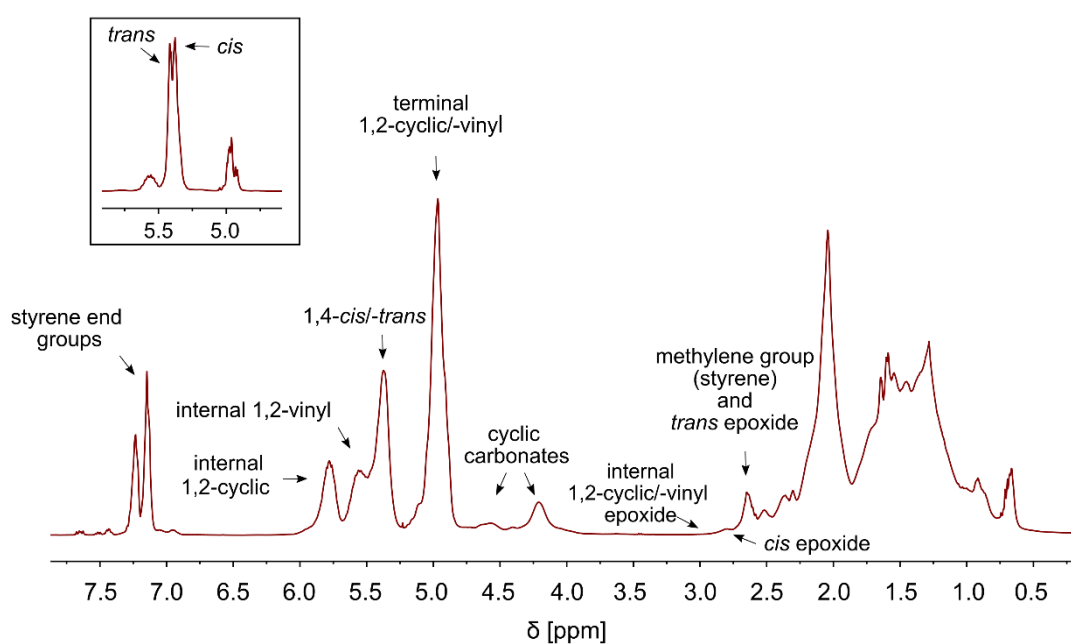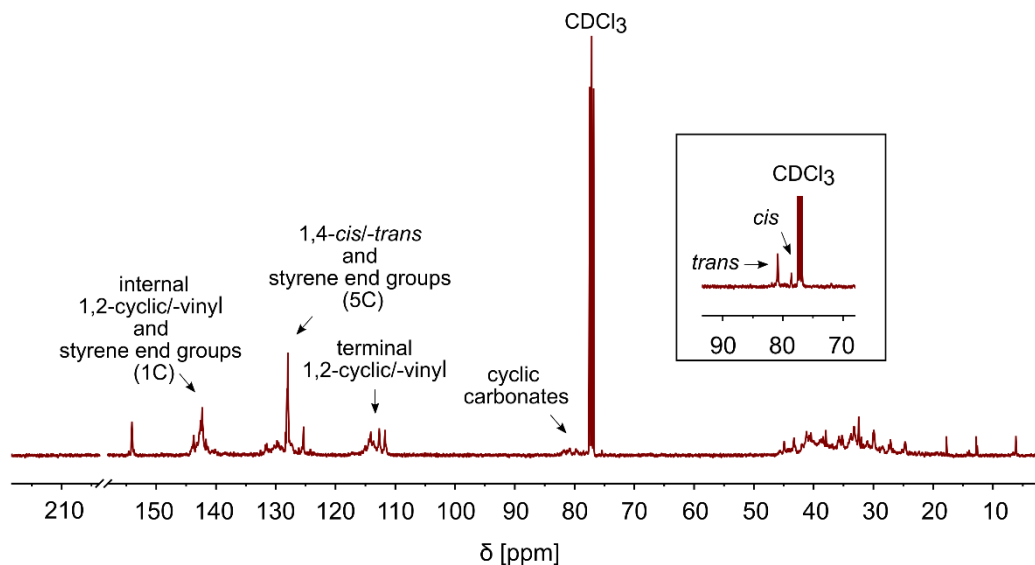
Figure 42. ^{13}C NMR spectrum of **PE-PBD1** exemplifying the signal assignment applicable for all **PE-PBDs**. Larger proportions of 1,4-*cis* and -*trans* double bonds combined with the applied *cis/trans* selective catalytic system yields higher amounts of 1,4-*cis* and -*trans* epoxides. This results into distinguishable 1,4-*cis* and -*trans* epoxide signals (frame on the up right, observable at **PE-PBD2 - PE-PBD4**).

$$x_{1,2-\text{cyclic}/-\text{vinyl epoxide}}\,[\%] = \frac{I_{1,2-\text{cyclic}/-\text{vinyl epoxide}}}{I_{\text{epoxides and double bonds,total}} - I_{\text{methylene group (styrene)}}} \cdot 100, \qquad (21)$$

$$x_{1,4-cis\,\text{epoxide}}\,[\%] = \frac{I_{1,4-cis\,\text{epoxide}}}{I_{\text{epoxides and double bonds,total}} - I_{\text{methylene group (styrene)}}} \cdot 100, \qquad (22)$$

and

$$x_{1,4-trans\,\text{epoxide}}\,[\%] = \frac{I_{\text{epoxide type}} - I_{\text{methylene group (styrene)}}}{I_{\text{epoxides and double bonds,total}} - I_{\text{methylene group (styrene)}}} \cdot 100, \qquad (23)$$

using normalized integrals (I), respectively. The total fraction of epoxides after double bond conversion is thereby given by:

$$x_{\text{epoxide,total}}\,[\%] = x_{1,2-\text{cyclic}/-\text{vinyl epoxide}} + x_{1,4-cis\,\text{epoxide}} + x_{1,4-trans\,\text{epoxide}}. \qquad (24)$$

The assignment for the ^{13}C NMR analysis is given in Figure 42. For ^{13}C NMR spectra, fractions were calculated from

$$x_{\text{epoxide,total}}(\%) = \frac{I_{\text{epoxide,total}}}{I_{\text{epoxides and double bonds,total}} - I_{\text{styrene}}} \cdot 100, \qquad (25)$$

using normalized integrals (I).

^{1}H and ^{13}C NMR spectra evaluation of PC-PBD1 - PC-PBD4. Mole fractions (x_i) and conversions (X_i) of epoxides (1,2-cyclic/-vinyl and 1,4-*cis/-trans*, respectively) were calculated from corresponding signals in ^{1}H and ^{13}C NMR spectra. Selectivities towards the conversion of 1,2-cyclic/-vinyl, 1,4-*cis*, and 1,4-*trans* epoxides were identified comparing the degrees of conversions and relative changes in mole fractions, respectively. The assignment for the ^{1}H analysis is given in Figure 43. According to the signal

assignment in the ^{1}H spectra, mole fractions of epoxides after carboxylation reaction were calculated using normalized integrals:

$$x_{1,2-\text{cyclic}/-\text{vinyl epoxide}}\ [\%] = \frac{I_{1,2-\text{cyclic}/-\text{vinyl epoxide}}}{I_{\text{epoxides,total @ t=0}} - I_{\text{methylene group (styrene)}}} \cdot 100, \qquad (26)$$

$$x_{1,4-cis\ \text{epoxide}}\ [\%] = \frac{I_{1,4-cis\ \text{epoxide}}}{I_{\text{epoxides,total @ t=0}} - I_{\text{methylene group (styrene)}}} \cdot 100, \qquad (27)$$

and

$$x_{1,4-trans\ \text{epoxide}}\ [\%] = \frac{I_{\text{epoxide type}} - I_{\text{methylene group (styrene)}}}{I_{\text{epoxides,total @ t=0}} - I_{\text{methylene group (styrene)}}} \cdot 100. \qquad (28)$$

$I_{\text{epoxide,total @ t=0}}$ represents the epoxide fraction before carboxylation reaction. Overall conversions were calculated correspondingly from

$$X_{\text{epoxide}}\ [\%] = 1 - \frac{I_{\text{epoxide,total}}}{I_{\text{epoxides,total @ t=0}}} \cdot 100 \qquad (29)$$

with

$$100\ \% = x_{\text{epoxide}} + x_{1,2-\text{cyclic}/-\text{vinyl epoxide}} + x_{1,4-cis\ \text{epoxide}} + x_{1,4-trans\ \text{epoxide}}, \qquad (30)$$

using $I_{\text{epoxide,total}}$ for the epoxide fraction after carboxylation reaction. Selective conversion of 1,2-cyclic/-vinyl, 1,4-*cis* and 1,4-*trans* epoxides were determined according to

$$X_{1,2-\text{cyclic}/-\text{vinyl epoxide}}\ [\%] = 1 - \frac{I_{1,2-\text{cyclic}/-\text{vinyl epoxide}}}{I_{1,2-\text{cyclic}/-\text{vinyl epoxide @ t=0}}} \cdot 100, \qquad (31)$$

$$X_{1,4-cis\ \text{epoxide}}\ [\%] = 1 - \frac{I_{1,4-cis\ \text{epoxide}}}{I_{1,4-cis\ \text{epoxide @ t=0}}} \cdot 100, \qquad (32)$$

and

$$X_{1,4-trans\ \text{epoxide}}\ [\%] = 1 - \frac{I_{1,4-trans\ \text{epoxide}}}{I_{1,4-trans\ \text{epoxide @ t=0}}} \cdot 100, \qquad (33)$$

Figure 43. ^{1}H NMR spectrum of **PC-PBD1** exemplifying the signal assignment applicable for all **PC-PBDs**. With larger proportions, 1,4-*cis* and -*trans* double bond signals become distinguishable (frame on the up left, observable at **PC-PBD2 - PC-PBD4**).

Figure 44. ^{13}C NMR spectrum of **PC-PBD1** exemplifying the signal assignment applicable for all **PE-PBDs**. Larger proportions of 1,4-*cis* and -*trans* double bonds combined with the applied *cis/trans* selective catalytic system yields higher amounts of 1,4-*cis* and -*trans* epoxides. This results into distinguishable 1,4-c*is* and -*trans* epoxide signals and consequently into distinguishable 1,4-*cis* and -*trans* carbonate signals (frame on the up right, observable at **PC-PBD2 - PC-PBD4)**.

using normalized integrals, respectively. The assignment for the ^{13}C NMR analysis is given in Figure 44. For ^{13}C NMR spectra, fractions were calculated from

$$X_{epoxide} [\%] = 1 - \frac{I_{epoxide,total}}{I_{epoxides,total @ t=0}} \cdot 100, \tag{34}$$

using normalized integrals (I). Correspondingly, selectivities regarding 1,4-*cis* and -*trans* epoxides were calculated from

$$X_{1,4-cis \text{ cyclic carbonate}} [\%] = \frac{I_{1,4-cis \text{ cyclic carbonate}}}{I_{1,4-cis \text{ and}-trans \text{ cyclic carbonates}}} \cdot 100 \tag{35}$$

and

$$X_{1,4-trans \text{ cyclic carbonate}} [\%] = \frac{I_{1,4-trans \text{ cyclic carbonate}}}{I_{1,4-cis \text{ and}-trans \text{ cyclic carbonates}}} \cdot 100. \tag{36}$$

Selectivities (S_i) towards Meinwald rearrangements showed to be > 99 % as no signal for ketone moieties around 212, 26.6 and 26.5 ppm were present, validating that the epoxides conversion $X_{epoxide}$ can be equaled with the cyclic carbonate content.

Evaluation of ^1H and ^{13}C NMR spectra of PPC. The backbone of PPC derived from CO_2 and PO is constituted from three different building blocks (carbonate linkage, carbonate ether linkage and ether linkage). The methyl groups of those building blocks cause four distinct signals (C, EC, CE and E) in the ^1H NMR spectrum (Figure 45). The
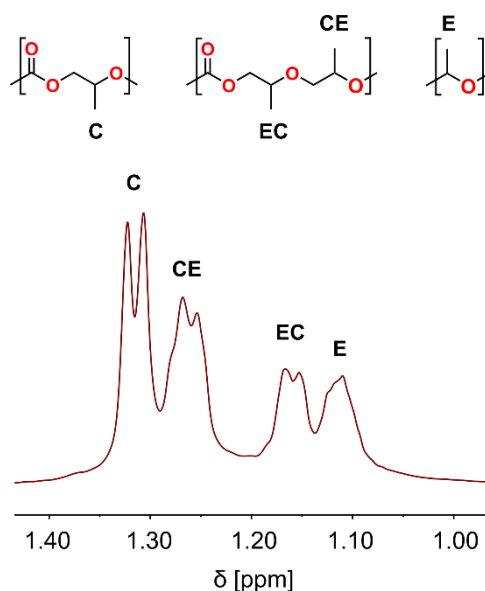
Figure 45. ^{1}H NMR spectrum of a PPC obtained by a copolymerization of CO_2 and PO mediated by **Zn-Fe^{II}-DMC** at a pressure of 3.1 MPa and a temperature of 60°C exemplifying the signal assignment for the PPC samples.

mole fractions of carbonate (X_{carb}) and ether (X_{ether}) units were calculated from the integrals of the methyl signals according to

$$X_{carb} = \frac{n_{carb}}{n_{carb}+n_{ether}} = \frac{C+0.5(EC+CE)}{C+EC+CE+E}, \tag{37}$$

$$X_{ether} = \frac{n_{ether}}{n_{ether}+n_{carb}} = \frac{E+0.5(EC+CE)}{C+EC+CE+E} \quad \text{or} \quad X_{ether} = 1 - X_{carb}. \tag{38}$$

The mole fractions of CO_2 (X_{CO2}) and PO (X_{PO}) were calculated from the methyl signals according to:

$$X_{CO2} = \frac{n_{CO2}}{n_{CO2}+n_{PO}} = \frac{C+0.5(EC+CE)}{2C+1.5(EC+CE)+E}. \tag{39}$$

$$X_{PO} = \frac{n_{PO}}{n_{PO}+n_{CO2}} = \frac{C+EC+CE+E}{2C+1.5(EC+CE)+E} \quad \text{or} \quad X_{PO} = 1 - X_{CO2}. \tag{40}$$
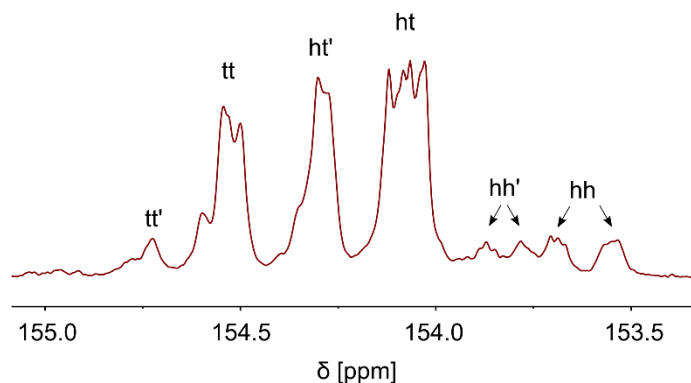
Figure 46. Carbonyl region in a ^{13}C NMR spectrum of a PPC obtained by a copolymerization of CO_2 and PO mediated by **Zn-Fe^{II}-DMC** at a pressure of 3.1 MPa and a temperature of 60°C exemplifying the signal assignment for all PPC samples.

The regioregularity of the carbonate backbone of a polymer chain can be obtained by integrating the signals of the different carbonyl species in the ^{13}C NMR spectrum (Figure 46). tt', ht' and hh' signals refer to carbonyl moieties surrounded by chained ether units. The mole fractions were calculated from the signal´s integral (I_i) according to:

$$X_{carbonyl\ species} = \frac{I_{carbonyl\ species}}{I_{carbonyl\ species,total}}.$$
(41)

4.4.2 Fourier-transform Infrared (FTIR) Spectroscopy

FT-IR measurements were performed on the **PBD** and **NIPU** samples using a Bruker Optics FTIR Alpha spectrometer equipped with a DTGS detector and KBr beam splitter. **DMC** samples were characterized on a Bruker Vertex 70 spectrometer equipped with TGS/MCT detectors. The spectrometers were operated with the OPUS software package at 4 cm^{-1}.

4.4.3 Differential Scanning Calorimetry (DSC)

Glass transition temperatures (T_g´s) and characteristic properties of **DMC** catalysts were studied on a Mettler Toledo equipment (DSC1). Samples of about 1 - 7 mg were weighed into 40 µL aluminum crucibles, cold-welded with aluminum foil lids and subjected to three heating cycles under a stream of nitrogen. For all polymers the T_g is given as the inflection point of the curve during the second cycle in the glass transition region.

PBD and NIPU samples. The experiments were started by heating the samples from - 120 to 200°C at 10 K/min heating rate. The temperature was held at 200°C for 10 min. The samples were subsequently cooled from 200 to - 120°C with a cooling rate of 10 K/min.

DMC catalysts. The samples were heated from 20 to 500°C at 10 K/min heating rate and subsequently cooled down to 20°C using a cooling rate of 10 K/min.

4.4.4 Thermogravimetric Analysis (TGA)

PBD and NIPU samples. Thermogravimetric analysis was performed on a Mettler Toledo equipment (TGA/SDTA851) between 20 and 600°C under a stream of nitrogen at a constant heating rate of 10°C/min. Samples of about 1 - 7 mg were weighed into 40 µL aluminum crucibles, cold-welded with aluminum foil lids and subjected to the measurement.

DMC catalysts. Thermogravimetric analysis was performed on a TGA 2 SF equipped with a XP1U scale between 25 and 1000°C under a stream of nitrogen at a constant heating rate of 10°C/min.

4.4.5 Size-exclusion Chromatography (SEC)

The number average molecular weight (M_n) and polydispersity ($Đ = M_w/M_n$) values of the polymers were determined by size-exclusion chromatography (SEC) in THF at RT (flow rate = 1.0 mL min^{-1}) on a Thermo Separation Products AS1000 auto sampler equipped with a Schambeck RI 2012 refractive index detector and a SDV (styrene-divinylbenzene) GPC linear column (5 μm). Samples were measured at a concentration of 5 mg/mL after filtration through a 0.45 μm pore-size membrane.

4.4.6 Epoxide Titration

Titration experiments to determine the epoxide content of the polymer samples were performed on a Fa. SI Analytics TitroLine alpha plus titration unit equipped with a TitriSoft 4.3 software and a N 6480 electrode. Samples of 1.5 mmol epoxide were weighed and dissolved into 5 mL of methyl ethyl ketone (MEK) followed by the addition of 10 mL of HCl/MEK solution (ratio 8 mL/300 mL). The flasks were sealed and stirred for 30 min after which 5 mL distilled water was added, and the samples were titrated with 0.1 M KOH in ethanol. Blank values were identified by following the same procedure, and duplicate experiments were carried out for every polymer.

The EP-number (here derived as the amount of epoxide in 100 g polymer) was calculated according to eq. 42:

$$EP - number = \frac{(V_{blind} - V_{sample}) \cdot c_{KOH} \cdot t_{KOH}}{m_{sample} \cdot 10} \tag{42}$$

with V_{blind} = consumption of 0.1 M KOH in ethanol for the blank value determination,
V_{sample} = consumption of 0.1 M KOH in ethanol for the sample titration,
c_{KOH} = conc. of KOH in ethanol (0.1 M),
t_{KOH} = titer (determined using potassium hydrogen phthalate), and
m_{sample} = sample mass.

4.4.7 Scanning Electron Microscopy (SEM)

Scanning electron microscope (SEM) images were taken on a Leo 1525 Gemini equipped with an InLens detector. Conductive samples were prepared prior to any measurement

through a carbon steaming process using a Leica ACE 600. The samples were exposed to an acceleration voltage of 5 kV.

4.4.8 Energy-dispersive X-ray Spectroscopy (EDX)

Energy-dispersive X-ray spectroscopy (EDX) measurements were performed on a Leo 1550 scanning electron microscope equipped with a SSD 100 mm² detector. The samples were exposed to an acceleration voltage of 20 kV.

4.4.9 Elemental Analysis (EA)

Elemental analysis of carbon, hydrogen and nitrogen (CHN) were performed on a Vario EL III and CHNS-O analysis was carried out on a EuroEA Elemental Analyzer equipped with a HEKAtech HT Oxygen-Analyzer.

Metal contents were determined through an ARCOS ICP-OES-spectrometer after dissolving the samples in a mixture of conc. HNO_3 (4 mL) and conc. $HClO_4$ (2 mL).

4.4.10 X-ray Diffraction (XRD)

X-ray diffraction (XRD) measurements were performed on a SROE Stadi P diffractometer and powder diffractograms were recorded between 4.5 - 90° (2 theta). Diffraction patterns at elevated temperatures were measured accordingly on a Pananalytical MPD X´Pert Pro. The samples were placed in a reaction chamber and heated up to 270°C in a nitrogen atmosphere. Both diffractometers were operated using a Cu source and a transmission geometry.

4.4.11 Matrix-assisted Laser Desorption/Ionisation (MALDI)

Matrix-assisted laser desorption/ionisation (MALDI) spectra were measured on a Bruker UltrafleXtreme MALDI-TOF/TOF spectrometer equipped with a Smartbeam II Laser. Samples were dissolved in tetrahydrofuran (THF) and a 2,5-Dihydroxybenzoic acid (2,5-DHB) matrix was applied.

4.4.12 Temperature-programmed Ammonia-desorption (NH_3-TPD)

Temperature-programmed ammonia-desorption (NH_3-TPD) measurements were performed on a self-made TPR/TPD flow system equipped with a TCD detector (filament: 10 - 454 Au/W)
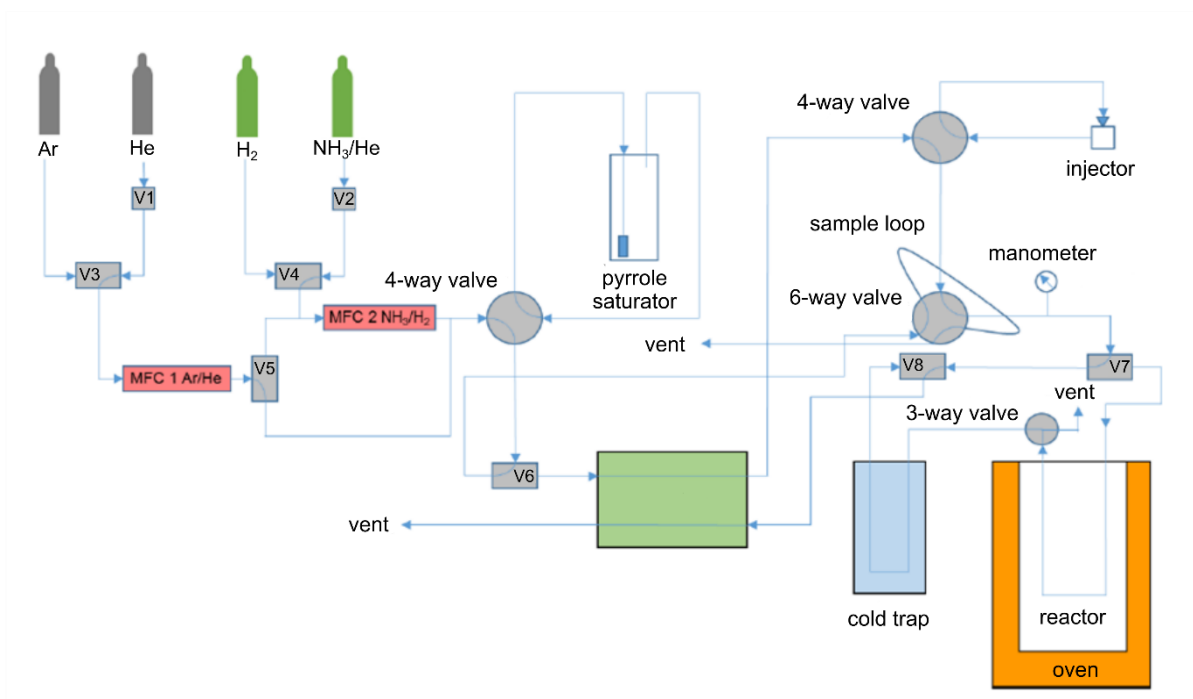
Figure 47. Schematic set-up of the TPR/TPD flow system equipped with a TCD detector.

(Figure 47). The instruments were operated with a JUMO dTron 316 software. Samples were repetitively pressed at 300 kPa/cm^2, fractionally crushed and sieved until a sufficient amount (typically 200 - 300 mg) of defined particles (215 - 300 μm) were obtained. The particles were weighed and placed in the u-shaped quarts glass reactor and heated up to 250°C within 23.5 min. The temperature was held for additional 36.5 min (total time for sample drying: 1 h) and cooled down to typically 90°C (110°C for **ZnGlu**) to proceed with ammonia adsorption. Holding this temperature for the following steps, ammonia (5 % in He) was streamed through the samples (flow rate: 25 mL/min) for 30 min. Removal of surplus, physisorbed ammonia (θ > 1) on the surface was performed through flushing the sample for additional 2.5 h with argon (flow rate: 50 mL/min). Desorption was carried out by heating up the sample using a programmed heating ramp of 8.6°C/min till a final temperature of 500°C was reached.

Safety and Disposal

All hazardous waste was disposed according to legal requirements. All chemicals used are listed in Table 11 and are accompanied by the corresponding hazard and precautionary statements.

Table 11. Utilized chemicals and corresponding hazard and precautionary statements.

Substance	GHS pictogram	Hazard statements	Precautionary statements
Acetone		H225 - H319 - H336	P210 - P240 - P305 + P351 + P338 - P403 + P233
Ammonia		H221 - H280 - H314 - H331 - H410	P210 - P260 - P273 - P280 - P377 - P381 - P304 + P340 + P310 - P304 + P340 + P315 - P305 + P351 + P338 - P405 - P403
Argon		H280	P403
Bis(triphenylphosphine) iminium bromide	-	-	-
Bis(triphenylphosphine) iminium chloride		H315 - H319 - H335	P280 - P302 + P352 - P304 + P340 - P312 - P332 + P313 - P337 + P313
Bis(triphenylphosphine) iminium iodide	-	-	-
Carbon dioxide		H280	P403
Chloroform-d		H302 - H315 - H319 - H331 - H336 - H351 - H361d - H372	P261 - P281 - P305 + P351 + P338 - P311
Cobalt nitrate hexahydrate		H272 - H302 - H317 - H334 - H341 - H350i - H360F - H410	P201 - P210 - P220 - P280 - P308 + P313 - P370 + P378
Cobalt sulfate heptahydrate		H302 - H317 - H334 - H341 - H350i - H360F - H410	P201 - P273 - P280 - P302 + P352 - P304 + P340 - P342 + P311

Dichloromethane		H315 - H319 - H335 - H336 - H351 - H373	P261 - P281 - P305 + P351 + P338 - P308
Diethyl ether		H224 - H302 - H336	P210 - P240 - P403 + P235
Ethanol		H225 - H319	P210 - P240 - P305 + P351 + P338 - P403 + P233
Formic acid		H226 - H302 - H314 - H331	P210 - P280 - P303 + P361 + P353 - P304 + P340 + P310 - P305 + P351 + P338 - P403 + P233
Lithene ultra® AL	-	-	-
Lithene ultra® PM4	-	-	-
Methyl ethyl ketone		H225 - H319 - H336	P210 - P305 + P351 + P338 - P403 + P233
Nitrogen		H280	P403
Potassium hexacyanocobaltate (III)		H351 - H302 - H312 - H332 - H317	P261 - P280 - P281 - P304 + P340 - P405 - P501
Potassium hexacyanoferrate(III)	-	-	-
Potassium tetracyanonickelate(II)		H300 + H310 + H330 - H317 - H334 - H359i - H410	P280 - P302 + P352 - P304 + P340 - P310 - P330 - P333 + P313
Propylene oxide		H224 - H311 + H331 - H302 - H315 - H319 - H335 - H340 - H350	P201 - P210 - P280 - P308 + P313 - P370 + P378 - P403 + P235
Sodium sulfate	-	-	-
tert-butyl alcohol		H225 - H319 - H332 - H335	P210 - P210 - P305 + P351 + P338 - P403 + P233

Chemical	Pictogram	Hazard Statements	Precautionary Statements
Tetra-*n*-butylammonium bromide		H-302 - H315 - H319	P261 - P280 - P302 + P352 - P305 + P351 + P338
Tetra-*n*-butylammonium chloride		H302 - H315 - H319	P261 - P280 - P302 + P352 - P305 + P351 + P338
Tetra-*n*-butylammonium iodide		H302	P301 + P312 + P330
Toluene		H225 - H304 - H315 - H336 - H361d - H373	P210 - P240 - P301 + P310 + P330 - P302 + P352 - P314 - P403 + P233
Zinc nitrate hexahydrate		H272 - H302 - H315 - H318 - H335 - H400 - H411	P210 - P280 - P305 + P351 + P338 - P371 + P380 + P375 - P273 - P391 - P501
TUBALL™ SWCNTs		H340	P201 - P280 - P308 + P313
[Dimethylsilanediyl bis(2-methyl-4-phenylindenyl)] zirconium dichloride	-	-	-
Ziegler-Natta catalyst (ZN-M/ZN-LB)		H314 - H317 - H318 - H330 - H335 - H370 - H372	P280 - P301 + 330 + 331 - P304 + 340 - P305 + 351 + 338 - P308 + 310
Trimethylaluminum		H250 - H260 - H314	P231 + P232 - P280 - P303 + P361 + P353 - P305 + P251 + P338 - P370 + P378
Triethylaluminum		H250 - H260 - H314	P210 - P231 + P232 - P280 - P302 + P334 - P303 + P361 + P353 - P304 + P340 + P310 - P305 + P351 + P338 - P370 + P378 - P422
Methylaluminoxane		H225 - H260 - H304 - H314 - H336 - H361d - H373 - H412	P210 - P231 + P232 - P280 - P301 + P330 + P331 - P303 + P361 + P353 - P304 + P340 + P310 - P305 + P351 + P338

Hydrogen		H220 - H280	P210 - P377 - P381 - P403
Propylene		H220 - H280	P210 - P377 - P381 - P403
Lithene ultra® N4-5000	-	-	-
LBR-300	-	-	-
Hydrogen peroxide (30 % aqueous solution)		H302 - H318	P280.3 - P305 + P351 + P338 - P313
1,5-pentanediamine		H314	P280 - P305 + P351 + P338 - P310
1,8-octanediamine		H302 - H314 - H31	P280 - P301 + P330 + P331 - P302 + P352 - P305 + P351 + P338 - P308 + P310
Dicalite 478	-	-	-

Utilized CMR chemicals and the number of experiments are listed in Table 12.

Table 12. Utilized CMR chemicals accompanied with the type of procedure they were used in, amount of substance, and number of conducted experiments.

CAS-No.	Compound name and Cat.	Procedure and utilized amount	No. of experiments
75-56-9	Propylene oxide (1B)	Polymerization, 0.3 L	130
67-66-3	Chloroform-d (2)	NMR solvent, 0.7 mL	869
10026-22-9	Cobalt nitrate hexahydrate (1B)	**DMC** synthesis, 16 g	5
10026-24-1	Cobalt sulfate heptahydrate (1B)	**DMC** synthesis, 10 g	4
75-09-2	Dichloromethane (2)	**PC-PBD** sample work-up, 5 mL (screening phase) and 10 mL (scale-up)	132 (screening phase) and 16 (scale-up)
13746-66-2	Potassium hexacyanocobaltate (III) (n.a.)	**DMC** synthesis, 10 g	2
339527-86-5	Potassium tetracyanonickelate(II) (1a)	**DMC** synthesis, 5 g	4

5 References

1   S. Koltzenburg, M. Maskos and O. Nuyken, in *Polymer Chemistry*, Springer Berlin Heidelberg, Berlin, Heidelberg, 2017, pp. 1–16.

2   P. Anastas and N. Eghbali, *Chemical Society reviews*, 2010, **39**, 301–312.

3   Q. Liu, L. Wu, R. Jackstell and M. Beller, *Nature Communications*, 2015, **6**, 5933 EP -, https://doi.org/10.1038/ncomms6933.

4   J. Klankermayer and W. Leitner, *Science (New York, N.Y.)*, 2015, **350**, 629–630.

5   X. Lim, *Nature*, 2015, **526**, 628–630.

6   R.-R. Ang, L. Tin Sin, S.-T. Bee, T.-T. Tee, A. Kadhum, A. R. Rahmat and B. A. Wasmi, *Journal of Cleaner Production*, 2015, **102**, 1–17.

7   Y. Wang and D. J. Darensbourg, *Coordination Chemistry Reviews*, 2018, **372**, 85–100.

8   a) D. W. Sauter, M. Taoufik and C. Boisson, *Polymers*, 2017, **9**; b) W. Kaminsky, *Polyolefins: 50 years after Ziegler and Natta I*, Springer Berlin Heidelberg, Berlin, Heidelberg, 2013, vol. 257;

9   a) R. Mülhaupt, *Macromol. Chem. Phys.*, 2003, **204**, 289–327; b) D. Braun, H. Cherdron, M. Rehahn, H. Ritter and B. Voit, *Polymer Synthesis: Theory and Practice*, Springer Berlin Heidelberg, Berlin, Heidelberg, 2013;

10 S. Inoue, H. Koinuma and T. Tsuruta, *J. Polym. Sci. B Polym. Lett.*, 1969, **7**, 287–292.

11 J. Xu, E. Feng and J. Song, *J. Appl. Polym. Sci.*, 2014, **131**.

12 A. J. Kamphuis, F. Picchioni and P. P. Pescarmona, *Green Chem*, 2019, **21**, 406–448.

13 Y. Qin and X. Wang, in *Encyclopedia of Sustainability Science and Technology*, ed. R. A. Meyers, Springer New York; Springer, New York, NY, 2019, pp. 1–25.

14 Y.-Y. Zhang and X.-H. Zhang, in *Sustainable polymers from biomass*, ed. C. Tang and C. Y. Ryu, Wiley-VCH, Weinheim, 2017, pp. 279–313.

15 G. A. Luinstra and E. Borchardt, in *Synthetic Biodegradable Polymers*, ed. B. Rieger, A. Künkel, G. W. Coates, R. Reichardt, E. Dinjus and T. A. Zevaco, Springer Berlin Heidelberg, Berlin, Heidelberg, 2012, vol. 245, pp. 29–48.

16 J. Sebastian and D. Srinivas, in *Sustainable polymers from biomass*, ed. C. Tang and C. Y. Ryu, Wiley-VCH, Weinheim, 2017, pp. 315–345.

17 Saudi Arabian Oil Co., *Saudi Aramco acquires Novomer's polyol business and associated technologies, enhancing its downstream expansion strategy,* available at: https://www.aramco.com/en/news-media/news/2016/acquires-novomers-polyol-business-downstream-expansion, accessed 11 October 2022.

18 K. Soga, E. Imai and I. Hattori, *Polymer Journal*, 1981, **13**, 407–410.

19 J.-S. Kim, H. Kim and M. Ree, *Chem. Mater.*, 2004, **16**, 2981–2983.

20 J. Kim, *Journal of Catalysis*, 2003, **218**, 386–395.

21 a) D. J. Darensbourg, K. M. Sanchez, J. H. Reibenspies and A. L. Rheingold, *Journal of the American Chemical Society*, 1989, **111**, 7094–7103; b) D. J. Darensbourg, B. L. Mueller, C. J. Bischoff, S. S. Chojnacki and J. H. Reibenspies, *Inorg. Chem.*, 1991, **30**, 2418–2424;

22 W. J. Kruper and D. J. Swart, *US Patent*, 1985, **4500704**, 5390–5395.

23 D. J. Darensbourg, *Green Chem*, 2019, **21**, 2214–2223.

24 M. Kerns, S. Henning and M. Rachita, in *Encyclopedia of polymer science and technology*, Wiley Interscience, Hoboken, NJ, 2004, vol. 127, p. 93.

25 J.-P. Dilcher, H. Jürgens and G. A. Luinstra, in *Multi-Component and Sequential Reactions in Polymer Synthesis*, ed. P. Theato, Springer International Publishing, Cham, 2015, vol. 269, pp. 163–201.

26 a) M. A. Gauthier, M. I. Gibson and H.-A. Klok, *Angewandte Chemie (International ed. in English)*, 2009, **48**, 48–58; b) E. Blasco, M. B. Sims, A. S. Goldmann, B. S. Sumerlin and C. Barner-Kowollik, *Macromolecules*, 2017, **50**, 5215–5252; c) K. A. Günay, P. Theato and H.-A. Klok, in *Functional Polymers by Post-Polymerization Modification*, ed. P. Theato and H.-A. Klok, Wiley-VCH Verlag GmbH & Co. KGaA, Weinheim, Germany, 2012, vol. 12, pp. 1–44; d) K. A. Günay, P. Theato and H.-A. Klok, *J. Polym. Sci. A Polym. Chem.*, 2013, **51**, 1–28;

27 M. I. Abdullin, A. A. Basyrov, O. S. Kukovinets, A. B. Glazyrin and G. I. Khamidullina, *Polym. Sci. Ser. B*, 2013, **55**, 349–354.

28 S. Bhaduri and D. Mukesh, *Homogeneous Catalysis. Mechanisms and Industrial Applications*, Wiley, Hoboken, 2nd edn., 2014.

29 G. Rothenberg, *Catalysis. Concepts and Green Applications*, Wiley-VCH, s.l., 1st edn., 2015.

30 I. Chorkendorff and J. W. Niemantsverdriet, *Concepts of modern catalysis and kinetics*, Wiley-VCH, Weinheim, 2005.

31 B. List, *Chem. Rev.*, 2007, **107**, 5413–5415.

32 V. Oliveira, M. Cardoso and L. Forezi, *Catalysts*, 2018, **8**, 605.

33 a) N. E. Leadbeater and M. Marco, *Angewandte Chemie (International ed. in English)*, 2003, **42**, 1407–1409; b) N. E. Leadbeater and M. Marco, *The Journal of organic chemistry*, 2003, **68**, 5660–5667;

34 N. E. Leadbeater, M. Marco and B. J. Tominack, *Organic letters*, 2003, **5**, 3919–3922.

35 D. Kristofikova, V. Modrocká, M. Mečiarová and R. Sebesta, *ChemSusChem*, 2020.

36 J. A. Dumesic, G. W. Huber and M. Boudart, in *Handbook of heterogeneous catalysis*, ed. G. Ertl, H. Knzinger, F. Schth and J. Weitkamp, Wiley-VCH, Weinheim, 2nd edn., 2008.

37 R. A. van Santen, ed., *Modern heterogeneous catalysis. An Introduction*, Wiley-VCH, Verlag GmbH & Co. KGaA, Weinheim, Germany, 2017.

38 R. Schlögl, *Angew Chem Int Ed*, 2015, **54**, 3465–3520.

39 R. Prins, *Top Catal*, 2018, **61**, 714–721.

40 D. H. Everett, *Transactions of the Faraday Society*, 1964, **60**, 1803–1813.

41 R.-R. Ang, L. T. Sin, S.-T. Bee, T.-T. Tee, A. Kadhum, A. R. Rahmat and B. A. Wasmi, *Chemical Engineering Journal*, 2017, **327**, 120–127.

42 L. Saikia, J. K. Satyarthi, R. Gonnade, D. Srinivas and P. Ratnasamy, *Catal Lett*, 2008, **123**, 24–31.

43 C. Marquez, M. Corbet, S. Smolders, P. Marion and D. de Vos, *Chemical communications (Cambridge, England)*, 2019, **55**, 12984–12987.

44 X. Li, Q. Deng, L. Yu, R. Gao, Z. Tong, C. Lu, J. Wang, Z. Zeng, J.-J. Zou and S. Deng, *Green Chem*, 2020, **22**, 2549–2557.

45 C. H. Tran, L. T. T. Pham, Y. Lee, H. B. Jang, S. Kim and I. Kim, *Journal of Catalysis*, 2019, **372**, 86–102.

46 J. Sebastian and S. Darbha, *RSC Adv.*, 2015, **5**, 18196–18203.

47 a) M. Kotwal, S. S. Deshpande and D. Srinivas, *Catalysis Communications*, 2011, **12**, 1302–1306; b) Z. Song, B. Subramaniam and R. V. Chaudhari, *ACS Sustainable Chem. Eng.*, 2019, **7**, 5698–5710;

48 R. Srivastava, D. Srinivas and P. Ratnasamy, *Journal of Catalysis*, 2006, **241**, 34–44.

49 P. S. Sreeprasanth, R. Srivastava, D. Srinivas and P. Ratnasamy, *Applied Catalysis A: General*, 2006, **314**, 148–159.

50 J. Sebastian and D. Srinivas, *Applied Catalysis A: General*, 2013, **464-465**, 51–60.

51 D. Srinivas and J. K. Satyarthi, *Catal Surv Asia*, 2011, **15**, 145–160.

52 J. Sebastian and D. Srinivas, *Applied Catalysis A: General*, 2014, **482**, 300–308.

53 Joby Sebastian and Darbha Srinivas, *Applied Catalysis A: General*, 2015, **506**, 163–172, https://www.sciencedirect.com/science/article/pii/S0926860X15301435.

54 J. Guan, Y. Song, Y. Lin, X. Yin, M. Zuo, Y. Zhao, X. Tao and Q. Zheng, *Ind. Eng. Chem. Res.*, 2011, **50**, 6517–6527.

55 A. Pizzolante, S.-E. Dechent, A. W. Kleij and C. M. Kozak, in *Carbon dioxide utilisation. From fundamentals to production processes*, ed. M. North and P. Styring, De Gruyter, Berlin/Boston, 2019, pp. 303–328.

56 L. Maisonneuve, O. Lamarzelle, E. Rix, E. Grau and H. Cramail, *Chemical reviews*, 2015, **115**, 12407–12439.

57 G. Rokicki, P. G. Parzuchowski and M. Mazurek, *Polym. Adv. Technol.*, 2015, **26**, 707–761.

58 H. Blattmann, M. Fleischer, M. Bähr and R. Mülhaupt, *Macromolecular rapid communications*, 2014, **35**, 1238–1254.

59 T. S. December, P. J. Harris, Curable coating composition containing a resin with latent functionality, 1999, USOO5994469A.

60 A. Meissner, P. Scholz and B. Ondruschka, *Collect. Czech. Chem. Commun.*, 2008, **73**, 88–96.

61 P. Lamprecht, G. A. Luinstra, I. Fink, Polybutadien mit 1,3-Dioxolan-2-on Gruppen, 2012, DE102012017055A1.

62 B. Nörnberg, *Dissertation*, Hamburg, 2015.

63 S. Chen, Z. Xiao and M. Ma, *J. Appl. Polym. Sci.*, 2008, **107**, 3871–3877.

64 N. J. Robertson, Z. Qin, G. C. Dallinger, E. B. Lobkovsky, S. Lee and G. W. Coates, *Dalton transactions (Cambridge, England : 2003)*, 2006, 5390–5395.

65 a) C. Aparicio, L. Machala and Z. Marusak, *J Therm Anal Calorim*, 2012, **110**, 661–669; b) M. B. Zakaria and T. Chikyow, *Coordination Chemistry Reviews*, 2017, **352**, 328–345; c) D. P. Domonov, S. I. Pechenyuk and Y. P. Semushina, *J Therm Anal Calorim*, 2020, **61**, 49; d) C. Aparicio, J. Filip and L. Machala, *Powder Diffr.*, 2017, **32**, S207-S212;

66 a) F. Herren, P. Fischer, A. Ludi and W. Haelg, *Inorg. Chem.*, 1980, **19**, 956–959; b) L. Hu, P. Zhang, Q. Chen, J. Mei and N. Yan, *RSC Adv.*, 2011, **1**, 1574; c) P. K. Thallapally, R. K. Motkuri, C. A. Fernandez, B. P. McGrail and G. S. Behrooz, *Inorg. Chem.*, 2010, **49**, 4909–4915;

67 S. J. Yu, Y. Liu, S. J. Byeon, D. W. Park and I. Kim, *Catalysis Today*, 2014, **232**, 75–81.

68 K. Alferov, S. Wang, T. Li, M. Xiao, S. Guan and Y. Meng, *Catalysts*, 2019, **9**, 632.

69 T. Niu, G. Crisci, J. Lu and A. J. Jacobson, *Acta Crystallogr C Cryst Struct Commun*, 1998, **54**, 565–567.

70 a) Y. Z. Meng, L. C. Du, S. C. Tiong, Q. Zhu and A. S. Hay, *J. Polym. Sci. A Polym. Chem.*, 2002, **40**, 3579–3591; b) M. Ree, Y. Hwang, J.-S. Kim, H. Kim, G. Kim and H. Kim, *Catalysis Today*, 2006, **115**, 134–145;

71 S. Padmanaban, S. Dharmalingam and S. Yoon, *Catalysts*, 2018, **8**, 393.

72 a) I. K. Lee, J. Y. Ha, C. Cao, D.-W. Park, C.-S. Ha and I. Kim, *Catalysis Today*, 2009, **148**, 389–397, https://www.sciencedirect.com/science/article/pii/S0920586109004398; b) J. Shi, Z. Shi, H. Yan, X. Wang, X. Zhang, Q. Lin and L. Zhu, *RSC Adv.*, 2018, **8**, 6565–6571; c) S. N. Ghosh, *Journal of Inorganic and Nuclear Chemistry*, 1974, **36**, 2465–2466, https://www.sciencedirect.com/science/article/pii/0022190274804549;

73 M. Ree, J. Y. Bae, J. H. Jung, T. J. Shin, Y.-T. Hwang and T. Chang, *Polym. Eng. Sci.*, 2000, **40**, 1542–1552.

74 C.-H. Tran, M.-W. Lee, S.-J. Lee, J.-H. Choi, E.-G. Lee, H.-K. Choi and I. Kim, *Polymers*, 2022, **14,** https://www.mdpi.com/2073-4360/14/12/2507.

75 a) R.-J. Wei, X.-H. Zhang, B.-Y. Du, Z.-Q. Fan and G.-R. Qi, *Polymer*, 2013, **54**, 6357–6362; b) Y. Gao, L. Gu, Y. Qin, X. Wang and F. Wang, *J. Polym. Sci. A Polym. Chem.*, 2012, **50**, 5177–5184; c) M. H. Chisholm, D. Navarro-Llobet and Z. Zhou, *Macromolecules*, 2002, **35**, 6494–6504; d) Y. Gao, Y. Qin, X. Zhao, F. Wang and X. Wang, *J Polym Res*, 2012, **19**;

76 L. Li, *MALDI mass spectrometry for synthetic polymers analysis*, Wiley, Chichester, 2010.

77 K. Nakamoto, *Infrared and Raman spectra of inorganic and coordination compounds*, Wiley, New York, 6th edn., op. 2009.

78 A. Cano, I. Monroy, M. Ávila, D. Velasco-Arias, J. Rodríguez-Hernández and E. Reguera, *New J. Chem.*, 2019, **43**, 18384–18393.

79 A. Cano, L. Reguera, M. Avila, D. Velasco-Arias and E. Reguera, *Eur. J. Inorg. Chem.*, 2020, **2020**, 137–145.

80 E. P. Alsaç, E. Ülker, S. V. K. Nune, Y. Dede and F. Karadas, *Chemistry (Weinheim an der Bergstrasse, Germany)*, 2018, **24**, 4856–4863.

81 J.-J. Wang, J.-T. Duan, L. Wang, X.-P. Gu and L.-F. Feng, *Journal of Chemical & Engineering Data*, 2010, **55**, 3379–3382.

82 E. G. Lundquist, J. C. Huffman, K. Folting, B. E. Mann and K. G. Caulton, *Inorg. Chem.*, 1990, **29**, 128–134.

83 Z. Fisher, J. A. Hernandez Prada, C. Tu, D. Duda, C. Yoshioka, H. An, L. Govindasamy, D. N. Silverman and R. McKenna, *Biochemistry*, 2005, **44**, 1097–1105.

84 S.-F. Stahl and G. A. Luinstra, *Catalysts*, 2020, **10**.

85 A. Chruściel, W. Hreczuch, J. Janik, K. Czaja, K. Dziubek, Z. Flisak and A. Swinarew, *Ind. Eng. Chem. Res.*, 2014, **53**, 6636–6646.

86 O. Figovsky and D. Beilin, *Green nanotechnology*, Pan Stanford Publishing, Singapore, 2017.

87 a) M. Bähr and R. Mülhaupt, *Green Chem*, 2012, **14**, 483; b) P. Loulergue, M. Amela-Cortes, S. Cordier, Y. Molard, L. Lemiègre and J.-L. Audic, *J. Appl. Polym. Sci.*, 2017, **134**, 45339;

88 a) L. Maisonneuve, A. S. More, S. Foltran, C. Alfos, F. Robert, Y. Landais, T. Tassaing, E. Grau and H. Cramail, *RSC Adv*, 2014, **4**, 25795–25803; b) A. Boyer, E. Cloutet, T. Tassaing, B. Gadenne, C. Alfos and H. Cramail, *Green Chem*, 2010, **12**, 2205; c) L. Maisonneuve, A.-L. Wirotius, C. Alfos, E. Grau and H. Cramail, *Polym. Chem.*, 2014, **5**, 6142–6147;

89 a) M. Bähr, A. Bitto and R. Mülhaupt, *Green Chem*, 2012, **14**, 1447; b) V. Schimpf, B. S. Ritter, P. Weis, K. Parison and R. Mülhaupt, *Macromolecules*, 2017, **50**, 944–955;

90 H. Blattmann and R. Mülhaupt, *Green Chem*, 2016, **18**, 2406–2415.

91 a) A. Chernykh, S. Alam, A. Jayasooriya, J. Bahr and B. J. Chisholm, *Green Chem*, 2013, **15**, 1834; b) S. Samanta, S. Selvakumar, J. Bahr, D. S. Wickramaratne, M. Sibi and B. J. Chisholm, *ACS Sustainable Chem. Eng.*, 2016, **4**, 6551–6561;

92 M. Bourguignon, J.-M. Thomassin, B. Grignard, C. Jerome and C. Detrembleur, *ACS Sustainable Chem. Eng.*, 2019.

93 B. Grignard, S. Gennen, C. Jérôme, A. W. Kleij and C. Detrembleur, *Chemical Society reviews*, 2019, **48**, 4466–4514.

94 A. Cornille, R. Auvergne, O. Figovsky, B. Boutevin and S. Caillol, *European Polymer Journal*, 2017, **87**, 535–552.

95 M. S. Kathalewar, P. B. Joshi, A. S. Sabnis and V. C. Malshe, *RSC Adv.*, 2013, **3**, 4110.

96 D. Cespi, F. Passarini, I. Vassura and F. Cavani, *Green Chem*, 2016, **18**, 1625–1638.

97 P. C. A. Bruijnincx and B. M. Weckhuysen, *Angewandte Chemie (International ed. in English)*, 2013, **52**, 11980–11987.

98 F. E. I. Deswarte and J. H. Clark, eds., *Introduction to chemicals from biomass*, Wiley, Chichester, U.K, 2008.

99 F. H. Isikgor and C. R. Becer, *Polym. Chem.*, 2015, **6**, 4497–4559.

100 H. Duan, Y. Yamada and S. Sato, *Chem. Lett.*, 2016, **45**, 1036–1047.

101 D. Sun, Y. Li, C. Yang, Y. Su, Y. Yamada and S. Sato, *Fuel Processing Technology*, 2020, **197**, 106193.

102 S. Tazawa, N. Ota, M. Tamura, Y. Nakagawa, K. Okumura and K. Tomishige, *ACS Catal.*, 2016, **6**, 6393–6397.

103 T. Wang, S. Liu, M. Tamura, Y. Nakagawa, N. Hiyoshi and K. Tomishige, *Green Chem*, 2018, **20**, 2547–2557.

104 a) Q. Wang, X. Zhang, L. Wang and Z. Mi, *Ind. Eng. Chem. Res.*, 2009, **48**, 1364–1371; b) L. B. Canto, G. L. Mantovani, E. R. deAzevedo, T. J. Bonagamba, E. Hage and L. A. Pessan, *Polym. Bull.*, 2006, **57**, 513–524; c) A. K. and D. D., in *Polyurethane*, ed. F. Zafar, InTech, 2012;

105 T. Saito, K. C. Harich and T. E. Long, *Macromol. Chem. Phys.*, 2008, **209**, 1983–1991.

106 A. R. Luxton, M. E. Burrage, G. Quack and L. J. Fetters, *Polymer*, 1981, **22**, 382–386.

107 J.-P. Dilcher, *Dissertation*, Hamburg, 2019.

108 a) D. Zuchowska, *Polymer*, 1980, **21**, 514–520; b) Y. Kurusu, Y. Masuyama and M. Miyamoto, *Polymer Journal*, 1994, **26**, 1163 EP -, https://doi.org/10.1295/polymj.26.1163;

109 a) M. M. Jacobi, C. P. Neto, C. G. Schneider and T. L. A. C. Rocha, 2004; b) D. R. Burfield, K.-L. Lim and K.-S. Law, *J. Appl. Polym. Sci.*, 1984, **29**, 1661–1673;

110 J. Rintjema and A. W. Kleij, *ChemSusChem*, 2017, **10**, 1274–1282.

111 N. Kindermann, À. Cristòfol and A. W. Kleij, *ACS Catal.*, 2017, **7**, 3860–3863.

112 a) A. Iraqi and D. J. Cole-Hamilton, *Journal of Materials Chemistry*, 1992, **2**, 183–190; b) A. Iraqi and D. J. Cole-Hamilton, *Polyhedron*, 1991, **10**, 993–995; c) A. N. Ajjou and H. Alper, *Macromolecules*, 1996, **29**, 5072–5074;

113 A. Prokofyeva, H. Laurenzen, D. J. Dijkstra, E. Frick, A. M. Schmidt, C. Guertler, C. Koopmans and A. Wolf, *Polym. Int.*, 2017, **66**, 399–404.

114 V. Froidevaux, C. Negrell, S. Caillol, J.-P. Pascault and B. Boutevin, *Chemical reviews*, 2016, **116**, 14181–14224.

115 F. A. L'Eplattenier and A. Pugin, *Helvetica Chimica Acta*, 1975, **58**, 917–929.

116 S. F. Shakhova, O. L. Rutenberg and M. N. Targanskaya, *Russ. J. Phys. Chem*, 1973, **47**, 894.

117 A. Rosehr and G. A. Luinstra, *Polymer*, 2017, **120**, 164–175.

118 a) K. A. Wepasnick, B. A. Smith, J. L. Bitter and D. Howard Fairbrother, *Analytical and bioanalytical chemistry*, 2010, **396**, 1003–1014; b) S. Freiman, S. Hooker, K. Migler and S. Arepalli, *No. Special Publication (NIST SP)-960.19*, 2008;

119 C. N. Rao, A. Müller and A. K. Cheetham, *Recent developments and new directions*, 2007, 1–420.

120 E. Mansfield, A. Kar and S. A. Hooker, *Analytical and bioanalytical chemistry*, 2010, **396**, 1071–1077.

121 A. Jorio, M. A. Pimenta, Souza Filho, AG, R. Saito, G. Dresselhaus and M. S. Dresselhaus, *New Journal of Physics*, 2003, **5**, 139.

122 C. Thomsen and S. Reich, in *Light Scattering in Solid IX*, Springer, 2006, pp. 115–234.

123 M. S. Dresselhaus, G. Dresselhaus, R. Saito and A. Jorio, *Physics Reports*, 2005, **409**, 47–99.

124 M. Milnera, J. Kürti, M. Hulman and H. Kuzmany, *Physical review letters*, 2000, **84**, 1324.

125 S. Reich, C. Thomsen and J. Maultzsch, *Carbon nanotubes: basic concepts and physical properties*, John Wiley & Sons, 2008.

126 M. S. Dresselhaus, A. Jorio, M. Hofmann, G. Dresselhaus and R. Saito, *Nano letters*, 2010, **10**, 751–758.

127 G. E. Romanos, V. Likodimos, R. R. N. Marques, T. A. Steriotis, S. K. Papageorgiou, J. L. Faria, J. L. Figueiredo, A. M. T. Silva and P. Falaras, *J. Phys. Chem. C*, 2011, **115**, 8534–8546.

128 a) J.-L. Capelo-Martínez, *Ultrasound in chemistry. Analytical applications / edited by Jose-Luis Capelo-MartŁnez*, Wiley-VCH, Weinheim, 2009; b) O. V. Kharissova and B. I. Kharisov, *Solubilization and Dispersion of Carbon Nanotubes*, Springer International Publishing, Cham, 2017; c) B. I. Kharisov, O. V. Kharissova and A. V. Dimas, *RSC Adv.*, 2016, **6**, 68760–68787;

129 D. B. Malpass and E. I. Band, *Introduction to industrial polypropylene. Properties, catalysts, processes / Dennis B. Malpass and Elliot I. Band*, John Wiley & Sons; Salem, Hoboken, N.J., 2012.

Appendix

A1   Section 3.1.3: Copolymerization Details

Table A1. Copolymerization mediated by **Zn-Fe^{II}-DMC** at 60°C.

p [MPa]	feed composition[a]			polymer composition						yield [g]	activity [g$_{polymer}$/g$_{cat}$]
	CO$_2$	PO	f [CO$_2$/PO]	CO$_2$[b]	PO[b]	F [CO$_2$/PO]	tt/tt'	ht/ht'	hh/ht'		
							linkages [mol%][c]				
0.6	0.04	0.96	0.04	0.231	0.769	0.300	19.9	67.5	17.8	4.35	43.2
1.1	0.09	0.91	0.10	0.301	0.699	0.431	/	/	/	3.66	36.2
1.6	0.14	0.86	0.16	0.320	0.68	0.471	/	/	/	3.43	33.8
2.1	0.19	0.81	0.24	0.341	0.659	0.517	/	/	/	3.22	31.6
2.6	0.24	0.76	0.32	0.349	0.651	0.536	/	/	/	3.28	32.5
3.1	0.30	0.71	0.42	0.351	0.649	0.541	/	/	/	3.49	34.7
3.6	0.35	0.65	0.53	0.371	0.629	0.590	/	/	/	3.29	31.7
4.1	0.40	0.60	0.66	0.366	0.634	0.577	22.5	65.7	16.4	3.50	36.1

[a]Determined according to Section 4.2.2. [b]Determined by ^{1}H NMR. [c]Determined by ^{13}C igated NMR. Addition of carbonate (tt, ht, hh) and ether carbonate (tt', ht' and hh') linkages.

Table A2. Copolymerization mediated by **Zn-Fe^{III}-DMC** at 60°C.

p [MPa]	feed composition[a]			polymer composition						yield [g]	activity [g$_{polymer}$/g$_{cat}$]
	CO$_2$	PO	f [CO$_2$/PO]	CO$_2$[b]	PO[b]	F [CO$_2$/PO]	tt/tt'	ht/ht'	hh/hh'		
							linkages [mol%][c]				
0.6	0.04	0.96	0.04	0.207	0.793	0.261	32.9	55.9	15.8	3.45	33.0
1.1	0.09	0.91	0.10	0.275	0.725	0.379	/	/	/	3.56	32.2
1.6	0.14	0.86	0.16	0.311	0.689	0.451	/	/	/	3.52	30.0
2.1	0.19	0.81	0.24	0.332	0.668	0.497	/	/	/	3.40	29.6
2.6	0.24	0.76	0.32	0.337	0.663	0.508	/	/	/	3.30	30.9
3.1	0.30	0.71	0.42	0.356	0.644	0.553	/	/	/	3.08	30.8
3.6	0.35	0.65	0.53	0.362	0.638	0.567	/	/	/	3.04	34.4
4.1	0.40	0.60	0.66	0.364	0.636	0.572	21.8	66.3	17.1	3.30	33.6

[a]Determined according to Section 4.2.2. [b]Determined by ^{1}H NMR. [c]Determined by ^{13}C igated NMR. Addition of carbonate (tt, ht, hh) and ether carbonate (tt', ht' and hh') linkages.

Table A3. Copolymerization mediated by **Zn-Ni-DMC** at 60°C.

p [MPa]	feed composition[a]			polymer composition						yield [g]	activity [$g_{polymer}/g_{cat}$]
	CO_2	PO	f [CO_2/PO]	CO_2[b]	PO[b]	F [CO_2/PO]	tt/tt'	ht/ht'	hh/hh'		
							linkages [mol%][c]				
0.6	0.04	0.96	0.04	0.251	0.749	0.335	44.2	51.4	9.3	1.69	15.5
1.1	0.09	0.91	0.10	0.300	0.700	0.429	/	/	/	1.77	16.5
1.6	0.14	0.86	0.16	0.315	0.685	0.460	/	/	/	1.52	15.1
2.1	0.19	0.81	0.24	0.328	0.672	0.488	/	/	/	1.24	13.4
2.6	0.24	0.76	0.32	0.341	0.659	0.517	/	/	/	1.26	12.1
3.1	0.30	0.71	0.42	0.345	0.655	0.527	/	/	/	1.27	12.2
3.6	0.35	0.65	0.53	0.342	0.658	0.520	/	/	/	1.02	10.4
4.1	0.40	0.60	0.66	0.329	0.671	0.490	29.6	63.1	12.2	1.44	14.3

[a]Determined according to Section 4.2.2. [b]Determined by ^{1}H NMR. [c]Determined by ^{13}C igated NMR. Addition of carbonate (tt, ht, hh) and ether carbonate (tt', ht' and hh') linkages.

Table A4. Copolymerization mediated by **Co-Ni-DMC** at 60°C.

p [MPa]	feed composition[a]			polymer composition						yield [g]	activity [$g_{polymer}/g_{cat}$]
	CO_2	PO	f [CO_2/PO]	CO_2[b]	PO[b]	F [CO_2/PO]	tt/tt'	ht/ht'	hh/hh'		
							linkages [mol%][c]				
0.6	0.04	0.96	0.04	0.156	0.865	0.156	78.9	23.8	0	35.65	366.8
1.1	0.09	0.91	0.10	0.237	0.803	0.245	/	/	/	19.48	238.7
1.6	0.14	0.86	0.16	0.204	0.774	0.292	/	/	/	15.96	172.0
2.1	0.19	0.81	0.24	0.214	0.768	0.302	/	/	/	17.28	202.5
2.6	0.24	0.76	0.32	0.218	0.757	0.321	/	/	/	16.89	184.4
3.1	0.30	0.71	0.42	0.252	0.752	0.33	/	/	/	19.38	186.7
3.6	0.35	0.65	0.53	0.260	0.745	0.342	/	/	/	12.67	127.1
4.1	0.40	0.60	0.66	0.266	0.735	0.361	65.9	36.3	0	12.67	125.3

[a]Determined according to Section 4.2.2. [b]Determined by ^{1}H NMR. [c]Determined by ^{13}C igated NMR. Addition of carbonate (tt, ht, hh) and ether carbonate (tt', ht' and hh') linkages.

Table A5. Copolymerization mediated by **Co-Co-DMC** at 80°C.

p [MPa]	feed composition[a]			polymer composition						yield [g]	activity [$g_{polymer}/g_{cat}$]
	CO_2	PO	f [CO_2/PO]	CO_2[b]	PO[b]	F [CO_2/PO]	tt/tt'	ht/ht'	hh/hh'		
							linkages [mol%][c]				
0.6	0.005	0.995	0.6	0.083	0.917	0.091	/	/	/	5.82	61.7
1.1	0.05	0.95	1.1	0.143	0.857	0.167	/	/	/	7.46	67.6
1.6	0.09	0.91	1.6	0.159	0.841	0.189	/	/	/	3.25	41.1
2.1	0.13	0.87	2.1	0.188	0.812	0.232	/	/	/	3.64	39.7
2.6	0.17	0.83	2.6	0.185	0.815	0.227	/	/	/	5.53	44.3
3.1	0.21	0.79	3.1	0.202	0.798	0.253	/	/	/	6.09	50.2
3.6	0.25	0.75	3.6	0.212	0.788	0.269	/	/	/	7.07	37.9
4.1	0.3	0.7	4.1	0.194	0.806	0.241	21.9	62.5	21.4	3.46	39.2

[a]Determined according to Section 4.2.2. [b]Determined by ^{1}H NMR. [c]Determined by ^{13}C igated NMR. Addition of carbonate (tt, ht, hh) and ether carbonate (tt', ht' and hh') linkages.

Table A6. Copolymerization mediated by **Co-Fe-DMC** at 80°C.

p [MPa]	feed composition[a]			polymer composition						yield [g]	activity [$g_{polymer}/g_{cat}$]
	CO_2	PO	f [CO_2/PO]	CO_2[b]	PO[b]	F [CO_2/PO]	tt/tt'	ht/ht'	hh/hh'		
							linkages [mol%][c]				
0.6	0.005	0.995	0.6	0.185	0.815	0.227	/	/	/	4.73	23.5
1.1	0.05	0.95	1.1	0.269	0.731	0.368	/	/	/	1.66	15.6
1.6	0.09	0.91	1.6	0.251	0.749	0.335	/	/	/	3.64	17.3
2.1	0.13	0.87	2.1	0.290	0.710	0.408	/	/	/	2.03	14.9
2.6	0.17	0.83	2.6	0.304	0.696	0.437	/	/	/	3.00	17.8
3.1	0.21	0.79	3.1	0.316	0.684	0.462	/	/	/	2.46	15.4
3.6	0.25	0.75	3.6	0.314	0.686	0.458	/	/	/	1.65	14.0
4.1	0.3	0.7	4.1	0.304	0.696	0.437	22.6	66.4	15.7	2.00	14.0

[a]Determined according to Section 4.2.2. [b]Determined by ^{1}H NMR. [c]Determined by ^{13}C igated NMR. Addition of carbonate (tt, ht, hh) and ether carbonate (tt', ht' and hh') linkages.

A2 Section 3.1.5: Model Analysis

A.2.1 Langmuir-Hinshelwood Model
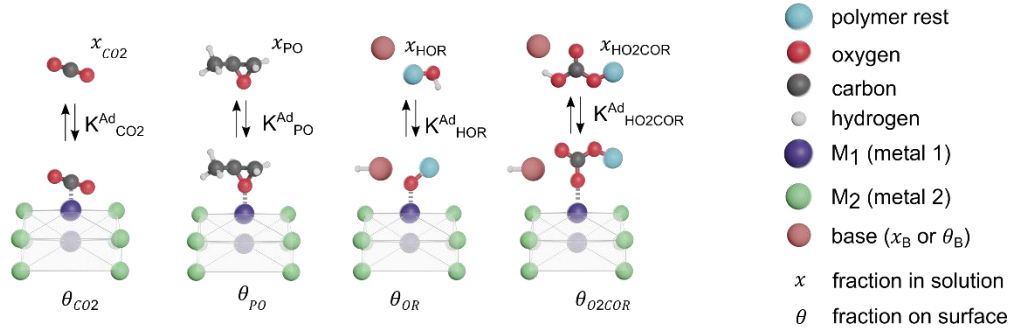
Scheme A1. Ad- and deadsorption pre-equilibria of reactants prior to polymerization reaction in the Langmuir-Hinshelwood model.

In the Langmuir-Hinshelwood model, all reactants are adsorbed to the surface prior to reaction (Scheme A1). The adsorption is reversible leading to the equilibria constants K^{Ad}_{CO2}, K^{Ad}_{PO}, K^{Ad}_{HOR}, and K^{Ad}_{HO2COR}, respectively. Empty sites are denoted as Θ_V in the following. The protonated polymer chain ends (HOR in case the last monomer was PO and HO_2COR in case the last monomer was a CO_2) presumably need the assistance of a base (x_B or Θ_B) to bind sufficiently to the surface. Collecting the steps that lead to the CO_2 fixation and dividing them by the PO consuming steps (Scheme A2), one defines the equation:

$$F = \frac{CO_{2,polymer}}{PO_{polymer}} = \frac{k_1\theta_{CO2}\theta_{OR} - k_{-1}\theta_{O2COR}\theta_V + k_3\theta_{O2COR}\theta_{PO}}{k_2\theta_{OR}\theta_{PO} + k_3\theta_{O2COR}\theta_{PO}}. \tag{1}$$

In the case the CO_2 inversion is in fact reversible, the equilibrium constant K_{car} can be assumed to be

$$K_{car} = \frac{k_1}{k_{-1}} = \frac{\theta_{O2COR}\,\theta_V}{\theta_{OR}\,\theta_{CO2}}. \tag{2}$$

By inserting eq. 1 into eq. 2, the following term for F is obtained:

$$F = \frac{k_3 K_{car}\theta_{CO2}\frac{1}{\theta_V}}{k_2 + k_3 K_{car}\theta_{CO2}\frac{1}{\theta_V}} \text{ and thus } \frac{1}{F} = \frac{k_2\theta_V}{k_3 K_{car}\theta_{CO2}} + 1. \tag{3}$$

This derivation obviously doesn't match the experimental findings in Section 3.1.3 (Figure 19b) as the linearized version shows a *y*-intercept of greater than 1. Simplifying the approach by assuming the CO_2-ether insertion as the rate determining step (RDS), the last two terms in the counter of eq. 1 become negligible leading to

$$F = \frac{k_1\theta_{CO2}\theta_{OR}}{k_2\theta_{OR}\theta_{PO} + k_3\theta_{O2COR}\theta_{PO}}. \tag{4}$$

a CO_2-ether

b PO-carbonate

c PO-ether

d CO_2-carbonate

θ_V = empty active site
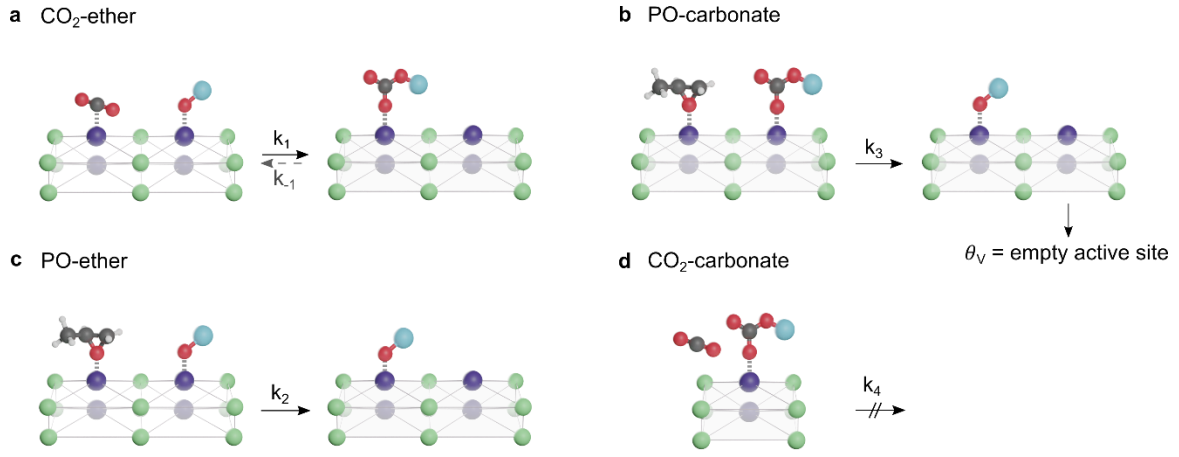
Scheme A2. Considerable reaction steps and reaction constants in the Langmuir-Hinshelwood model including (a) (reversible) CO_2-ether insertion, (b) PO-carbonate ring-opening reaction, (c) PO-ether ring-opening reaction, and (d) CO_2-carbonate insertion.

Eq. 2 thus turns into

$$F = \frac{k_1 \theta_{CO2}}{k_2 \theta_{PO} + k_3 K_{car} \theta_{CO2} \theta_{PO} \frac{1}{\theta_V}} \text{ and } \frac{1}{F} = \frac{k_2 \theta_{PO}}{k_1 \theta_{CO2}} + \frac{k_3 K_{car} \theta_{PO}}{k_1 \theta_V}. \tag{5}$$

Similarly, this approach doesn't seem to offer a satisfying solution as it seems unlikely that empty sites Θ_V will exist in the liquid PO bulk. The second term thus becomes unsolvable as $\Theta_V \approx 0$ leads to very high, unrealistic values.

The assumption of the irreversible CO_2 insertion, on the other hand, results into

$$F = \frac{k_1 \theta_{CO2} \theta_{OR}}{k_2 \theta_{OR} \theta_{PO} + k_3 \theta_{O2COR} \theta_{PO}} \text{ and } \frac{1}{F} = \frac{k_2 \theta_{PO}}{k_1 \theta_{CO2}} + \frac{k_3 \theta_{O2COR} \theta_{PO}}{k_1 \theta_{CO2} \theta_{OR}}. \tag{6}$$

With the steady-state assumption $\frac{d\theta_{O2COR}}{dt} = k_1 \theta_{CO2} \theta_{OR} - k_3 \theta_{O2COR} \theta_{PO} = 0$, leading to

$$\theta_{O2COR} = \frac{k_1 \theta_{CO2} \theta_{OR}}{k_3 \theta_{PO}} \tag{7}$$

and with

$$f = \frac{x_{CO2}}{x_{PO}}, \tag{8}$$

and

$$\theta_{PO} = \frac{K_{PO}^{Ad} x_{PO}}{1 + K_{CO2}^{Ad} x_{CO2} + K_{PO}^{Ad} x_{PO} + K_{HOR}^{Ad} x_{HOR} x_B + K_{HO2COR}^{Ad} x_{HO2COR} x_B} \text{ (in case } x_B) \text{ or} \tag{9}$$

$$\theta_{PO} = \frac{K_{PO}^{Ad} x_{PO}}{1 + K_{CO2}^{Ad} x_{CO2} + K_{PO}^{Ad} x_{PO} + K_{HOR}^{Ad} x_{HOR} \theta_B + K_{HO2COR}^{Ad} x_{HO2COR} x_B + K_B^{Ad} x_B} \text{ (in case } \theta_B), \tag{10}$$

and

87

$$\theta_{CO2} = \frac{K_{CO2}^{Ad}x_{CO2}}{1+K_{CO2}^{Ad}x_{CO2}+K_{PO}^{Ad}x_{PO}+K_{HOR}^{Ad}x_{HOR}x_B+K_{HO2COR}^{Ad}x_{HO2COR}x_B} \text{ (in case } x_B) \text{ or} \qquad (11)$$

$$\theta_{CO2} = \frac{K_{CO2}^{Ad}x_{CO2}}{1+K_{CO2}^{Ad}x_{CO2}+K_{PO}^{Ad}x_{PO}+K_{HOR}^{Ad}x_{HOR}\theta_B+K_{HO2COR}^{Ad}x_{HO2COR}x_B+K_B^{Ad}x_B} \text{ (in case } \theta_B) \qquad (12)$$

the eq. 7 simplifies to

$$F = \frac{k_1\theta_{CO2}}{k_2\theta_{PO}+k_1\theta_{CO2}} \text{ and } \frac{1}{F} = \frac{k_2K_{PO}^{Ad}}{k_1K_{CO2}^{Ad}}\frac{1}{f}+1. \qquad (13)$$

Again, the *y*-intercept does not correspond the experimental results in Section 3.1.3 (Figure 19b).

A 2.2 Eley-Rideal Model

The analysis was proceeded under the assumption of an Eley-Rideal mechanism. Adsorption equilibria were adjusted accordingly (Scheme A3). The CO_2 molecule was assumed to not undergo any adsorption while colliding and reacting with the adsorbed Θ_{OR} moieties on the surface (Scheme A4). Adjusting eq. 1 correspondingly leads to

$$F = \frac{k_1x_{CO2}\theta_{OR}-k_{-1}\theta_{O2COR}+k_3\theta_{O2COR}\theta_{PO}}{k_2\theta_{OR}\theta_{PO}+k_3\theta_{O2COR}\theta_{PO}}, \qquad (14)$$

and with the reversibility of the CO_2 insertion according to eq. 2 the following term is obtained:

$$F = \frac{k_3K_{car}x_{CO2}}{k_2+k_3K_{car}x_{CO2}} \text{ and } \frac{1}{F} = \frac{k_2}{k_3K_{car}x_{CO2}}+1. \qquad (15)$$

Assuming the CO_2 insertion as being the RDS, the eq. 14 transforms into

$$F = \frac{k_1x_{CO2}}{k_2\theta_{PO}+k_3K_{car}\theta_{PO}x_{CO2}} \text{ and } \frac{1}{F} = \frac{k_2\theta_{PO}}{k_1x_{CO2}}+\frac{k_3K_{car}\theta_{PO}}{k_1}. \qquad (16)$$

a CO_2-ether

b PO-carbonate

k_1 / k_{-1}

k_3

θ_V = empty active site

c PO-ether

d CO_2-carbonate

k_2

k_4
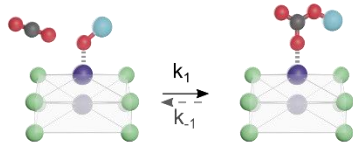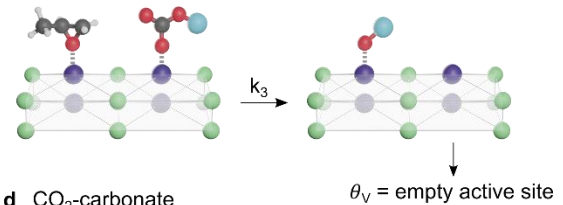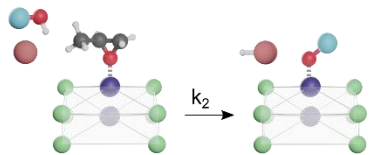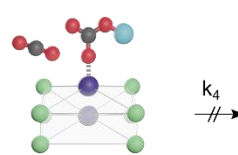
Scheme A3. Variation of considerable reaction steps and reaction constants in the Eley-Rideal model including (a) (reversible) CO₂-ether insertion, (b) PO-carbonate ring-opening reaction, (c) PO-ether ring-opening reaction, and (d) CO₂-carbonate insertion.
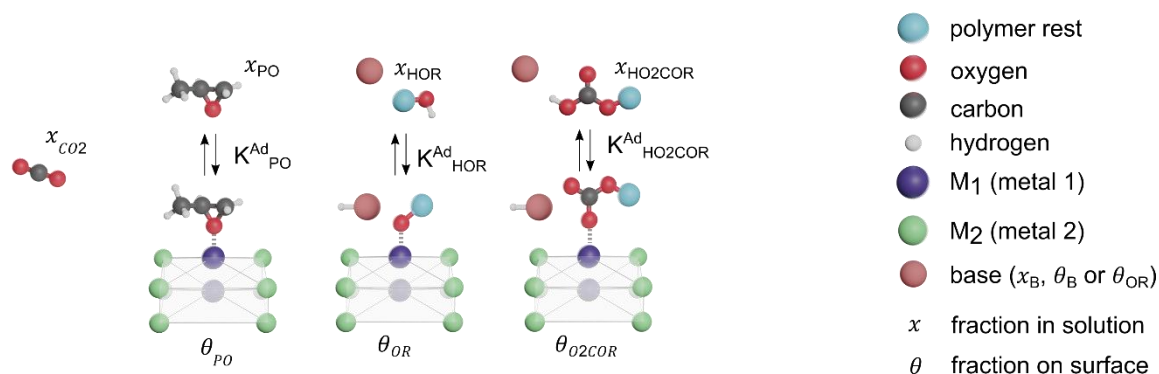
Scheme A5. Ad- and deadsorption pre-equilibria of reactants prior to polymerization reaction in the Eley-Rideal model.

These derivations can now be extended to different scenarios suggesting that not only CO_2 is participating in an uncoordinated state but also hydroxy chain ends. The attack would be assisted by a base (Scheme A5). The results are shown in Table A7 covering the possibilities that the base is adsorbed (Θ_B) and not adsorbed to the surface (x_B), as well as that CO_2 is adsorbed in contrast to x_{HOR}.

Similarly, the non-reversible CO_2 insertion (CO_2 not adsorbed, alkoxide chain ends adsorbed) was analyzed resulting into the expression:

$$F = \frac{k_1 x_{CO2} \theta_{OR}}{k_2 \theta_{OR} \theta_{PO} + k_3 \theta_{O2COR} \theta_{PO}}. \tag{17}$$

This taken with the steady-state assumption in eq. 7 leads to

$$F = \frac{k_1 x_{CO2}}{k_2 \theta_{PO} + k_1 x_{CO2}} \text{ and } \frac{1}{F} = \frac{k_2 \theta_{PO}}{k_1 x_{CO2}} + 1. \tag{18}$$

As performed for the reversible case, the non-adsorbed species can be varied. In addition to the non-adsorption of the CO_2 molecule, HOR chain ends can be assumed to attack the epoxide from
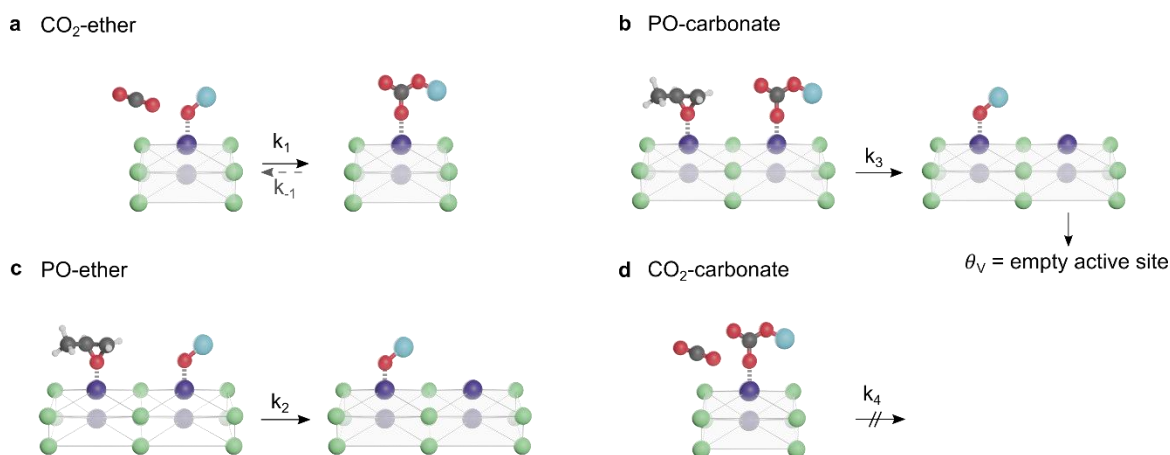
Scheme A4. Considerable reaction steps and reaction constants in the Eley-Rideal model including (a) (reversible) CO_2-ether insertion, (b) PO-carbonate ring-opening reaction, (c) PO-ether ring-opening reaction, and (d) CO_2-carbonate insertion.

the liquid phase assisted by a base. The results for this case and the combination of non-adsorbed CO_2 and free HOR chain ends are collected in Table A8. All the derivations conducted for the Eley-Rideal mechanism presented above and in Table A7 and A8 reveal no fitting equations for the experimental results. Thus, the conventional approaches (Langmuir and Eley-Rideal) do not provide sufficient models to describe the polymerization mechanisms.

Table A7. Results for the reversible CO_2 insertion in an Eley-Rideal model assuming various combinations of non-adsorbed HOR ether chain ends (x_{HOR}). Assisting bases might be adsorbed (Θ_B, Θ_{OR}) or non-adsorbed (x_B), and CO_2 remains adsorbed for reaction (left case) or similarly non-adsorbed (x_{CO2}, right case).

		non-adsorbed species	
		x_{HOR}	x_{HOR} and x_{CO2}
type of base assisting the PO-ether insertion	Θ_B	$\frac{1}{F} = \frac{k_2 x_{HOR}\theta_B\theta_V}{k_3 K_{car}\theta_{CO2}\theta_{OR}} + 1$ $\frac{1}{F} = \frac{k_2 x_{HOR}\theta_B K_{PO}^{Ad}}{k_1 \theta_{OR} K_{CO2}^{Ad}}\frac{1}{f} + \frac{k_3 K_{car}\theta_{PO}}{k_1 \theta_V}\ *$	$\frac{1}{F} = \frac{x_{HOR}\theta_B}{k_3 K_{car} x_{CO2}\theta_{OR}} + 1$ $\frac{1}{F} = \frac{k_2 K_{PO}^{Ad}}{k_1 K_{HOR}^{Ad}}\frac{1}{f} + \frac{k_3 K_{car}\theta_{PO}}{k_1}\ *$
	x_B	$\frac{1}{F} = \frac{k_2 x_{HOR} x_B\theta_V}{k_3 K_{car}\theta_{CO2}\theta_{OR}} + 1$ $\frac{1}{F} = \frac{k_2 x_{HOR} x_B K_{PO}^{Ad}}{k_1 \theta_{OR} K_{CO2}^{Ad}}\frac{1}{f} + \frac{k_3 K_{car}\theta_{PO}}{k_1 \theta_V}\ *$	$\frac{1}{F} = \frac{x_{HOR} x_B}{k_3 K_{car} x_{CO2}\theta_{OR}} + 1$ $\frac{1}{F} = \frac{k_2 K_{PO}^{Ad}}{k_1 K_{HOR}^{Ad}}\frac{1}{f} + \frac{k_3 K_{car}\theta_{PO}}{k_1}\ *$
	$\Theta_B = \Theta_{OR}$	$\frac{1}{F} = \frac{k_2 x_{HOR}\theta_V}{k_3 K_{car}\theta_{CO2}} + 1$ $\frac{1}{F} = \frac{k_2 x_{HOR} K_{PO}^{Ad}}{k_1 K_{CO2}^{Ad}}\frac{1}{f} + \frac{k_3 K_{car}\theta_{PO}}{k_1 \theta_V}\ *$	$\frac{1}{F} = \frac{k_2 x_{HOR}}{k_3 K_{car} x_{CO2}} + 1$ $\frac{1}{F} = \frac{k_2 x_{HOR}\theta_{PO}}{k_1 x_{CO2}} + \frac{k_3 K_{car}\theta_{PO}}{k_1}\ *$

*Derived by the assumption that CO_2 insertion is the RDS.

90

Table A8. Results for the irreversible CO_2 insertion in an Eley-Rideal model assuming various combinations of non-adsorbed HOR ether chain ends (x_{HOR}). Assisting bases might be adsorbed (Θ_B, Θ_{OR}) or non-adsorbed (x_B) and CO_2 remains adsorbed for reaction (left case) or similarly non-adsorbed (x_{CO2}, right case).

		non-adsorbed species	
		x_{HOR}	x_{HOR} and x_{CO2}
type of base assisting the PO-ether insertion	Θ_B	$\dfrac{1}{F} = \left(\dfrac{k_2 x_{HOR}\theta_B K_{PO}^{Ad}}{k_1\theta_{OR}K_{CO2}^{Ad}} + \dfrac{k_3\theta_{O2COR}K_{PO}^{Ad}}{k_1\theta_{OR}K_{CO2}^{Ad}} \right)\dfrac{1}{f}$ $\dfrac{1}{F} = \dfrac{k_2 x_{HOR}\theta_B K_{PO}^{Ad}}{k_1\theta_{OR}K_{CO2}^{Ad}}\dfrac{1}{f} + 1 *$	$\dfrac{1}{F} = \left(\dfrac{k_2 x_{HOR}\theta_B K_{PO}^{Ad}}{k_1\theta_{OR}} + \dfrac{k_3\theta_{O2COR}K_{PO}^{Ad}}{k_1\theta_{OR}} \right)\dfrac{1}{f}$ $\dfrac{1}{F} = \dfrac{k_2 K_{PO}^{Ad}}{k_1 K_{HOR}^{Ad}}\dfrac{1}{f} + 1 *$
	x_B	$\dfrac{1}{F} = \left(\dfrac{k_2 x_{HOR}x_B K_{PO}^{Ad}}{k_1\theta_{OR}K_{CO2}^{Ad}} + \dfrac{k_3\theta_{O2COR}K_{PO}^{Ad}}{k_1\theta_{OR}K_{CO2}^{Ad}} \right)\dfrac{1}{f}$ $\dfrac{1}{F} = \dfrac{k_2 x_{HOR}x_B K_{PO}^{Ad}}{k_1\theta_{OR}K_{CO2}^{Ad}}\dfrac{1}{f} + 1 *$	$\dfrac{1}{F} = \left(\dfrac{k_2 x_{HOR}x_B K_{PO}^{Ad}}{k_1\theta_{OR}} + \dfrac{k_3\theta_{O2COR}K_{PO}^{Ad}}{k_1\theta_{OR}} \right)\dfrac{1}{f}$ $\dfrac{1}{F} = \dfrac{k_2 K_{PO}^{Ad}}{k_1 K_{HOR}^{Ad}}\dfrac{1}{f} + 1 *$
	$\Theta_B = \Theta_{OR}$	$\dfrac{1}{F} = \left(\dfrac{k_2 x_{HOR} K_{PO}^{Ad}}{k_1 K_{CO2}^{Ad}} + \dfrac{k_3\theta_{O2COR}K_{PO}^{Ad}}{k_1\theta_{OR}K_{CO2}^{Ad}} \right)\dfrac{1}{f}$ $\dfrac{1}{F} = \dfrac{k_2 x_{HOR} K_{PO}^{Ad}}{k_1 K_{CO2}^{Ad}}\dfrac{1}{f} + 1 *$	$\dfrac{1}{F} = \left(\dfrac{k_2 x_{HOR} K_{PO}^{Ad}}{k_1} + \dfrac{k_3\theta_{O2COR}K_{PO}^{Ad}}{k_1\theta_{OR}} \right)\dfrac{1}{f}$ $\dfrac{1}{F} = \dfrac{k_2 x_{HOR}\theta_{PO}}{k_1 x_{CO2}} + 1 *$

*Derived by the steady-state assumption $\dfrac{d\theta_{O2COR}}{dt} = 0$.

A2.3 Eley-Rideal Mechanism Adjusted with an Everett Isotherm; Additional Results for Section 3.1.5

Table A9. Additional results for the Eley-Rideal model modified with a physisorbed CO_2 layer described by an Everett isotherm. Reversible (left side) and non-reversible (right side) CO_2 insertion were considered combined with a non-adsorbed HOR ether chain end (x_{HOR}). Assisting bases might be adsorbed (Θ_B, Θ_{OR}) or non-adsorbed (x_B).

		non-adsorbed species	
		x_{HOR} and x_{CO2}, **reversible**	x_{HOR} and x_{CO2}, **non-reversible**

type of base assisting the PO-ether insertion

Θ_B, reversible:
$$\frac{1}{F} = \frac{k_2 x_{HOR}\theta_B}{k_3 K_{car}\theta_{OR}K_E}\frac{1}{f} + 1 + \frac{k_2 x_{HOR}\theta_B}{k_3 K_{car}\theta_{OR}}$$
$$\frac{1}{F} = \frac{k_2 x_{HOR}\theta_B\theta_{PO}}{k_1 x^p_{CO_2}\theta_{OR}} + \frac{k_3 K_{car}\theta_{PO}}{k_1}*$$

Θ_B, non-reversible:
$$\frac{1}{F} = \left(\frac{k_2 x_{HOR}\theta_B\theta_{PO}}{k_1\theta_{OR}K_E}\frac{1}{f} + \frac{k_3\theta_{O2COR}\theta_{PO}}{k_1\theta_{OR}K_E}\frac{1}{f}\right)(1+K_E f)$$
$$\frac{1}{F} = \frac{k_2 K_{PO}^{Ad}}{k_1 K_{HOR}^{Ad}K_E}\frac{1}{f} + 1*$$

x_B, reversible:
$$\frac{1}{F} = \frac{k_2 x_{HOR}x_B}{k_3 K_{car}\theta_{OR}K_E}\frac{1}{f} + 1 + \frac{k_2 x_{HOR}x_B}{k_3 K_{car}\theta_{OR}}$$
$$\frac{1}{F} = \frac{k_2 x_{HOR}x_B\theta_{PO}}{k_1 x^p_{CO_2}\theta_{OR}} + \frac{k_3 K_{car}\theta_{PO}}{k_1}*$$

x_B, non-reversible:
$$\frac{1}{F} = \left(\frac{k_2 x_{HOR}x_B\theta_{PO}}{k_1\theta_{OR}K_E}\frac{1}{f} + \frac{k_3\theta_{O2COR}\theta_{PO}}{k_1\theta_{OR}K_E}\frac{1}{f}\right)(1+K_E f)$$
$$\frac{1}{F} = \frac{k_2 K_{PO}^{Ad}}{k_1 K_{HOR}^{Ad}K_E}\frac{1}{f} + 1*$$

$\Theta_B = \Theta_{OR}$, reversible:
$$\frac{1}{F} = \frac{k_2 x_{HOR}}{k_3 K_{car}K_E}\frac{1}{f} + 1 + \frac{k_2 x_{HOR}}{k_3 K_{car}}$$
$$\frac{1}{F} = \frac{k_2 x_{HOR}\theta_{PO}}{k_1 K_E}\frac{1}{f} + \frac{k_2 x_{HOR}\theta_{PO}}{k_1} + \frac{k_3 K_{car}\theta_{PO}}{k_1}*$$

$\Theta_B = \Theta_{OR}$, non-reversible:
$$\frac{1}{F} = \left(\frac{k_2 x_{HOR}\theta_{PO}}{k_1 K_E}\frac{1}{f} + \frac{k_3\theta_{O2COR}\theta_{PO}}{k_1\theta_{OR}K_E}\frac{1}{f}\right)(1+K_E f)$$
$$\frac{1}{F} = \frac{k_2 x_{HOR}}{k_1 K_E}\frac{1}{f} + \frac{k_2 x_{HOR}}{k_1} + 1*$$

*Derived by the assumption that CO_2 insertion is the RDS.

## A3.1 ^{1}H and ^{13}C NMR Spectra of PDB1 - PBD4
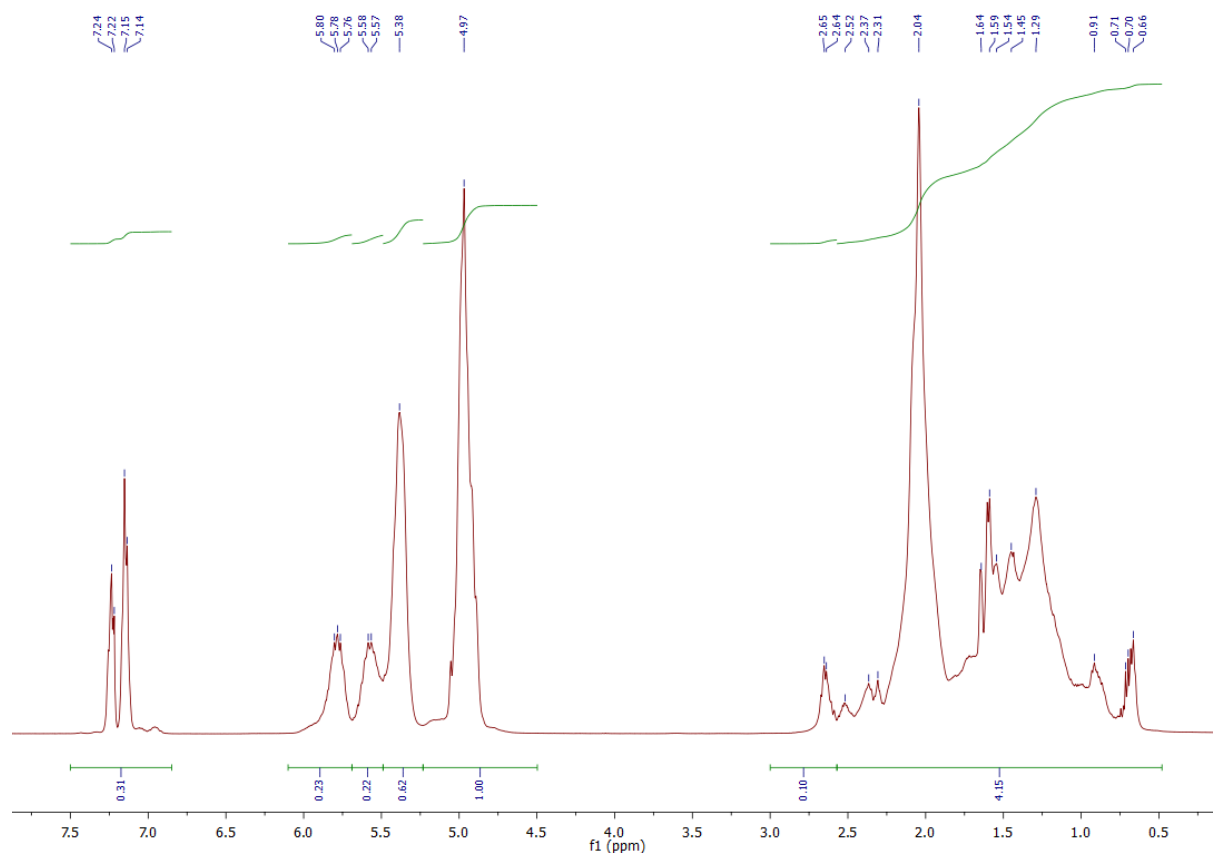
Figure A1. ^{1}H NMR spectrum of **PBD1** in CDCl$_3$.
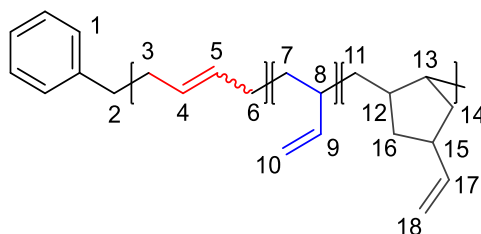
^{1}H NMR (CDCl$_3$, 400 MHz): δ (ppm) = 7.50 - 6.85 (m, 5H, 1-CH), 6.1 - 5.69 (m, 1H, 17-CH), 5.69 - 5.49 (m, 1H, 9-CH), 5.49 - 5.23 (m, 2H, 4-CH, 5-CH), 5.23 - 4.50 (m, 2H, 10-CH$_2$, 18-CH$_2$), 3.00 - 2.57 (m, 2H, 2x2-CH), 2.57 - 0.48 (m, 16H, 2x3-CH, 2x6-CH, 2x7-CH, 8-CH, 2x11-CH, 12-CH, 13-CH, 2 x 14-CH, 15-CH, 2 x 16-CH).
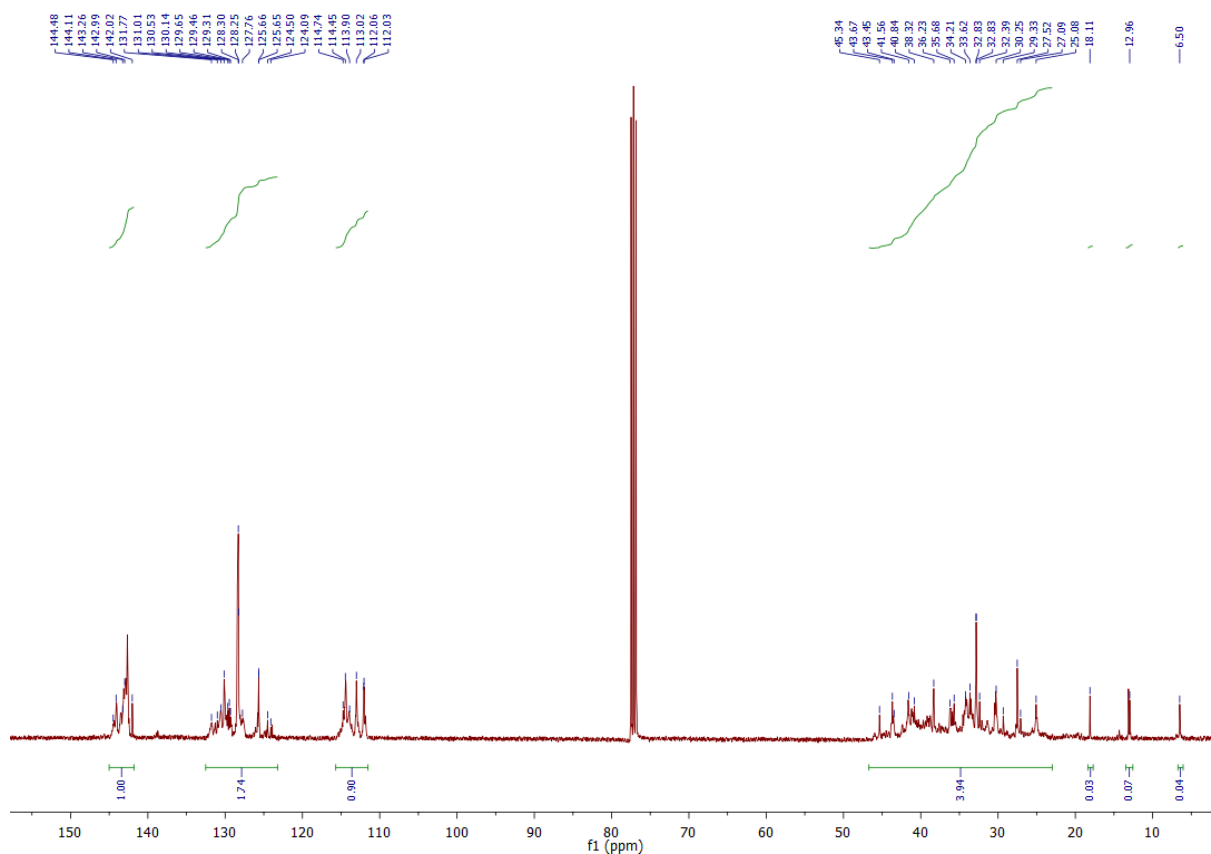
Figure A2. ^{13}C NMR spectrum of **PBD1** in CDCl$_3$.
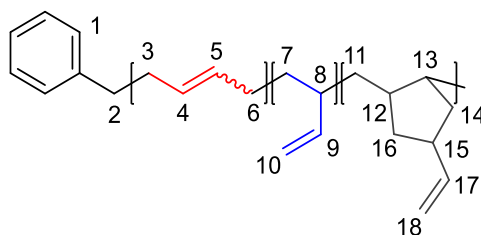
^{13}C NMR (CDCl$_3$, 125 MHz): δ (ppm) = 145.0 - 141.8 (1 x 1-C (styrene end group), 9-C, 17-C), 132.5 - 123.2 (5 x 1-C (styrene end group), 4-C, 5-C), 115.7 - 111.5 (10-C, 18-C), 46.7 - 6.05 (2-C, 3-C, 6-C, 7-C, 8-C, 11-C, 12-C, 13-C, 14-C, 15-C, 16-C).

Please note the peak assignments in Figure A1 and A2. The signal for 1,4-*cis* and 1,4-*trans* double bonds splits into the signals at δ (ppm) = 5.42 (m, 2H (*trans*)) and 5.38 (m, 2H, (*cis*)).
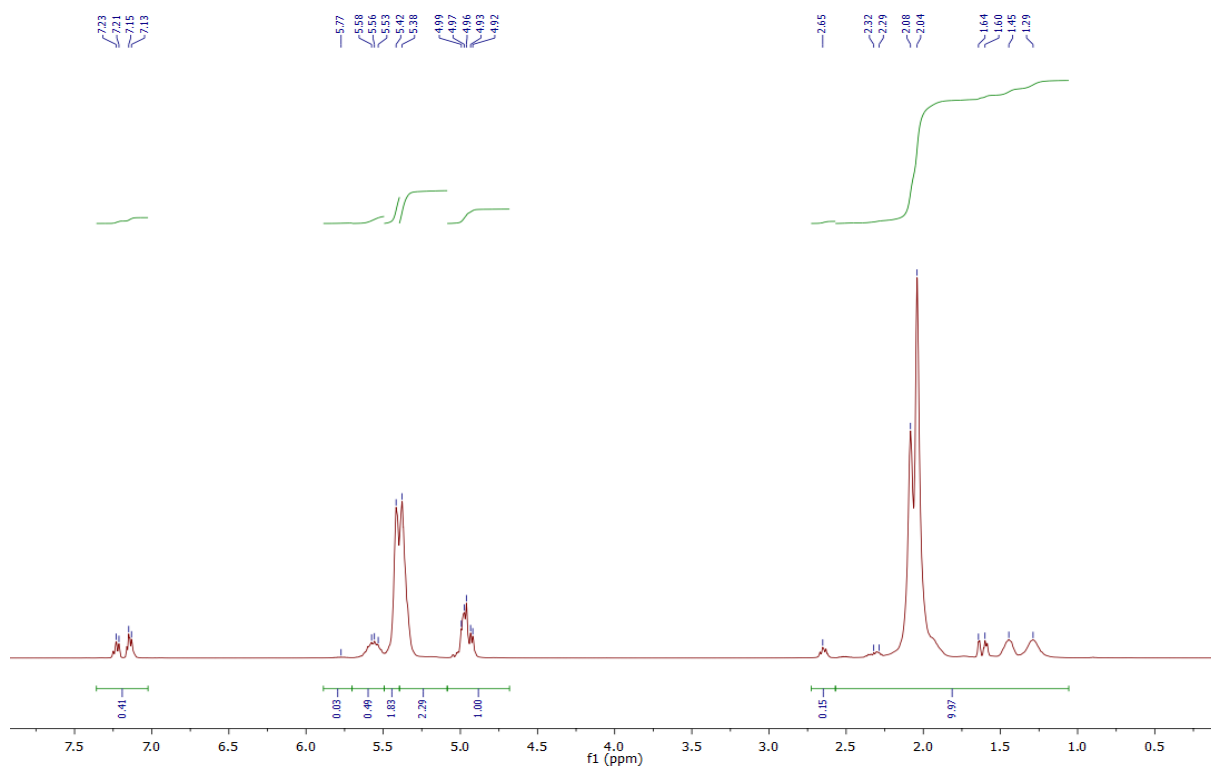
Figure A3. ^{1}H NMR spectrum of **PBD2** in CDCl$_3$.
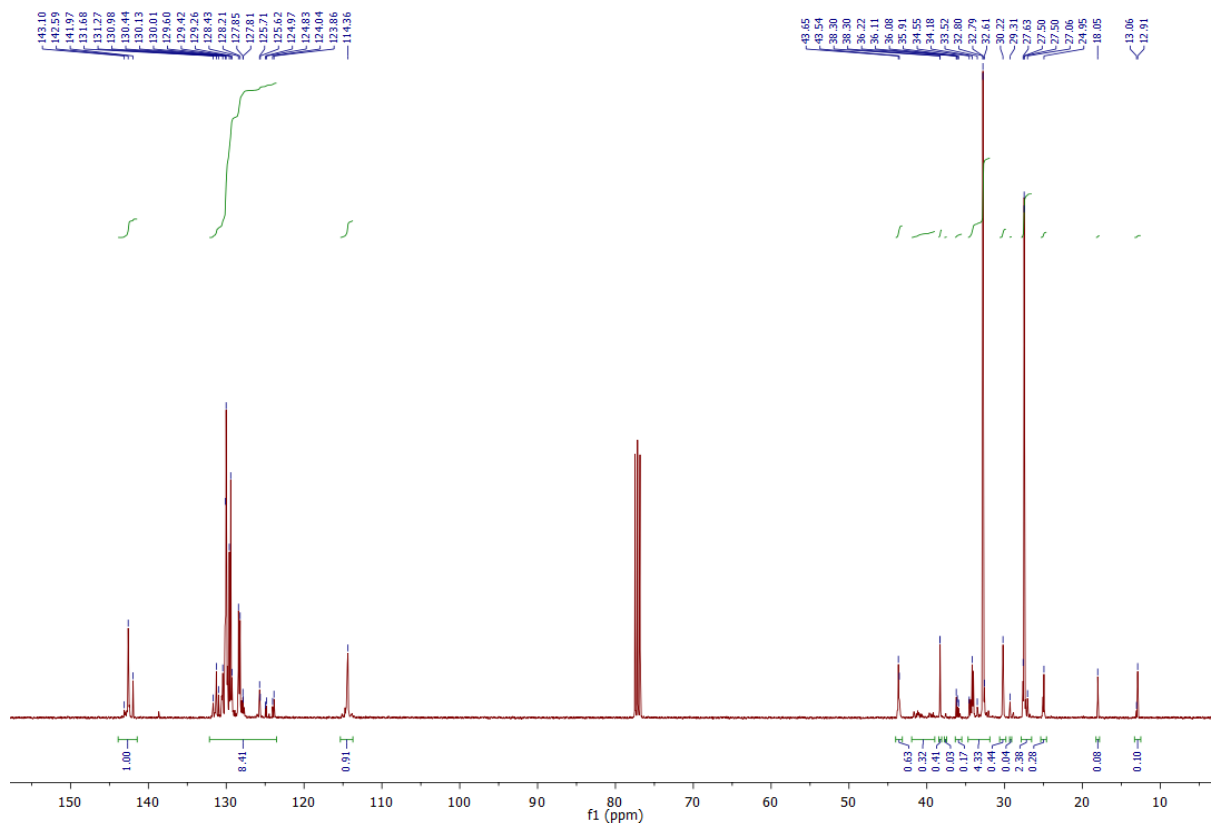
Figure A4. ^{13}C NMR spectrum of **PBD2** in CDCl$_3$.

Please note the peak assignments in Figure A1 and A2. The signal for 1,4-*cis* and 1,4-*trans* double bonds splits into the signals at δ (ppm) = 5.46 (m, 2H (*trans*)) and 5.41 (m, 2H, (*cis*)).
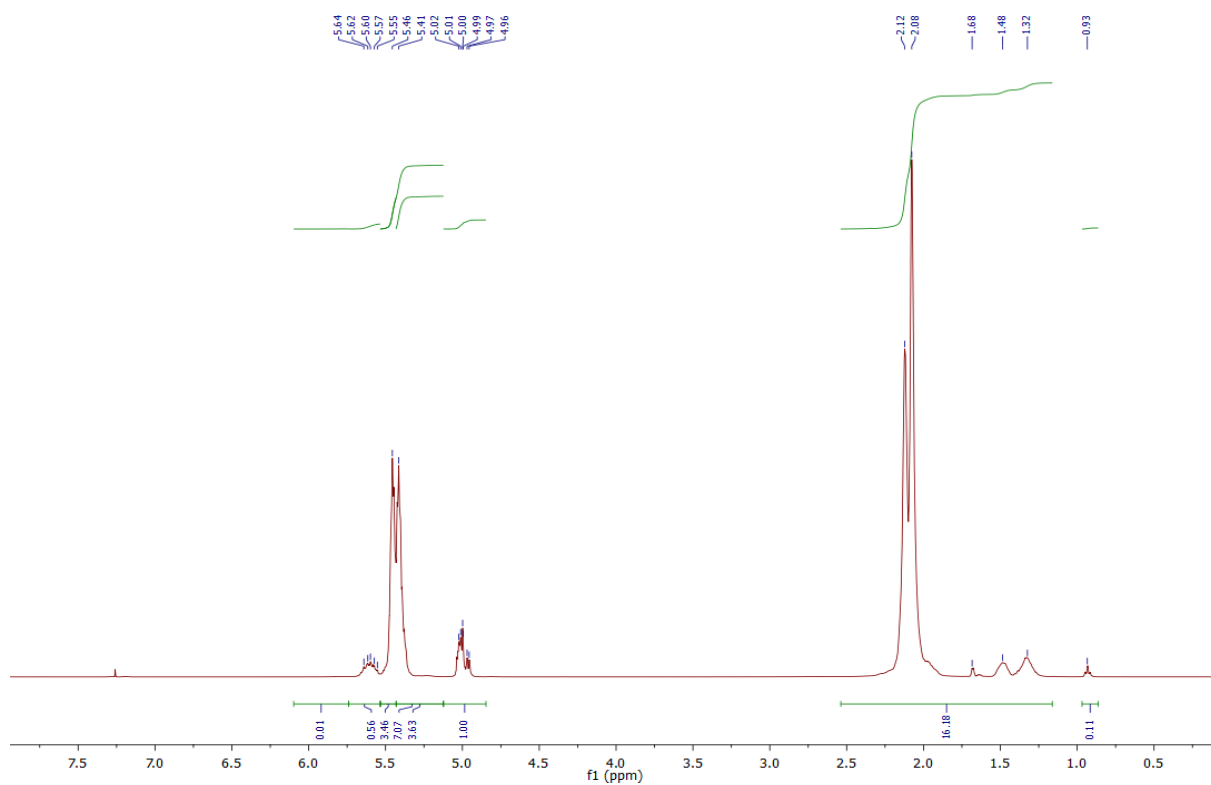
Figure A5. ^{1}H NMR spectrum of **PBD3** in CDCl$_3$.
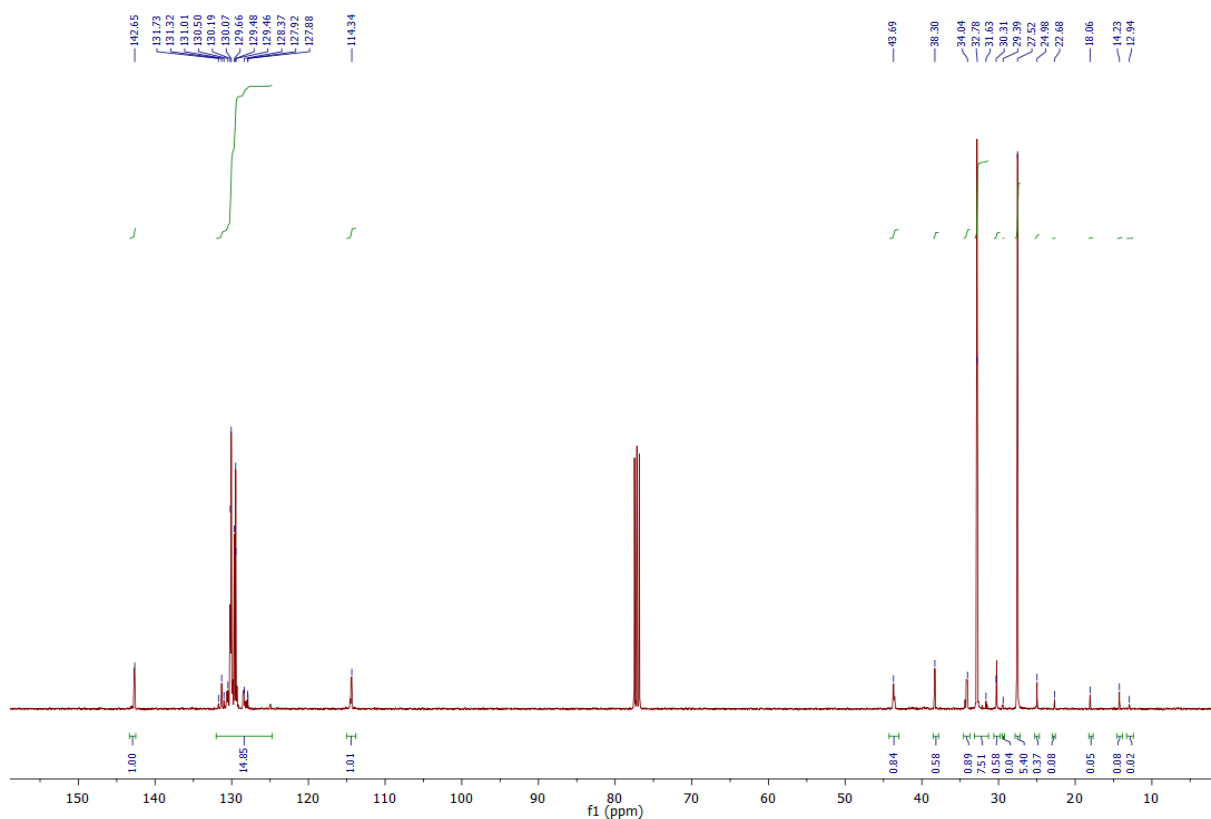
Figure A6. ^{13}C NMR spectrum of **PBD3** in CDCl$_3$.

Please note the peak assignments in Figure A1 and A2. The signal for 1,4-*cis* and 1,4-*trans* double bonds splits into the signals at δ (ppm) = 5.46 (m, 2H (*trans*)) and 5.41 (m, 2H, (*cis*)).
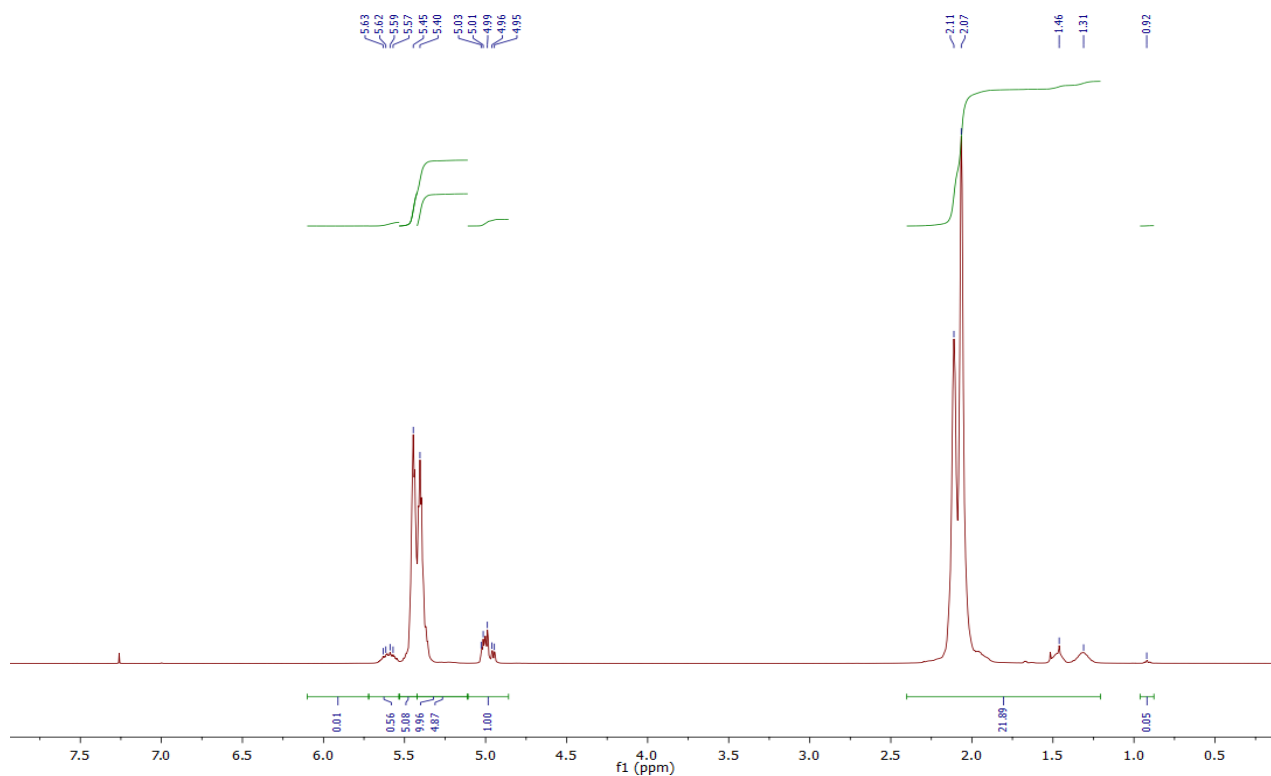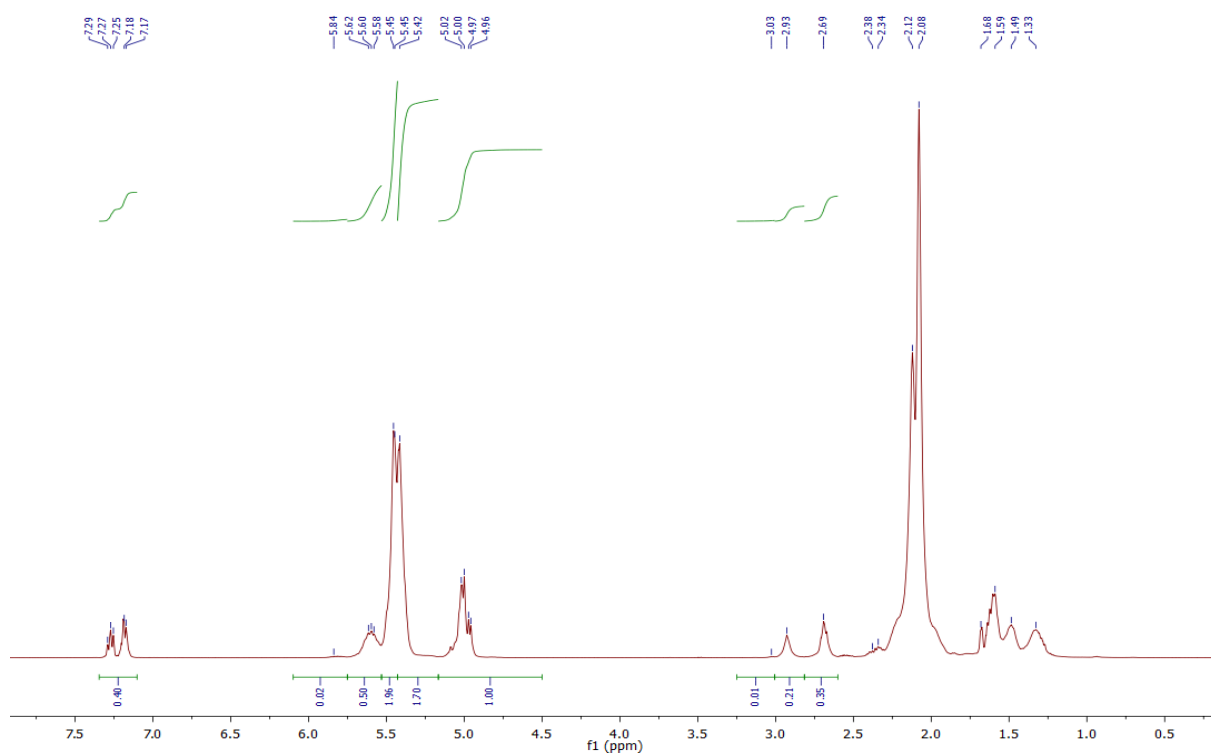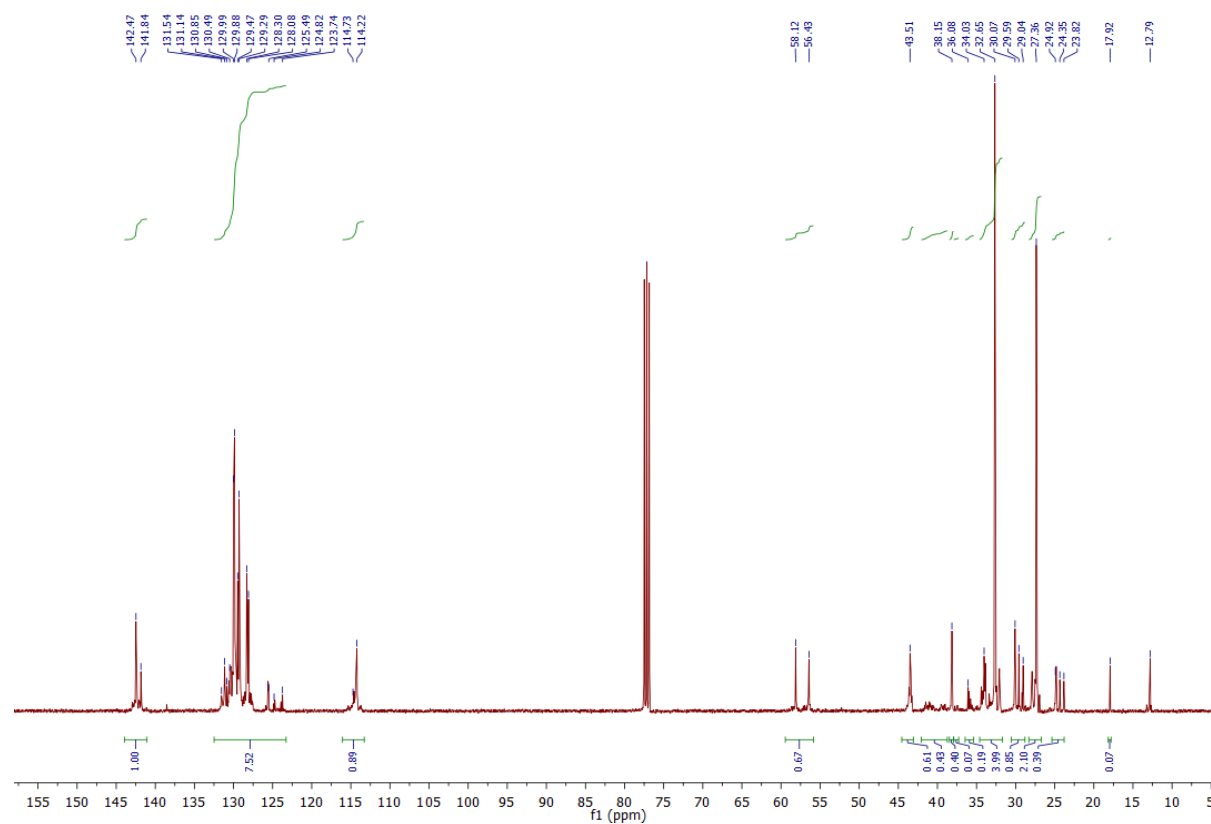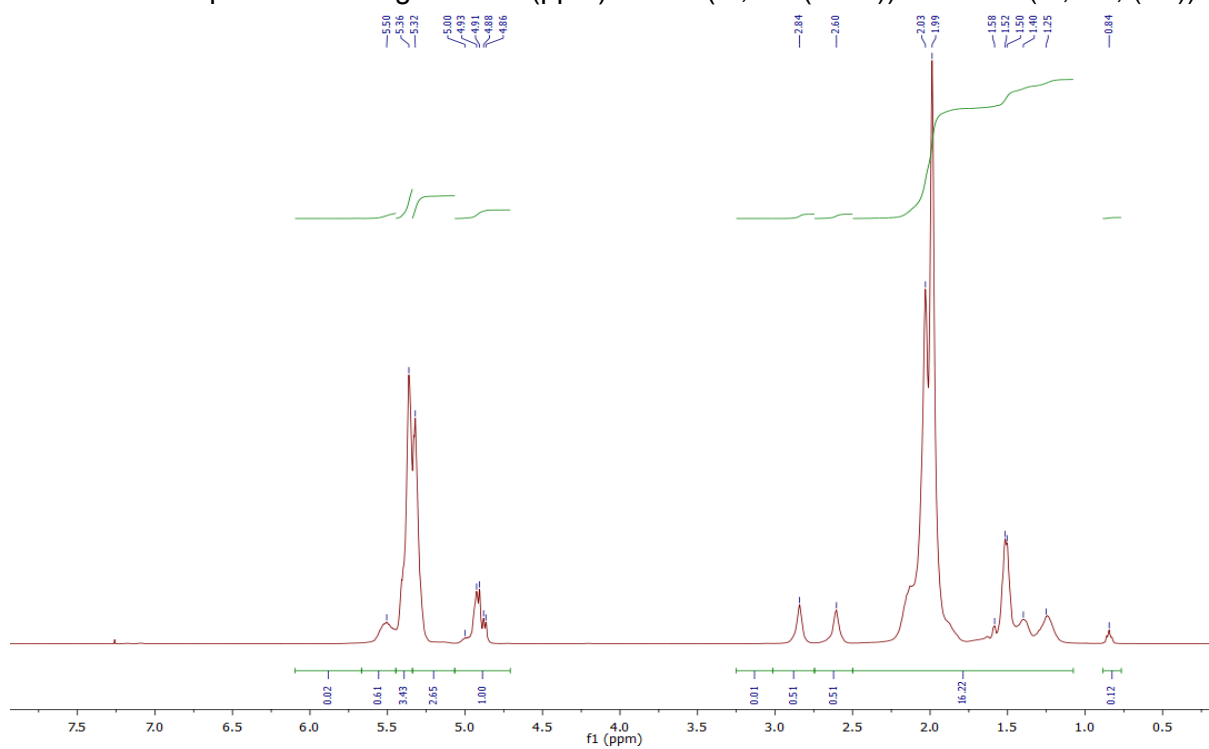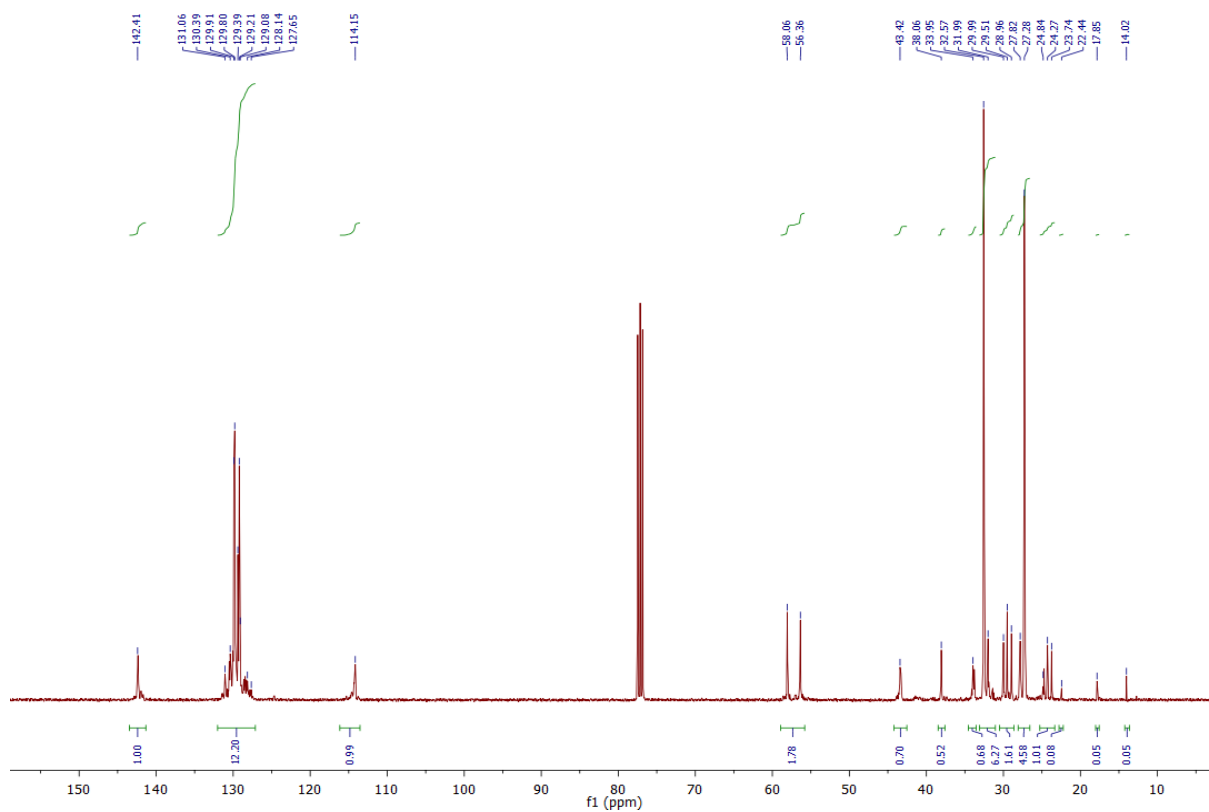
Figure A7. ¹H NMR spectrum of **PBD4** in CDCl₃.
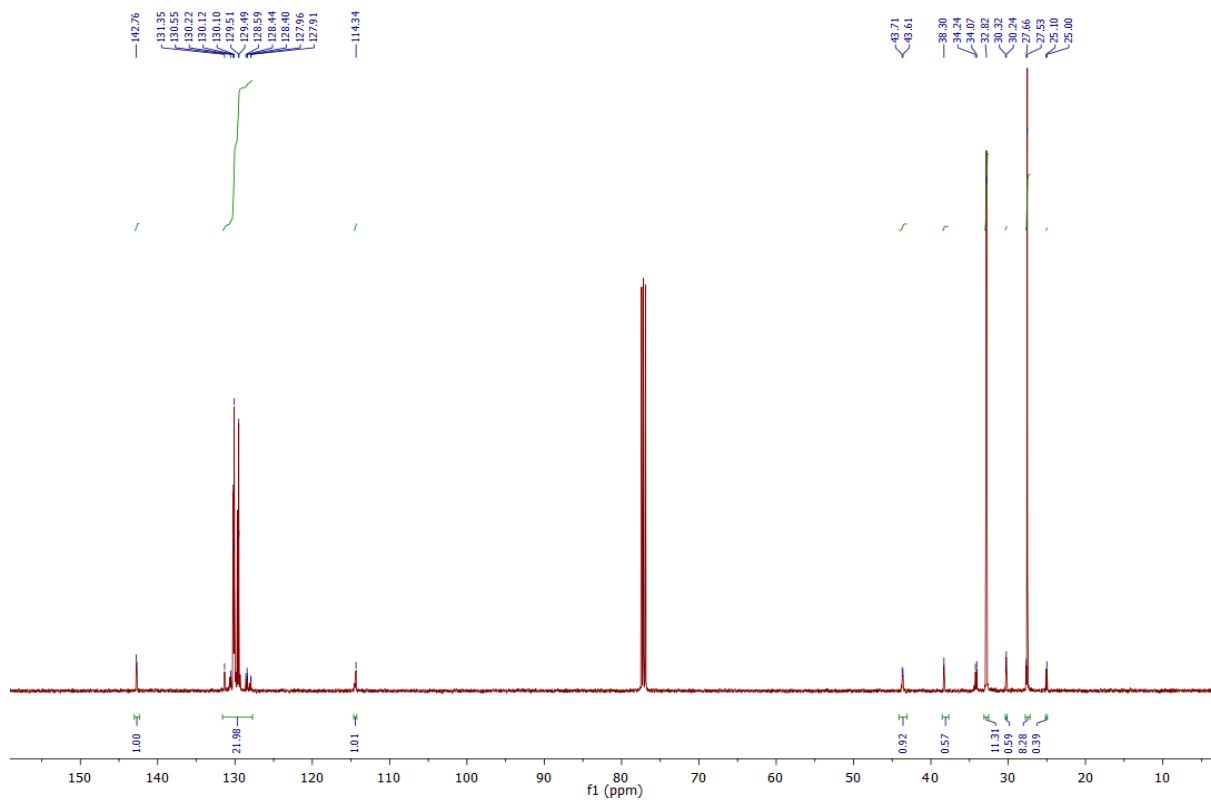
Figure A8. ¹³C NMR spectrum of **PBD4** in CDCl₃.

A3.2 ^{1}H and ^{13}C NMR Spectra of PE-PDB1 - PE-PBD4
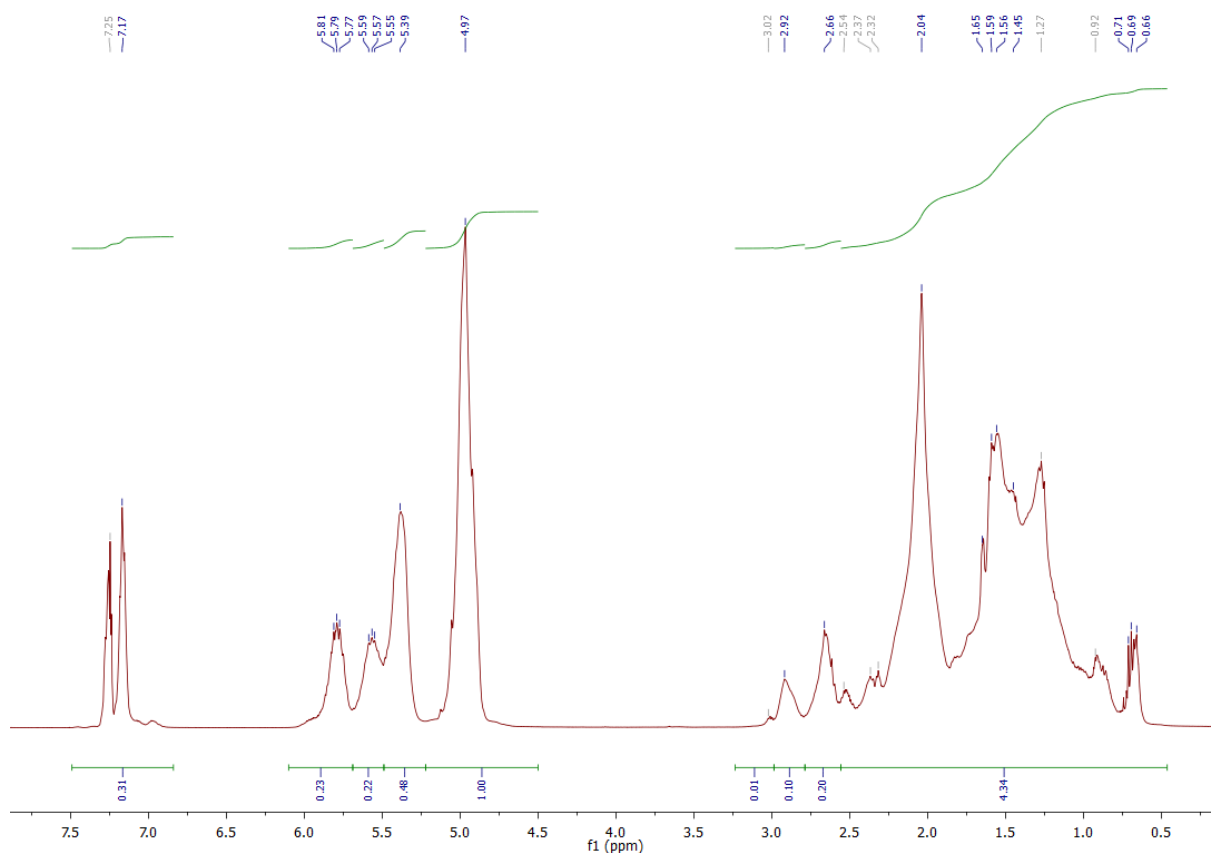
Figure A9. ^{1}H NMR spectrum of **PE-PBD1** in CDCl$_3$.
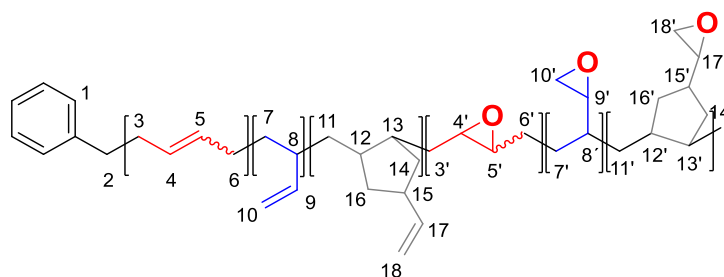
^{1}**H NMR** (CDCl$_3$, 400 MHz): δ (ppm) = 7.50 - 6.85 (m, 5H, 1-CH), 6.0 - 5.69 (m, 1H, 17-CH), 5.69 - 5.49 (m, 1H, 9-CH), 5.49 - 5.22 (m, 2H, 4-CH, 5-CH), 5.23 - 4.50 (m, 2H, 10-CH$_2$, 18-CH$_2$), 3.25 - 3.00 (m, 2H, 9'-CH, 17'-CH), 3.00 - 2.80 (m, *cis* epoxide, 2H, 4'-CH, 5'-CH), 2.80 - 2.57 (m, *trans* epoxide, 4H, 2 x 2-CH, 4'-CH, 5'-CH), 2.57 - 0.48 (m, 36H, 2 x 3-CH, 2 x 3'-CH, 2 x 6-CH, 2 x 6'-CH, 2 x 7-CH, 2 x 7'-CH, 8-CH, 8'-CH, 2 x 10'-CH, 2 x 11-CH, 2 x 11'-CH, 12-CH, 12'-CH, 13-CH, 13'-CH, 2 x 14-CH, 2 x 14'-CH, 15-CH, 15'-CH, 2 x 16-CH, 2 x 16'-CH, 2 x 18'-CH).

Signals from side reactions, e. g., epoxide ring-opening (-OH formation) and cross-linking (C-O-C formation) typically between δ (ppm) = 3 - 6 ppm were not observed for all samples.

98
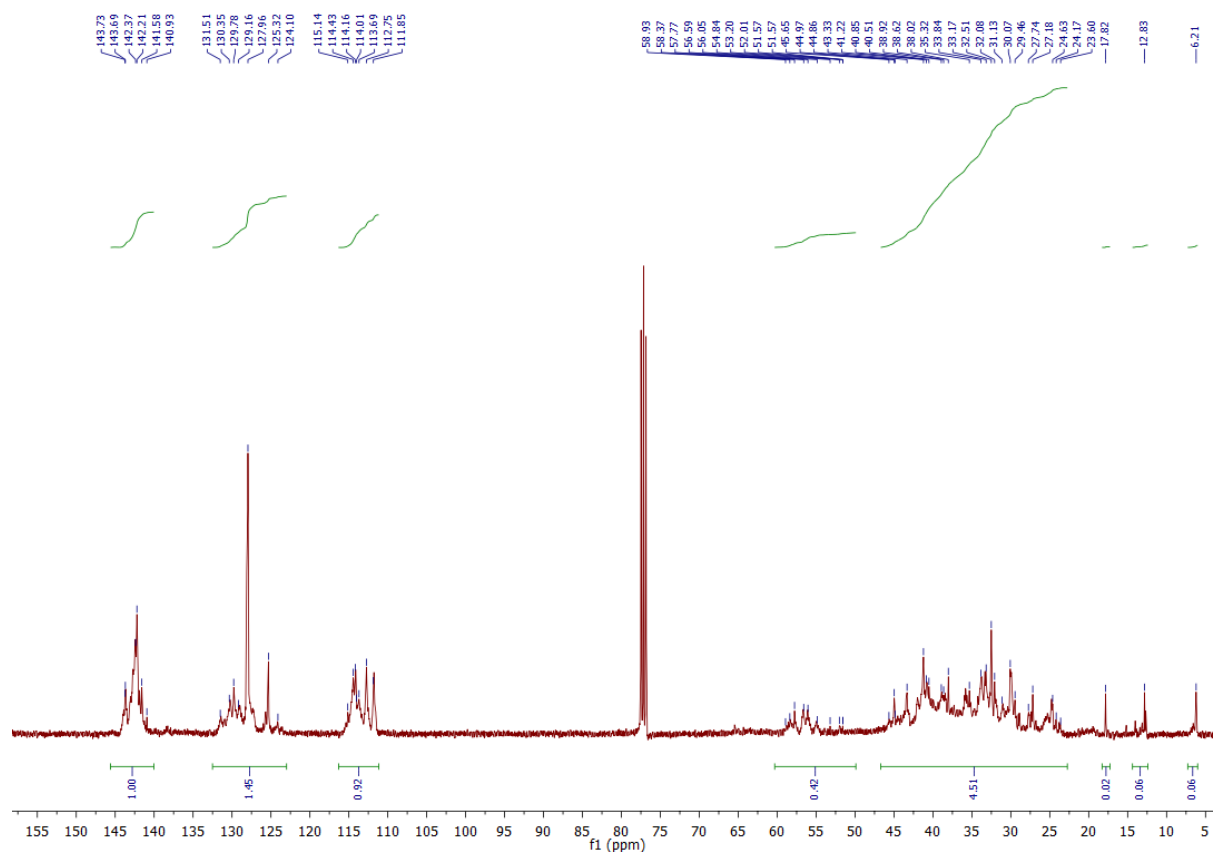
Figure A10. ^{13}C NMR spectrum of **PE-PBD1** in CDCl$_3$.
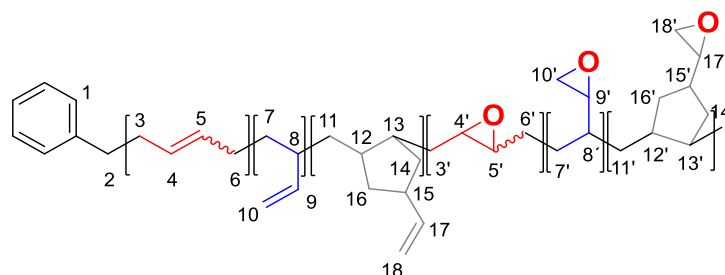
^{13}**C NMR** (CDCl$_3$, 125 MHz): δ (ppm) = 145.0 - 141.8 (6 x 1-C (styrene), 9-C, 17-C), 132.5 - 123.2 (4-H, 5-C), 115.7 - 111.5 (10-C, 18-C), 66.0 - 63.5 (9'-C, 17'-C), 59.5 - 51.0 (4'-C, 5'-C), 46.7 - 6.05 (10'-C, 18'-C, 2-C, 3-C, 3'-C, 6-C, 6'-C, 7-C, 7'-C, 8-C, 8'-C, 11-C, 11'-C, 12-C, 12'-C, 13-C, 13'-C, 14-C, 14'-C, 15-C, 15'-C, 16-C, 16'-C).

Please note the peak assignments in Figure A9 and A10. The signal for 1,4-*cis* and 1,4-*trans* double bonds splits into the signals at δ (ppm) = 5.45 (m, 2H (*trans*)) and 5.42 (m, 2H, (*cis*)).
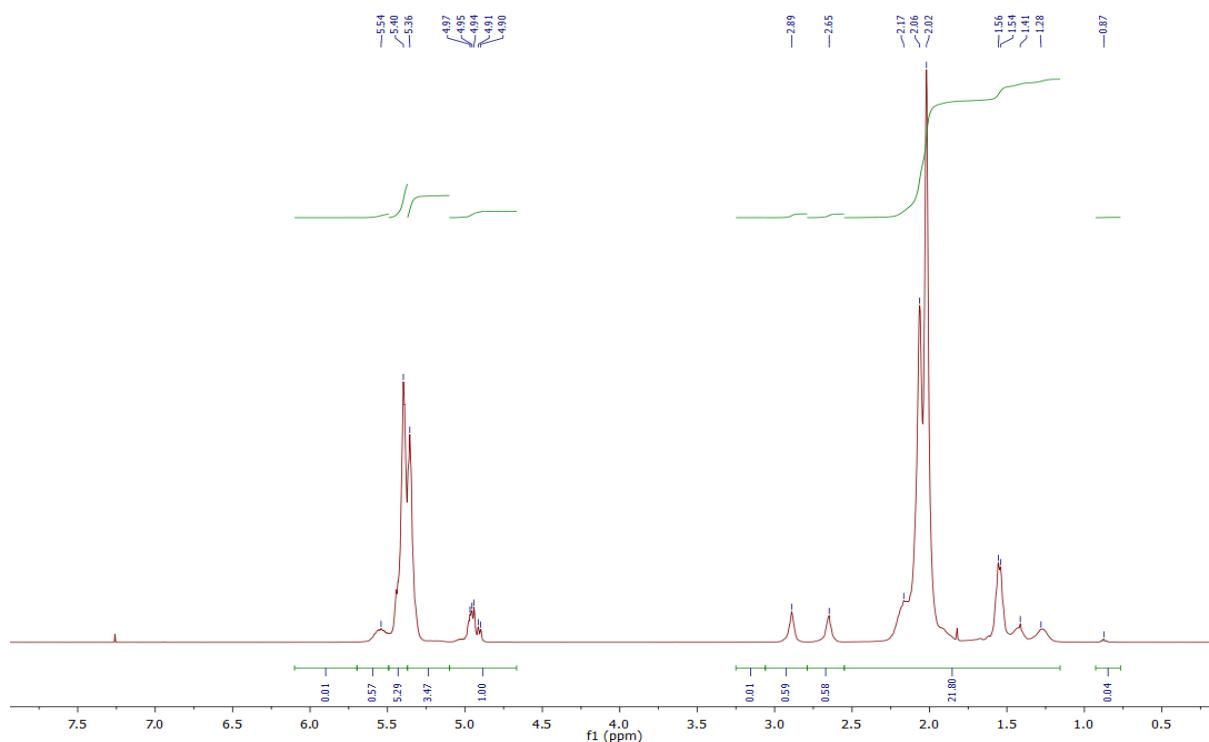

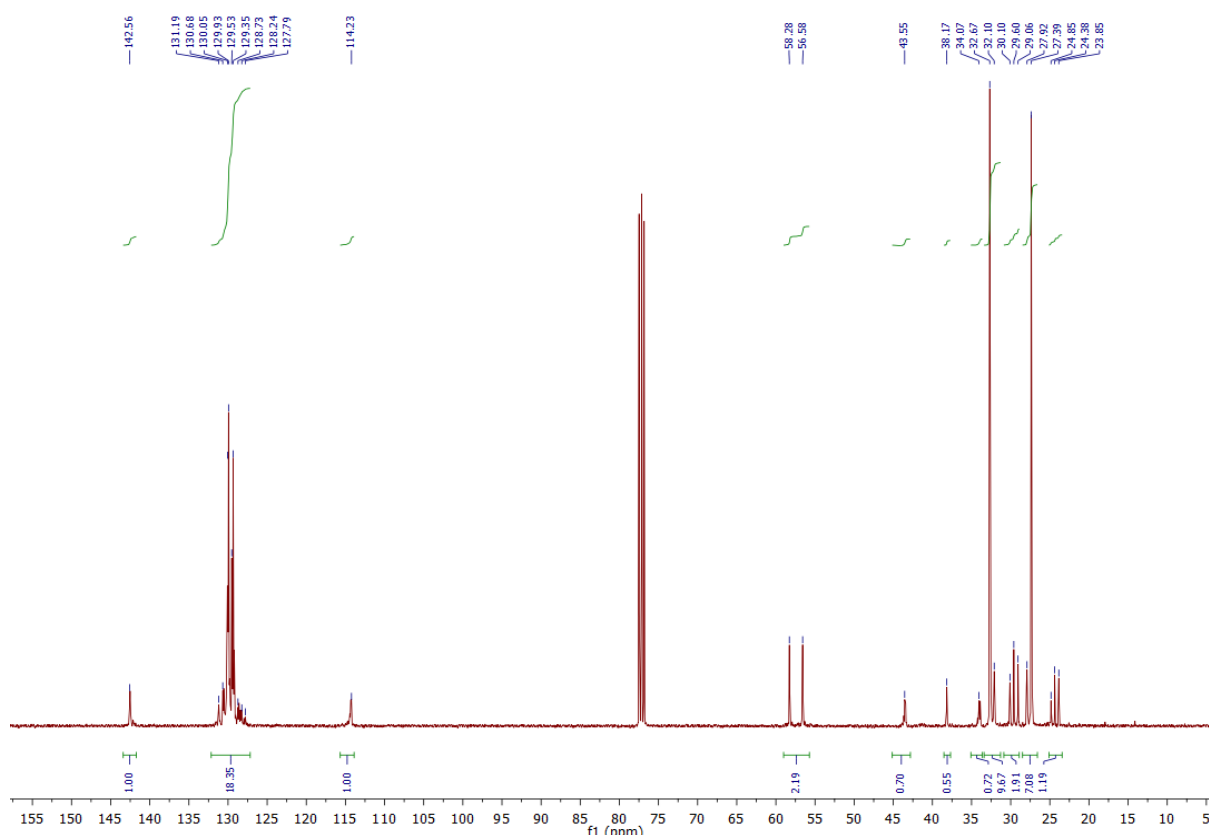**Figure A11.** ¹H NMR spectrum of **PE-PBD2** in CDCl₃.

Figure A12. ¹³C NMR spectrum of **PE-PBD2** in CDCl₃.

Please note the peak assignments in Figure A9 and A10. The signal for 1,4-*cis* and 1,4-*trans* double bonds splits into the signals at δ (ppm) = 5.36 (m, 2H (*trans*)) and 5.32 (m, 2H, (*cis*)).

Figure A13. ¹H NMR spectrum of **PE-PBD3** in CDCl₃.

Figure A14. ¹³C NMR spectrum of **PE-PBD3** in CDCl₃.

Please note the peak assignments in Figure A9 and A10. The signal for 1,4-*cis* and 1,4-*trans* double bonds splits into the signals at δ (ppm) = 5.40 (m, 2H (*trans*)) and 5.36 (m, 2H, (*cis*)).

Figure A15. ^{1}H NMR spectrum of **PE-PBD4** in CDCl$_3$.

Figure A16. ^{13}C NMR spectrum of **PE-PBD4** in CDCl$_3$.

A3.3 ¹H and ¹³C NMR Spectra of PC-PDB1 - PC-PBD4
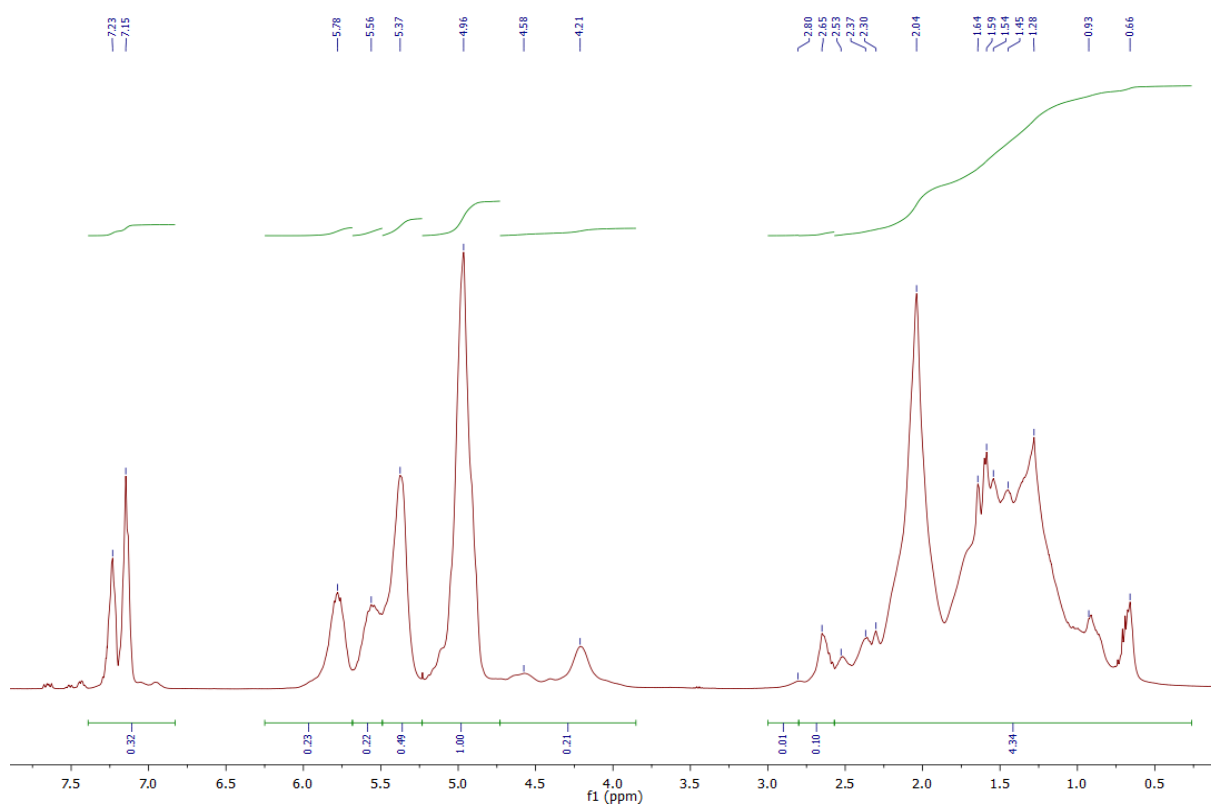
Figure A17. ¹H NMR spectrum of **PC-PBD1** in CDCl₃.
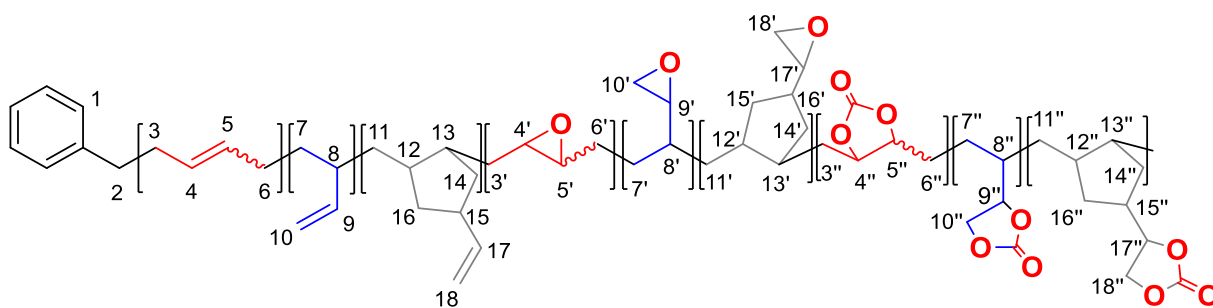
¹H NMR (CDCl₃, 400 MHz): δ (ppm) = 7.39 - 6.85 (m, 5H, 1-CH), 6.25 - 5.68 (m, 1H, 17-CH), 5.68 - 5.49 (m, 1H, 9-CH), 5.49 - 5.23 (m, 2H, 4-CH, 5-CH), 5.23 - 4.73 (m, 2H, 10-CH₂, 18-CH₂), 4.73 - 3.85 (m, 8H, 4''-H, 5''-H, 9''-H, 10''-H, 17''-H, 18''-H), 3.25 - 3.00 (m, 2H, 9'-CH, 17'-CH), 3.00 - 2.80 (m, *cis* epoxide, 2H, 4'-CH, 5'-CH), 2.80 - 2.57 (m, *trans* epoxide, 4H, 2 x 2-CH, 4'-CH, 5'-CH), 2.57 - 0.48 (m, 52H, 2 x 3-CH, 2 x 3'-CH, 2 x 3''-CH, 2 x 6-CH, 2 x 6'-CH, 2 x 6''-CH, 2 x 7-CH, 2 x 7'-CH, 2 x 7''-CH, 8-CH, 8'-CH, 8''-CH, 2 x 10'-CH, 2 x 11-CH, 2 x 11'-CH, 2 x 11''-CH, 12-CH, 12'-CH, 12''-CH, 13-CH, 13'-CH, 13''-CH, 2 x 14-CH, 2 x 14'-CH, 2 x 14''-CH, 15-CH, 15'-CH, 15''-CH, 2 x 16-CH, 2 x 16'-CH, 2 x 16''-CH).
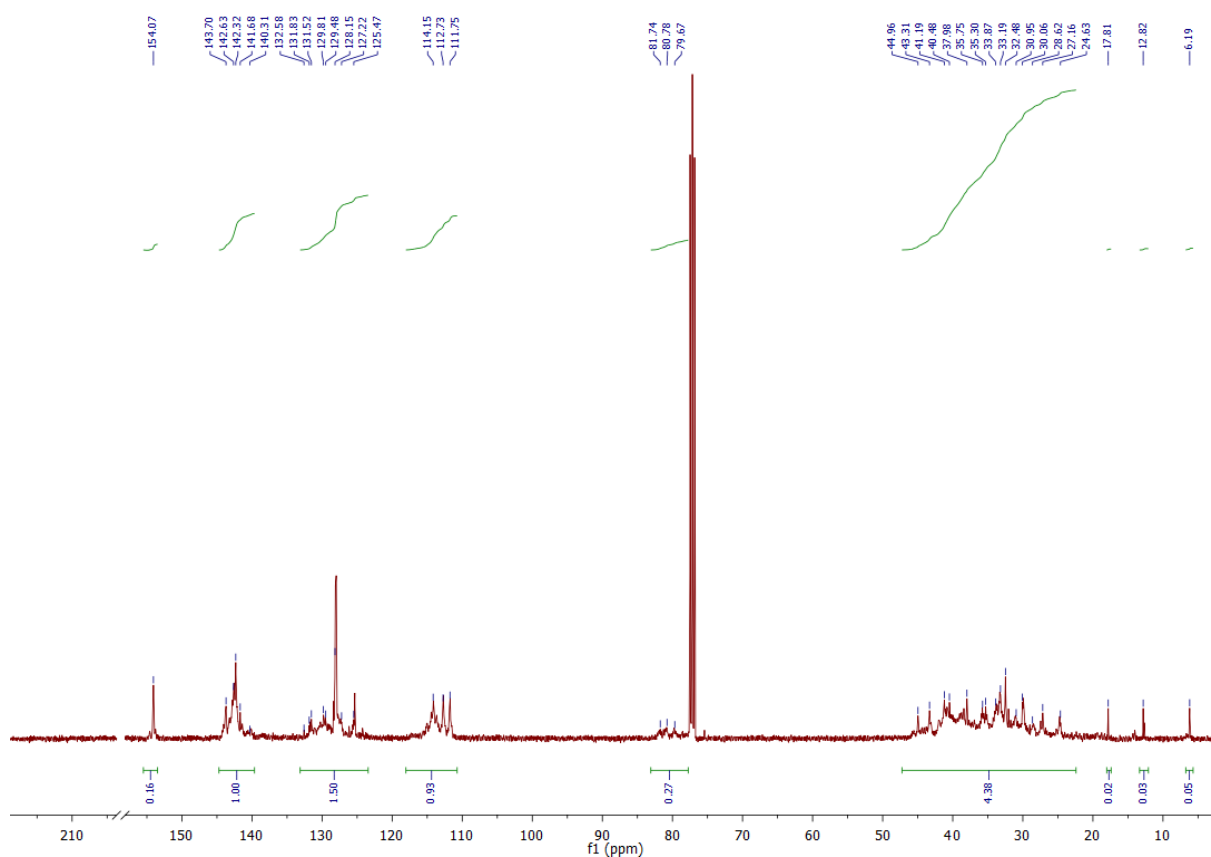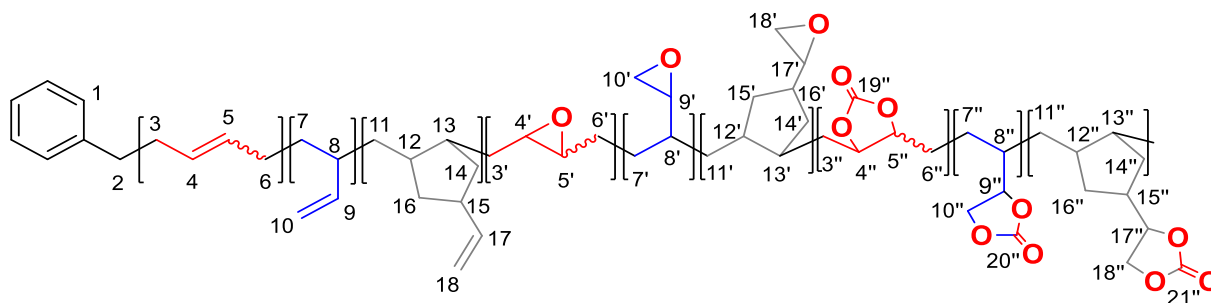
Figure A18. ^{13}C NMR spectrum of **PC-PBD1** in CDCl$_3$.

^{13}**C NMR** (CDCl$_3$, 125 MHz): δ (ppm) = 145.0 - 141.8 (6 x 1-C (styrene), 9-C, 17-C), 132.5 - 123.2 (4-H, 5-C), 115.7 - 111.5 (10-C, 18-C), 83.0 - 77.7 (4''-C, 5''-C, 9''-C, 10''-C, 17''-C, 18''-C), 66.0 - 63.5 (9'-C, 17'-C), 59.5 - 51.0 (4'-C, 5'-C), 46.7 - 6.05 (2-C, 3-C, 3'-C, 3''-C, 6-C, 6'-C, 6''-C, 7-C, 7'-C, 7''-C, 8-C, 8'-C, 8''-C,11-C, 11'-C, 11''-C, 12-C, 12'-C, 12''-C, 13-C, 13'-C, 13''-C, 14-C, 14'-C, 14''-C, 15-C, 15'-C, 15''-C, 16-C, 16'-C, 16''-C).

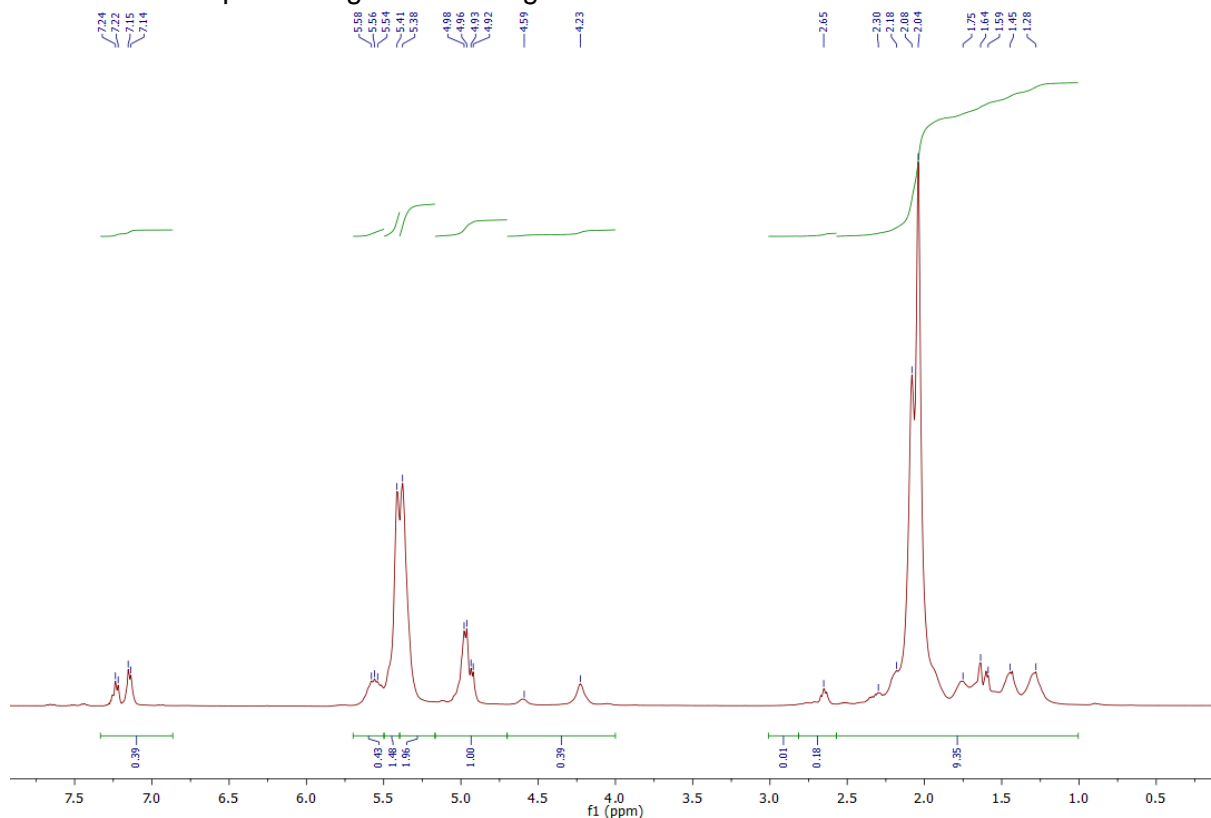Please note the peak assignments in Figure A17 and A18.
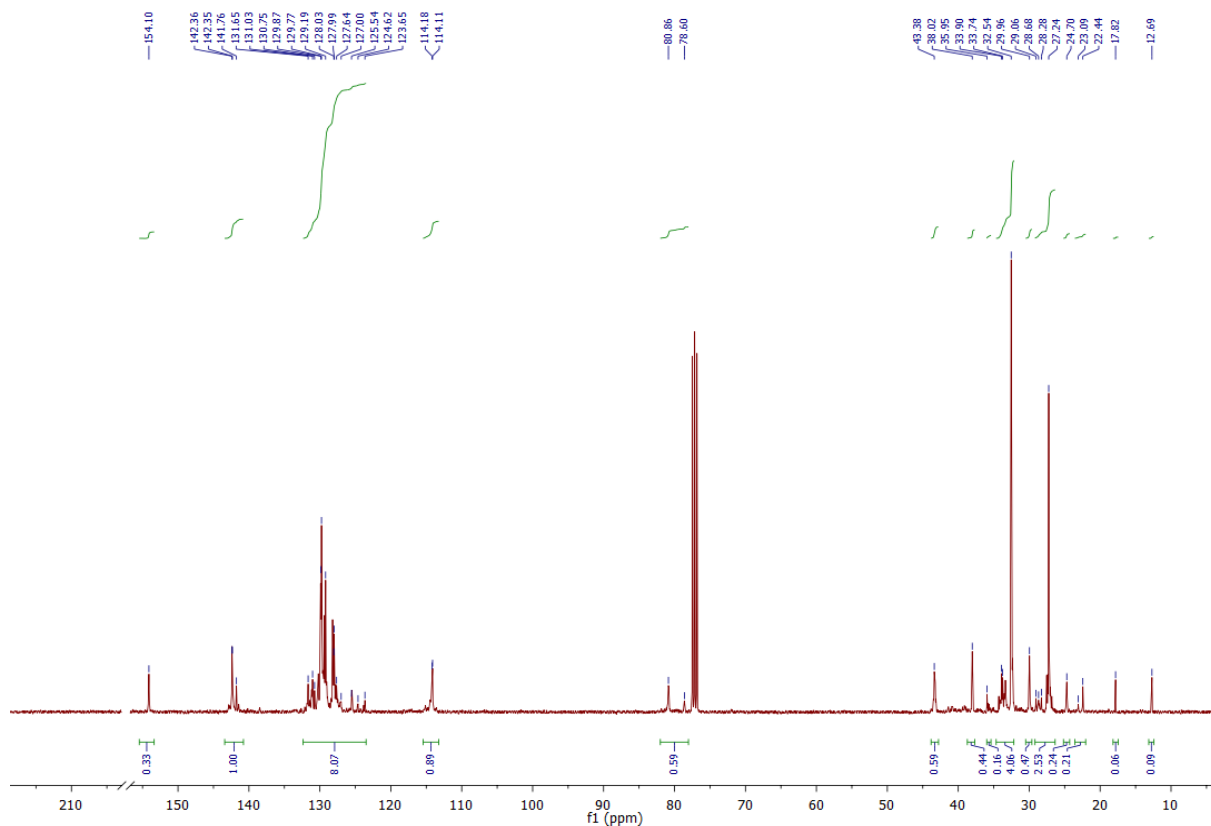

Figure A19. ^{1}H NMR spectrum of **PC-PBD2** in CDCl$_3$.

Figure A20. ^{13}C NMR spectrum of **PC-PBD2** in CDCl$_3$.

Please note the peak assignments in Figure A17 and A18.
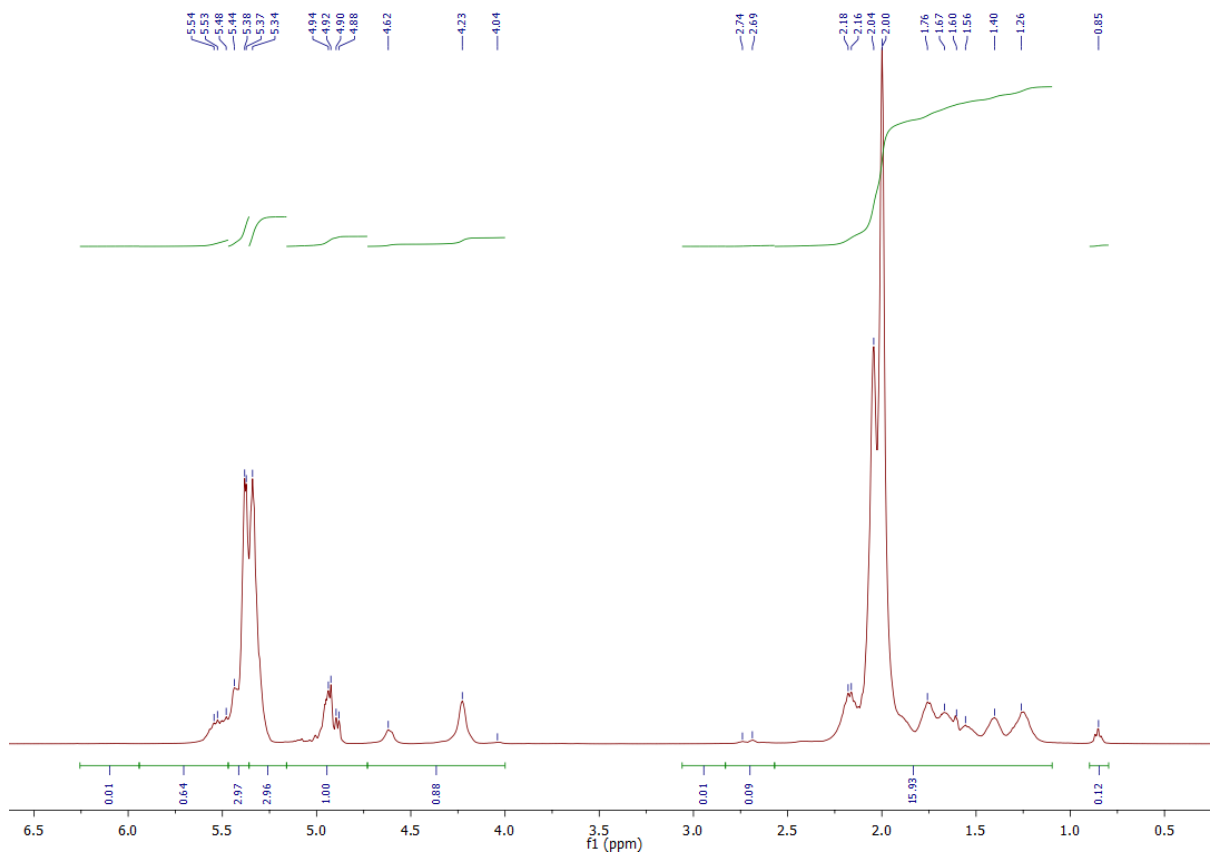
Figure A21. ^{1}H NMR spectrum of **PC-PBD3** in CDCl$_3$.
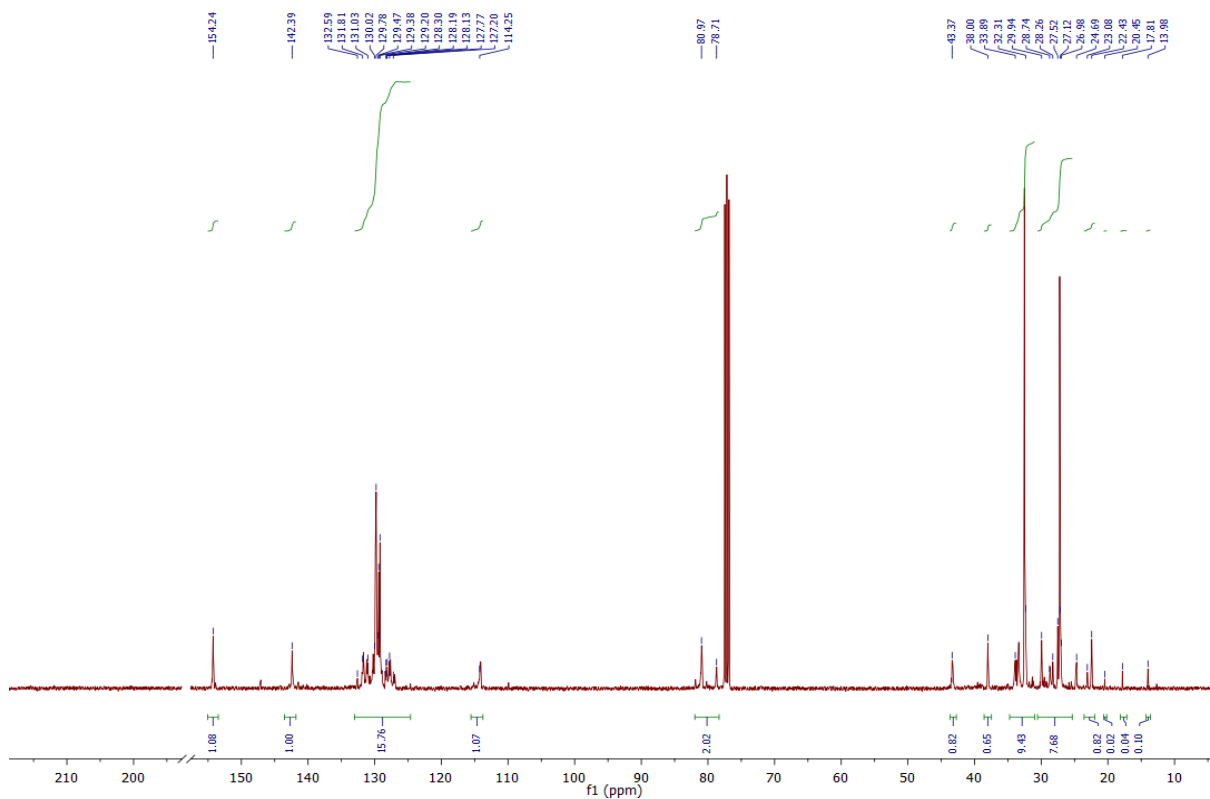

Figure A22. ^{13}C NMR spectrum of **PC-PBD3** in CDCl$_3$.

Please note the peak assignments in Figure A17 and A18.
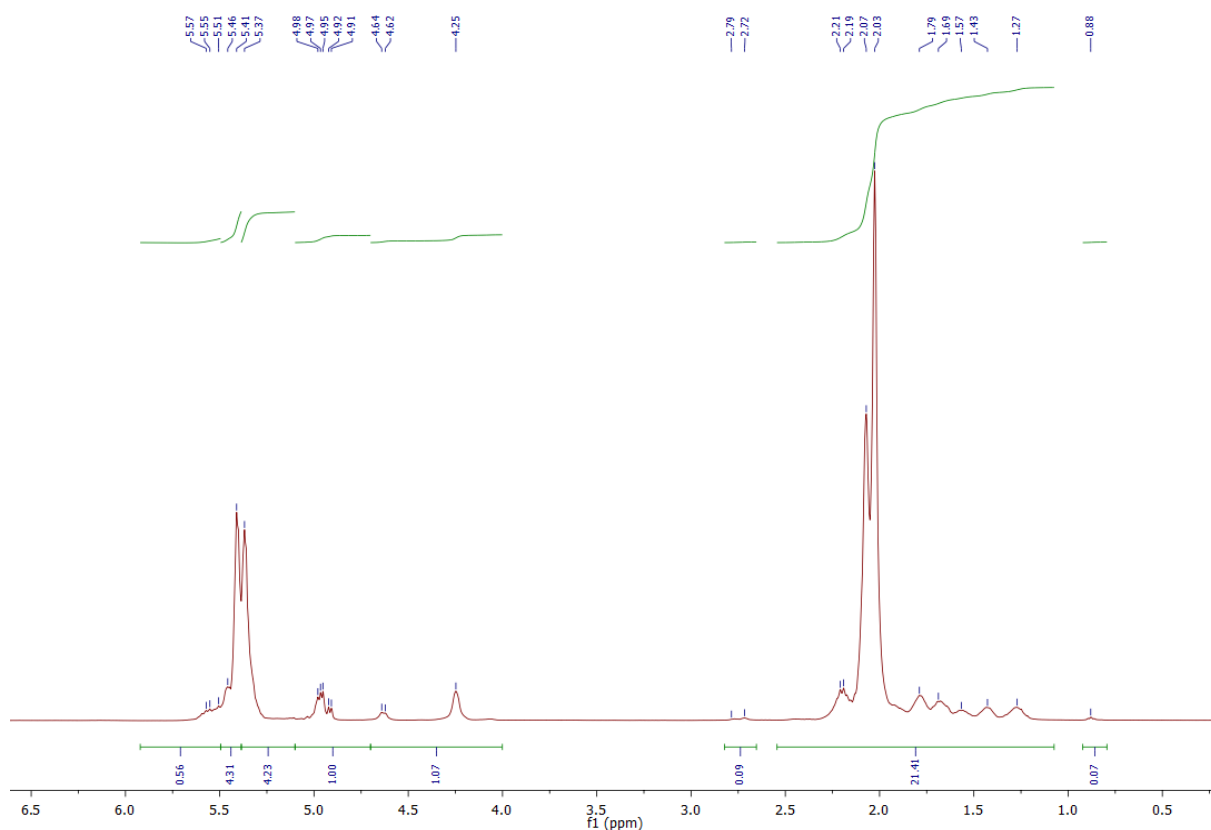
Figure A23. ^{1}H NMR spectrum of **PC-PBD4** in CDCl$_3$.
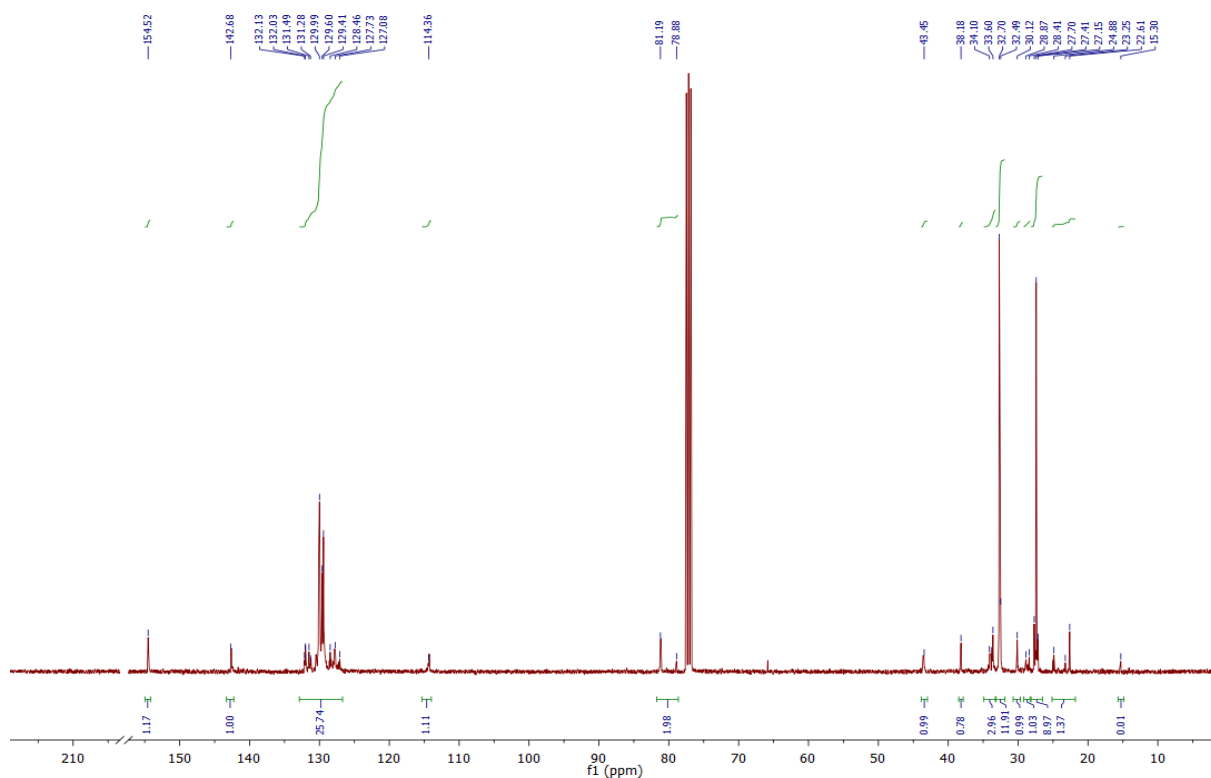

Figure A24. ^{13}C NMR spectrum of **PC-PBD4** in CDCl$_3$.

A4 Section 3.2.3: Selectivity under Screening Conditions

Figure A25. Epoxide ratios in partly carboxylated **PE-PBD1** after the application of different reaction conditions, solvents, and reaction times.

Figure A25. Epoxide ratios in partly carboxylated **PE-PBD2** after the application of different reaction conditions, solvents, and reaction times.
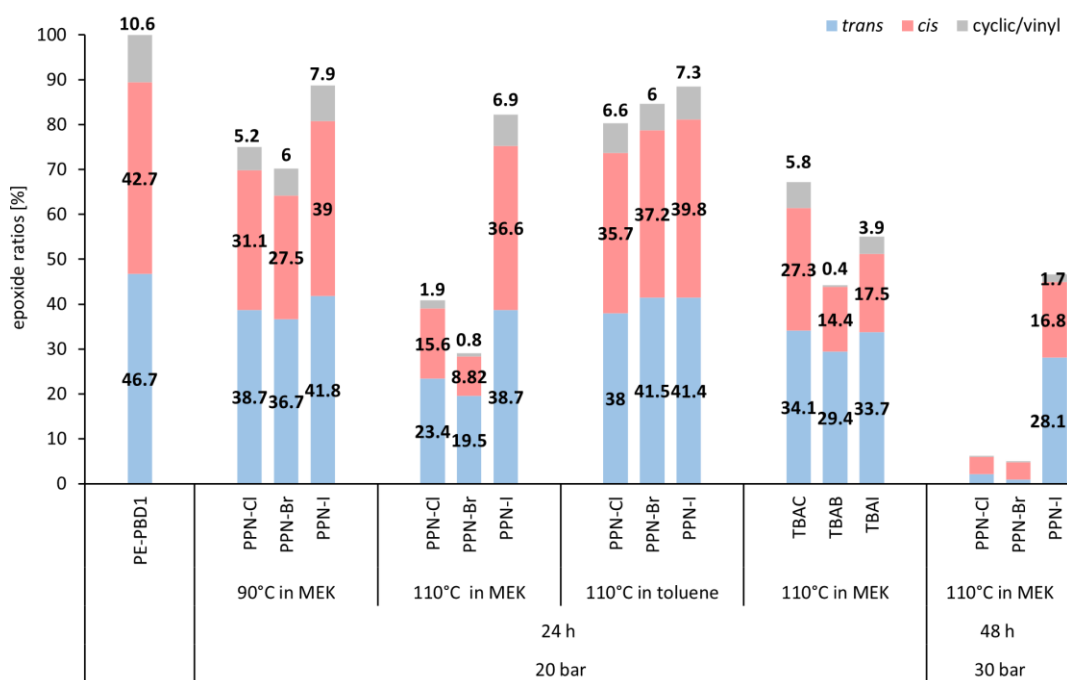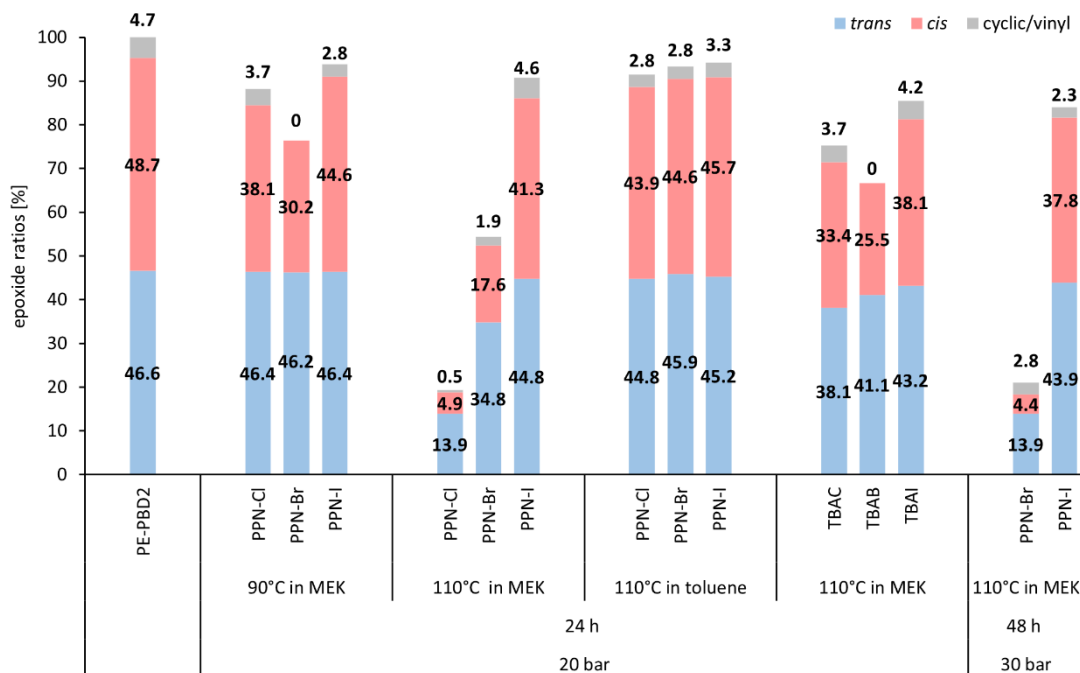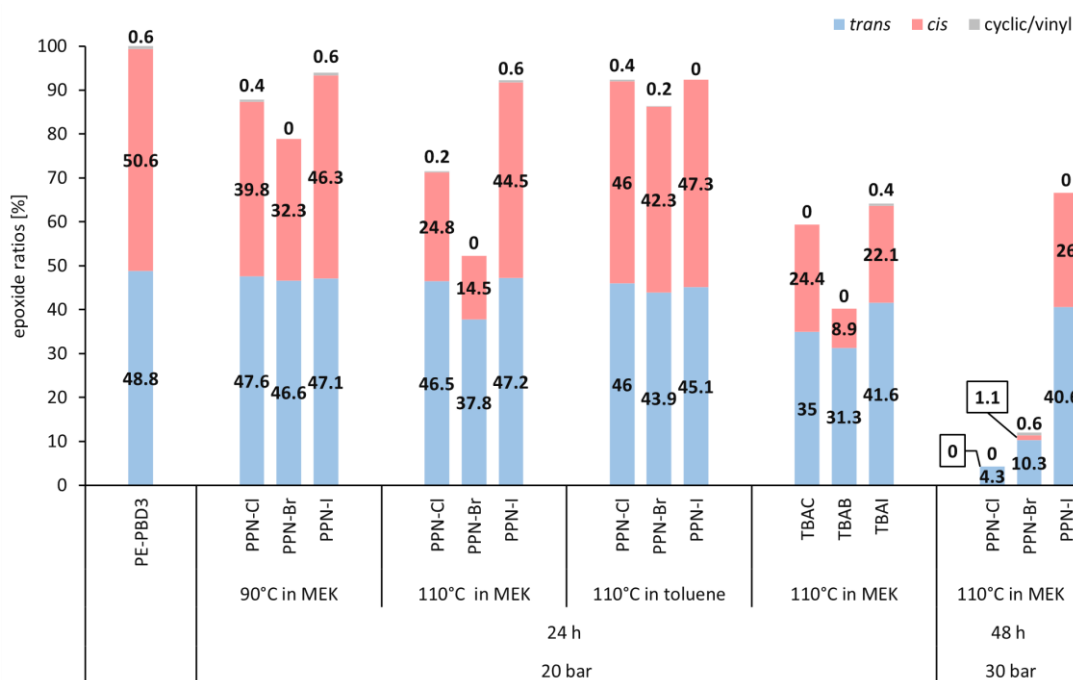
Figure A27. Epoxide ratios in partly carboxylated **PE-PBD3** after the application of different reaction conditions, solvents, and reaction times.
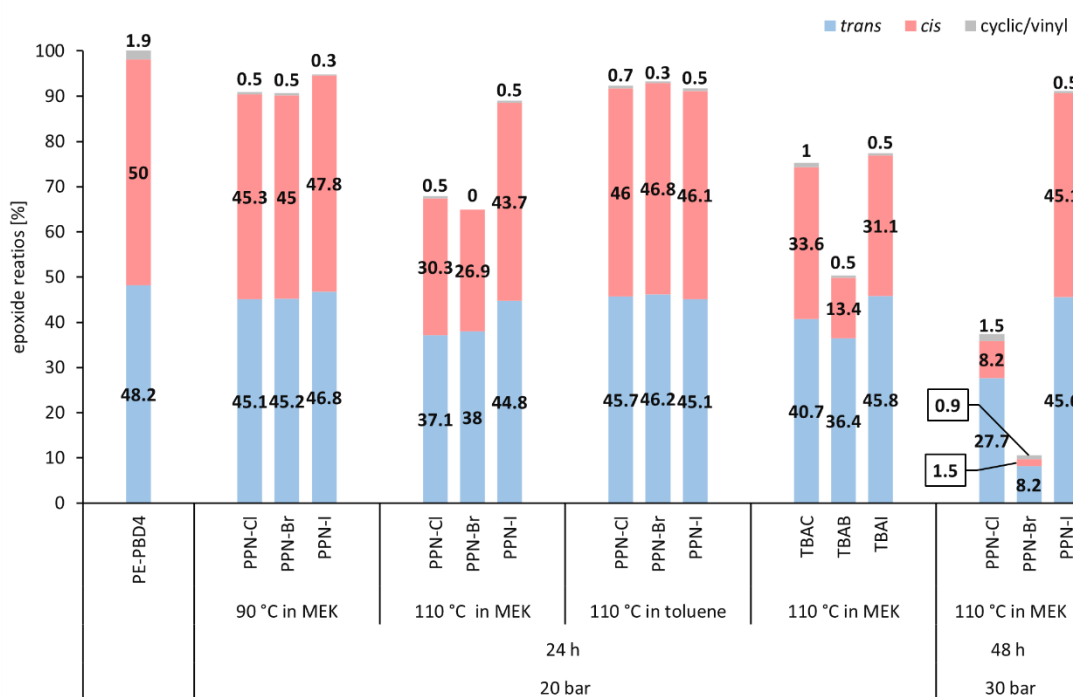

Figure A28. Epoxide ratios in partly carboxylated **PE-PBD4** after the application of different reaction conditions, solvents, and reaction times.

A5   Report: Synthesis of SWCNTs/PP Composites

This project is centered around the synthesis of single-walled carbon nanotube (SWCNT)/polypropylene (PP) composites merely using commercially available substrates. Prior studies proposed the feasibility of producing multi-walled carbon nanotubes (MWCNT)/PP composites with percolation thresholds applying less than 1 wt% MWCNTs.[117] In this study, we explore synthetic routes for combining single-walled carbon nanotubes and PP into composites. The CNTs were sonicated and then subjected to in situ polymerization slurry techniques using a metallocene/methylaluminoxane (MAO) catalyst system. In this system, the co-catalyst MAO anchors itself to the CNT surface by reacting with the present functional groups, initiates the PP polymerization in close proximity to the CNT, and thus promotes an enhanced filler embedding in the polymer matrix. Using this system and substituting MWCNTs with SWCNTs should even lower the filler content to likely below 0.1 wt%. The following reports on first results conducted within this project. First a detailed analysis on commercially acquired TUBALL™ SWCNTs is given followed by an investigation of (potential) functional groups on the CNT surfaces and their interaction with the co-catalysts MAO and trimethylaluminum (TMA). Then, a study on the dispersibility of the CNTs via sonication in two different solvents is provided followed by first results on the synthesis of reference PP. In addition to the homogeneous Zr-based metallocene catalyst mentioned above, two commercial heterogeneous Ziegler-Natta catalysts were analyzed and one was tested giving first results for an alternative catalytic heterogeneous system.

A5.1   SWCNT Characterization

The TUBALL™ SWCNTs were characterized according to well established techniques described in literature.[118] Scanning electron microscope (SEM) images were taken showing highly bundled CNTs (Figure A29). A more detailed analysis with transmission electron microscopy (TEM) and energy-dispersive X-ray spectroscopy (EDX) analysis methods revealed residues of iron catalysts
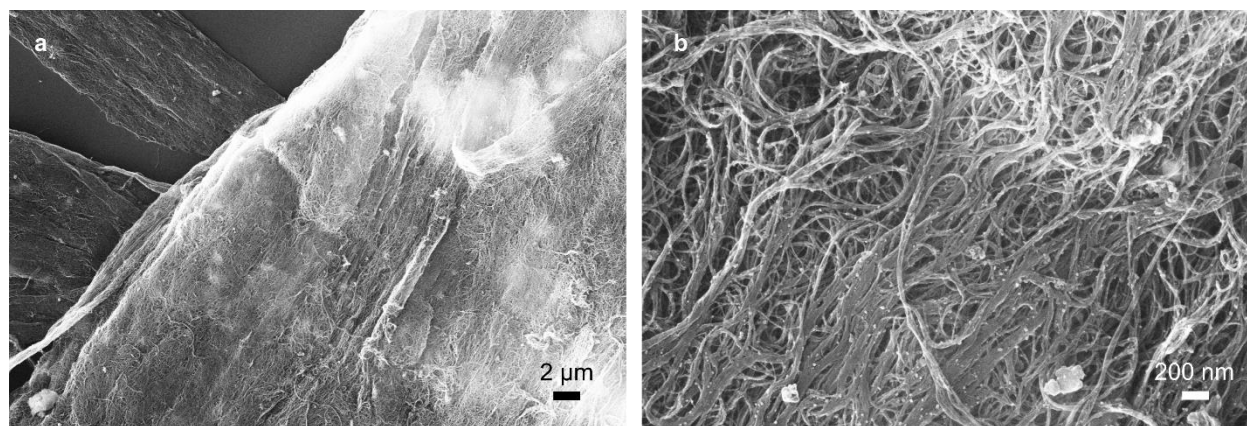

Figure A29. SEM images of untreated TUBALL™ SWCNTs applying the magnifications (a) 2.5 K and (b) 25 K.
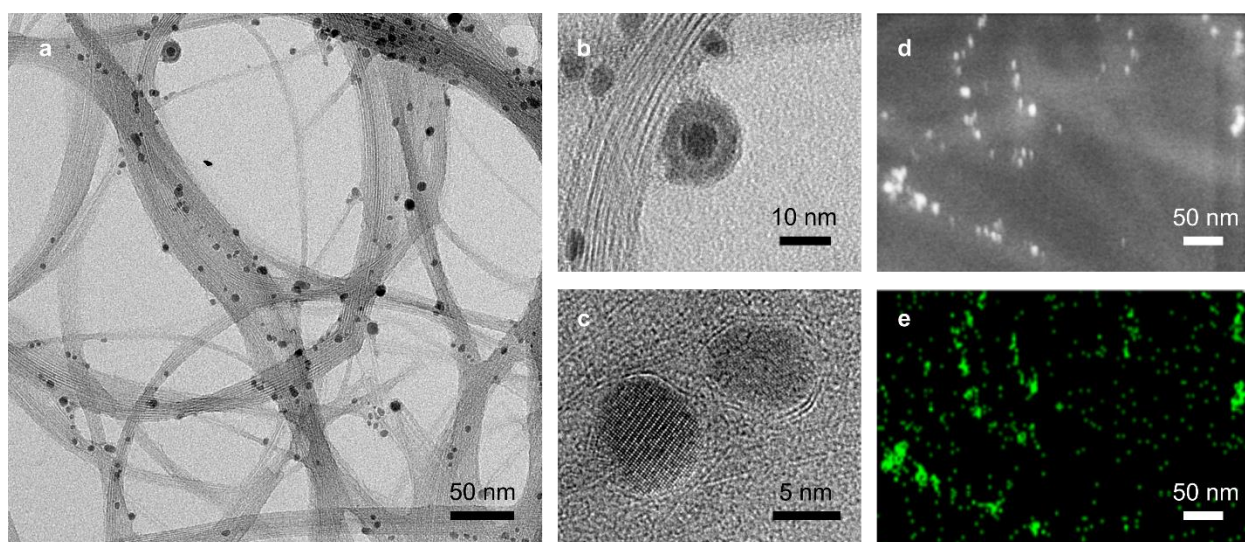
Figure A30. TEM images of (a) untreated SWCNTs, (b) oxidized iron catalyst particles, (c) lattice structure of oxidized iron catalyst particles, (d) overview, and (e) EDX mapping of iron in a TUBALL™ SWCNT sample.

typically used during CNT synthesis (dark particles, Figure A30a – c, and light and green patterns, Figure A30d and e).[119] The iron residues and additionally carbon, hydrogen, oxygen, and sulfur contents were quantified by elemental analysis techniques using three different samples, respectively (Table A10). The carbon content was determined to be 76.2 ± 0.5 wt% and represents an agglomeration of SWCNTs, MWCNTs and amorphous carbon in the provided

Table A10. Properties of TUBALL™ SWCNTs.

mean tube diameter [nm][a]	main tube diameters [nm][b]		tube lenghts [μm][c]	carbon content [wt%][d]	detected non-carbon species [wt%]				G/D ratio[b]	SWCNT content [wt%][e, f]
	metallic	semicond.			H[d]	O[d]	S[d]	Fe[e]		
1.55 ± 0.40	2.05 (532 nm) 1.59 (780 nm)	2.54, 1.68, 1.42, 1.36, 1.33 (532 nm) 1.90, 1.53, 1.09, 1.03 (633 nm)	> 5	76.2 ± 0.5	0.66 ± 0.13	6.56 ± 0.96	0.48 ± 0.06	13.4 ± 0.3	73.1 ± 8.3 (532 nm) 32.9 ± 5.2 (633 nm)	74.0 ± 0.6

[a]Determined by TEM image analysis. 100 nanotubes diameters were evaluated. [b]Determined by Raman measurements using different laser wavelengths (532, 633 and 780 nm). The tube diameters were computed using the equation $d\,(nm) = \frac{234}{\omega_{RBM}-10}$ and were categorized into metallic and semiconducting CNTs using the Kataura plot. The D/G ratios were determined by using the integrals of the D and G signals from 3 different samples. [c]Determined by AFM, conducted and provided by the supplier OCSiAl. [d]Determined by elemental analysis from 3 different samples. [e]Determined by atomic absorption spectroscopy (AAS) techniques from 3 different samples. [f]Determined by TGA and EA analysis.
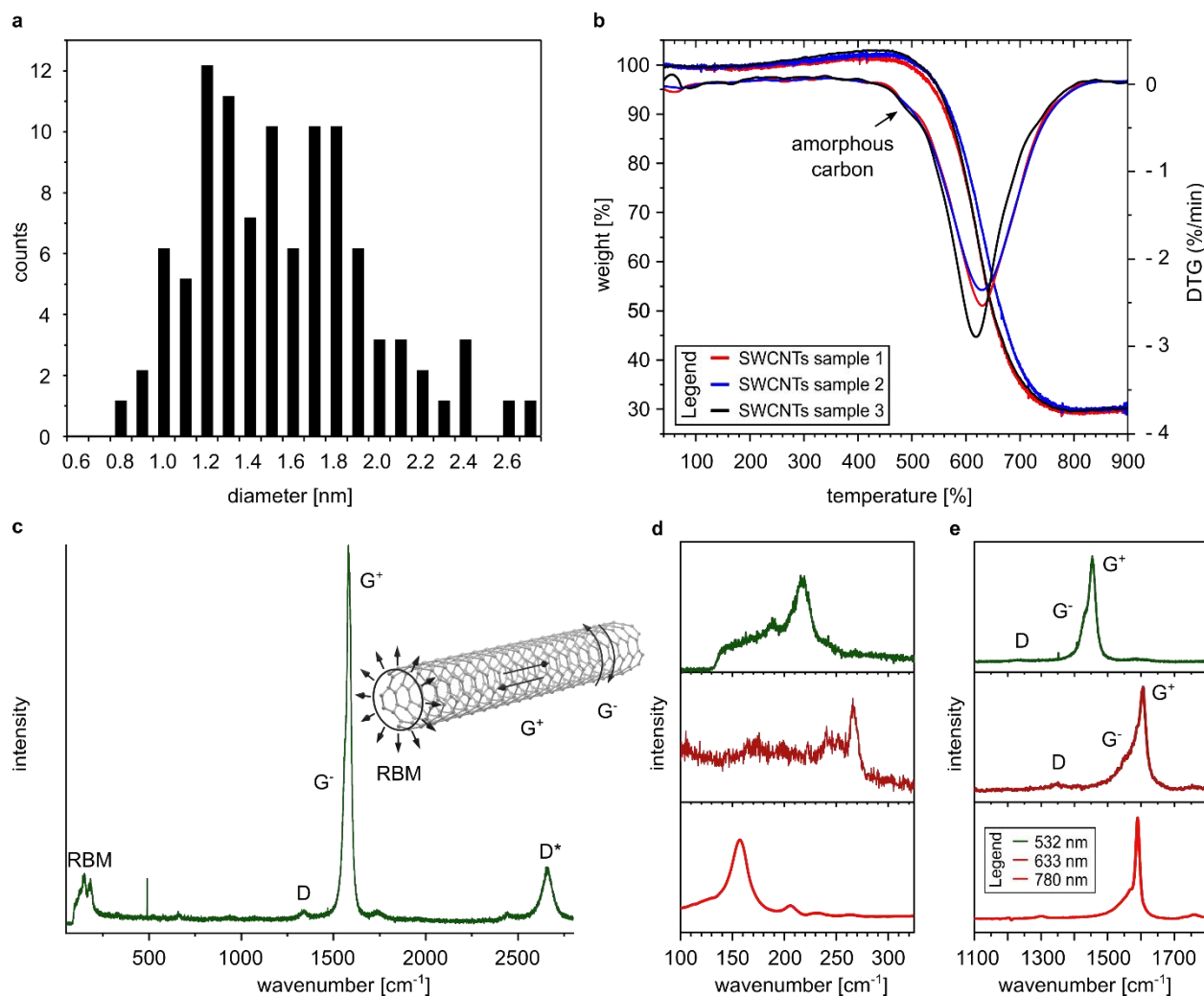
Figure A31. (a) TUBALL™ SWCNT diameter size histogram determined by TEM image analysis techniques on 100 tubes, (b) TGA profiles of TUBALL™ SWCNT samples showing residues of amorphous carbon, (c) Raman spectrum of TUBALL™ SWCNTs measured using a laser wavelength of 532 nm, (d) radial breathing mode (RBM), and (e) D/G ratio and G⁻/G⁺ signals for metallic and non-metallic TUBALL™ SWCNT determined at three different laser wavelengths.

batch. These three species can be distinguished and quantified by thermal gravimetric analysis (TGA).[120] Typically within a thermal degradation profile, amorphous carbon degrades first followed by SWCNTs and then MWCNTs. Runs of three samples were performed revealing 2.2 ± 0.1 wt% of amorphous carbon and no clear indication for MWCNTs (Figure A31b). The SWCNT content can be thus reduced to 74.0 ± 0.6 wt%. TEM images were further used for image analysis techniques to determine the CNT mean tube diameter and its distribution (1.55 ± 0.4 nm, Table A10, and corresponding histogram, Figure A31a). These findings correspond closely to the results found with Raman spectroscopy analysis (Table A10, Figure A31c and d). Three different wavelengths (532, 633 and 780 nm) were used to excite increased fractions of SWCNTs. A certain laser wavelength only meets the resonance energy of some SWCNTs in the sample. The required energy is dependent on the diameter and the nature (metallic or semiconducting) of the CNT. The Kataura plot provides an analytical tool to distinguish between metallic and

semiconducting SWCNTs at given laser energies and known diameters (Table A10).[121–123] The main tube diameters can be calculated from the radial breathing mode (RBM) peaks using the equation $d\,(nm) = \frac{234}{\omega_{RBM}-10}$ provided by earlier works.[124] A deeper look into literature[121,123,125] reveals a broad range of slightly different, but still applicable equations. Depending on the method and CNT sample, researcher derived varying equations and it remains left to the user to choose the best fit. The broadened line shape of the G⁻ feature indicates the presence of metallic CNTs and confirms the findings in the RBM (Figure A31e).[121,123] The high D/G ratios indicate a good
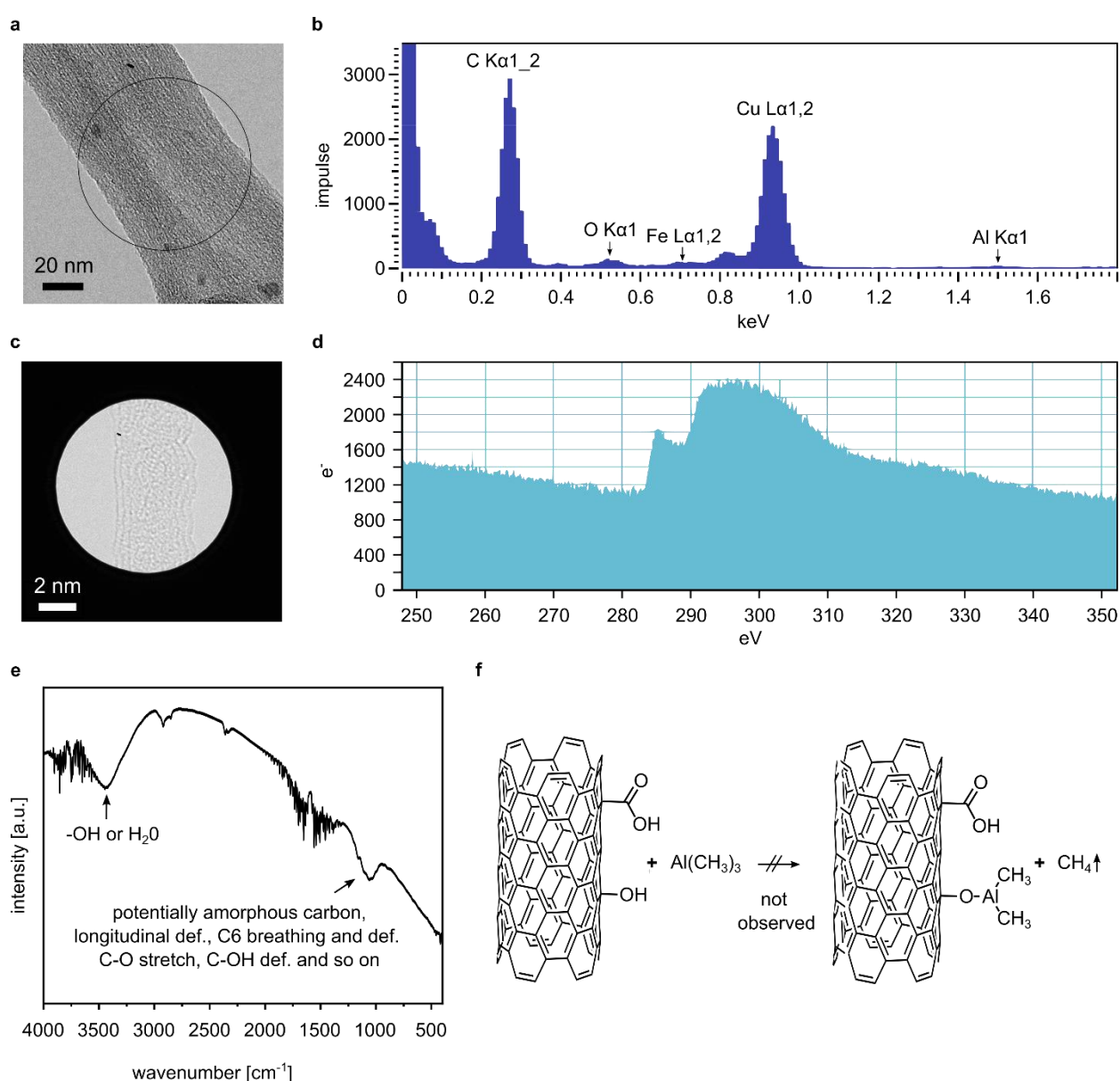
Figure A32. Functional groups analysis of TUBALL™ SWCNTs was performed on (a) nanotube bundles in a TEM apparatus to determine (b) EDX spectra. (c) A Lochfilm in a high resolution (HR)-TEM set-up was used to allow (d) EELS measurements showing merely the carbon edge. Additionally, (e) FTIR measurements in KBr were performed and (f) gas titrations using TMA. The results are representative for several measurement attempts for each technique presented.

structural integrity with little defects and little amorphous carbon contents (Table A10, Figure A31e).[121,125,126]

The existence of (oxygen-containing) functional groups on the CNT surface was investigated by several analytical techniques. TGA measurements did not indicate any functional group decomposition (e. g., carboxylic acid group degradation which is typically between 100 and 400°C, and carboxylic anhydrides degradation with starting temperature around 280°C) before CNT degradation (Figure A31b). Other relevant functional groups such as lactones, carbonyls, quinones, and phenols typically decompose at elevated temperatures at around 400°C which overlaps with the thermal stability limits of the SWCNTs themselves.[127] Further analysis with electron energy loss spectroscopy (EELS), energy-dispersive X-ray spectroscopy (EDX), Fourier-transform infrared spectroscopy (FTIR) and gas titration experiments with TMA confirmed the findings in the TGA and could not (clearly) indicate the existence of other functional groups which were not theoretically detectable during thermal analysis (Figure A32). The intensity of the oxygen signal in the EDX spectrum is too weak to exclude its origin from impurities in the analysis chamber and the signals in the FTIR measurement provide no clear group assignments.

A5.2   Sonication Studies

The SWCNTs were subjected to sonication studies which were conducted in two different solvents: toluene and heptane, to improve the dispersion. The former solvent is typical for academic evaluations and the latter for industrial applications. The treatment with a sonotrode is proven to be very efficient for the separation of CNTs in solvents. The formation of stable dispersions may be assisted by the addition of suitable surfactants. The performance of such sonication attempts is typically influenced by the nature of solvent, its temperature, dissolved gases, particle concentration, immersion depth of the sonotrode tip, and so on. The intensity of the ultrasound and thus the size and probability of cavitation in a given volume is regulated by the amplitude of the vertically moving tip. The bigger the rash the higher the intensity and the harsher the cavitation bubble collapses. Low ultrasound frequencies are beneficial to build up large cavitation bubbles and accordingly equipment with a low processing frequency of 20 kHz was chosen. Despite the advantageous use of ultrasound to exfoliate SWCNTs, it is known that strong sonication may induces defects and/or tube scission.[128] Therefore, TUBALL™ SWCNTs were analyzed during sonication and after applying up to 100 % amplitude in both solvents, 60 % cycle time, constant stirring and 20 min of treatment (Figure A33). *In-line* Raman techniques revealed no further defect evolution in both solvents at max. amplitude (unaltered D/G ratios, Figure A33a and b) and SEM and TEM images did not indicate noticeable tube scission events (Figure A33c - f). SEM images additionally showed degrees of disentanglement in comparison to untreated CNTs in Figure A29.

The *in-line* Raman approach was then used to evaluate the degree of dispersion in both solvents. The same settings were used and experiments were conducted at 80 and 100 %
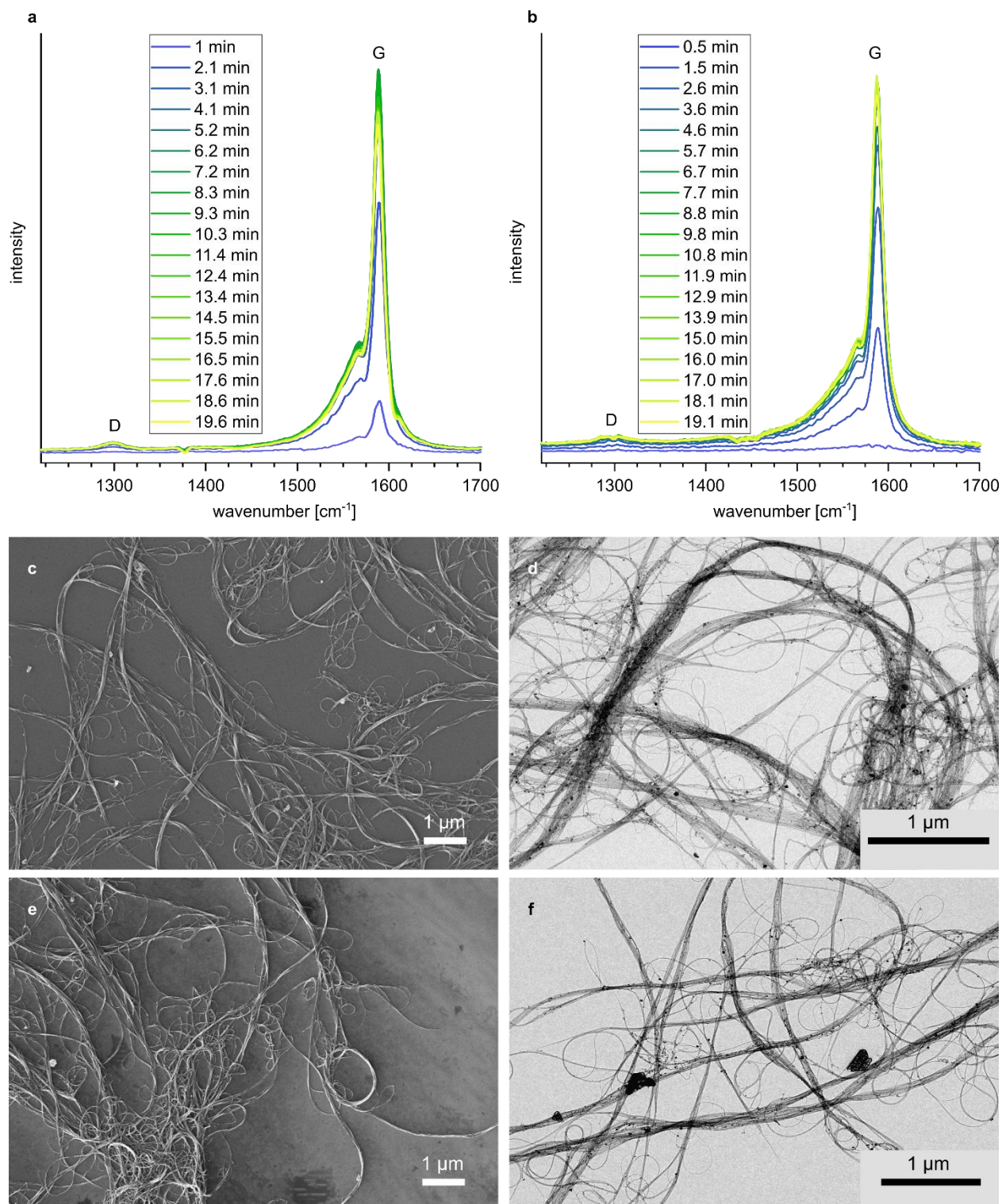
Figure A33. *In-line* Raman analysis of TUBALL™ SWCNT in (a) toluene and (b) heptane performed at 100 % amplitude and 60 % cycle time at RT. The concentration was 0.07 mg/mL, respectively, using 150 mL solvent. G/D ratio is shown, respectively, following the sonication/dispersion for 20 min treatment time with spectra taken every 62 seconds. (c) SEM and (d) TEM analysis of TUBALL™ SWCNTs dispersed in toluene. (e) SEM and (f) TEM analysis of TUBALL™ SWCNTs dispersed in heptane.

amplitude, respectively (Figure A34a). The D* signal was used to evaluate the progress. At time equals zero, no signal is detected as the CNTs are still highly bundled and the sensor highly overproportionally detects solely the solvent. As soon as the sonication starts, the CNTs exfoliate gradually, and the Raman sensor counts more and more passing tubes. A constant signal maximum was detected after about 5 min in toluene independent of the applied amplitude and slightly later at around 8 min in heptane, respectively. This analysis reduces the initially set treatment time to less than half and down to a quarter. Purely visual, following the change of
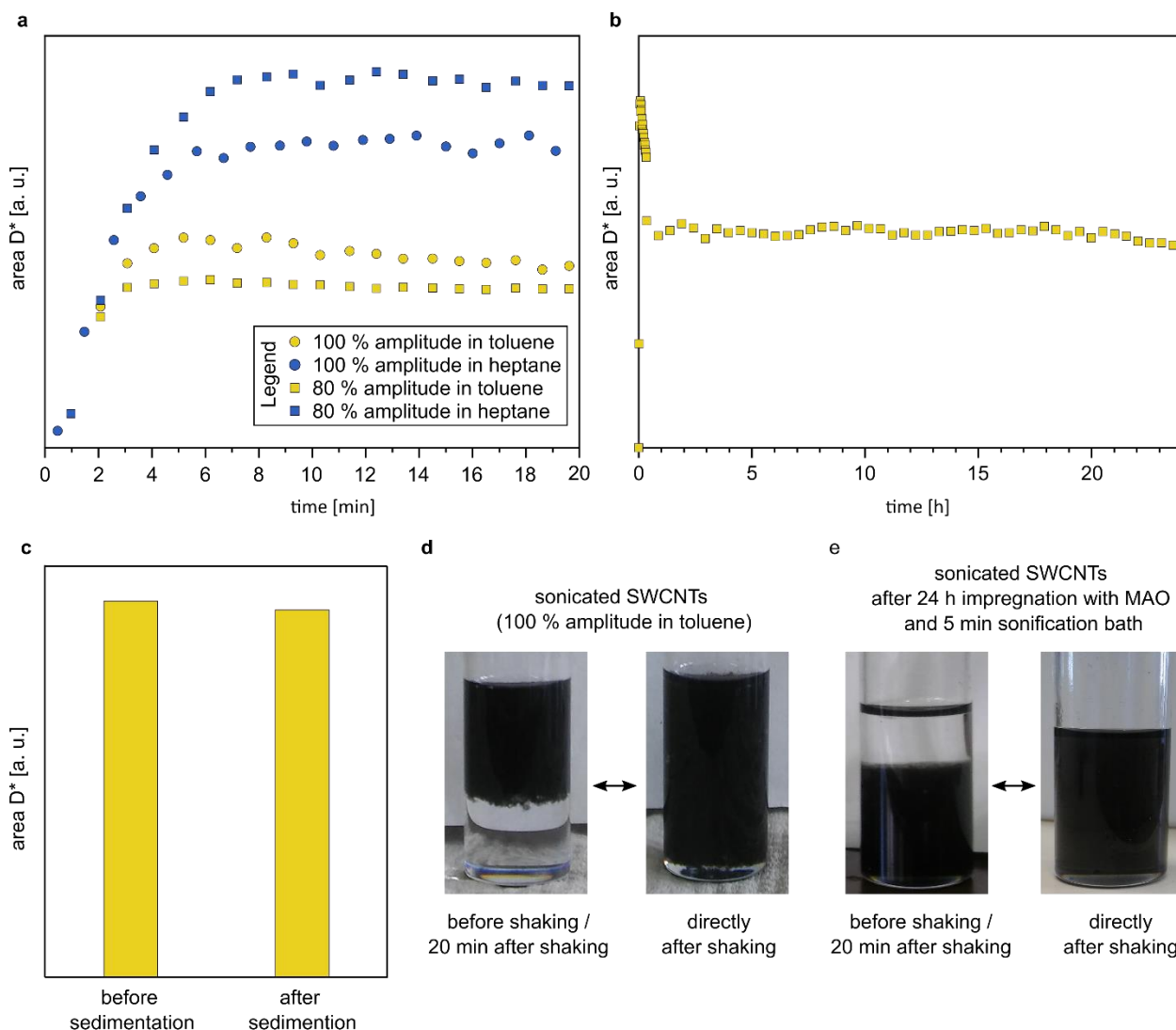
Figure A34. *In-line* Raman analysis on the signal intensities of D* vibrations determined (a) during sonication at 80 and 100 % amplitude and 60 % cycle time in toluene and heptane, respectively, and (b) during and after sonication in toluene at 80 % amplitude and 60 % cycle time. Signal was observed for additional 24 h. All measurements were conducted under constant stirring. (c) Sedimentation study on dispersed TUBALL™ SWCNT in toluene after 20 min treatment at 80 % amplitude and 60 % cycle time. Stirring was stopped and reinitiated after 10 min. (d) Optical analysis of sonicated nanotubes in toluene before and after shaking, and (e) the influence of MAO impregnation on the dispersion grade and behavior. All experiments were conducted using 150 mL solvent and 10 mg SWCNTs giving a concentration of 0.07 mg/mL.

dispersing process was not feasible as the dispersion already appeared deeply black after only 30 s treatment time.

The stability of the dispersion was controlled in a similar fashion. After 20 min sonication treatment at 80 % amplitude in toluene, the dispersion was monitored for additional 24 h applying continuous stirring (Figure A34b). The dispersion appeared to be stable and more importantly recoverable after stopping the stirring for 10 min (Figure A34b - d). Visually, same observations were made for the dispersion in heptane. These findings are predominantly important as they allow for transfers from the sonication vessel to the polymerization reactors without losses of initial quality. Similar to literature[117], it was observed that the impregnation with MAO enhances the degree of CNT separation (Figure A34e). Since no evidence for functional groups on the CNT surface could be provided, it is indicated that MAO is able to interact with CNTs in secondary ways than just the formation of covalent bonds.

A5.3 Reference Polymers

The reference polymer was produced using a homogeneous Zr-based metallocene/MAO catalyst system described in literature.[117] In this system, MAO is supposed to "bind" to the CNTs later on through an impregnation process prior to the in situ isotactic PP polymerization which is conducted under similar conditions as the reference polymerization. This approach seems to increase the dispersion quality and it is believed to allow for iPP initiation and chain propagation close to the CNT surface. The presented results correspond closely to previous findings[117] and match the $M_w \approx 300000$ g/mol required for this project and for favorable (industrial) mechanical properties later on (Table A11). Additionally, yields meeting the desired 50 g scale were accomplished which is necessary to guarantee sufficient amounts for subsequent material analysis.

As an alternative system, industrial heterogeneous Ziegler-Natta catalysts (ZN-M and ZN-LB) were acquired. Elemental analysis revealed 2.54 ± 0.11 wt% (ZN-M) and 2.43 ± 0.02 wt% (Zn-LB) titanium. Slurry polymerization techniques are typical for performance evaluations[129] and

Table A11. Reference polymers synthesized with Zr-based metallocene/MAO catalyst system.^{a}

ref. polymer no.	stirring rate [rpm]	yield [g]	activity [g/mmol·h·bar]	M_w [g/mol]^b
1	250	42.3	131000	270000
2	300	38.9	122000	360000

^{a}Polymerizations were conducted at 45°C in toluene using dimethyl silanediyl bis(2-methyl-4-phenylindenyl)] zirconium dichloride, 2 h reaction time, and a propylene partial pressure of 2 bar. ^{b}Determined using rheology measurements.
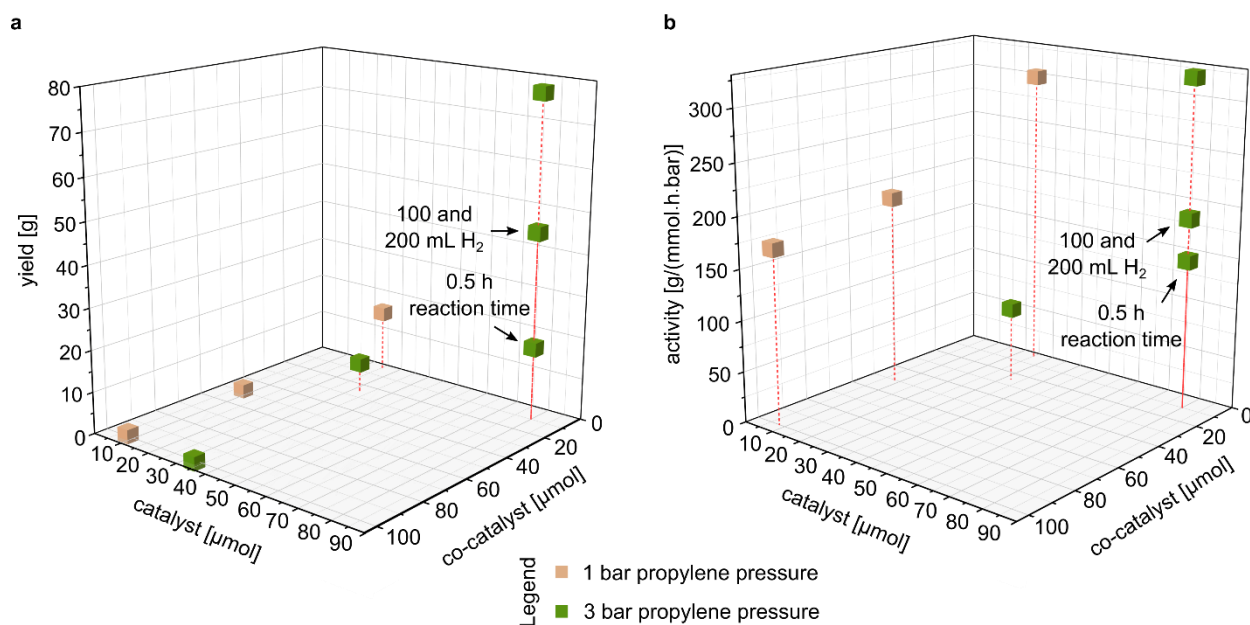
Figure A35. Polymerization results applying the Ziegler-Natta catalyst from Mitsui and TMA as co-catalyst. Experiments were conducted for 1 h at 70°C in toluene, predominantly 150 mL hydrogen was added.

polymerizations were performed largely following standard testing procedures provided by the corresponding supplier. For the ZN-M catalysts, a pre-polymerization followed by a main polymerization in heptane is usually conducted. As the synthesis of finely dispersed CNT composites does not allow for such pre-polymerization procedures, only main-polymerizations were performed. Further, for first studies and logistical reasons, reactions were conducted in toluene and without C-donors. Recommended 0.008 mmol titanium and Al/Ti ratio = 100 molar with triethylaluminum as co-catalyst were used and since no pre-polymerization was undertaken earlier, propylene was initially polymerized applying 1 instead of 5 bar partial pressure. In the following it showed that even smaller Al/Ti ratios assumable in the range between 3 - 10, catalyst amounts of 0.08 mmol, and higher propylene partial pressures of 3 bar are indispensable to reach the desired 50 g scale (Figure A35a and b). Reaction times were typically one hour and generally 150 mL hydrogen was added for molecular weight control (according to the supplier the amount to generate approximately $M_w \approx 300000$ g/mol) prior to initiation. Changes in hydrogen amounts did not seem to drastically change the activity, but it needs to be noted that the reproducibility of these experiments demands further investigations. This system provides an alternative in situ polymerization approach in which the co-catalyst TEA may also bind to the surface of the CNT but only the "free" species is able to activate the active sites in and on the heterogeneous catalyst particles. A comparison of these two systems should give answers to the questions on how much the MAO impregnation and the use of metallocenes substantially enhances the composite properties or if such materials can be produced on an easier level applying commercial and industrially more relevant ZN-catalysts.

A5.4   Experimental Part

A5.4.1 Materials

The TUBALL™ single-walled carbon nanotubes (SWCNTs) were provided by OCSiAl. The catalyst [dimethylsilanediyl bis(2-methyl-4-phenylindenyl)] zirconium dichloride was donated by the former Hoechst AG. The Ziegler-Natta catalysts (denoted as ZN-M and ZN-LB) were provided by Mitsui & Co., Ltd. and LyondellBasell Industries N.V.. Toluene was purchased from BCD Chemie and dry heptane was acquired from Acros Organics B.V.B.A.. Trimethylaluminum (TMA) and Triethylaluminum (TEA) were acquired from Sigma Aldrich. Methylaluminoxane (10 % MAO solution in toluene, 1.72 mol/L aluminum in solution, 5.24 wt% Al) was used as received from Crompton GmbH. Propylene (grade 3.5) was obtained from Westfalen AG and hydrogen (grade 5.0) from Praxair, Inc.. All reactions were carried out using standard Schlenk type techniques. Propylene was purified by the passage through beds containing a molecular sieve (4 Å) and the BASF catalyst R3-11/G. Toluene was distilled and treated similarly.

A5.4.2 Synthetical Procedures

Sonication experiments. The SWCNTs (10 mg) were placed in a three-necked round-bottom flask and dried at 350°C for one hour *in vacuo*. Dry solvent (150 mL) was added under nitrogen flow. Under vigorous stirring with a stirring bar (150 rpm), the dispersion was sonicated using a Bandelin Sonopuls HD 3200 equipped with a titanium cone tip (VS 70) for 20 min.

Polymerization. Zn-based metallocene/MAO catalyst system. Polypropylene was synthesized in a 1 L glass reactor which was dried at 80°C *in vacuo* for 2 h prior to any polymerization reaction. Dry toluene (300 mL) was added, the reactor was flushed with nitrogen and was heated up to 45°C. Then, the system was saturated with 2 bar propylene partial pressure followed by the addition of 4 mL MAO solution and 0.4 mL of a 0.2 M dimethyl silanediyl bis(2-methyl-4-phenylindenyl)] zirconium dichloride solution. The reactions were carried out at constant pressures and were quenched after 2 h with 2 mL ethanol. The products were washed with hydrochloric acid (7 %) and water and were dried at 40°C *in vacuo* to constant weight.

Polymerization. ZN-M/TEA catalyst system. Polypropylene was synthesized in a 1 L metal reactor which was dried at 80°C *in vacuo* for 2 h prior to any polymerization reaction. Dry toluene (300 mL) was added, the reactor was flushed with nitrogen and subsequently heated up to 70°C. Then, hydrogen was added and the system was saturated with the desired (1 - 3 bar) propylene partial pressure followed by the addition of a 1.82 M TEA solution and a 117.7 mg/mL (0.062 mmol/mL Ti) catalyst dispersion. The reactions were carried out at constant pressures and were quenched after typically 1 h with 2 mL ethanol. The products were washed with hydrochloric acid (7 %) and water and were dried at 40°C *in vacuo* to constant weight.

A5.4.3 Instrumentation and Measurements

Scanning electron microscopy (SEM). SEM images were taken on a Leo 1550 equipped with an Everhart-Thornley, InLens and ESB (energy selected backscatter) detector. The samples were exposed to an acceleration voltage of 20 kV.

Transmission electron microscopy (TEM). TEM analysis was performed on a JEOL JEM 1011 equipped with a SIS CCD camera system (1376 x 1032 Pixel). TEM images were applied to image analysis using the software imageJ to evaluate the diameter distributions of the SWCNTs.

Electron energy loss spectroscopy (EELS). EELS spectra were taken on a JEOL JEM 2200 FS equipped with an in-column Omega Filter and an energy resolution of 0.8 eV. The samples were placed on a Lochfilm.

Energy-dispersive X-ray spectroscopy (EDX). EDX was performed on a JEOL JEM 1011 equipped with a SIS CCD camera system (1376x1032 Pixel) and mapping experiments were conducted on a Philips CM 300 UT equipped with a Gatan Multiscan CCD camera system (1024 x 1024 Pixel).

Thermogravimetric analysis (TGA). Thermogravimetric analysis was performed on a NETZSCH STA 409C/CD between 20 and 1000°C under a stream of air at a constant heating rate of 5°C/min. Samples were placed in a Al_2O_3 pan.

Elemental analysis (EA). Elemental analysis (CHNS-O analysis) was carried out on a EuroEA Elemental Analyzer equipped with a HEKAtech HT Oxygen-Analyzer. Titanium contents were determined through an ARCOS ICP-OES spectrometer after dissolving the samples in a mixture of conc. HNO_3 (0.5 mL)/H_2SO_4 (5 mL). Iron contents were determined on a Solaar S Series AAF-F apparatus after dissolving the samples in a mixture of 4 mL aqua regia and conc. $HClO_4$ (2 mL).

Fourier-transform infrared spectroscopy (FTIR). FTIR spectroscopy was performed on a Varian Cary 500. SWCNTs were measured after mixing with KBr and pressing the corresponding pellets.

Raman spectroscopy. Raman measurements were performed on a home-made apparatus equipped with an argon, helium and high-power optically pumped semiconductor laser as well as with a 1000 mm double monochromator and a front-illuminated Open Electrode CCD camera. Spectra were taken applying 532 and 633 nm. *In-line* Raman analysis was performed on a Renishaw System 100 equipped with SDL-laser (780 nm, 500 mW, cw) and a CCD camera. G/D ratios were determined applying a Voigt signal fit using the Software Fityk. The *in-line* measurements were additionally analyzed using the software The Unscrambler. Solvent signals were subtracted.

Rheology. All rheological measurements were carried out on a DHR-2 controlled stress rheometer (TA Instruments, New Castle, USA) equipped with a 25 mm diameter parallel plate geometry. Irganox® 1010 (0.5 wt%) was added to the polymer sample prior to measurements. The experiments were conducted with a plate-to-plate geometry and a gap of 1 mm under a nitrogen stream. Samples were molten at 220°C and held at that temperature for 5 minutes between the plates prior to measurements. Small amplitude oscillatory shear experiments were conducted in a frequency range of 0.1 to 628.3 rads^{-1} at a temperature of 220°C. The strain amplitude γ_0 was set at 0.5 %, which was within the linear viscoelastic regime for all samples. The results of SAOS experiments were evaluated using the TRIOS software of TA Instruments. The application of reference polymers with known molecular weights and rheology curves allows for the determination of molecular weights (M_w) using the horizontal shift factor a_m and the power law $a_m = 10^{-18.3} M_w^{3.4}$.

Gas titration. Gas titrations were performed after sonicating the CNTs as described. After the samples were cooled down to room temperature, TMA (2 M) was added dropwise via a drip funnel and gas evolution was measured with a gas burette (100 mL and 5 mL sizes).

Acknowledgements

First and foremost, I would like to express my gratitude to Prof. Luinstra who provided me with these two highly interesting and challenging research projects. The scientific discussions were most instructive and inspiring.

I am very thankful for the analytical and pragmatic assistance of Felix Scheliga, Kathleen Pruntsch, Stefan Bleck and Jens Pagel. Without the analytical and technical performance and expertise provided by the employees of the Chemistry Department writing this thesis would not have been possible.

Less scientific but not the slightest less important, I would like to thank my working group for all the good times in the social room drinking beer, eating cake, having a chat. Most importantly, I would like to highlight my great times in lab C-318. Thank you, Martin and Marcel, for all the good laughter, ice cream and the support. I will miss it!

I would like to thank my friends and family for their support and the most needed/wanted distraction from time to time. You are the best! However, my very special gratitude is going to Sarah, which literally lived this through with me.

Finally, but most importantly, my deepest gratitude is going to Edvin. Thank you for everything.

Declaration of Oath

I, Sarah-Elisabeth Dechent, hereby declare on oath that this dissertation is written independently and solely by my own based on the original work of my PhD and has not been used other than the acknowledged resources and aids.

Hamburg, February 12, 2023

Sarah-Elisabeth Gertrud Dechent